Marius Reichardt

Multiscale X-ray Structural Analysis of Cardiac Cells and Tissues

Universitätsverlag Göttingen

Marius Reichardt

Multiscale X-ray Structural Analysis of Cardiac Cells and Tissues
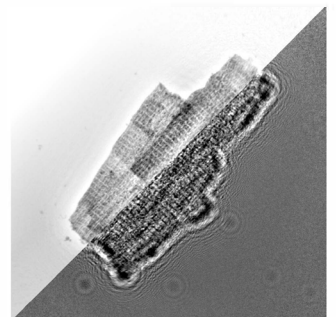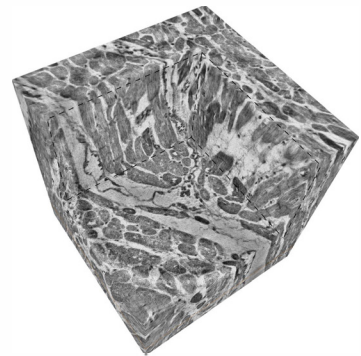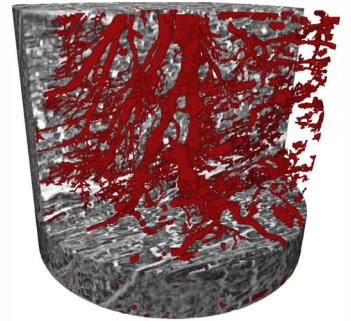
Marius Reichardt

Multiscale X-ray Structural Analysis of Cardiac Cells and Tissues

Göttingen series in X-ray physics
Volume 28

Bibliographic information

Address of the author
Marius Reichardt
Email: marius.reichardt@phys.uni-goettingen.de

Dissertation
for the award of the degree "Doctor rerum naturalium"
of Georg-August-Universität Göttingen
within the doctoral program
"IMPRS for Physics of Biological and Complex Systems"
der Georg-August University School of Science (GAUSS)

Thesis Advisory Committee
Prof. Dr. Tim Salditt, Institute for X-Ray Physics, Georg-August University, Göttingen
Prof. Dr. Stefan Luther, Biomedizinische Physik, Max-Planck-Institut für Dynamik und Selbstorganisation, Göttingen
Prof. Dr. Wolfram-Hubertus Zimmermann, Institut für Pharmakologie und Toxikologie, Universitätsmedizin, Göttingen

Date of the oral examination: 11.10.2021

Preface of the series editors

The Göttingen series in x-ray physics is intended as a collection of research monographs in x-ray science, carried out at the Institute for X-ray Physics at the Georg-August-Universität in Göttingen, and in the framework of its related research networks and collaborations.

It covers topics ranging from x-ray microscopy, nano-focusing, wave propagation, image reconstruction, tomography, short x-ray pulses to applications of nanoscale x-ray imaging and biomolecular structure analysis.

In most but not all cases, the contributions are based on Ph.D. dissertations. The individual monographs should be enhanced by putting them in the context of related work, often based on a common long term research strategy, and funded by the same research networks. We hope that the series will also help to enhance the visibility of the research carried out here and help others in the field to advance similar projects.

Prof. Dr. Tim Salditt
Prof. Dr. Sarah Köster
Editors
Göttingen June 2014

Preface to the present volume

Muscle contraction has fascinated biophysics from the beginning on.

As in the time of Hermann von Helmholtz, muscle physiology bridges physics, life sciences and medicine, also today. The refined understanding in particular of heart muscle has to be built on quantitative modelling, which in turn requires multi-scale structural analysis, from the sarcomere to the entire organ.

To this end, the current thesis has advanced X-ray diffraction and phase contrast imaging tools, using state-of-the-art synchrotron and laboratory X-ray setups. The progress achieved has already helped to address the pathophysiology of heart involvement in Covid-19.

Find out how this works in this well-compiled and excellent cumulative thesis, and do not miss the enjoyable historical perspective on a topic close to our heart!

Prof. Dr. Tim Salditt
Göttingen, December 2021

Contents

Introduction

<div style="text-align: right">1</div>

As the central part of the circulatory system of the human body, the heart is primarily responsible for the distribution of oxygen and nutrients via the blood throughout the body to enable the essential functions of muscles, the brain and other organs [1]. Through the cardiovascular system, a network of arteries and veins with a total length of almost 100 000 km, the human heart pumps oxygenated blood from the left ventricle through the aorta and smaller arteries in the capillary network. On the capillary level, oxygen and nutrients are released and carbon-dioxide (CO_2) and waste materials, such as creatinine (waste product of muscle activity) and urea (by-product of protein and amino acid breakdown) are absorbed. Veins allow the back-transport of the desoxygenated blood to the right atrium of the heart. From the right ventricle the blood is pumped via the lung arteries into the capillary network of the lung. Here, CO_2 is released and new oxygen is absorbed. Oxygenated blood is then transported back to the left atrium and the left ventricle, starting the next cycle.

An average human heart is formed by about 10 billion cells, has the size of a fist and a weight of about 300 grams. The contractile force of a heart muscle cell, named cardiomyocyte, is generated by molecular motors. The smallest contractile unit, the *sarcomere*, is formed by an actomyosin complex which reduces its length during an action potential-triggered, ATP consuming reaction. In a resting state, the human heart beats about 60 to 90 times per minute, resulting in approximately 100 000 heart beats per day. Considering an average volume of 70 ml to 80 ml per beat, more than 7 000 liters of blood are pumped through the body each day. The synchronized contraction of the excitable cardiac tissue cells is controlled by the conduction system, which initiates an electric signal in the sinoatrial node and coordinates the propagation of the action potential through the heart. The continuous function of the heart during its entire lifetime is essential for the proper maintenance of all vital organs. Small dysfunctions or abnormalities can cause drastic changes and effects in the human organism. Therefore, it is very important to understand the cardiac structure from the molecular level up to the scale of the entire organ, as well as its function within the body.

The primary aim of this thesis is to develop imaging protocols to probe the entire cy-

toarchitecture of cardiac tissue using X-ray techniques. To this end, the cardiac structure is investigated using a multiscale and multimodal imaging approach. The 3d arrangement of the cellular network of the heart is investigated by propagation-based phase-contrast X-ray tomography, while the molecular structure of the actomyosin complex is probed by scanning X-ray diffraction. In this context, the concept of 3d virtual histology of cardiac tissue by X-ray phase-contrast tomography is being further developed. The data quality in terms of contrast, resolution and structural preservation is investigated for different sample preparation methods and image acquisition schemes. Additionally, novel data analysis pipelines, including structural analysis and feature segmentation, are presented.

This thesis is a cumulative dissertation consisting of an introduction followed by four peer-reviewed manuscripts published in the context of my work [2–5] and a summary and outlook section. The introduction provides background information on the research on cardiac structure, conventional imaging methods as well as X-ray based imaging techniques. In the first publication, laboratory investigations of entire murine hearts are presented, followed by investigations at higher resolution obtained by synchrotron radiation.

In chapter 2 an experimental imaging approach for the investigation of entire murine hearts by propagation-based phase-contrast tomography using a laboratory liquid metal jet source is presented [2]. In this context, the influence of sample preparation, including paraffin embedding, heavy-Z element staining, dehydration of the tissue using ethanol solutions and the Evaporation of Solvent method is compared. Further, the arrangement of the cellular network is reconstructed by a novel approach to identify local structural orientation and degree of alignment based on Fourier-analysis, as well as by an established gradient based method.

The functionality of the algorithm is also confirmed by high resolution datasets acquired at a synchrotron radiation facility, as presented in chapter 3 [3]. In this work, the 3d murine heart structure was analyzed in a multiscale X-ray imaging approach based on three different configurations set up at the *Göttingen Instrument for Nano-Imaging with X-Rays* (GINIX) setup of the P10 beamline (DESY, Hamburg, Germany). Overview scans of entire murine hearts are acquired using a cone beam illumination provided by Kirkpatrick-Baez-mirrors, before region of interest tomograms with higher resolution were acquired in parallel beam geometry. The sub-cellular structure of cardiac biopsies was probed by a cone beam wave guide illumination.

The concepts of image acquisition and reconstruction explained in the previous chap-

ters were then used to investigate histopathological changes of cardiac tissue structure caused by influenza, typical coxsackie virus myocarditis or Covid-19 (see chapter 4) [4]. Overview scans of tissue samples with a cross section of 3.5 mm were acquired at the laboratory liquid metal jet setup and the tissue structure was investigated based on structure tensor analysis. Additionally, the synthesis of new vessels (angiogenesis) was observed in severe cases of Covid-19. To this end, the vascular network of diseased and control samples was segmented by a deep learning based approach and analyzed by graph theory. By the formation of intraluminar pillars, small capillaries bifurcate from an intraluminar intussusception of myofibroblasts, creating a core between the two new vessels. The presence of intraluminar pillars was also observed using high resolution cone beam CT.

Chapter 5 presents a proof-of-concept experiment, describing how the sub-cellular structure of isolated cardiomyocytes can be analyzed by X-ray imaging techniques [5]. The 3d arrangement of myofibrils in a freeze-dried cell as well as the distribution of mitochondria was determined by high resolution X-ray tomography. Additionally, the actin network of the cell was investigated by confocal fluorescence microscopy. Furthermore, X-ray diffraction experiments on isolated cardiomyocytes were performed to probe the actomyosin lattice. Additionally to the structural analysis of freeze-dried and chemically fixed cells, we investigated for the first time isolated cardiomyocytes in living state.

The type of sample preparation, data acquisition and analysis schemes provided in this work can help to investigate cardiac tissue affected by different cardiovascular diseases. Furthermore, it allows for the analysis of the 3d structure of unstained formalin-fixed, paraffin-embedded (FFPE) tissue. Thus, the histopathological tissue archives of departments all over the world can be accessed and structural changes due to different diseases (not only in respect to cardiac dysfunction) can be investigated, thereby paving the way for better understanding of the body function.

1.1 Cardiac structure and (dys)function

Cardiovascular diseases (CVDs) are the main cause of death worldwide with a rising incidence. While CVDs were responsible for less than 10% of the deaths worldwide by the beginning of the 20th century, the number of CVD-related deaths increased to over 30% by 2016 [6–8]. This corresponds to 17.9 million global deaths due to CVDs in one year. The major share of these death (85%) is attributed to heart attacks and

strokes [6].

Especially in high-income countries, where injuries, infections and nutritional deficiencies play a minor role, almost 50% of all deaths are related to CVDs [9]. In Germany, the leading cause of death in 2019 were CVDs with more than 330 000 deaths, followed by about 231 000 deaths due to cancer [10].

There are many known causes that increase the risk of developing CVD, such as lack of exercise, unhealthy diet, smoking, harmful use of alcohol as well as genetic reasons. Additionally, the risk for CVDs can be reduced pharmaceutically by drug treatment of diabetes, hypertension and high level blood lipids. However, there is no possibility to eliminate the risk completely as of yet.

The increased survival rate for coronary artery disease and myocardial infarction due to medical progress goes along with a high number of patients suffering from ischemic heart disease, including heart failure and fibrosis. Thereby, the structure of the heart is irreparably damaged in the long term. Hence, treating the cause of CVDs efficiently remains one of the biggest challenges to solve in today's medicine. The life quality as well as the life expectancy of millions of individuals could be improved while costs for the health system could be reduced by a better understanding of the cardiovascular system. To tackle this problem, it is essential to understand the underlying structure of the heart.

Until now, the fundamental physiology of the heart, regardless of the influence of diseases, is not completely understood. The exact arrangement of the complex, dense and codependent cardiac network formed by cells of different types is still unknown [11–13]. Hence, it is not possible to explain the contractile function of the human heart in full detail, yet. Throughout history, many studies on the cardiac anatomy were performed to improve the understanding of cardiac structure and function.

1.1.1 A brief history of cardiac anatomy

This section presents a summary of the historical development of cardiac anatomy and function over the last 5000 years and is based on the following review articles [14–17].

Figure 1.1 shows a timetable of the understanding of cardiac anatomy over the last centuries.

First reports about the anatomy of the human heart date back to ancient Egypt around 3000 BC. Figure 1.1A shows a hieroglyph representing the heart with the main ves-
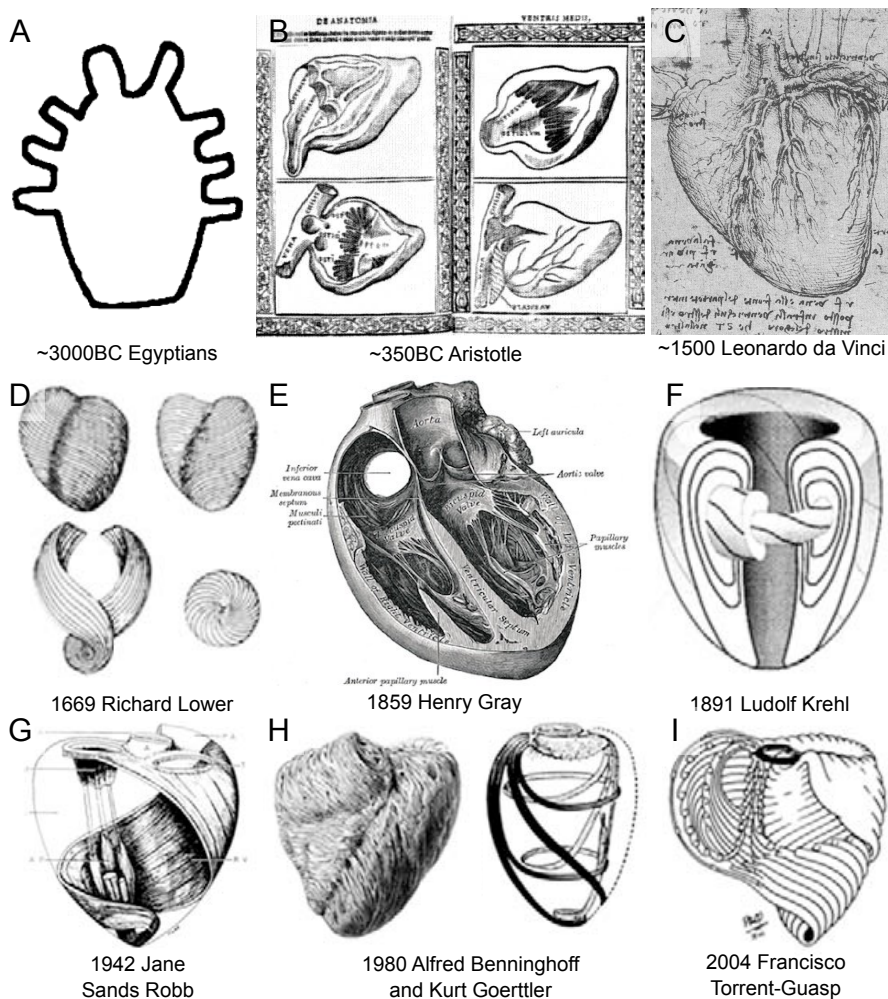
Fig. 1.1: Historic timetable of cardiac anatomy. (A) Hieroglyphic representation from the ancient Egyptians [17]. (B) Drawing of the cardiac anatomy by Aristotle [15]. (C) Sketch of the heart by Leonardo da Vinci [15]. (D) Cardiac model by Richard Lower [18]. (E) Text book figure of Henry Gray's anatomy [16]. (F) Concept of a "Triebwerk" by Ludolf Krehl [18]. (G) Jane Sands Robb's model of the heart [18]. (H) Cardiac fiber model of Alfred Benninghoff and Kurt Goerttler [18]. (I) Model of the helical ventricular band by Francisco Torrent-Guasp [18].

sels attached to the top of the organ. Already back then, the heart was considered the central organic motor of the body. Egyptians believed the heart was responsible for the transport of blood, air, urine and feces, as well as allocated human intelligence, emotions and desire. Knowledge of the heart structure and function was still in its infancy and mostly obtained from the mummification process and veterinary dissections. However, it enabled medical progress such as for example pulse-monitoring of patients in the 17th century BC by correlating the heart rate to a water clock.

Next important information on human anatomy was delivered by the Greeks. After Homer claimed the heart to be the source of bravery and human courage, noteworthy historical figures such as Asclepios and Alcmaeon (a student of Pythagoras) started to study the heart from an anatomical viewpoint. Around 460 BC an anatomical series of 70 books without any philosophical speculations, the Hippocratic Corpus, was published by Hippocrates from the school of Cos. In the book titled "On the Heart", the macroscopic structure of the heart was described for the first time as a strong muscle. The interventricular septum, semilunar valves and morphological differences between the thick-walled left ventricle and thinner right ventricle were described. Furthermore, the atria were mentioned for the first time, though their function was misinterpreted as "ears" to capture air.

The next update on the cardiac anatomy was made by Aristotle around 350 BC, who believed the heart to be formed by three chambers. He described the right and left ventricle as well as a medial chamber, which can be related to the left atrium. Since the right atrium is directly connected to the venae cavae, he did not consider it to be a part of the heart. Within the right chamber, he identified sinews, later known as "chordae tendinae", connected to the papillary muscles. He pictured that all chambers were connected to the lung via "ducts" and that there was a connection between the left and right ventricle. The idea of oxygen exchange in the lung and of a closed blood circuit did not exist yet. Instead, the Greeks believed that the brain was the origin of all blood vessels and that arteries narrow to become nerve fibers. This idea was refuted around 300 BC by Erasistus, who identified a connection between arteries and veins. He defined the heart as a double pump which distributes blood through the right ventricle into the veins and pneuma (air and vital spirits) through the left ventricle into the arteries.

In the Roman era around 130 AD, Claudius Galen discovered that arteries contain blood. Further, he recognized fibers with different orientations (long, sectional and diagonal) within the heart wall. However, he did not classify the heart as a muscle

since heart function is autonomously and cannot be moved voluntarily. He believed that the heart is formed by two chambers. The left ventricle contained air and was connected to the right ventricle by a diaphragm permeable for blood, allowing it to flow in an ebb-flow motion from right to left ventricle through invisible holes in the septum.

This assumption was state of the art in the western world until the 16th century, when Leonardo da Vinci described the anatomy of the heart as we know it today: a four chambered organ with two ventricles and one atrium on top of each ventricle including the auricular appendages. He described the heart as a pump and identified the spiral blood flow in the aorta near the aortic valve, but he could not conclude the directed circular flow of the blood. He supported Galen's assumption that the ventricles are communicating by invisible pores and misjudged that the heart has the purpose to produce "vital heat" by friction of the blood.

Matteo Realdo Colombo is credited to be the first who implied that air and blood mix in the lung and the heart valves allow an unidirectional blood flow. Here, it is worth noting that the idea of separated ventricles as well as an oxygen exchange in the pulmonary circulation was already discovered in the 13th century in the Islamic area by Ibn-Al-Nafis.

During the 17th century, research on cardiac function and anatomy continued. In Richard Lowers work "Tractatus de Corde", he described the heart as a four-chambered fibrous muscular organ. He also described the contraction of myocardial fibers resulting in the blood flow from the heart to the lungs and back. In the first half of the 19th century, Wilhelm His and Johann Evangelist Purkinje discovered the conduction system of the heart, which enables a controlled contraction of the cardiac muscle cells. Further, sub-cellular structures such as muscle fibers, striated myofibrils and the cellular membrane (sarcolemma) were identified by Bowman in 1840 [19].

In the middle of the 19th century, it was assumed that all discoveries of the human anatomy had been made. In this era many textbooks were published by renowned physicians all over the world such as Jakob Henle ("Handbuch der systematischen Anatomie des Menschen"), Xavier Bichat ("Anatomie Generale") and Henry Gray and Henry Vandyke Carter ("Grays Anatomy"). Nevertheless, due to ongoing research and new discoveries the textbooks had to be updated constantly. In October 2020, the 42th edition of "Grays Anatomy" was released. Concerning the cardiac anatomy, most of the open questions were related to the cardiac function and structural changes caused by CVDs. For example, in 1891 Ludolf Krehl introduced the idea of a circumferential

arrangement of cardiomyocytes in the middle layers of the left ventricle wall, called
"Triebwerk", to provide a driving force for ventricular contraction. Following the idea
of a fiber-like alignment of cardiomyocytes, many other models were published in the
20th century. The lower part of Fig. 1.1 shows the models of Jane Sands Robb (1942),
Alfred Benninghoff and Kurt Goerttler (1980) as well as a more recent model of the
"helical ventricular myocardial band" by Francisco Torrent-Guasp [18].

Most of these models indicate that the muscle cells are arranged in a helical manner,
emerging from the apex spinning up to the base [18, 20] or also as a nested set of
warped "pretzels" [21]. So far, no model of the cardiac structure can explain its con-
tractile function in full detail. Another more recent approach is to describe the heart
as a complex network of cardiomyocytes which are arranged in a mesh of extra cel-
lular matrix [13, 22, 23]. A short summary of the current state of cardiac anatomy is
given in the next section.

1.1.2 Current state of cardiac anatomy

The cardiac function relies on an intricate, hierarchical molecular and cellular archi-
tecture. On the molecular scale actomyosin complexes form sarcomeric units, which
are arranged in elongated myofibrils within a single cardiomyocyte. Chains of my-
ocytes are embedded in connective tissue and form aggregation within a complex cel-
lular mesh supported by an extra-cellular matrix (ECM). The specific composition
and alignment of this network represents the foundation of the life-sustaining heart
function [11, 13].

A sketch of the cardiomyocyte blueprint is shown in Fig. 1.2. On the nanoscale, the
contractile force of the heart is generated by molecular motors composed of an acto-
myosin complex. The smallest contractile unit is called *sarcomere* [25–27]. An aver-
age sarcomere of a human cardiomyocyte has a length of about 2.2 µm in the relaxed
state and is composed of thick myosin filaments and thin filaments formed by actin,
troponin and tropomyosin. The structure of single actin and myosin filaments is well
understood. While the thick filaments are a composite of multiple myosin molecules
arranged in a helical manner with a distance of 14.3 nm between their head groups
and a periodicity of 42.9 nm, the thin filaments are composed of a single filamentous
actin (f-actin) strand. F-actin is a double helix of single actin molecules with an inter-
molecular distance of 0.55 nm and a periodicity of 35.75 nm. One sarcomere reaches
from one Z-disc to the next one. The area around the Z-discs contains thin filaments
and is called I-band [19, 28, 29]. The myosin rods are located in the A-band. The
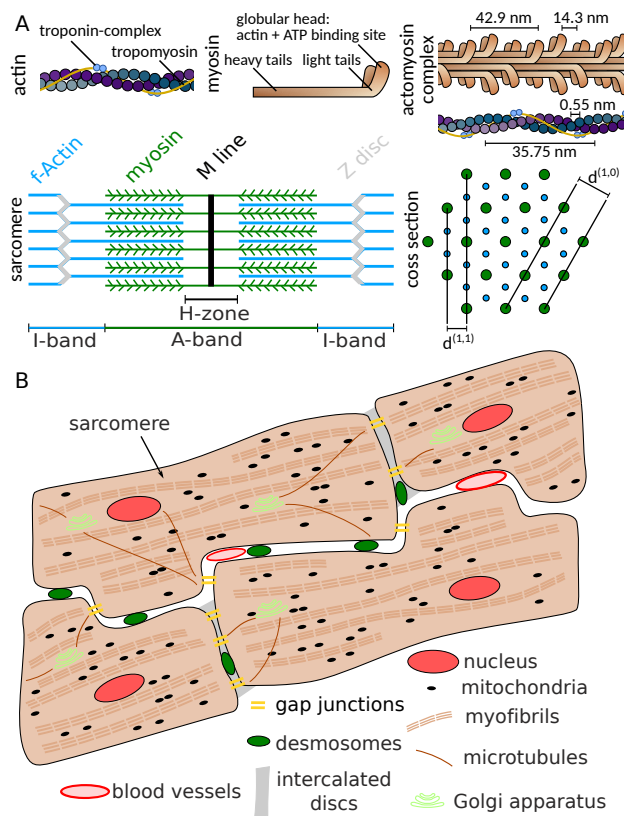
Fig. 1.2: Sketch of the cardiomyocyte structure. (A) A sarcomere is composed of thin filamentous actin and thick myosin filaments. Thick filament bundles are an assembly of multiple myosin molecules with heavy tails and a globular head with an actin and ATP binding site arranged in a helical manner. They exhibit a periodicity of 42.9 nm and a distance of 14.3 nm between their head groups. Thin filaments, composed of actin, troponin and tropomyosin, form a double helix with an intermolecular distance of 0.55 nm and a periodicity of 35.75 nm. Sarcomeres are mirror symmetrical structures connected by Z-discs. The area around the Z-discs (A-band) is composed of actin filaments, which overlap with myosin on the side facing the center. The area containing thick filaments is called I-band. In the center of the sarcomere, where only myosin is present (H-zone), the thick filaments are connected by the M-line which also forms the mirror axis. The cross section of the hexagonal sarcomere lattice has a 2:1 actin-to-myosin-filament ratio and is described by the distances $d^{(1,1)}$ and $d^{(1,0)}$. Figures adapted from [24]. (B) Sketch of the cardiomyocyte network. The contractile function of individual cardiomyocytes is provided by chains of sarcomeres called myofibrils. Energy is provided by mitochondria. Further, cardiomyocytes contain a nucleus, a Golgi apparatus and microtubules. The cardiomyocytes are connected via intercalated discs, gap junctions and desmosomes and surrounded by extracellular matrix containing the capillary network. Adapted from [5].

naming of the areas is related to its imaging properties: A for anisotropic and I for isotropic scattering of polarized light. The center of the A-band, where no thick and thin filaments overlap, is called H-zone, corresponding to the German word "Hellerscheibe" (clear disc). The dense line connecting the thick filaments is named M-line ("Mittelscheibe", middle disc).

Each myosin filament is surrounded by six thin actin filaments and each thin filament by three myosin filaments, resulting in a hexagonal sarcomere lattice with 2:1 actin-to-myosin-filament ratio. The inter-filament lattice can be described by the distances $d^{(1,1)}$ and $d^{(1,0)}$.

The contraction process is caused by an action potential-triggered, ATP consuming, isothermal reaction with an efficiency of almost 50% [30]. The process of shortening of the sarcomere can be explained by the sliding filament theory [19, 31]. In a rowing-like motion the actin filaments slide over the myosin filaments, pulling the Z-discs toward the center of the sarcomere. The link between electrical excitation triggered by the action potential and muscle contraction is given by the release of calcium (Ca^{2+}) ions.

The sarcomeres form long chains, connected by Z-discs, called myofibrils [32]. About 80% of the volume load of a single cardiomyocyte with a length of about 100 µm to 150 µm is filled with myofibrils. The dimensions of the cardiomyocyte is defined by the cell membrane, called sarcolemma. Besides covering the cell, it contributes to the excitation and contraction process due to its electroconductivity and elasticity. Next to myofibrils, a cardiomyocyte contains mitochondria, which are located in close proximity to the myofibrils and provide ATP, a nucleus, containing the DNA, the rough endoplasmic reticulum and sarcoplasmic reticulum for ion storage [33]. The decay-time of the ions channels located in the sarcolemma is in the range of hours. Therefore, microtubules serve as "highways" from the Golgi apparatus to the membrane and enable directed transport of the channels [33].

Cardiomyocytes tend to form long myocyte chains which are connected by intercalated discs at the longitudinal side of the cell. A lateral connection of the cells is provided by gap junctions. These connections allow the flow of the action potential caused by a depolarizing current from one cell to another. Inter-cellular stability is increased by desmosomes, linking neighboring cells [34]. Aggregations of cardiomyocyte chains are embedded in connective tissue, the extracellular matrix, including elastic and collagenous fibers and a capillary network supporting the cells with oxygen and nutrients.

The heart muscle tissue, called the myocardium, is formed by a complex network of cardiomyocyte aggregations, which are arranged in several layers and enable the contractile function of the heart. The outer surface of the heart is covered by a thin layer of tissue, named pericardium, which acts as a protective film. On the inside of the ventricles, another layer of tissue, the endocardium, separates the myocytes from the blood pool. A sketch of the gross cardiac anatomy is shown in Fig. 1.3.

The intrinsic electrophysiological system controls the cardiac contraction cycle. Starting at the sinoatrial node, which is located in the wall of the right atrium, an electrical signal excites the atria by the Bachman's bundle causing the contraction of cardiac
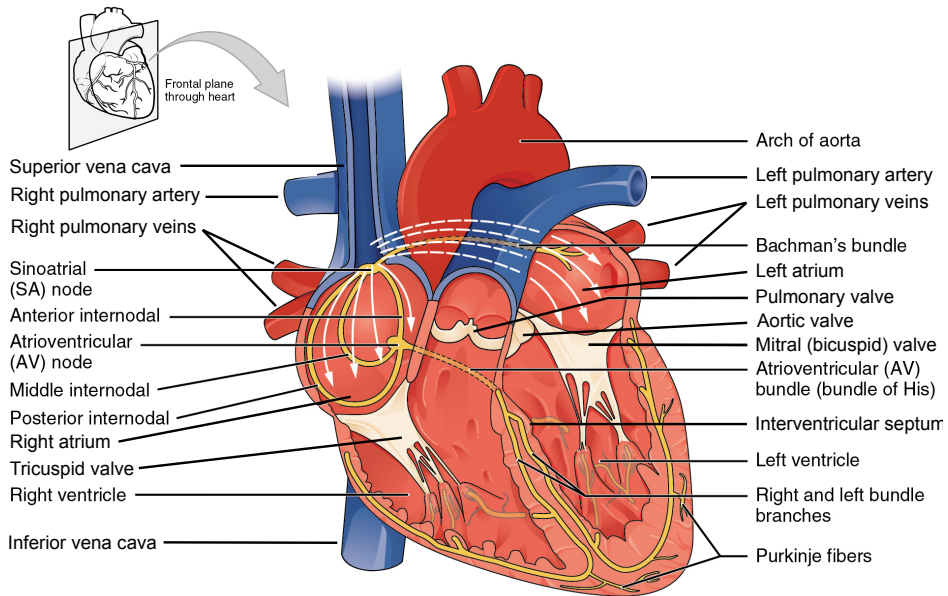
Fig. 1.3: Cardiac anatomy. The heart consists of four chambers (two atria and two ventricles separated by the interventricular septum). Through the pulmonary veins oxygenated blood is transported to the left atrium and ventricle and is distributed through the aorta into the body. Desoxygenated blood is then pumped back through the venae cavae to the right atrium and ventricle of the heart and back to the lungs through the pulmonary arteries. The cardiac valves prevent a backflow of the blood. The cardiac conduction system is indicated in yellow. The sinoatrial and the atrioventricular node control the time gating of the contraction cycle, while the Bachman's and His bundle as well as the Purkinje fibers act as conduction pathways. The direction of action potential propagation is indicated by the white arrows. Adapted from [35].

muscle cells of both atria. This process is named atrial systole. After the signal reaches the atrioventricular node it propagates along the ventricular impulse-conducting system including the bundle of His and the Purkinje fibers to the base of the heart, triggering the ventricular systole. A backflow of the blood during diastole, cardiac muscle relaxation, is prevented by the cardiac valves.

During the continuous contraction cycle, different pressures, strains and electrical stimuli occur in each chamber of the heart. Therefore, the basic function of the heart cannot be provided by a unified type of cell but requires a variety of different cardiac cells types. One can differentiate atrial cardiomyocytes, ventricular cardiomyocytes, fibroblasts, endothelial cells, pericytes, smooth muscle cells, immune cells, adipocytes, mesothelial cells and neuronal cells. Each cell group has its own functionality and specialized structure [11, 36].

These cell types can also be separated in populations by gene expression. For example, there are at least five different types of ventricular cardiomyocytes with different proportions in the left and right ventricle. Furthermore, the composition of the ventricular cardiomyocytes not only differs locally but is also gender-specific [11].

The entire human heart is formed by about 10 billion cells, which interact in a complex, dense and codependent network. Even though the gross anatomy is well described, the multiscale structure and its functionality is still not completely understood [11–13].

So far, it is not possible to give a generalized answer how the entire (healthy) heart is formed. Considering diversity between individuals or structural changes due to aging or CVDs such as e.g. myocardial infarction or hypertension for an individual patient, the problem is even more complex to understand. The question how exactly the action potential propagates through the entire organ of a patient, triggering the time-gated contraction of the heart remains unsolved.

To improve the understanding of the cardiac structure and function, computational modeling of the heart is conducted [37]. It is possible to model, analyze and control cardiac dynamics based on the coupling of nonlinear (chaotic) systems such as the electrical wave propagation in cardiac tissue [38, 39]. These simulations can for instance help to understand the cause and effects of cardiac arrhythmia. The fundamental mechanisms such as the propagation of the action potential, as well as the mechanical response, highly depend on the material properties of the cardiac cells. While defects like scar tissue (caused by aging or myocardial infarctions) disturb the propagation, the speed of propagation is higher along the orientation of the cardiomy-

ocytes [40, 41]. In order to overcome the challenge of upscaling cardiac models from the sub-cellular and cellular level to the tissue and organ scale, it is mandatory to link the models to experimental data [42–44]. For instance, the cardiac dynamics of a beating (pig) heart mounted on a Langendorff perfusion system was analyzed using fluorescence imaging of the calcium wave propagation and four-dimensional ultrasound imaging. The reconstruction of the 3d structural dynamics as well as the calcium wave propagation along the surface of the heart revealed scroll waves which are considered to be the organizing center of cardiac arrhythmia [45].

Another approach to support the computational modeling of cardiac function is the combination with diffusion tensor MRI [37, 46]. Since the propagation of the electrochemical signal within the heart depends on the orientation of the cardiomyocytes, the vectorfield obtained by diffusion tensor MRI is of high value for computational simulations [47]. In addition to electro-mechanical simulations of the heart based on its 3d structure, it is also possible to perform computational modeling of blood flow and pressure distribution within the heart [37].

There are a variety of models to describe the cardiac function on multiple scales. However, it is still unclear how exactly the cardiac cells are arranged within the heart to enable the contractile function in full detail.

From the current state of research one can conclude that it is essential to understand the structure of the heart to improve the computational modeling and the general understanding of a complex organ as the heart. Therefore, imaging of cardiac tissue is and has always been one of the fundamental conditions for progress in cardiac research.

1.2 Conventional imaging of heart tissue

1.2.1 Histology

Historically, the observation of the heart structure started by documenting visual impressions gained from evisceration of animals or autopsies. With progress in the manufacture of optics and the invention of the microscope in the 17th century, it was possible to investigate structures in the micrometer range [48]. During this time, Marcello Malpighi was the first who identified small capillaries in the lungs of bats and established the process of oxygen uptake [49]. This procedure, later called histology (from Greek: *histos*, tissue and *logos*, study), revealed its full potential during the 19th

century, when fixation techniques and staining protocols were developed. Those lead to increased contrast for specific tissue structures and made it possible to characterize healthy as well as diseased tissue by light microscopic analysis [50].

Today, conventional histology is the goldstandard in clinical practice worldwide. In a standardized procedure, the dissected tissue is chemically fixed by a liquid fixing agent, such as formaldehyde. In a diffusion-based process, the tissue gets slowly penetrated by the fixative, which cross-links proteins to stop the disintegration of the tissue. The fixed sample is then dehydrated using an ethanol series with increasing concentrations and cleared by xylene in order to be transferred to melted paraffin wax. After the entire sample is infiltrated by liquid paraffin, it is poured out into a block with an attached cassette [50, 51]. Samples embedded in paraffin wax blocks are very stable and make up the majority of archived tissue stored in pathology departments all over the world. In a further step, thin slices with a thickness of a few µm are cut from the paraffin blocks using a microtome. These slices have to be transferred to microscopy glass slides, where they are deparaffinized, before histological staining. Depending on the aim of the investigation, a variety of different histological staining procedures, such as Hematoxilin and Eosin (HE) stain, Masson-Trichrome stain or antibody-based immunohistological staining can be performed [52]. The stained sections can then be sealed to increase their durability. At the end of this labor-intensive and time-consuming process, a pathologist can analyze the tissue structure by light microscopy at different magnification, to identify morphological changes [53]. Based on his diagnosis, the pathology of the sample can be classified and if applicable further treatment such as drug treatment, surgery or radiation be prescribed.

However, conventional histology has three major disadvantages when analyzing the 3d tissue structure. Since the procedure is based on the microscopic analysis of thin slices of paraffin embedded tissue, histology is a *destructive*, *two-dimensional* technique with *limited, anisotropic resolution*.

In order to analyze an entire organ, hundreds to thousands of paraffin slices need to be prepared, analyzed under the microscope and stitched together. Since artefacts of the paraffin embedding (such as shrinking of the tissue), tissue deformations or even destruction while cutting, and inhomogeneities of the histological staining procedure cannot be excluded, it is very challenging to visualize an entire organ using conventional histology. Nevertheless, there are some datasets available [54, 55]. For example, entire human brains were analyzed in a multiscale approach by MRI and histology [56]. Microscopy images with a pixelsize of 4 µm of 25 µm thick, stained

slices were acquired and co-registered with the low resolution MRI data. To reduce redundancies, the workload and the amount of data only every 10th or 20th section was analyzed, depending on the brain region and its cell density.

There are comparable histological investigations of the heart in animal models, but there is no human investigation with such high detail so far [57, 58]. An exemplary histological slice of a murine heart is shown in Fig. 1.4A. For human heart tissue, it is more common to take photographs of short-axis sections with a thickness of a few mm and record micrographs of stained sections of paraffin biopsies taken from regions of interest of embedded tissue afterwards [59–61].

So far, histology as a 2d technique seems to be the best combination of resolution and identification of (sub-)cellular structures. However, the resolution of conventional histology in combination with light microscopy is also limited. According to Ernst Karl Abbe, the resolution d of an optical system is diffraction limited [62]. In the lateral plane it is given by

$$d = \frac{\lambda}{2n\sin(\alpha)} \tag{1.1}$$

with numerical aperture $NA = n\sin(\alpha)$ and wavelength λ. For visible light the lateral Abbe limit is in the range of 200 nm. The axial resolution limit for ($d = \frac{2\lambda n}{NA^2}$) is larger, though it does not play a role for histological investigations since the resolution is limited by the slice thickness and the distance between consecutive slices, stained with the same histological dye. Hence, the resolution of histological investigations is anisotropic.

Furthermore, when analyzing cardiac structures such as the actomyosin complex, the diffraction limit of visible light microscopy is about one order of magnitude too high to resolve the single protein bundles.

Other light microscopy techniques such as high resolution episcopic (reflection) microscopy or polarized light microscopy enable a different contrast. However, their limitations in terms of resolution and invasive sample preparation are congruent with conventional histology [63–66].

In order to analyze molecular structures, different imaging modalities which allow for higher resolution are necessary. In the following, two of those techniques, electron microscopy and fluorescence (super resolution) microscopy, are briefly described.

1.2.2 Electron microscopy

One option to image (biological) structures at higher resolution is electron microscopy. Due to a smaller wavelength of the accelerated electrons compared to visible light, a higher resolution can be reached (see Eq.(1.1)). This technique is already well established in cardiac research and is especially well suited to analyze the structure of mitochondria and sarcomeric structures at high resolution [36, 67]. Additionally, molecular structures can be labeled by gold nanoparticles coupled to antibodies. Figure 1.4C shows an electron micrograph of cardiomyocytes of a wild type mouse, where the attachment sites of desmin filaments (of the intermediate filament family of cytoskeletal proteins) were immuno-gold-labeled [68].

Since the penetration depth of the electrons through the tissue, usually stained by heavy elements such as uranium and tungsten, is very small, the axial resolution is limited by the slice thickness. Thus, the samples have to be sectioned to slices with a thickness in the range of a few nm. Similar to conventional histology, the third dimension can be accessed by labor-intensive and artefact sensitive serial sectioning [69, 70]. For instance, in 2018 the 3d structure of two neighboring cardiomyocytes was acquired from 1019 serial sections of 50 nm thickness [71]. Electron microscopy is a technique which is more commonly used to analyze the 2d ultrastructure of cells and tissue and to support results obtained from techniques with a lower resolution and larger field of view such as conventional histology or (confocal) fluorescence microscopy [36, 68, 72].

1.2.3 Fluorescence imaging

With fluorescence imaging it is possible to image specific protein complexes of labeled (biological) specimens. Fluorescent dyes absorb electromagnetic radiation and consequently emit light with a certain wavelength. This consequence also allows the same sample to be stained with multiple dyes at various binding sites of different protein complexes. By point wise scanning of the sample with a focused excitation laser, slices of stained tissue can be analyzed.

Figure 1.4B shows an example of a fluorescence micrograph of cardiomyocytes. In this case nuclei (blue) and desmin (green) were labeled with different fluorescent dyes.

The resolution of these measurements is also limited by diffraction, thus molecular structures such as the actomyosin lattice cannot be resolved. The resolution limitation by Abbe was overcome by the invention of *stimulated emission depletion* (STED)
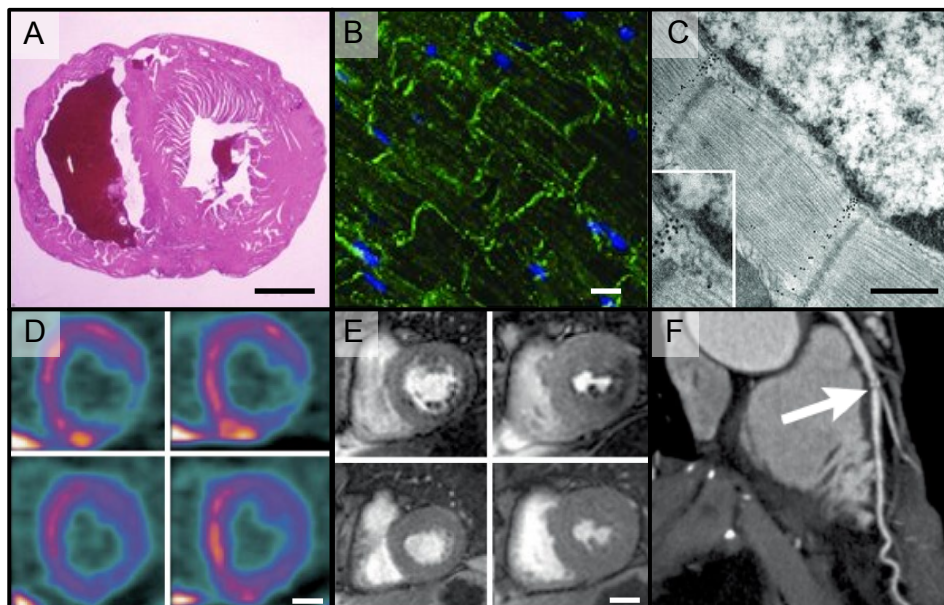
Fig. 1.4: Conventional imaging of cardiac tissue. (A) Histological HE stain of a wild type mouse. (B) Fluorescence imaging using an immunostaining with a desmin antibody. (C) Electron micrograph of cardiomyocytes of a wild type mouse. In this case, attachment sites of desmin filaments were immuno-gold-labeled using antibodies. Adapted from [68] (D) SPECT image of two human hearts in stress (top) and resting (bottom) state [73]. (E) Cardiovascular MRI perfusion analysis of two human hearts in stress (top) and resting (bottom) state using a gadolinium contrast agent [73]. (F) An exemplary slice of a coronary CT angiography. A coronary artery stenosis is marked by a white arrow. Scale bars: A: 1 mm, B: 5 µm, C: 0.25 µm, D and E: 2 mm. Adapted from [74]

microscopy by Stephan Hell and Jan Wichmann in 1994 [75]. The excited fluorescent molecules can be switched off again by stimulated emission using a second, doughnut shaped laser pulse. The time gated depletion of the point of illumination and the detection of the emitted light not depleted allows "super resolution" to be achieved. Recently, this invention was further developed by a combination of STED and single molecule localization microscopy such as *stochastic optical reconstruction microscopy* (STORM). The novel technique called *minimal photon fluxes* (MINFLUX) allows to analyze single molecules in 3d with a resolution in the range of a few nm while also reducing the problem of photobleaching [76, 77]. MINFLUX uses a doughnut shaped excitation laser and is based on stochastic assumptions, the dose can be reduced and

theoretically an image can be recorded without the excitation of the dyes. In terms of cardiovascular research super resolution microscopy is very promising regarding the investigation of structures within the cells such as the function of single mitochondria, ion channels, membranes or the sarcomeric structure [72, 78, 79]. Research in the field of fluorescent imaging is still ongoing. On the biochemical side, new dyes are being developed while on the imaging side a large research field is continuously working on improvements of image quality. This is not only relevant in terms of nanoscale imaging, since new developments of fluorescent dyes also enable functional time resolved *in vitro* imaging of hydrated cells or tissue. For instance, Ca^{2+} sensitive dyes allow to perform surface imaging of calcium waves propagating over the heart [45].

Note, that the advantage of fluorescence imaging techniques to label specific structures is also one of its disadvantages. It requires staining with suitable fluorescent dyes and only labeled structures can be identified, while unlabeled tissue appears dark in the images. Furthermore, 3d imaging using light microscopy is challenging since the penetration depth of visible light through the sample is limited by self absorption and light scattering. Hence, to analyze larger volumes, serial sectioning of the tissue is mandatory. One possibility to reduce the self absorption and scattering of the emitted photons within the sample is tissue clearing [80–82]. During this process the refractive index of a chemically fixed tissue is homogenized so that it turns transparent for visible light. The preparation usually includes decalcification, decolorization, delipidation, dehydration and clearing of the sample. In combination with fluorescent staining and light sheet microscopy, larger volumes in the range of the size of murine brain, a zebra fish or even an entire mouse can be analyzed [81–84]. However, this technique is also limited by diffraction and has an anisotropic resolution due to the properties of the excitation laser. Furthermore, the molecular and cellular organization in tissues is affected during the preparation process. The delipidation has an especially large effect on the tissue structure. Additionally to the clearing of the tissue, the uniform injection of fluorescent dyes e. g. by immunostaining, is very challenging especially for dense 3d biological material such as murine cardiac tissue [82, 85, 86]. One possibility to image entire hearts by light sheet microscopy is the combination of transgenic modification with the cardiomyocytes. By the expression of green fluorescent protein (GFP), originally found in jellyfish *Aequorea victoria*, or by the expression of *TdTomato* the problem of the tissue penetration can be overcome [85, 86].

In order to analyze larger and denser structures such as an entire human heart or even the full body of a patient, different imaging techniques are used in clinical routine.

1.2.4 Clinical 3d imaging

Conventional techniques used to clinical imaging of cardiac tissue include echocardiography, positron emission tomography (PET), single-photon emission computed tomography (SPECT), (diffusion tensor) magnetic resonance imaging (d)MRI, as well as absorption-based computed X-ray tomography (CT) and angiography. For all of these clinical techniques, a unifying principle is the injection of contrast agents into a peripheral vein [63, 74, 87].

PET and SPECT, as imaging techniques based on radioactive tracers, are well suited to characterize cardiac function and can help identify coronary artery diseases, hypertrophic cardiomyopathies and abnormalities in heart wall motion. Figure 1.4D shows SPECT images of two human hearts in a stressed (top) and resting (bottom) state. Such images are used to quantify the extent of left ventricular myocardial ischaemia [74]. However, their spatial resolution is in the cm to mm range and thus too low to characterize the cardiac structure in detail.

Echocardiography, a non invasive imaging technique without ionizing radiation, is based on ultrasonography and uses microbubbles as contrast agent to visualize the blood flow. Echocardiography can be performed at the bedside of the patient, however compared to other imaging techniques presented, it is noisy and yields many artefacts. Further, it is not reproducible and most importantly for the structural analysis of the cardiac muscle structure it only yields intravascular contrast for the blood flow but not for cardiomyocytes. Thus, it is not suited to study the cytoarchitecture of the heart.

MRI, as a technique which is well suited to image the dynamics of hydrogen nuclei, enables an excellent contrast for soft tissue. Due to the high anisotropy of the cardiomyocyte organization within the heart, the cardiac structure can be estimated by diffusion tensor MRI, which represents a suitable option to characterize orientation of the cardiomyocyte arrangement indirectly in *in vivo* and *ex vivo* experiments [88, 89]. The signal can be enhanced by gadolinium-based contrast agents. MRI is commonly used to characterize myocardial ischemia with a high sensitivity and specificity [90]. The recent development of real time MRI also allows the study of blood flow during cardiac contraction. Exemplary data of MRI acquisitions of two hearts in a stressed and resting state is shown in Fig. 1.4E. Such data provides myocardial blood flow values [74]. After all, clinical MRI is well suited to study the cardiac structure, including the cardiomyocyte orientation, and can also reveal the dynamics of the cardiac blood flow. However, the resolution depends on the strength of the magnetic field and is typically allocated in the (sub-)millimeter range. Even *ex vivo* studies of cardiac struc-

ture using MRI can reach resolutions down do 50 µm, but cannot achieve sub-cellular resolution, yet [63, 91].

Conventional CT and radiography is a cost efficient, widely available imaging technique used for multiple clinical applications [74, 92, 93]. It is based on the attenuation of X-rays and provides a good contrast for highly absorbing materials such as teeth or bone, but also enables several cardiovascular examinations. For example, ischemic heart disease can be detected using coronary angiography. In the procedure a iodine-based contrast dye is injected into the coronary artery through a catheter. The spread of the agent in the blood is detected by a series of 2d radiography images. In this way, blockages in the coronary arteries caused by plaque buildup can be identified. A coronary angiography is recommended by European guidelines to detect ischemic heart disease of patients with a low to intermediate clinical likelihood. The 3d morphology of the heart can be investigated by chest CT in combination with the injection of contrast agents. A slice of a coronary CT angiography indicating a coronary artery stenosis is shown in Fig. 1.4F. Cardiac CT is used to quantify stenosis and plaques in 3d at high resolution e. g. by calcium scoring. Furthermore, in combination with vasodilators (medications that dilate blood vessels) myocardial CT perfusion imaging can be performed. It allows to identify defects of the myocardium.

The disadvantage of conventional CT is the comparatively weak contrast for soft unstained tissue and the delivered radiation dose, which also limits the temporal resolution of the medical image acquisition [94]. An average coronary computed tomography angiography with a resolution of about 0.5 to 0.7 mm delivers a dose of approximately 8.7 millisievert to the patient. This equals about 3 years of background radiation [95, 96]. For comparison, the dose limitation for occupationally exposed persons is 20 millisieverts in a calendar year in all European countries [97]. Furthermore, scatter artefacts of absorbing structures reduce the quality of soft tissue recordings. However, even for *ex vivo* experiments, in which the radiation dose can be increased, the absorption contrast for soft tissue is very weak [63].

In summary, imaging of cardiac function and structure in the clinical routine is subject to more stringent conditions on the imaging technology compared to pre-clinical research. Since data acquisition is performed *in vivo*, motion artefacts and penetration depth of the imaging modality as well as the delivered dose plays an important role. The clinical methods are well suited to identify and characterize cardiomyopathies, but neither the resolution nor the contrast of the given modalities is high enough to resolve sub-cellular structures of *in vivo* human cardiac tissue. Even under *ex vivo*

conditions and when using small animal models, imaging the entire cardiac architecture remains challenging. To uncover the myocyte arrangement, a destruction free, multiscale imaging approach, reaching from an entire organ down to sub-cellular resolution is required. A possible solution is given by recent progress in X-ray imaging techniques and especially by the advent of X-ray phase-contrast CT, introduced in the next section.

1.3 X-ray phase-contrast CT

X-ray imaging of human tissue goes back to its discovery by Wilhelm Conrad Röntgen in 1895, when he noticed a glow on a nearby phosphor screen caused by an invisible ray [98]. On 22 December 1895 he acquired an X-ray radiograph of his wife's hand. In the slightly unsharp projection on photosensitive film, shown in Fig. 1.5A, one can identify her hand bones and a large ring, despite the contrast for soft tissue being quite low. Given that it took approximately 30 to 45 minutes to acquire the image, it is quite impressive how little motion artefacts are visible.

Due to further development of X-ray sources and detectors, patients do not need to be this patient anymore. The first conventional CT scanners developed in 1971 by the group of Sir Godfrey Hounsfield required about 25 to 30 minutes to acquire an entire tomogram. Today, an average CT scan can be recorded within a quarter of a second. The reason for these improvements is related to the progress in X-ray generation and detection of X-ray radiation [99, 100].

1.3.1 X-ray generation and detection

While the basic principle of X-ray generation in X-ray tubes based on electron impact has not changed in the last 125 years, the efficiency of modern X-ray sources and X-ray detection techniques has increased. A schematic X-ray tomography setup is shown in Fig. 1.5B. In a conventional X-ray tube electrons emitted by a cathode, are accelerated onto an anode material (usually tungsten, molybdenum or copper), where their kinetic energy is transferred into heat and electromagnetic radiation [102]. The emitted energy spectrum of the X-rays can be traced back to two physical processes: *Bremsstrahlung* and the *characteristic emission* of the anode material. The *Bremsstrahlung* X-rays are named after the German word for braking and emerge from the kinetic energy loss of the electrons passing through the anode material. The de-
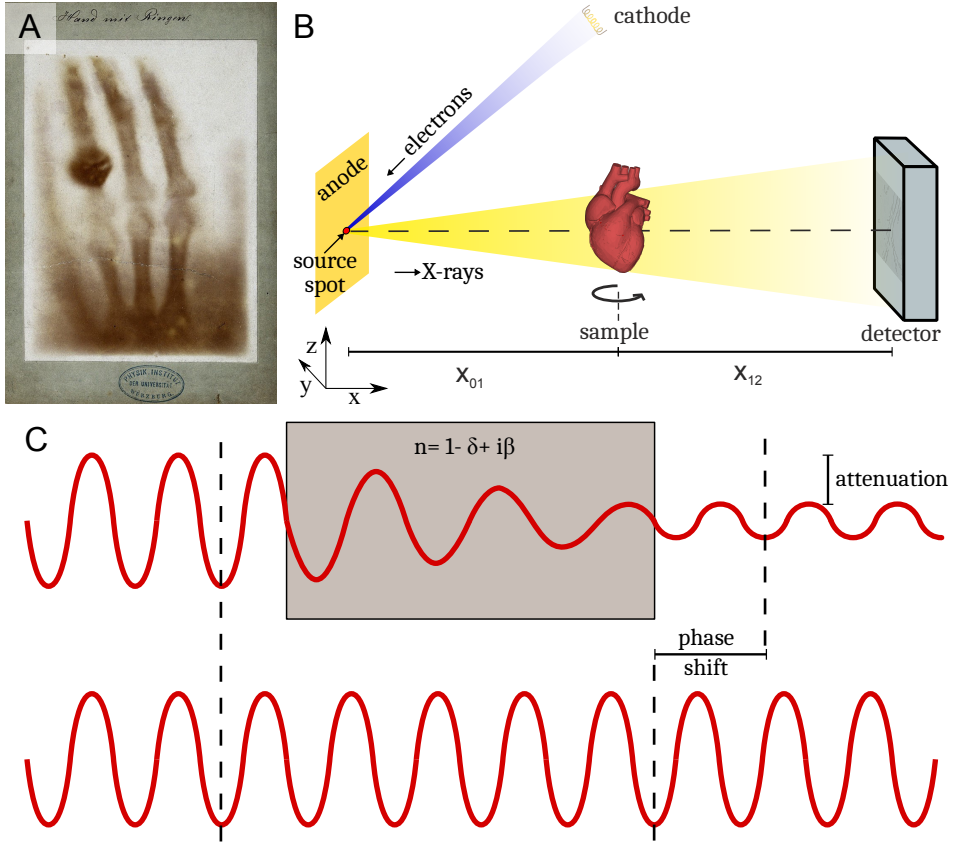
Fig. 1.5: Principles of X-ray imaging. (A) One of the first X-ray images was acquired in 1895 on a photographic plate showing the hand of Anna Bertha Röntgen [101]. (B) Sketch of a cone beam X-ray tomography setup. X-rays are generated by electrons, which are emitted by a cathode and accelerated onto an anode material. Projections of a sample are acquired by an X-ray detector. (C) Interaction of an electromagnetic wave with matter. When passing through an object, the amplitude of the incoming wavefront is reduced. Furthermore, the phase of the wave is shifted compared to a reference wave propagating in vacuum.

celeration of the scattered electrons in the external electric field of the anode nuclei results in a continuous X-ray emission spectrum. Photons emitted by excited atoms of the anode material contribute to the *characteristic spectrum*. The generated X-rays are emitted in all directions, thus a conventional X-ray source is a 4π radiator.

Since only about 1% of the electron energy is transformed into radiation, an overheat-

ing or even melting of the anode material is the most important limiting factor when increasing the power. In order to reduce skin dose, the amount of X-ray used for clinical imaging is further reduced by radiation shielding and collimation of the beam as well as trimming of the X-ray energy spectrum. In the end, only a fraction of about 0.03% of the energy is used for image acquisition [102]. The power of an X-ray source can be characterized by the brightness defined as source photons (ph) per solid angle and per source area (ph mrad^{-2} mm^{-2}).

Development of laboratory X-ray sources

The first X-ray tubes used by Röntgen were initially designed to study energetic electron beams. These tubes were invented around 1875 by William Crookes and unintentionally radiated X-rays with photon energies below 30 keV as a byproduct. The Crookes tubes could not be actively cooled and the photon emission was very low since the electrons were emitted from ionized gas near the cathode and thus the tubes were not well evacuated.

In 1913, the first high vacuum X-ray tubes designed by Coolidge were produced. This next generation of X-ray tubes emitted electrons from a heated cathode filament which were then accelerated onto a solid anode target which could be cooled actively by water. The progress in the generation of a stable vacuum enabled higher electron energies and flux.

A further increase in heat dissipation and photon flux was achieved by the invention of the rotating anode tube [103]. By rotating the anode, the source spot moves over the anode surface. Thus, the heat is distributed over a larger area of the anode material, which still reaches up to 2500°C despite active water cooling. Another approach based on the same principle is the rotating frame anode, which rotates inside the housing assembly. This design allows for a direct contact of the anode with oil and enables high cooling rates. These designs enables a relatively high photon flux and are used as the gold standard for most clinical applications [100, 102].

The reason the source spot can not be expanded limitless, thus enabling a limitless increase in flux, is the effect of source blurring. The resolution which can be achieved by a cone beam X-ray system depends on the configuration of the imaging setup sketched in Fig. 1.5B. The geometric magnification $M = \frac{x_{01} + x_{12}}{x_{01}}$ can be enlarged by increasing the sample-to-detector-distances x_{12} or decreasing the source-to-sample distances x_{01}. Thus, the effective pixelsize $px_{\text{eff}} = \frac{px}{M}$ is reduced. However, the shadow created by the extended source spot s increases for higher magnifications. In order to optimize

the resolution of the setup, the width of the point spread function of the system σ_{sys} should not be larger than the detector pixel size. σ_{sys} can be determined by [104]

$$\sigma_{\text{sys}} = \sqrt{\left(s\frac{M-1}{M}\right)^2 + \left(\frac{px}{M}\right)^2}\,.$$

Note that while the effective spot size of the source is reduced by larger source-to-detector distances x_{02}, the photon flux in the detector plane is reduced. For high resolution imaging of samples with a high contrast, the effect of source blurring is one of the most limiting factors for the resolution.

The problem was tackled with the development of micro- and nano-focus sources. By using magnetic lenses the accelerated electrons can be focused onto a small source spot with a diameter of a few μm or hundreds of nm. One can differentiate between three types of microfocus sources, characterized by the design of the anode [105, 106]:

The first design of microfocus sources is based on a reflection target. It is similar to the conventional Coolidge tube, but the (effective) source spot is minimized by focusing the electrons and tilting the anode. In this way, the source spot can be reduced to an effective size of 5-20 μm and be operated at 4-8 W (10 μm spot size).

To further decrease the source spot size, a transmission target can be used. It is built from a thin-film of anode material deposited on a diamond window to stabilize the anode [105, 107]. By this design, the source spot expansion through electron avalanches inside the anode material is limited. Hence, nanofocus sources are based on transmission targets. To further improve the capability of electron focusing, the electron source spot of the cathode has to be minimized. One possibility is the use of a lanthanum hexaboride (LaB6) filament as cathode material which allows to emit electrons based on the electric field instead of the common electrical heating of a tungsten coil. The sharp tip LaB6 cathode reduces the electron source spot and enables to focus the electrons to source spots down to 100 nm.

The maximum power of these two designs based on solid target materials is again limited by heat transfer. To overcome this problem and to increase the power of a microfocus source, an X-ray generator based on a liquid metal anode can be used. Instead of the solid target, the anode is made of a metal alloy, such as Galinstan (86.5% Ga, 21.5% In, 10% Sn) which is liquid at room temperature. This alloy is pumped with high pressure through a nozzle into the vacuum tube and forms a metal jet anode. The advantage of this setup is the heat dissipation, due to the steady renewing of the anode material. These sources can be operated at a power of more than 100 Watt (10

µm spot size). With this setup a brightness of 10^{10} ph mrad^{-2} mm^{-2} for the K_α line of Gallium was measured [108].

Developments in X-ray detection

Another reason for the faster image acquisition compared to the era of Röntgen is the development of new X-ray detection techniques [100, 109]. Instead of photosensitive glass plates or X-ray films, X-ray radiation is nowadays usually detected by digital X-ray detectors. From today's perspective, the X-ray detection technology can be divided into direct and indirect detection. In an indirect system a composition of different components serves to slow down or stop the photons to create an initial signal which then can be amplified or converted to another form of energy before being detected. In a direct detector the signal is created and imaged in the same component, such as in a photographic plate.

For 3d imaging, digital processing of the data is required. Usually, an indirect, scintillator-based detection systems is used for this purpose[109]. It is based on the luminescence of a scintillator material, which can be excited by ionizing radiation. The emitted light in the visible range is then collected by a lens or fiber optic and recorded by a photodiode, which converts the photon energy to an electronic signal. Thus, a digital image can be saved.

The spatial resolution, dynamic range, noise contributions and the read-out time of the X-ray detector depend on the absorption and emission spectrum and the thickness of the scintillation-screen as well as the magnification of the coupled optical imaging system and the sensitivity and pixel size of the photodiode [110]. Usually, a photodiode based on a metal-oxide-semiconductor, such as a Charge-Coupled Device (CCD) or Complementary Metal-Oxide Semiconductor (CMOS) is used [111]. In 2009 Willard Boyle and George E. Smith were honored with the Nobel Prize for the invention of the CCD [112].

In present conventional clinical CT, up to 320 X-ray detectors are arranged in a fixed outer ring of the scanner. Due to the fan-shaped X-ray beam created by the X-ray source, which is rotated around the patient, the duration of the scan could be reduced to less than a second [100].

Novel ideas to increase image quality in clinical applications also include dual-source and dual-energy CT. They allow the acquisition of two images from different angular positions at the same time (to correct for motion artefacts) or with different photon energies to gain more information on the tissue properties [93]. Further developments in

X-ray detection technology include single photon counting detectors, which enable a high signal to noise ratio, zero dark signal and avoid an afterglow which is common for scintillator materials [100, 107]. They are for instance based on a cadmium telluride (CdTe) CMOS technology, which directly convert photons to electrical signals. They allow for fast acquisition, improved resolution and higher contrast. Furthermore, they show less artefacts due to smearing or blurring within the scintillator. Another novel research branch in the detector improvement is dedicated to the development of 2d energy resolving detectors (similar to Silicon Drift Detectors) such as a hybrid silicon pixel detector based on charge integration and analog readout [113–115].

However, for some applications the current efficiency of laboratory X-ray imaging setups is still not sufficient. The temporal and spatial coherence of the illumination is limited by the broad X-ray spectrum and by the extended source spot. Furthermore, the brightness is limited by undirected radiation of the source with limited power. Especially when analyzing small structures with low contrast at high resolution or time resolved processes, laboratory systems reach their limits.

Synchrotron radiation facilities

One possible solution for increased image quality and acquisition speed is the use of coherent X-ray radiation with a high photon flux created at large scale synchrotron radiation facilities. X-rays are created by the deceleration of electron bundles with relativistic velocities within a magnetic field (bending magnet, wiggler or undulator). Thereby, a high photon flux with a small divergence is obtained. Further, the spectrum can be trimmed by attenuators and monochromators. The photon flux is characterized by its brilliance, defined as brightness per spectral width of the radiation and can reach up to 10^{25} ph/(s mrad^2 mm 2 0.1% BW), more than 10 orders of magnitude higher than a conventional rotating anode source (10^{12} ph/(s mrad^2 mm 2 0.1% BW)) [116, 117].

However, since these large scale synchrotron radiation facilities have high operating costs and limited accessibility, not everyone can be granted the opportunity to carry out an experiment.

After all, the progress in X-ray generation and detection techniques since the Röntgen s discovery is remarkable. Nevertheless, conventional absorption contrast, which is well established in hospitals, yields only a small contrast for soft tissues such as the heart. To improve data quality and increase the signal-to-noise ratio even for laboratory X-ray imaging, the phase-shifting properties of an X-ray wave can be accessed.

For soft tissues and hard X-rays the phase information encoded in the dispersion part of the index of refraction is higher by a factor of 100 to 1000 compared to the attenuation [118]. The concept of X-ray phase contrast will be examined in more detail in the next section.

1.3.2 The origin of X-ray phase contrast

Imaging with X-ray radiation is based on the interactions of electromagnetic waves with matter. These energy dependent interactions occur in terms of photoelectric absorption, scattering or pair production of single photons. The wave interpretation of electromagnetic radiation is well suited to characterize the principles of image formation with X-rays.

The propagation of a plane electromagnetic wave of wavelength λ along direction x in vacuum can be described by its wave field Ψ_x

$$\Psi_x = e^{-i\frac{2\pi}{\lambda}x} = e^{-ikx} ,$$

with wavevector $k = 2\pi/\lambda$. If the wave passes a homogeneous object with a refractive index of $n = 1 - \delta + i\beta$ and a of thickness Δx the wavefront after an object is given by

$$\Psi_{\Delta x} = e^{-ik\Delta x(1-\delta+i\beta)},$$

where δ is the dispersion term and β the imaginary part of the energy dependent complex refractive index. Thus, it has a phase shifted wavefront of $\Delta\Phi = -k\delta\Delta x$ and a reduced amplitude compared to a reference wave propagating in vacuum. The intensity behind the object is given by the absolute square of the wavefront

$$I = |\Psi_x|^2 = \Psi_x \cdot \Psi_x^* = |e^{-ik\Delta x(1-\delta+i\beta)}|^2 = e^{-2k\Delta x\beta} = e^{-\mu\Delta x} , \qquad (1.2)$$

describing the Lambert Beer's law with attenuation factor $\mu = 2k\beta$, used for conventional X-ray imaging and spectroscopy [119]. Since the attenuation depends on the material thickness and its attenuation coefficient, it contains information about the object properties.

As mentioned before, the attenuation of hard X-rays in soft tissue is very weak and depends on the photon energy $E = \frac{hc}{\lambda}$, with Planck constant h and speed of light c. The energy dependence of the absorption β is proportional to E^{-4}, while dispersion term δ scales with E^{-2} [120]. Hence, the contrast is very low for conventional hard

X-ray radiography. Although the dispersion term δ of the refractive index is usually larger than the attenuation β, it cannot be detected directly. This phenomenon is known as *phase problem* and will be targeted in the next section.

1.3.3 Solving the phase problem

The basic idea of phase-contrast imaging goes back to the early 1930s, when Frits Zernike developed phase-contrast microscopy for visible light [121, 122]. In 1953, his work was honored with the Nobel prize. This technique enabled living cells to be imaged, which give too little absorption contrast to be investigated using bright field microscopy. Using a -90° phase shifting ring, the light scattered by the sample interferes with the illumination resulting in a higher contrast for the unstained tissue.

When using hard X-ray radiation, it is much more difficult to make the phase difference visible. Since the interaction of the electromagnetic wave with the material is very weak, conventional lenses and phase rings do not work as efficient as for visible light. There are different approaches to visualize the phase information of X-rays, which can be categorized in three groups [120]:

1. X-ray interferometry, which allows to directly measure the phase shift Φ,

2. diffraction-enhanced X-ray imaging, measuring the first derivative of the phase shift $\nabla \Phi$ and

3. X-ray holography, which is based on the second derivative of the phase shift $\nabla^2 \Phi$.

The first approach was developed in 1965 by Ulrich Bonse and Michael Hart. It is based on a crystal interferometer, creating interference of the scattered wavefront and a reference wave using a beam splitter [123]. This delicate setup has extremely high (sub nm) stability requirements on the setup and its monochromatic illumination [120]. Thus, X-ray phase-contrast imaging remained challenging.

About 30 years later, X-ray imaging modalities based on the first order of spatial derivative were developed. For instance, they are based on crystal analyzers, edge illumination, speckles/diffusors or (phase shifting) gratings [124–130]. These techniques are well suited to detect small changes in phase properties, but are still limited by the optical components needed for imaging formation. For instance, high resolution is challenging since the resolution is limited by the properties of the grating structure and the accuracy of its fabrication [131]. However, even if the dose-efficiency is affected due to absorption of the optical components, diffraction-enhanced X-ray imaging is a good

opportunity for laboratory and also *in vivo* imaging at lower resolution. Especially the grating-based approach established by the groups of Franz Pfeiffer, Timm Weitkamp, Christian David and Atsushi Momose as well as the edge-illumination developed by Alessandro Olivo yield a higher contrast for for soft tissue compared to absorption-based imaging [132–135]. Thus, are well suited for the application of phase contrast in medical diagnostics.

While the first two approaches are limited by their optical components, in-line holography imaging does not require additional optics between the X-ray source and detector. Thus, there are less requirements on component fabrications and stability of the setup.

The propagation of the wavefront Ψ_0 along x can be described for small angles using the paraxial approximation by the Fresnel propagator D_x [118]

$$D_x = \exp(ikx)\mathcal{F}^{-1} \exp\left(\frac{-ix\mathbf{k}_\perp^2}{2k}\right) \mathcal{F} \,,$$

where $\mathcal{F}$ denotes the Fourier transform and $\mathbf{k}_\perp$ the reciprocal vector of the sample plane coordinates. The propagated wavefront Ψ_x can be approximated as

$$\Psi_x \approx D_x \Psi_0 \,.$$

The principle of in-line or propagation-based phase contrast is sketched in the top part of Fig. 1.6. If the sample is placed immediately in front of the detector, a conventional absorption image (as shown in Eq. (1.2)) is recorded. Thus, in case of a non-absorbing, pure phase object no contrast can be measured. If now the detector is moved further away from the sample and thus the propagation distance of the scattered wave is increased, fringes around the edges of the sample start to appear. The so called "edge enhancement" is caused by interference of scattered photons and can be described by the propagation of the disturbed wavefront. If the sample is placed further away from the detector, the fringes spread and start to overlap until only a fringe pattern, called hologram, is detected.

The imaging regime is characterized by the Fresnel number F

$$F = \frac{a^2}{d\lambda} \,,$$

with the characteristic length a (pixelsize for X-ray imaging) and propagation distance

d. While the edge enhancement or direct contrast regime can be characterized by Fresnel or near field diffraction ($F \approx 1$), the holographic regime can be described by Fraunhofer or far field diffraction ($F \ll 1$).

Figure 1.6 shows the intensity distributions behind a pure phase object ($\pi/2$-phase shift) as well as for an object with a maximum absorption of 10% for different Fresnel numbers. Additionally, a magnification of the area marked in the absorption image is shown for each propagation distance. The intensity distributions are obtained by projections of a 3d phantom. This phantom was created by the segmentation of the murine heart tissue published in [2]. The voxels of the phantom were assigned with a constant index of refraction. Note that the noise in experimentally measured intensities, acquired by an X-ray detector, is not included in the simulated data shown. The Matlabcode used for this example is shown in Appendix A.1. By the propagation of the wavefront towards smaller Fresnel numbers, the edges of the object are emphasized by phase effects which expand and form stronger, overlapping fringes until the small structures cannot be recognized visually anymore. However, the structural information is still encoded in the measured intensity pattern. While the absorption contrast of the object defines the contrast for large Fresnel numbers, the influence of phase effects increases upon propagation until it dominates the image. Experimentally, phase-contrast imaging is a good technique to analyze samples with a low attenuation coefficient. Since the image formation origins from scattering of photons by electrons, phase-contrast X-ray tomography enables a contrast proportional to electron density.

In order to obtain phase information of the image properties, the intensities measured at the detector plane have to be properly back propagated to reconstruct the phase distribution in the sample plane. This process is called *phase retrieval*. The original technique of holographic imaging goes back to 1948, when Dennis Gabor described interference patterns of electrons and eventually improved electron microscopy [136]. First experiments using X-ray holography measurements were performed at the European Synchrotron Radiation Facility (ESRF) by Snigirev et al. and were published in 1995 [137]. Followup experiments were performed by Cloetens et al. [138]. Only one year later, phase-contrast imaging in combination with laboratory sources was performed by Stephen William Wilkins associated with the Commonwealth Scientific and Industrial Research Organisation (CSIRO) [139].

There is a variety of different phase retrieval approaches, which are based on prior knowledge of the image formation. The lower part of Fig. 1.6 shows a selection of
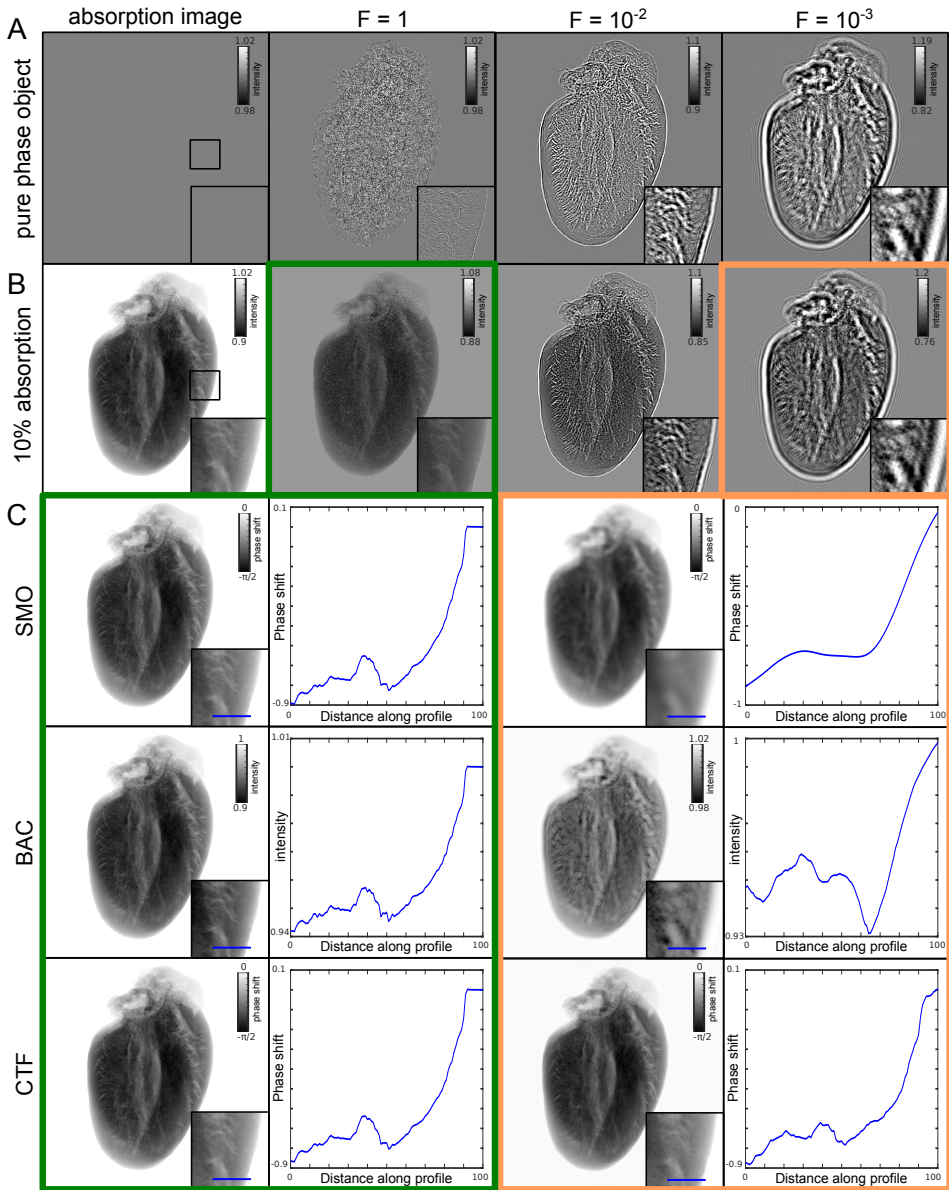
Fig. 1.6: Simulation of the propagation and phase retrieval for a heart phantom. In the top rows, the intensity distributions for a $\pi/2$-phase shifting object without attenuation (A) and for an object with weak absorption (B) is shown for different Fresnel numbers. For the weakly absorbing object in the contrast regime (marked in green) and the holographic regime (orange), phase retrieval was performed by the SMO, BAC and CTF approach. The respective phase reconstructions are shown in (C). Additionally, the signal along a line marked in the magnified images is plotted for each phase retrieval algorithm.

phase retrieved images for an object with a maximum absorption of 10% after propagation to $F = 1$ and $F = 10^{-3}$ obtained by algorithms introduced in the following.

The image formation can be simplified either by the *transport of intensity equation (TIE)* or the *contrast transfer function (CTF)* [118, 140]. The *TIE* states that changes in intensity $\frac{\partial}{\partial x} I_x(r_\perp)$ of a paraxial wavefront along infinitesimal propagation distances can be calculated if the intensity and phase information are known

$$\nabla_\perp |I_x(\mathbf{r}_\perp) \nabla_\perp \Psi_x(\mathbf{r}_\perp)| = -\frac{2\pi}{\lambda} \frac{\partial}{\partial x} I_x(\mathbf{r}_\perp) \,,$$

where $I_x(\mathbf{r}_\perp)$ is the empty beam corrected intensity measured at propagation distance x in the plane $\mathbf{r}_\perp = (y, z)$ perpendicular to the optical axis.

Consider a homogeneous object consisting of a single material with a constant refractive index. By replacing the lateral Laplace operator with a Fourier-based pseudo operator, the TIE can be converted into an expression for the phase information of the object obtained from a measurement of the intensity at distance x

$$\Phi = \frac{\delta}{2\beta} \cdot \ln \mathcal{F}^{-1} \left[\frac{\mathcal{F}[I_x]}{\frac{\delta x}{2k\beta} |\mathbf{k}|^2 + 1} \right] \,.$$

This phase retrieval approach was first described by Paganin et al. and is named after its initial assumption as *single material object reconstruction (SMO)* [141].

Exemplary reconstructions of the phase SMO phase retrieval are shown in the first row of Fig. 1.6C. While the SMO reconstruction is well suited for the direct contrast regime and a single material object with a low $\frac{\delta}{\beta}$ ratio, the pseudo differential operator leads to image blurring for higher $\frac{\delta}{\beta}$ ratios.

Another approach suited for the direct contrast regime is the *Bronnikov-aided correction (BAC)* [142]. It is a two step reconstruction of the object properties. First the phase information is obtained by the *Modified Bronnikov algorithm (MBA)* which is also based on the *TIE*

$$\Phi = 2\pi F \mathcal{F}^{-1} \left[\frac{\mathcal{F}[I_x - 1]}{|\mathbf{k}|^2 + \alpha} \right] \,,$$

where α is an absorption-dependent regularization parameter to suppress numerical instability caused by the singularity at $\mathbf{k} = 0$. For $\alpha = \frac{4\pi\beta}{\delta}$, the MBA reconstruction scheme delivers the similar results for a weak object as the SMO. In order to restore image sharpness, a second step is applied for the BAC reconstruction. For weakly

absorbing materials, the intensity in the object plane can be approximated by the the near-field TIE

$$I = \frac{I_x}{1 - \frac{x}{k}\nabla^2\Phi} \ .$$

Using the MBA to approximate the phase of the object and by introducing a regularization parameter $\gamma \approx \frac{x}{k}$, an effective intensity distribution in the object plane can be calculated. Compared to the SMO, the BAC maintains the sharpness of the reconstructions in the direct contrast regime [143]. However, both algorithms introduced above fail in the holographic regime.

The original approach for holographic phase reconstruction is based on the Fresnel diffraction operator and was proposed by Gabor [144]. By a back propagation of the measured intensity, the phase information in the object plane can be approximated. However, this scheme yields strong artefacts from twin images emerging from the ambiguity of the Fresnel back propagation.

In our group other phase retrieval algorithms for propagation-based X-ray phase retrieval in the holographic regime were developed[94]. For instance, they are based on the TIE for arbitrary propagation distances (Holo TIE) or iterative propagation schemes [145–147].

The most commonly used approach for is based on the CTF and was proposed by Peter Cloetens and coworkers more than 20 years ago [148]. It allows to combine information from projections acquired at different propagation distances. Considering a homogeneous object with a slowly varying phase, the phase distribution in the object plane $\Phi(\mathbf{r}_\perp)$ is given by

$$\Phi(\mathbf{r}_\perp) = F^{-1}\left[\frac{\sum_N(\sin(\chi) + \frac{\beta}{\delta}\cos(\chi)) \cdot F\left[I_x^N(\mathbf{r}_\perp) - 1\right]}{\sum_N 2(\sin(\chi) + \frac{\beta}{\delta}\cos(\chi))^2 + \alpha(\mathbf{k}_\perp)}\right] \ ,$$

with natural units $\chi = \frac{\lambda x \mathbf{k}_\perp^2}{4\pi}$ for the squared spatial frequencies, a frequency-dependent regularization parameter $\alpha(\mathbf{k}_\perp)$ for regularization of low and high frequencies and N indicating the index of the respective distance x. The bottom row of Fig.1.6C shows the performance of the CTF in direct contrast regime and the holographic regime for a weakly absorbing object with a strong phase shift measured at a single distance.

Compared to the other two approaches, the CTF is well suited to retrieve the phase information for small Fresnel numbers. Despite it being initially developed to solve the phase problem in the holographic regime, image contrast and details are comparable

to SMO and BAC reconstruction for the direct contrast regime. Image quality can further be improved by using a non-linear approach of the CTF based on a minimization of the Tikhonov functional [149, 150].

Since propagation-based phase contrast is a phenomenon based on interference, it requires spatial and temporal coherence of the illuminating radiation. Some phase retrieval algorithms, such as the CTF and most iterative approaches, only work for highly coherent monochromatic illuminations of single material objects. For others such as BAC and SMO, the restrictions are not so severe and also partially coherent laboratory sources can be used. The advantage of the BAC algorithm compared to the SMO approach was shown for laboratory data by Töpperwien at al. in 2016 [143].

Note, that for cone beam geometries, the geometry of the setup also influences the wave propagation. The Fresnel scaling theorem states that the coordinate system of a cone beam acquisition can be transformed to a parallel geometry by considering an effective propagation distance x_{eff}

$$x_{\text{eff}} = x_{12}/M .$$

Hence, the Fresnel number has to be adjusted with the magnification $F_{\text{eff}} = F/M$.

After image acquisition and phase retrieval, the integrated phase information along the propagation path of the X-ray can be determined. In order to obtain the 3d volume from 2d projections a tomographic reconstruction has to be performed.

1.3.4 Tomographic reconstruction

The phase retrieved images yield the accumulated phase information along the propagation path of the X-rays. In order to access the 3d structure of the sample, a set of 2d projections at different angular positions has to be acquired.

The process of image acquisition can be mathematically described by the Radon transform developed in 1917 by Johann Radon [151]. In the following we consider one 2d slice of the 3d volume described by $f(x, y)$ which lies orthogonal to the rotation axis in a setup with a parallel beam geometry. The corresponding pixel line of the detector perpendicular to the rotation axis at rotation angle θ can be described by $s = x \cos \theta - y \sin \theta$. The integrated phase shift P_θ along s is given by [152]

$$P_\theta = \int_{-\infty}^{\infty} \int_{-\infty}^{\infty} f(x,y) \delta_D(x \cos \theta - y \sin \theta - s) \mathrm{dx\, dy} ,$$

where δ_D denotes the Dirac delta distribution.

Based on the inversion of the Radon transform, a 3d volume can be reconstructed slice by slice from the 2d projections. In order to retain image sharpness, a *ram-lak* (high-pass) filter has to be applied in Fourier space [118, 152].

The minimum number of angular positions N_θ, which has to be acquired to perform a proper tomographic reconstruction, depends on the number of detector pixels perpendicular to the axis of rotation N_y and is given by the Nyquist sampling theorem $N_\theta \geq N_y \frac{\pi}{2}$ [152].

However, it is also possible to achieve reasonable image quality for sampling rates below Nyquist. For instance, undersampling artefacts in low dose CT can further be reduced by mathematical approaches such as by minimizing the total variation of the estimated image [153], equally sloped tomography [154] or Bayesian statistical reconstructions [155]. Another growing field in artefact reduction of tomographic data is the combination with machine and deep learning networks [156–158].

1.3.5 Virtual histology

After image acquisition, phase retrieval and tomographic reconstruction, the 3d volume can be further investigated. Compared to conventional absorption-based X-ray imaging, phase-contrast tomography yields a relatively high signal to noise level even for unstained, formalin-fixed, paraffin-embedded (FFPE) tissues and allows the destruction free investigation of 3d tissue structures with an isotropic resolution. Tomographic reconstructions of biological samples can be cut virtually in arbitrary orientations. Thus, the 3d structure can be analyzed to improve the understanding of the tissue properties. Hence, high-resolution X-ray CT is often referred to *virtual histology*, extending conventional histology by a third dimension [159–162]. Furthermore, X-ray phase-contrast tomography of FFPE blocks enables conventional histology after image acquisition. It can be beneficial to know the 3d sample structure within the paraffin block prior to the sectioning process. For instance, knowing the position of a tumor within the tissue facilitates the search via histology for further characterization. Moreover, the paraffin block can be mounted in an optimized orientation [163]. Virtual and conventional histology can be superimposed to improve the understanding of the tomographic data.

Additional data from post processing of the volume, such as segmentation of certain cellular features or the investigation of cell densities, structural orientation or

distances between nuclei in 3d, can reveal new insight on functionality. For example, previously unknown correlations between the orientation of granular cells and the dendrite tree of purkinje cells in the human cerebellum were recently discovered [164].

3d virtual histology is a growing field in neuroscience as well as in research concerning other organs, such as the pancreas [165], the kidneys [166], the vasculature or the skin [167, 168]. Related to the current world wide pandemic, structural changes in lung architecture for severe cases of Covid-19, previously observed by conventional methods [169, 170], were recently also confirmed by propagation-based phase-contrast X-ray tomography [171, 172]. In our work, we performed a segmentation of small capillaries and the hyaline membranes covering the surface of the alveoli and thus hindering the transport of oxygen. Furthermore, characteristic distances from tissue interior to the closest air compartment and the distribution and density of lymphocytes within the tissue were characterized. Parameters like these can help to categorize pathologies in the future.

In order to access the 3d structure, one does not necessarily need to apply for beam-times at synchrotron radiation facilities. Also partially coherent laboratory sources allow for sufficient image quality to analyze 3d tissue properties [143, 173, 174].

New staining procedures for 3d X-ray analysis are under development to increase image quality. Using high-Z materials such as iodine or phosphotungstic acid (PTA), tissue contrast can be enhanced [175]. However, 3d tissue staining yields the uncertainty of staining artefacts such as unspecific binding or a contrast gradient between the surface and the sample core caused by spatially and temporally anisotropic stain penetration. Protocols for conventional histological stains such as the HE stain were adapted for 3d X-ray imaging [176–178]. This stain is already established and also works for dense tissues such as liver tissue.

The advent of 3d virtual histology has delivered first new insights on the correlation between organ structure and function. Nevertheless, it is still a new technology that needs to be further optimized. The full potential of 3d virtual histology can be exploited by improving image quality and establish novel analysis workflows to characterize the tissue structures.

The next section gives an overview of the current status and recent progress of 3d virtual histology of cardiac tissue.

1.3.6 Virtual histology of cardiac tissue

Compared to clinical imaging of the heart, which is optimized for diagnostics, virtual histology of cardiac tissue aims to resolve the structure of the heart on the sub-cellular scale for the entire organ. In this context the architecture of the cellular arrangement, its development as well as the influence of CVDs is analyzed [63]. Since the objective of fundamental and preclinical research differs from clinical imaging, the boundary conditions are set differently. First of all, most image acquisition is performed post mortem. Hence, dose delivery is usually not limiting during image acquisition. Furthermore, most investigations are performed on small animal models, such as mice or rabbit, before human studies are performed. In the following, the current state of preclinical cardiac imaging, including the work related to this thesis, is presented.

The first reconstructions of entire small animal hearts using laboratory instruments were obtained with a resolution of down to 30 μm using iodine-based contrast agents [179, 182]. A slice of the tomographic reconstruction is shown in Fig. 1.7A. Furthermore, the cardiac conduction system as well as the influence of congenital heart disease was investigated [179, 183, 184].

In context with this work, the influence of heavy-metal staining agents as well as alternative preparation methods such as tissue dehydration on the cardiac structure was analyzed [2]. Using a liquid metal jet setup, samples were investigated at a resolution of about 5 μm, which was previously not achieved with laboratory X-ray sources. Additionally, the tomographic reconstruction of a murine heart, prepared by the Evaporation of Solvent method, was also probed by a novel approach to identify the cardiomyocyte orientation. The orientation analysis is based on a local Fourier transform of the electron density and was compared to an established gradient-based method, which was previously applied to synchrotron data [185].

In order to achieve higher resolution and contrast (also for hydrated tissue) coherent and brilliant illumination from synchroton radiation facilities is needed. In Fig. 1.7B and C, the gain in image quality is visualized for a PTA stained murine heart recorded by Dullin et. al. [180]. Figure 1.7B shows a reconstruction from an absorption-based laboratory system with a voxelsize of 40 μm. The same heart was also analyzed at the SYRMEP beamline at the Synchrotron Light Source Elettra (Trieste, Italy) using propagation-based phase contrast at a voxelsize of 18 μm (Fig. 1.7C). Due to the higher photon flux and monochromatic illumination, the signal-to-noise ratio was increased and the pixel size reduced.

Further studies of (stained) cardiac tissue were performed on small animal and hu-
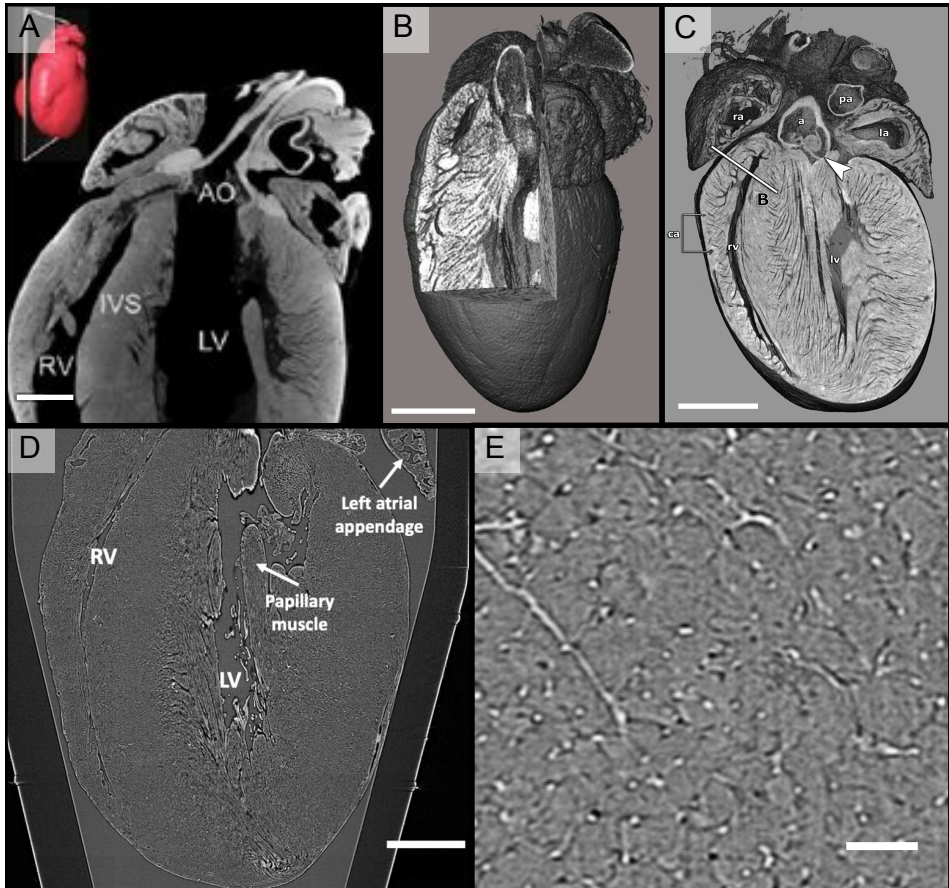
Fig. 1.7: 3d virtual histology of cardiac tissue. In the top row tomographic reconstructions of small animal hearts stained with heavy Z elements are shown. (A) One of the first laboratory reconstructions of an entire rat heart stained by an iodine solution recorded at a resolution of 30 µm [179]. (B) PTA stained murine heart first analyzed at a laboratory setup at a voxelsize of 40 µm [180]. (C) The same heart analyzed at a synchrotron radiation facility at a voxelsize of 18 µm [180]. The lower part shows tomographic reconstructions of unstained murine hearts aquired at a synchrotron radiation facility [181]. (D) First low resolution scans with a voxelsize of 6.5 µm were acquired. (E) Afterwards, high resolution scans of region of interests were recorded at a voxelsize of 650 nm. Scale bars: A,B,C: 2 mm, D: 3 mm, E: 250 µm.

man hearts using grating interferometry or edge illumination [186–189]. This approach also enables a high contrast for soft tissue, but is limited in resolution by the grating or mask properties.

Propagation-based X-ray phase contrast studies of hydrated cardiac tissue from human and murine hearts allow to study the myofiber network in higher detail [181, 190–194]. The lower part of Fig.1.7 shows an examplary study of a hydrated murine heart by Dejea et. al. [181]. First, the entire heart was scanned at an effective pixel size of 5.8 μm (Fig.1.7D). Afterwards, high resolution tomograms with a voxelsize of 0.65 μm were acquired in regions of interest (see Fig.1.7E). In this study, the vascularity and collagen network was segmented and the myocyte orientation was calculated. In order to facilitate the identification of the collagen, the segmentation was performed based on a tomographic reconstruction without phase retrieval and compared to histological microscopy images afterwards. The bright spaces between the cardiomyocytes are claimed to be a collagen matrix supporting the myocyte network. However, there is a risk that edge enhancement artefacts of the reconstruction were mistakenly claimed to be collagen. In order to confirm conclusions from tomographic reconstructions of sub-cellular structure, artefacts from incorrect or missing phase reconstruction have to be excluded. A solution to this issue is a proper phase retrieval using iterative phase retrieval algorithms. Furthermore, tomographic reconstructions at smaller voxelsizes can be used to confirm the assumptions.

In a previous proof-of-concept experiment performed by our group, biopsies of cardiac tissue were first scanned at a laboratory setup in parallel beam geometry at a voxelsize of 0.65 μm. Afterwards, high resolution tomograms with a voxelsize of about 190 nm were acquired at the synchrotron in cone beam geometry [195]. Within the scope of this thesis, the cardiac structure is investigated in a multiscale X-ray phase-contrast tomography approach [3]. Three different configurations of the GINIX endstation were used to record projections at different levels of magnification [165, 196]. First, overview scans of entire murine hearts were acquired at 3.25 μm voxelsize. Regions of interest were than analyzed at 0.65 μm voxelsize before a biopsy punch was taken and scanned at a voxelsize of 167.5 nm. Using iterative phase retrieval algorithms the challenge of a proper phase retrieval in the field of virtual histology is overcome. Phase retrieval was performed by a non-linear approach of the CTF.

So far propagation-based X-ray imaging at synchrotron radiation facilities seems to be the best technique to image the 3d cardiac structure in high detail. It enables a high contrast even for unstained tissue, either embedded in paraffin or in solution. Using

this approach, studies on the influence of cardiovascular disease in mouse models were performed [181, 197]. Besides differences in fiber orientation, the wall thickness of the myocardium was analyzed and a few single cardiomyocytes were manually segmented. Experiments and analyses of this kind can provide the basis for a deeper understanding of various diseases.

Recently, we investigated cardiac tissue samples of patients who succumbed to Covid-19 by propagation-based phase contrast [4]. Previously, structural changes of the vascularity due to the disease were observed in lung tissue of Covid-19 patients [169–171]. In severe cases of the disease, the body forms new vessels via a process named intussusceptive angiogenesis, possibly to compensate for disturbances of the blood circulation due to microthrombi. By a deep learning based segmentation of the vascular system and graph theory we could show that these changes also occur in cardiac tissue. Furthermore, structural changes on a cellular level were also observed from laboratory recordings and are described by an analysis of the cellular alignment. The high resolution synchrotron reconstructions reveal sub-cellular structures such as myofibrils, nuclei but also "pillars" within small capillaries, which are a hallmark for intususseptive angiogenesis.

On the sub-cellular level, X-ray virtual histology is very challenging. Most of the work presented above was performed at setups which are designed for a minimal voxelsize of 650 nm. The advantage of the comparably large penetration depth for X-rays compared to conventional imaging techniques as fluorescence imaging does not play a role when analyzing single cardiomyocytes. Contrarily, the weak interaction of hard X-ray and soft matter is challenging when analyzing single cardiomyocytes. However, the fact that X-ray tomography can be performed independent of labeling and yields a contrast for the 3d electron distribution, it reveals the unaltered structure of the object. Thus, it can be used to verify or extend studies obtained by other imaging techniques.

Within the scope of this thesis, we performed a proof-of-concept experiment showing that it is possible to reconstruct the 3d electron density distribution of isolated cardiomyocytes using propagation-based X-ray tomography [5]. Using the high resolution cone beam waveguide setup of the GINIX endstation we could image freeze-dried cells at a voxelsize of 45 nm. Furthermore, the actin network of the cell was labeled by a fluorescent dye and imaged using a confocal microscope. In the tomographic reconstruction myofibrils and mitochondria can be identified. The limit in resolution of X-ray phase-contrast tomography of biological samples is not set by Abbe, but rather by the low contrast for soft tissue and by the geometry and stability of the imaging

setup. One possibility to probe molecular structures smaller than mitochondria, such as the actomyosin lattice, is X-ray diffraction presented in the next section.

1.4 X-ray diffraction of muscle tissue

1.4.1 Development of X-ray diffraction

X-ray diffraction is an imaging technique known from crystallography, which allows the molecular structure of crystalline samples to be probed [30]. The concept of X-ray diffraction dates back to Bragg's law for constructive interference, which was published in 1913 by Lawrence Bragg and his father William Henry Bragg [198]. In current research, X-ray crystallography is used to encode the structure of protein complexes by analyzing far field diffraction patterns. Recently, the structure of the SARS-CoV-2 virus and its binding properties to different drugs were characterized using X-ray diffraction [199]. One of the biggest challenges in conventional X-ray diffraction crystallography of protein structures is the manufacture of protein crystals without changing the gross and local molecular arrangement and the natural function [200, 201]. However, it is also possible to probe the structure of samples which do not have a perfect crystalline structure.

First X-ray diffraction studies of biological materials were performed on samples containing natural protein fibers such as silk, wool, but also nerve, tendons and muscle tissue using laboratory X-ray sources [202, 203]. Moreover, in 1953, the helical desoxyribonucleic acid (DNA) structure was encoded by James Watson and Francis Crick with diffraction data from Rosalind Franklin [204]. Around the same time, X-ray diffraction studies on muscle tissue were resumed using rotation anode sources [205, 206].

The orientation dependent scattering properties of muscle tissue were already known from polarized light microscopy before the discovery of X-rays by Röntgen [19]. The naming of the A and I band of the sarcomere goes back to the scattering properties and indicates the diffractive properties of muscle. The presence of myosin rods in the A-band with a constant length was confirmed in the 1860s [207, 208]. However, it took another 100 years until the basic principle of muscle contraction was revealed by a correlative imaging approach involving light microscopy, electron microscopy and X-ray diffraction.

In 1954 X-ray diffraction experiments as well as light and electron microscopy record-
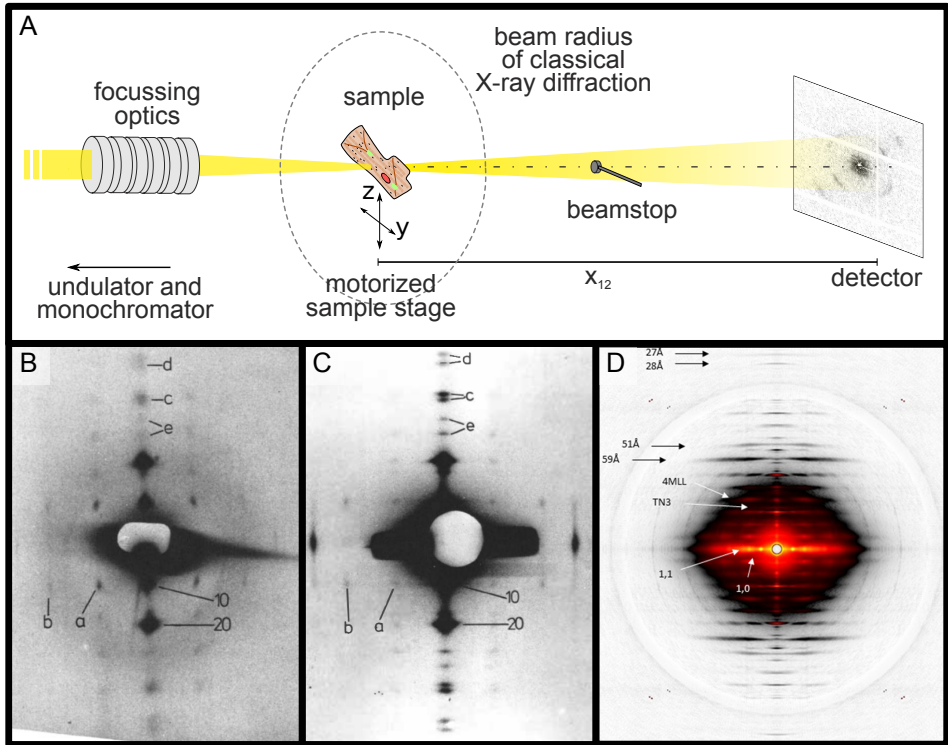
Fig. 1.8: X-ray diffraction of muscle tissue. (A) Schematic setup of a scanning X-ray diffraction beamline. Monochromatic beam, focusing optics (usually beryllium lenses or a pair of KB mirrors), sample stage, beamstop to block primary beam and detector. (B) Laboratory diffraction pattern, acquisition time 14 hours [215]. (C) Diffraction pattern acquired at DESY synchrotron in 1 hour [215]. (D) X-ray diffraction pattern of a murine calf muscle acquired at Beamline 18 (Advanced Photon Source, Argonne National Laboratory) in 0.375 seconds [216].

ings on frog muscle were performed by Hugh Huxley and Jean Hanson as well as by Andrew Huxley and Rolf Niedergerke. Both groups observed a correlation between the change in length of H-zone and Z-disc movement, supporting the sliding filament theory [19, 209, 210]. Their results were confirmed by follow up studies in the 1960s, which involved electron microscopy and laboratory X-ray diffraction and could prove the existence of cross-bridges between actin and myosin by the globular heads of myosin [211–214]. However, the photon flux of laboratory sources and the data quality of the pattern was too low to carry out dynamic measurements on muscle contraction at that time.

Due to developments in X-ray generation using synchrotron radiation facilities, acquisition times and data quality of diffraction measurements could be improved. In August 1970 the first X-ray diffraction experiment at a synchrotron was performed on an insect flight muscle [217]. The acquisition time at laboratory diffraction setups is in the range of hours to days when analyzing soft tissue samples such as muscle tissue [215]. Figure 1.8B shows a diffraction pattern of a bug flight muscle recorded in 14 hours using a rotation anode source. The same tissue was analyzed at the DESY synchrotron. The corresponding diffraction pattern was acquired in one hour and is shown in Figure 1.8C. The reflections marked with a 10 and 20 corresponds to the $d^{(1,0)}$ and $d^{(2,0)}$ myosin-myosin filament distance. They define the equatorial plane. The doublets occur from different lattice planes (e. g. c: $d^{(2,1)}$ and $d^{(3,0)}$). The horizontal reflections (meridional plane) occur from the cross-bridge repeat at the myosin head binding sites and the helical arrangement of cross bridges around the thick filament. Intensity changes of reflections a and b indicate changes of cross-bridges positions.

The first beamline designed for X-ray diffraction started its operation in 1972 inside bunker 2 of DESY in Hamburg. The focused monochromatic beam had a cross section of 200×250 μm^2 and a flux of 10^9 ph/s. Compared to a rotating anode source, the flux density was two orders of magnitude higher. However, time-resolved studies of oscillating insect flight muscle remained without the success hoped for [215]. One of the reasons for the failure of the experiment is the small change of the actomyosin lattice spacing for insect flight muscle. In 1981 Huxley could show changes in meridional reflections obtained from contracting frog muscle at the EMBL outstation of the DORIS facility in Hamburg [218]. The advantage of frog muscle studies is the easy dissection process, the possibility to induce a contraction by electrical stimulus and the comparably large variation in actomyosin lattice spacing during contraction. However, compared to insect flight muscles with a highly crystalline structure, the signal of the reflections is comparably weak.

Further improvements in X-ray generation led to higher quality and increased photon flux. Third generation synchrotron radiation enabled to measure the dynamic changes in the diffraction patterns on the millisecond time scales [219, 220]. The gain in image quality is visualized in the lower row of Figure 1.8. Compared to laboratory (B) and first synchrotron results (C), the diffraction pattern of a murine calf muscle recorded in 0.375 seconds at beamline 18 (Advanced Photon Source, Argonne National Laboratory) shows clear reflections with higher detail (D) [216].

In 1990 , the substructure of the actin and myosin rods as well as the ATP binding sites could be decoded by protein crystallography [30]. Furthermore, it was shown by X-ray diffraction that the actin and myosin molecules are not totally rigid, but show variation in length of about 0.3 to 0.5% under tension [221, 222].

1.4.2 Scanning small angle X-ray scattering

The real space resolution of classical X-ray diffraction is given by the area illuminated by the X-ray beam. Thus, it is not possible to identify local differences in the cellular structure or dynamics at scales smaller than the beam diameter. With recent progress in X-ray focusing capabilities such as Beryllium lenses and KB mirror systems, a new field of application for X-ray diffraction evolved [223–225].

Figure 1.8A shows a sketch of a scanning small angle X-ray scattering (scanning SAXS) setup. Compared to classical X-ray diffraction experiments, the X-ray beam is additionally focused. By lateral movement of the sample through the nano- or micro-focused beam, diffraction patterns are recorded at different positions. Since the diffraction pattern yields the structural information of the illuminated area, local structural parameters can be observed.

For the analysis of muscle tissue, scanning SAXS is a suitable technique to probe the local actomyosin structure. In previous work of our group we investigated the structure of 2d cardiac tissue slices. Besides identification of the local lattice spacing by the peak positions, the total scattered intensity and the degree of myofiber orientation was determined [226, 227]. By the analysis of the local diffraction patterns, differences in structural arrangement were observed for diseased heart tissue compared to a healthy control sample [228].

Furthermore, the structure of isolated biological cells was investigated by former members of our group [229–232]. In combination with fluorescent staining and STED or with X-ray holography, the orientation of single myofibrils can be determined by X-ray diffraction of single cells [233–235]. However, the sample preparation for single cell analysis is challenging. First experiments of isolated cells were performed on freeze-dried cardiomyocytes mounted on thin silicon nitrite foils. The diffraction patterns obtained in these experiments show a local anisotropy, however they do not show the characteristic peaks [236].

Using a liquid chamber, hydrated chemically fixed cells can be investigated [226]. The diffraction patterns obtained from hydrated cardiomyocytes show a characteris-

tic peak for the actomyosin lattice. Hence, the molecular structure of the sarcomere is better preserved compared to the freeze-dried preparation. While the intra-cellular signal as well as myofiber orientation do not show large deviations, variations of the mean lattice spacing were observed between different cells. Furthermore, the choice of the fixing agent affects the actomysin structure.

In this work, the scanning SAXS analysis was combined with high resolution X-ray tomography. In addition to the investigation of freeze-dried and hydrated cells, the previous work was extended to *in vivo* studies of freshly isolated cardiomyocytes [5]. The combination of X-ray diffraction, fluorescent imaging and phase-contrast tomography allows to probe the molecular structure of the cells, as well as the 3d electron density distribution.

In order to investigate the entire structure of the heart, a multiscale imaging approach ranging from the scale of the entire organ down to the actomyosin arrangement is needed and can be provided by the the work flow developed in this thesis.

Fiber orientation in a whole mouse heart reconstructed by laboratory phase-contrast micro-CT

2

M. Reichardt, M. Töpperwien, A. Khan, F. Alves, and T. Salditt

Abstract

Purpose: Here we present a phase contrast X-ray tomography study of wild type C57BL/6 mouse hearts, as non-destructive approach to the microanatomy on the scale of the entire excised organ. Based on the partial coherence at a home-built phase-contrast µ-CT setup installed at a liquid metal jet (LMJ) source, we exploit phase retrieval and hence achieve superior image quality for heart tissue, almost comparable to previous synchrotron data on the whole organ scale.

Approach: In this work, different embedding methods and also heavy metal-based stains have been explored. From the tomographic reconstructions, quantitative structural parameters describing the 3D architecture have been derived, by two different fiber tracking algorithms. The first algorithm is based on the local gradient of the reconstructed electron density. By performing a principal component analysis (PCA) on the local structure-tensor of small sub-volumes the dominant direction inside the volume can be determined. In addition to this approach which is already well established for heart tissue, we have implemented and tested an algorithm which is based on a local 3D Fourier transform.

Results: In this study, we could show that the choice of sample preparation influences the 3D structure of the tissue, not only in terms of contrast, but also with respect to the structural preservation. A heart prepared with the Evaporation Of Solvent method was used to compare both algorithms. The results of structural orientation

were very similar for both approaches. in addition to the determination of the fiber orientation, the degree of filament alignment and local thickness of single muscle fiber bundles was obtained using the Fourier-based approach.

Conclusions: Phase contrast X-ray tomography allows to investigate the structure of heart tissue with an isotropic resolution below 10 μm. The fact that this is possible with compact laboratory instrumentation opens up new opportunities for screening samples and to optimize sample preparation, also prior to synchrotron beamtimes. Further, results from the structural analysis can help to understand cardiovascular diseases or can be used to improve computational models of the heart.

2.1 Introduction

Heart contractility as one of the most important physiological functions relies on an intricate, hierarchical molecular and cellular architecture. The macroscopic structure of the heart and the inner structure of heart muscle is known for more than a hundred years from classical anatomy and histology. However, by the invasive nature of histological sectioning impedes the reconstruction of the detailed three-dimensional (3D) arrangement of cardiomyocytes and myofibrils for the whole organ. Accordingly, the 3D structure of heart muscle is not completely understood and there are many different attempts to describe it, as for example the controvers discussed helical ventricular myocardial band[20] or the idea of a complex 3D mesh of cardiomyocytes surrounded by a fibrous matrix[13, 22]. Verification of these fundamental models requires high resolution imaging of the heart structure. Ultrasound and diffusion tensor magnetic resonance imaging (MRI) are incapable to resolve the cellular structures of the entire heart with a resolution in the range a few micrometer [91]. Conventional absorption-based X-ray imaging results in low contrast, since the X-ray absorption of heart tissue is relatively small compared to mineralized tissues such as bone. One way to increase contrast is the use of metal-based stains such as iodine[179, 237, 238]. In order to increase contrast for unstained tissue, its phase-shifting properties can be exploited for contrast formation in weakly absorbing objects. For soft tissue the real-valued decrement δ of the refractive index $n = 1 - \delta + i\beta$ is by one to three orders of magnitude larger (depending on tissue composition and X-ray wavelength λ) than the imaginary part β. Phase-contrast X-ray imaging therefore offers superior image quality and in particular visibility of small features down to cellular and sub-cellular scale, while keeping the penetration depth at the scale of the whole organ. The overall potential

of the method has already been convincingly lined out using synchrotron radiation (SR) with a parallel beam geometry[181, 187, 190, 193, 194, 239]. In prior work, we could show that even sub-cellular features in heart tissue biopsies can be resolved [195] by cone beam phase contrast tomography with SR.

In this work we explore an approach to small animal heart imaging based on compact laboratory instrumentation. Firstly, this offers broader accessibility of the method, including further clinical settings in future. Secondly, high end SR beamtimes can be better prepared if different samples can be screened and sample preparation protocols can be optimized beforehand using laboratory instrumentation. In particular, we show that the image quality and resolution is high enough to deduce the 3D (pseudo-)vector field of heart tissue. Note that the structure of heart poses a multi-scale challenge for structure analysis, based on the different hierarchies: heart, cardiac mesh, aggregation of myocyte chains (aggregated units), connective tissue, myocyte chain, single cardiomyocyte, myofibril and finally the sarcomere as the molecular machine underlying contractility. Here we present phase contrast reconstructions of whole mouse hearts with pixel sizes around five microns. Based on the reconstructed electron density, the orientation of the muscle fiber bundles can be determined. To this end, we compare two different sub-volume-based algorithms. The first algorithm is based on the Fourier transform[191, 240]. Its implementation and validation was one of the main goals of the present work. By analyzing the Fourier space of small sub-volumes, the fiber orientation, the degree of filament alignment and also structural information as local thickness of single muscle fiber bundles can be obtained. Results from this algorithm are then compared to a more established approach based on the local gradient of the reconstructed electron density, which was already applied to high resolution synchrotron data[185, 193, 194].

The manuscript is organized as follows. Following the introduction, the procedure of sample preparation, data acquisition, phase reconstruction and tomographic reconstruction is described in Sec. 2.2. The quality of the 3D electron density obtained for the different preparations is than evaluated in terms of resolution, signal-to-noise and preservation of the cardiac structure in Sec. 2.2.3. In Sec. 2.3 the Fourier-transform-based algorithm including the analysis of orientation, degree of alignment and fiber thickness is introduced and compared to the gradient-based approach. In Sec. 2.4 the work is summarized and further possibilities for data analysis and possible applications as well as restrictions of this procedure are pointed out.

2.2 Three-dimensional structure of a whole mouse heart

2.2.1 Sample preparation

Fig. 2.1 presents the imaging setup, coordinate system and representative images of the samples. The heart structure of wild type C57BL/6 mice was investigated, using five different preparations, in view of comparing contrast and signal-to-noise ratio:

1. paraffin embedding[166],

2. paraffin embedding with an iodine stain[238],

3. paraffin embedding with a phosphotungstic acid (PTA) stain[166, 241],

4. embedding in liquid ethanol[242],

5. evaporation of solvent method (EOS)[173].

The whole explanted hearts were washed in phosphate-buffered saline and fixated in 4% formaldehyde solution for 24 hours. The stains were administered in solution by diffusion of the staining agent, with incubation times of 24 hours (iodine) or 7 days (PTA). Afterwards the samples were dehydrated in an increasing series of ethanol. For paraffin embedding the hearts were transferred to xylene and cast in paraffin. Excess paraffin was removed with a scalpel before imaging the sample. The heart embedded in 100% ethanol solution was mounted in a polyimide tube (*Kapton, Professional Plastics, Inc.*) with an inner diameter of 6 mm and a wall thickness of 75 μm. The EOS method was performed following the protocol described in [173].It is based on dehydration of the fixed sample in ethanol, removal of lipids using xylene similar to the classical histology procedure. The major difference is a evaporation of xylene instead of the transfer to liquid paraffin. The evaporation of xylene results in tissue shrinkage but does not alter the gross morphology[173]. The sample was also mounted in a polyimide tube with an inner diameter of 6 mm. An image of the different samples can be seen in Fig. 2.1c.

2.2.2 Data acquisition and phase reconstruction

Data acquisition was performed at a laboratory liquid metal jet μ-CT (*Excillum Metaljet-D2*) shown in Fig. 2.1a. The X-rays were produced by electrons focused on a liquid Galinstan (68.5% Ga, 21.5% In and 10% Sn) jet with a diameter of approximately 180 μm. For the experiments in this work the electrons were focused down to $10 \times 40 \ \mu m^2$
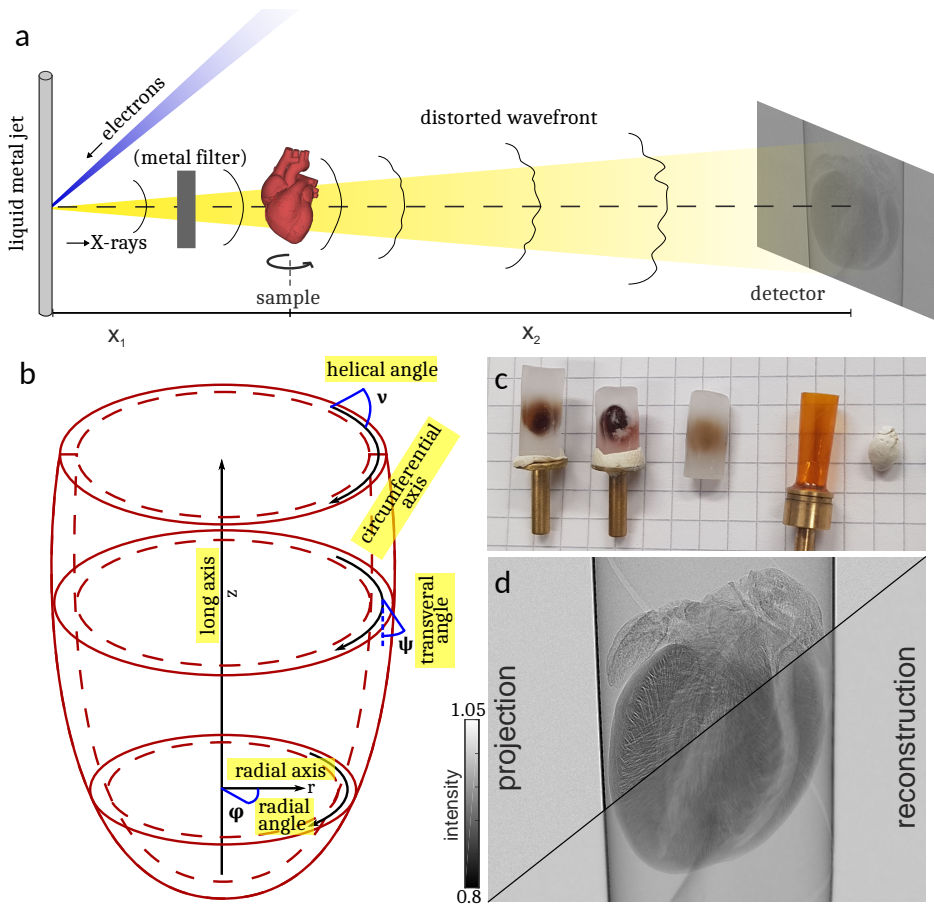
Fig. 2.1: (a) Sketch of the laboratory liquid metal jet μ-CT setup with electron beam sketched in blue and X-ray beam in yellow. The emission spectrum can be filtered (i.e. pre-hardened) by metal foils. The sample is placed at a distance x_1 behind the source spot and projections are recorded with a flat panel detector at distance x_2. (b) Definition of the coordinate system. Point in the heart are parameterized by cylindrical coordinates, i.e. z along the long axis positioned in the center of the left ventricle, azimuthal angle φ, and radial distance r. The fiber orientation are parameterized by the in-plane angle ψ and the helical angle ν. (c) Image of the different samples. From left to right: unstained, iodine and PTA stained paraffin embedded hearts, polyimide tube for sample mounting, EOS heart. (d) Empty beam-corrected projection acquired at the laboratory setup and the corresponding phase reconstruction.

resulting in an effective spot size of approximately 10×10 µm². The source was operated with a power of 100 W at an acceleration voltage of 70 keV. For samples with a higher absorption the emission spectrum of Galinstan with a characteristic energy at 9.25 keV (Ga K_α) was pre-hardened by a metal filter (35 µm Ag, 25 µm Ni) resulting in a peak energy of the K_α emission line at 24.2 keV[243–245]. The metal filter was installed behind the exit window of the source. The samples were mounted on a motorized triaxial translation and rotation stage (*SmarAct GmbH, PI miCos GmbH*) at a distance $x_1 = 10$ - 13 cm behind the source. Two additional translations stages (*PI miCos GmbH*) below the rotation axis allow the positioning of the rotation axis along the optical axis. For image acquisition a flat panel detector with a GsOS:Tb-scintillator screen (*Dexela CMOS, PerkinElmer Inc.*) consisting of 1536×1944 pixels with an isotropic pixel size of $dx = 75$ µm on motorized three directional translation system was placed at a distance of $x_2 = 150$ - 180 cm behind the sample. The cone beam geometry of the setup allows to customize zoom and field of view (FOV) by geometric magnification $M = \frac{x_1 + x_2}{x_1}$ and leads to effective pixel sizes of $dx_{\text{eff}} = \frac{dx}{M} = 5.2$ - 5.5 µm for the different data sets[140]. Due to a small effective source spot the effects of source blurring are relatively small. Considering the cone beam geometry projections were taken from 1001 equidistant angular positions over 185° for all data set. To increase the signal without saturating the detector, five acquisitions at each position were recorded and averaged. For the metal stained samples, the increased photon absorption of the tissue leads to a decrease in detectable photons at the detector plane. Most notably, low energy photons are absorbed by the sample. To reduce beam-hardening artifacts, the spectrum of the emitted X-rays was pre-hardened by a metal filter and the acquisition time was adapted to keep the photon flux of the empty beam comparable between the measurements. The acquisition and geometric parameters are given in Tab. 2.1, and were chosen in view of magnification/sample size and visibility of phase contrast effects (edge enhancement).

There are different approaches for the phase retrieval of the single projections such as Paganin's Single Material Object approach[141, 246], the contrast transfer function[148] or iterative algorithms[145]. In this work the Bronnikov-aided correction (BAC) was used[142]. The BAC approach provides optimal results for the imaging of weak objects such as soft tissue in the direct contrast regime, in particular at low coherence sources[143]. In addition to the phase shifting properties of an object, BAC also takes the absorption into account. This leads to a reconstruction of the image properties based on coupled (mixed) phase and absorption contrast, without losing resolution due to a blurring of the reconstruction. Fig. 2.1d shows an empty beam-corrected

Table 2.1: Acquisition parameters for the tomographic measurements at the laboratory μ-CT setup.

preparation method	Paraffin	Paraffin + PTA	Paraffin + Iodine	Ethanol	EOS
x_1 (cm)	10.00	10.00	12.75	12.75	12.75
$x_1 + x_2$ (cm)	144.60	144.60	174.40	174.40	180.50
effective pixel size (μm)	5.2	5.2	5.5	5.5	5.3
beam pre-hardening	no	yes	yes	no	no
acquisition time (s)	5×0.6	5×1.6	5×1.6	5×0.6	5×0.6

projection from the analysis of the EOS preparation on the left hand side. The corresponding reconstruction in which the edge enhancement was corrected is given on the right hand side of the image. For small propagation distances x between the object and the detector, the transport of intensity equation (TIE) can be linearized[118], and the intensity can be written as $I_x = I_0(1 - \frac{x 2\pi}{\lambda} \nabla_\perp^2 \phi)$. In a first step, the phase ϕ of a projection is approximated by the modified Bronnikov algorithm (MBA)[247], based on the TIE inversion of a pure phase object

$$\phi = \frac{2\pi}{\lambda x} \cdot \mathcal{F}^{-1} \left[\frac{\mathcal{F}[I_x - 1]}{|k|^2 + \alpha} \right].$$

To account for singularities at $k = 0$, an absorption-dependent regularization parameter α is introduced to prevent strong artifacts and blurring. These would amplify low spatial frequencies in the image and would inevitably corrupt these Fourier components resulting in strong artifacts and blurring. The assumption of a weak object leads to blurred reconstructions of objects with non-negligible absorption. In order to resharpen the image, a second reconstruction step is applied, in which a weakly absorbing and homogeneous object is assumed and the (effective) intensity distribution at the object plane is reconstructed from the approximated phase ϕ via

$$I_{x_1} = \frac{I(\Delta x)}{(1 - \gamma \nabla_\perp^2 \phi)},$$

where γ is a second α-dependent regularization parameter[143]. All parameters for the phase reconstruction of the different samples are shown in Tab. 2.2.

Table 2.2: List of the phase retrieval parameters for the Bronnikov-aided correction.

Embedding	Staining	α	γ
Paraffin	none	0.02	0.0690
Paraffin	PTA	0.05	0.0690
Paraffin	Iodine	0.03	0.0785
Ethanol	none	0.02	0.0785
Air (EOS)	none	0.02	0.0850

2.2.3 Evaluation of the tomographic reconstructions

The tomographic reconstruction was performed using the ASTRA toolbox[248]. Additionally, a ring correction[249] was performed. In order to characterize the three-dimensional structure of the heart, it is necessary to image the whole organ with sufficient resolution and contrast to identify the direction of the muscle fibers. Therefore, the results are evaluated with respect to resolution, signal-to-noise ratio and preservation of the tissue structure. Orthogonal slices of all tomographic reconstructions of the hearts are shown in Fig. 2.2. Each row of the figure shows a slice of the 3D volume along the long and short axis of the heart. In the lateral slices an area of the inter-ventricular septum is marked in yellow and a zoom of the region is shown on the right. Furthermore, a histogram of all gray values within the 3D volume is given on the right. The values are defined by the tomographic reconstruction of the effective absorption coefficient μ

$$\ln\left(\frac{I(r)}{I_0}\right) = -\mu N dx_{\text{eff}},$$

with the normalized intensity $\frac{I(r)}{I_0}$ of the projections and $N = 1944$ the number of horizontal detector pixels. The resolution of the respective data sets was calculated by the Fourier shell correlation (FSC) [250] of two independent reconstructions obtained by splitting the projections in two sets with odd and even angles. The signal-to-noise ratio (SNR) was determined by

$$\text{SNR} = \frac{\overline{A}_{\text{signal}} - \overline{A}_{\text{noise}}}{\sigma_{\text{noise}}}$$

where $\overline{A}_{\text{signal}}$ describes the mean amplitude of 100 voxels from a selected area of tissue of the centered slice with the highest signal, $\overline{A}_{\text{noise}}$ the mean amplitude of the surrounding medium and σ_{noise} its standard derivation. The resolution obtained by

Table 2.3: List of the signal-to-noise ratio as well as the resolution obtained at the laboratory μ-CT for different sample preparations.

Embedding	Staining	SNR	Resolution (μm)	Normalized resolution (dx_{eff})
Paraffin	none	8.8	8.15	1.57
Paraffin	PTA	25.3	6.80	1.31
Paraffin	Iodine	29.2	9.10	1.65
Ethanol	none	5.1	8.78	1.60
Air (EOS)	none	13.0	6.20	1.17

FSC and the SNR for each preparation is given in Tab. 2.3.

The overall structure of the hearts can be seen in all reconstructions, but the visibility of detailed structures within the cardiac tissue differ based on the different preparations. The resolution of all data sets is in the range below two pixel and mostly depends on the geometric magnification of the setup. Differences of the normalized resolution can be explained by the contrast and quality of phase reconstruction. Thus, the main focus is set to the evaluation of contrast and the conservation of the cardiac structure. In terms of contrast, metal-based staining of tissue samples result in highest SNR. Due to the penetration with high Z-elements the electron density of the tissue increases and thus the interactions with the x-ray in terms of absorption and phase shifting properties. Consequently, the difference between tissue and background leads to a better contrast. The SNR of both metal stained tissues is over 25 and about three times higher compared to other preparation, but there are differences in the details of the tissue structure in both stains, as can be seen in the zoom of the radial slices in Fig. 2.2. PTA can bind with a higher affinity to various cardiac tissue structures such as collagen, fibrin and other fibers of connective tissue[251]. On the contrary, iodine seems to lack this specificity hence, results in blurry reconstructions and randomly clusters at a few regions of the tissue. Furthermore, salt crystals from the buffer can be identified within the left ventricle. The data set of the dehydrated heart in ethanol has the lowest SNR, nevertheless single muscle fibers can be identified. The noise could be suppressed by a longer acquisition time and the contrast enhanced by a longer incubation in ethanol[242]. In order to keep the results comparable, experiments with higher acquisition time or incubation in ethanol are not shown in this study. For the preparation of the samples in liquid, it is mandatory to prevent bubbles
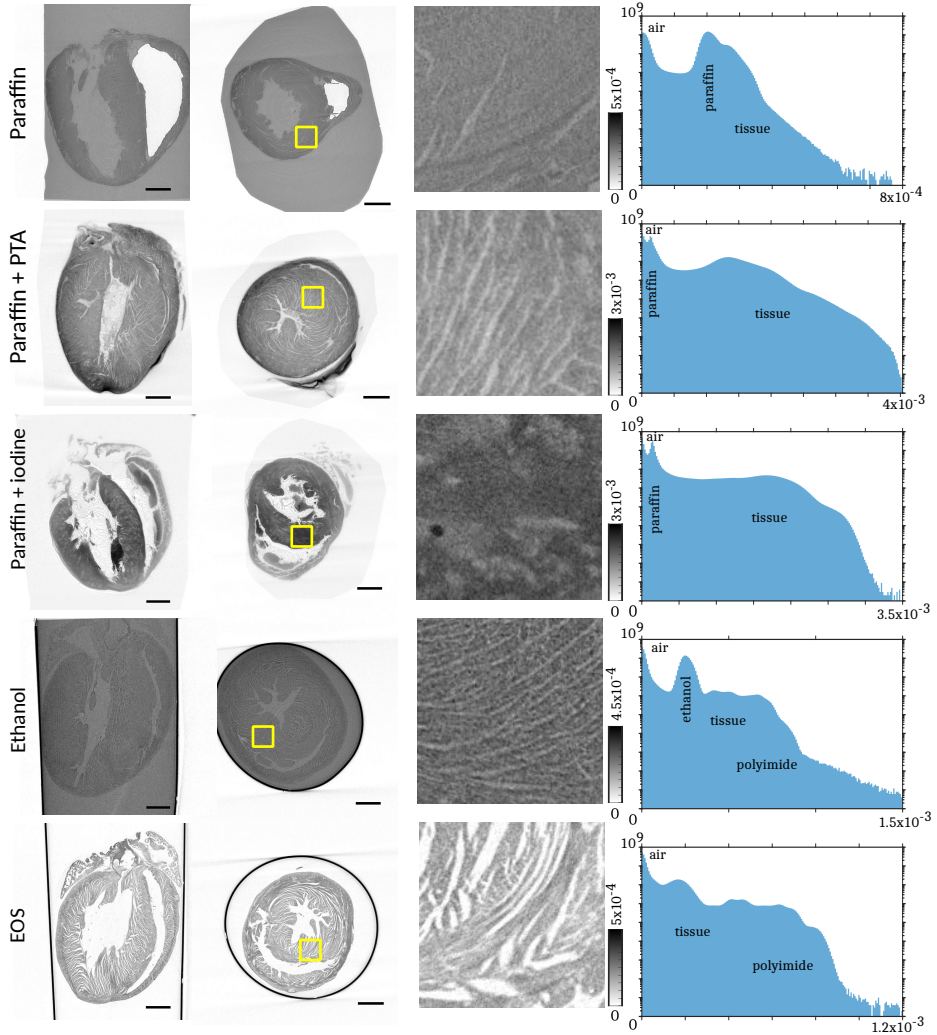
Fig. 2.2: Results of the tomographic reconstructions of the different sample preparations. For each row, the following items are shown from the left to right: a slice of the reconstructed volume along the long axis of the heart, a slice along the short axis, a zoom of the marked area of the inter-ventricular septum and a histogram of all gray values within the volume. Scale bars: 1 mm.

because even small bubbles in the liquid can grow and cause motion artifacts. For the preparations of the hearts mounted in paraffin air bubbles in the heart chamber do not cause motion artifacts due to the stability of the paraffin. Nevertheless, especially for the unstained tissue the sharp edges from air to paraffin lead strong scattering of the x-ray and result in small artifacts in phase reconstruction. The air bubbles can be removed by vacuumizing the tissue in liquid paraffin. The EOS preparation leads to a very structured reconstruction of the heart tissue. The removal of water and lipids lowers the absorption of the sample, but enables an enhanced contrast between tissue and air. The single muscle bundles separates from each other due to the dehydration and shrinking of the sample. This leads not only to an increase in contrast but allows to analyze the thickness of these bundles. Since the cardiomyocytes primary separate from each other and do not rupture or break, the principal structure of the heart should not be affected by this preparation. Further, the EOS reconstruction has a high SNR and the structure of the tissue is not affected by any staining agent. Hence, the it set is used for further analysis.

2.3 Orientation of the cardiomyocytes in the heart

2.3.1 Fourier-transform-based algorithm

For the analysis of the heart structure an algorithm based on a local 3D Fourier transform was implemented in Matlab (*The MathWorks, Inc.*). It is based on the reconstructed electron density of the sample and delivers the fiber orientation, as well as the degree of fiber alignment and the local fiber thickness. Due to the clearly recognizable structure, the high SNR and resolution the algorithm was applied on the heart which was treated with the EOS method. Before the data was analyzed, the volume was filtered with a three-dimensional Gaussian function with a standard derivation of 1 px. The schematic workflow of the analysis is shown in Fig. 2.3. The algorithm is applied to small sub-volumes (probing volumes) of the tomographic reconstruction, which are then shifted through the entire heart. For each data point a cube with a defined edge length $l = 48$ px is virtually cut from the volume. Fig. 2.3 shows (a) the volume rendering from the tomographic reconstruction carried out with Avizo (*FEI Visualization Science group*), (b) a typical sub-volume and (c) a 2D slice of this sub-volume. In order to reduce edge effects from the Fourier transform, the sub-volume
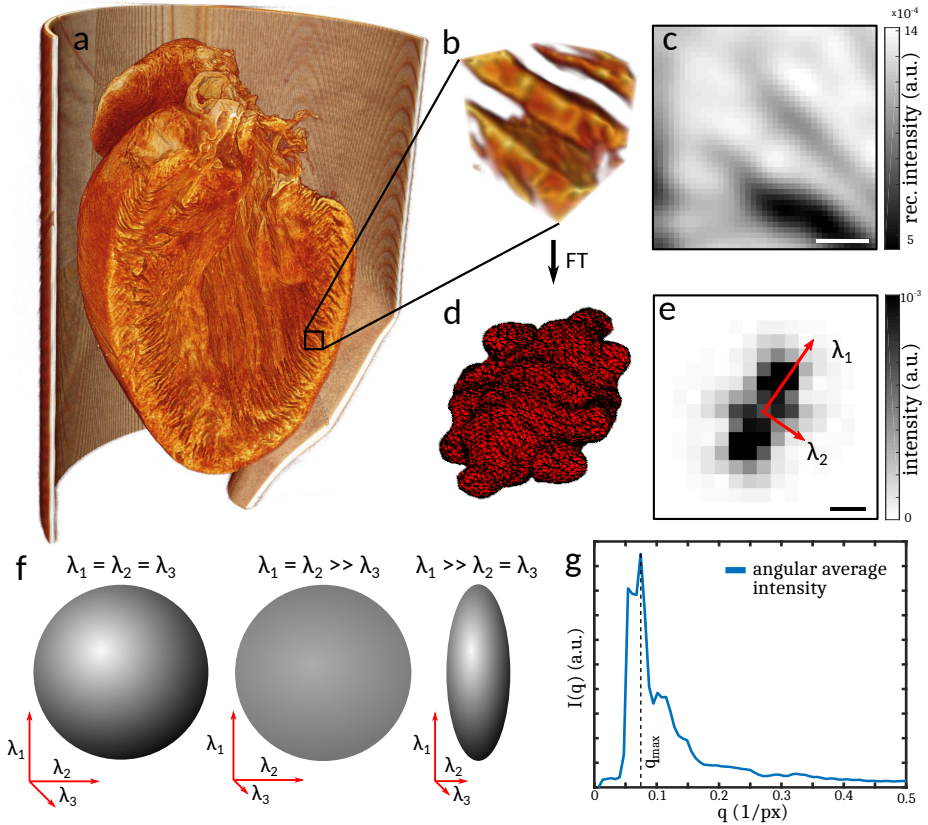
Fig. 2.3: Workflow of the fiber tracking algorithm. (a) Volume rendering of the reconstructed electron density of a mouse heart treated with the evaporation of solvent method. (b) Small cubic sub-volume with a defined edge length. (c) Two-dimensional slice of the sub-volume. Scale bar: 50 μm. (d) 3D Fourier space of this volume. By comparing the eigenvalues of the PCA, a degree of anisotropy in each sub-volume can be defined. (e) 2D slice of the Fourier transform. Sketch of two eigenvectors. Scale bar: $0.1\,\frac{1}{\mathrm{px}}$. (f) Possible shapes of the ellipsoid spanned by the results from the PCA: Sphere, disc, rod. (g) Angular average of the intensity of the Fourier space. Peaks appear along the direction of the main component and correspond to main fiber thicknesses in the real space volume.

is multiplied with a 3D Kaiser-Bessel window $W(r)$ in the form

$$W(r) = \frac{I_0(\beta)\sqrt{1 - (\frac{r - l/2}{l/2})^2}}{I_0(\beta)},$$

with the zero-order modified Bessel function of the first kind $I_0(x) = \sum_{n=0}^{\infty} [\frac{\frac{x}{2}^n}{n!}]^2$ and the distance r to the center of the sub-volume and the tuning parameter $\beta = 8$. A typical outcome of the Fourier transform can be seen in Fig. 2.3d. It is similar to a tri-axial ellipsoid and yields information about the spatial frequencies in the volume. In order to quantify the orientation and degree of alignment of this ellipsoid a principal component analysis (PCA) is applied to the co-variance matrix C

$$C = \begin{pmatrix} \langle q_{xx} \rangle & \langle q_{xy} \rangle & \langle q_{xz} \rangle \\ \langle q_{yx} \rangle & \langle q_{yy} \rangle & \langle q_{yz} \rangle \\ \langle q_{zx} \rangle & \langle q_{zy} \rangle & \langle q_{zz} \rangle \end{pmatrix},$$

with

$$\langle q_{ij} \rangle = \frac{\int I(q_x, q_y, q_z)\, q_i q_j\, d\vec{q}}{\int I(q_x, q_y, q_z) d\vec{q}}$$

for each sub-volume of the reconstruction. The corresponding eigenvalue problem

$$C \cdot \vec{b_i} = \lambda_i \cdot \vec{b_i}$$

yields three eigenvectors $\vec{b_i}$ with $i \in 1, 2, 3$, which form a new orthogonal basis. The eigenvalues $\lambda_i = \sigma_i^2$ correspond to the variance along the three principal directions. All eigenvectors are sorted by the corresponding eigenvalues in descending order. Two eigenvectors are sketched in the 2D slice of the Fourier transform in Fig. 2.3e.

Fiber orientation. The vector related to the largest eigenvalue describes the direction with the highest variance in Fourier space, i.e. the direction of greatest structural changes. In the present case, this direction is orthogonal to the elongated muscle bundles. Thus, the orientation of the fibers in real space is directed perpendicular to the pattern orientation. It corresponds to the eigenvector with the lowest eigenvalue. While the orientation is given, the direction ($\pm$) remains undefined due to the point symmetry in reciprocal space. The angles obtained from this analysis in Cartesian coordinates are transformed to the coordinate system of the heart as described in Sec. 2.2.3.

Degree of orientation. The results of the principal component analysis spans a tri-

axial ellipsoid in the eigenspace with an orthogonal basis of eigenvectors. The relation of the eigenvalues gives information about the degree of anisotropy ω, defined as [252]

$$\omega = \sqrt{\frac{(\lambda_1 - \lambda_2)^2 + (\lambda_2 - \lambda_3)^2 + (\lambda_3 - \lambda_1)^2}{2(\lambda_1^2 + \lambda_2^2 + \lambda_3^2)}}$$
$$= \sqrt{\frac{1}{2}\left(3 - \frac{1}{\text{trace}(R^2)}\right)}$$

with $R = \frac{D}{\text{trace}(D)}$ and the normalized diagonalized co-variance matrix D from the analysis. Depending on the relation of the eigenvalues λ_k the shape of the ellipsoid can be approximated by a sphere ($\lambda_1 \approx \lambda_2 \approx \lambda_3$), a three-dimensional disk ($\lambda_1 \approx \lambda_2 \gg \lambda_3$) or as a rod ($\lambda_1 \gg \lambda_2 \approx \lambda_3$). A sketch of these shapes is shown in Fig. 2.3f. If all eigenvalues are the same length and therefore indistinguishable, $\omega = 0$, the ellipsoid degenerates to a perfect sphere. For $\omega = 1$, the ellipsoid becomes an infinitely long rod in the direction of the the largest eigvenvalue.

In order to maximize the anisotropy for a disc shaped ellipsoid which is the most relevant shape in Fourier space for fiber tracking, we modify the above definition according to $\lambda_i \rightarrow \lambda_i^{-1}$, defining a 'reciprocal' anisotropy Ω

$$\Omega = \sqrt{\frac{(\frac{1}{\lambda_1} - \frac{1}{\lambda_2})^2 + (\frac{1}{\lambda_2} - \frac{1}{\lambda_3})^2 + (\frac{1}{\lambda_3} - \frac{1}{\lambda_1})^2}{2(\frac{1}{\lambda_1}^2 + \frac{1}{\lambda_2}^2 + \frac{1}{\lambda_3}^2)}}$$
$$= \sqrt{\frac{1}{2}\left(3 - \frac{1}{\text{trace}(R'^2)}\right)}$$

with $R' = \frac{\frac{1}{D}}{\text{trace}(\frac{1}{D})}$. In this case, the anisotropy is 0 for the sphere shape, 1 for a disc shaped ellipsoid and 0.5 for an infinitely long rod. Hence, Ω is well suited to describe the strength of the orientation of the cardiomyocytes in the sub-volume probed.

Fiber distance. In addition, we stress that Fourier-based analysis in sub-volumes processed in a sliding window approach can go well beyond simple analysis of anisotropy, since all structural information is contained in the phase and amplitude data. Fig. 2.3g illustrates a simple example, showing a characteristic peak in the intensity distribution $I(q)$ after a radial average. The peak at $q_{max} = 0.071\frac{1}{\text{px}}$ corresponds to a real space periodicity of 14 px = 74.2 µm, attributed to distances between adjacent car-
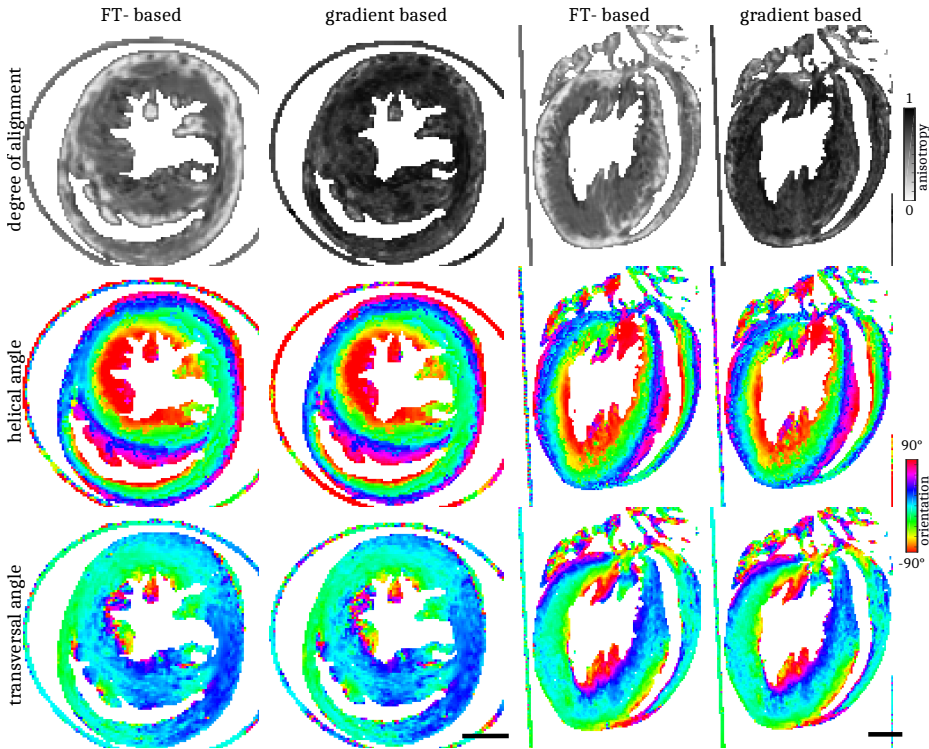
Fig. 2.4: Results of the structural orientation obtained by the FT- and gradient-based algorithm. For each approach the anisotropy, the helical angle and the transversal angle of a slice along the long and short axis of the reconstruction is shown. Both algorithms provide similar results for the orientation of the inner structures of the heart. The values of the anisotropy, however, are systematically smaller for the Fourier-based approach. Scale bars: 1 mm.

diomyocyte chains. Note that in order to highlight this signal, the signal was divided by a background curve computed from a cone-shaped integration along the direction of the shortest eigenvalue where no peak is observed.

2.3.2 Comparison to a gradient-based algorithm

In the following, we compare the sliding-window Fourier method to the established gradient-based structure tensor analysis[185, 194]. The local structure-tensor ST is

constructed from the first derivative of the intensity changes as

$$ST = \begin{pmatrix} \sum g_{xx} & \sum g_{xy} & \sum g_{xz} \\ \sum g_{yx} & \sum g_{yy} & \sum g_{yz} \\ \sum g_{zx} & \sum g_{zy} & \sum g_{zz} \end{pmatrix},$$

with $\sum g_{ij}$ sum of the products of the gradient along i and j within a cube with a certain edge length l around the central pixel. The analysis based on the gradient of intensities is similar to the Fourier analysis. The solution of the eigenvalue problem

$$ST \cdot \vec{b_i} = \lambda_{i,\text{grad}} \cdot \vec{b_i}$$

yields three eigenvectors $\vec{b_i}$ and eigenvalues $\lambda_{i,\text{grad}}$ which also delivers information of structural orientation within the sub-volume. The structures within the sub-volumes are oriented towards the direction with the lowest changes in intensity. Thus, their orientation is also described by the eigenvector with the smallest eigenvalue. Furthermore, the reciprocal anisotropy of the ST is a measure for the alignment of the filaments within the volume as well.

The analysis of the structural orientation within the tissue was performed using the two different algorithms explained above. The results for the anisotropy, helical angle and transversal angle are displayed in Fig. 2.4. Both algorithms show similar results. The values of the anisotropy, however, are systematically smaller for the Fourier-based approach, since the weight of Fourier components by (scattering) intensity is higher for small spatial frequencies. In fact, it is an advantage of the Fourier-based analysis, that the window of q-values which are exploited for anisotropy analysis could be tuned by different weighting (or window) functions. A further concern is to match the real space resolution or probing volumes of the two approaches. For the gradient-based approach, the gradient values are averaged over a cube of side length l_{grad}. We match the real space volume of the Fourier space approach, taking into account the Kaiser-Bessel window $W(r)$, which is required to prevent aliasing effects, as

$$l_{\text{grad}}^3 = l_{FT}^3 \int dr W(r).$$

In this work, a side length of $l_{\text{grad}} = 20$ px leading to $l_{FT} = 48$ px was chosen. The respective volumes were shifted by 10 px per analysis point. The application of the 3D Kaiser-bessel window leads to a smoothing of the edges and thus to small differences

of the local information compared to the gradient based approach. However, the extracted orientation from both algorithm is very similar. The results of a centered slice in the lateral and axial plane are shown in Fig. 2.4. Note that the gradient-based approach is computationally much faster since it is missing the calculation of the fiber distance.

The FT-based analysis on the other hand retain the spatial information of the structure in the sub-volume. They are encoded in Fourier space and can be used to obtain information of the orientation of all the structures within the volume as well as structural information within the sub-volume such as a dominant inter fiber distance as described in section 2.3.1. In the following the results of such an analysis are presented.

2.3.3 Organization of the three-dimensional heart muscle structure by Fourier analysis

The reconstruction of the three-dimensional mouse heart structure obtained at the laboratory liquid metal setup, as shown in Fig. 2.5, was analyzed with the two different fiber tracking algorithms described before. The analysis of the heart was performed as sketched in Fig. 2.3 and the final results of the complete analysis including the 3D vector field of alignment, degree of orientation, helical and radial angle, as well as the fiber thickness are shown in Fig. 2.6. The 3D representations are created by Paraview (*Kitware, Inc.*). The anisotropy i.e. degree of orientation is color-coded in the 3D visualization of the vector field in Fig. 2.6a. For an improved display, the vector field is cut in the same way as the reconstructed electron density in Fig. 2.3a. Based on the direction of the structures and its anisotropy, a stream-tracing algorithm implemented in Paraview was performed. It results in a complex mesh of traces which is shown in Fig. 2.6b. The traces are winding around the ventricle in a helical manner but there are also paths crossing with a high helical angle. In order to give a more ordered impression of the structure, two orthogonal slices of the heart are shown in Fig. 2.6c and Fig. 2.6d. On the left, the reconstructed electron density of the 2D slices is shown. The structure of the muscle tissue can clearly be derived from the background. Furthermore the surrounding polyimide tube, with a higher electron density can be identified. The middle left shows the radial angle obtained from the analysis. It indicates that the cardiomyocytes are arranged in a loop surrounding the ventricle. In the middle at the right, the slices are color coded by the the helical angle. The value of the helical angle decreases from epicardium to endocardium. It is approximately $20°$ and decreases to

Fig. 2.5: The volume rendering of the reconstruction of the electron density. Still image from Video 1 (Video 1, MPEG, 10 MB). For the video and the data files of the tomographic reconstruction and calculated vector filed of the Fourier analysis see https://doi.org/10.5281/zenodo.3403379.

almost -90° near the left ventricle. Thus, there is a borderline in the middle of the myocardium around the left ventricle where the helical angle is close to zero. Consequently, the structures are oriented in the radial plane. The combination of radial and helical orientation indicates an arrangement of cardiomyocytes in a closed loop in the radial plane. This supports the old concept of the *Triebwerkzeug* by Krehl[253, 254], according to which a strong muscle ring is surrounding the left ventricle to assist the contraction of the heart. In addition, the thickness of the structures was determined by the procedure explained above, see the color-coded in slices displayed on the right. It indicates a smaller inter-fiber distance in the apex of the heart and in the wall of the right ventricle. Note that the reconstructed distance highly depends on the preparation and dehydration of the tissue. Nevertheless, the thickness of the polyimide tube with a wall thickness of 75 µm can be exactly reconstructed by the algorithm.
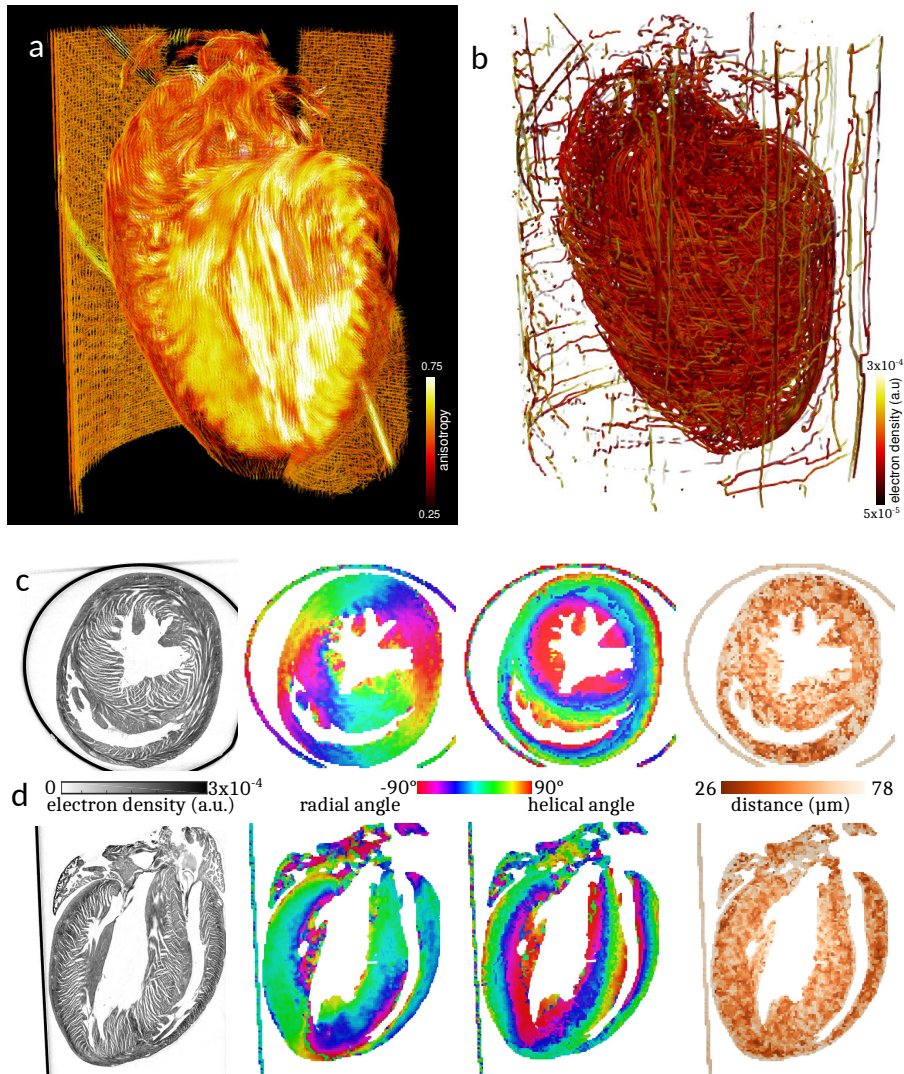
Fig. 2.6: Results of the FT-based algorithm. (a) Virtual cut of the three dimensional vector field from the FT analysis color-coded with the anisotropy. (b) Streamlines calculated from the vector field (c) lateral and (d) transversal slice of the reconstructed electron density, radial angle, helical angle and calculated fiber distance.

2.4 Outlook

In the present work we have imaged whole mice hearts by propagation-based phase contrast using a laboratory µCT. The contrast of the reconstruction was found to be highly dependent on the preparation of the tissue. Metal-based stains enhance the contrast, but the specificity of the binding to the muscle tissue depends on the staining agent. In the present work, PTA provided a more homogeneous and specific staining result than the iodine stain. Importantly, we have also shown that preparation without any staining agent, notably embedding in paraffin, ethanol and especially the EOS method, resulted in satisfactory tomographic reconstruction of the heart muscle network. Based on these reconstructions, the orientation of muscle bundles was analyzed by two different algorithms. The gradient-based approach enables the possibility to determine the orientation of the muscle fibers in a small volume. Its functionality and certainty was already proven by comparisons to diffusion tensor MRI and histology[193, 194, 239]. By extending the analysis of the algorithm by the degree of orientation, i.e. the anisotropy Ω, a further important structural parameter was included.

The Fourier-based approach implemented in this work, which also operates on small sub-volumes of the tomographic reconstruction, delivers a similar output for the orientation of the structures. The Fourier transform of the sub-volume is a representation of the entire structural information contained in real space. It allows to extract a number of parameters beyond the anisotropy based on PCA. For instance, peaks in the 3D Fourier intensity pattern, correspond to periodicities in the electron density, and can be used to deduce distances between myocyte chains. These peaks appear in the angular average of the background corrected Fourier pattern. Besides the identification of peaks in Fourier space this type of analysis enables further possibilities to extract information from the data. For instance the variance of the distribution of fiber thicknesses can be extracted. It is also possible to look for specific distances and analyze the direction of multiple features by applying different q masks and perform multiple PCA. For example it would be possible to analyze the sarcomere period as well as the thickness of the cardiomyocytes for high resolution scans. Furthermore, it is possible to find multiple maxima in Fourier space and identify the orientation of multiple fibers in the sub-volume, not only the average orientation for all structures within the volume.

Finally, it should be noted that the reconstruction with laboratory radiation at the present voxel size only allow for the extraction of the muscle fiber orientation in a

rather indirect way, since the different structural hierarchies are coupled. Small interfaces between aggregated units and or connective tissue, and in particular small tissue walls opening up during the preparation can serve as 'reporters' of the underlying structural levels. Only by SR, it will be possible to bridge whole heart imaging, for example based on stitch tomography with the true capability to image individual myocyte chains. Further extension of this work, will include application of the Fourier space algorithm to high resolution SR, including the most suitable preparations in excess buffer, which avoids structural alteration by drying.The possibility to image the heart in buffer solution also opens the opportunity to analyze a beating heart using a Langendorff perfusion system[45]. Future high resolution 3D imaging will be a fundamental requirement for the understanding of the contractile function. Building up on high resolution data, local information about the structural parameters of heart tissue could be used to improve the understanding of heart function. For instance, results from the analysis could be used to model the electro-mechanical properties of the heart. Since the propagation speed of the neuronal signal is faster in the direction of fiber orientation, results from the presented analysis can improve existing computational models of the heart[45]. By comparing the structure of healthy tissue to pathologies, such as in cardiac fibrosis for example, structural controls can be developed also for novel different diagnostic and treatment strategies.

ONLINE SUPPLEMENTAL INFORMATION

A video showing the 3D reconstruction of heart

For a video (.mp4) and the data files of the tomographic reconstruction and calculated vector filed of the Fourier analysis see https://doi.org/10.5281/zenodo.3403379.

Disclosures

This work was presented at SPIE Optics and Photonics 2019 as contribution 11113-25 'Fiber orientation in a whole mouse heart by a laboratory μ-CT'. Presentation Date: 14 August 2019. It is published in the corresponding conference proceedings (Optics and Photonics 2019: X-Ray, Gamma-Ray, and Particle Technologies). Apart from that, there are no relevant financial interests in the manuscript and no other potential conflicts of interest to disclose.

Acknowledgments

Multi-scale X-ray phase-contrast tomography of murine heart tissue

3

M. Reichardt, J. Frohn, A. Khan, F. Alves, and T. Salditt

Abstract

The spatial organization of cardiac muscle tissue exhibits a complex structure on multiple length scales, from the sarcomeric unit to the whole organ. Here we demonstrate a multi-scale three-dimensional imaging (3d) approach with three levels of magnification, based on synchrotron x-ray phase contrast tomography. Whole mouse hearts are scanned in an undulator beam, which is first focused and then broadened by divergence. Regions-of-interest of the hearts are scanned in parallel beam as well as a biopsy by magnified cone beam geometry using a x-ray waveguide optic. Data is analyzed in terms of orientation, anisotropy and the sarcomeric periodicity via a local Fourier transformation.

3.1 Introduction

The contractile function of the heart relies on an intricate structure spanning multiple length scales: starting with the molecular scales of the myosin motors and the actomyosin assembly, the formation of the sarcomeric units and myofibrils, to the cellular scale of single cardiomyocytes, arrangement of myocyte chains embedded in connective tissue, all the way to the aggregation of cardiomyocyte chains forming a complex cardiac mesh and finally the scale of the entire organ [13]. While the macroscopic architecture of heart muscle is known for more than hundred years from classical anatomy and histology, the detailed three-dimensional (3d) arrangement of muscle

cells and myofibrils cannot be reconstructed from histology alone, due to the invasive nature of sectioning [66]. Different models for the description of cardiac architecture are therefore still under intensive debate [20, 22]. With recent advances in medical imaging techniques, most notably magnetic resonance imaging (MRI) and ultrasound, the 3d structure of the heart can now even be imaged dynamically, however, not at a resolution to resolve the complete network down to the level of a single muscle cell [91, 255].

With the advent of phase-contrast micro-CT and improvements in data acquisition and reconstruction, it has now become possible to characterize the entire heart with voxel sizes in the range of a few micrometers using synchrotron radiation [181, 187, 190, 193, 194, 239], or even laboratory x-ray sources [256]. These results indicate that the heart is a complex 3d mesh of aggregated cardiomyocytes with a supporting fibrous matrix [13, 22]. In contrast to conventional x-ray imaging which is based on absorption and shows little contrast for heart tissue in the absence of heavy metal staining [179, 237, 238], phase contrast tomography exploits the intrinsic density variations within the tissue. These small spatial variations of electron density ρ_e determine the real-valued decrement δ of the x-ray refractive index $n = 1 - \delta + i\beta$, which is from 1 up to 3 orders of magnitude larger (depending on tissue composition and wavelength λ) than its imaginary part β which accounts for absorption. Phase-contrast x-ray imaging can hence visualize even small features down to cellular and sub-cellular scale for heart tissue biopsies [195]. At the same time, molecular structures of acto-myosin networks can be probed in thin heart sections by scanning diffraction with micro- and nano-focused beams [226, 227], also in combination with coherent imaging and correlative super-resolution microscopy [233, 234]. However, the acquisition time and dose of scanning diffraction would be prohibitive for 3d imaging of the whole heart, making it preferable to use full-field illumination and phase contrast CT to study the arrangement of cardiomyocytes within the heart.

While the orientation, degree of filament alignment and thickness of individual muscle bundles in the whole organ can be roughly estimated by sub-volume based algorithms also for laboratory CT data, the contrast and resolution are insufficient to make accurate statements about single myofibrils[185, 194, 256].

In this work, we present a multi-scale approach to phase contrast CT of heart tissue, combining whole heart overview scans of voxel size $vx = 3.25$ µm with region-of-interest (ROI) scans acquired at voxel size $vx = 650$ nm, and even $vx = 168$ nm by means of cone beam magnification. In a proof-of-concept experiment involving three levels of magnification we probe unstained fixed hearts of wild type mouse, com-

paring paraffin and ethanol embedding. To preserve image sharpness and to obtain quantitative density reconstructions, we use iterative phase phase retrieval algorithms [145, 257], which do not follow the conventional linearization schemes. These algorithms either work at large Fresnel number F and linearize the contrast in terms of the defocus distance [141, 246] or use linearization of the optical properties of the sample [148]. We then use reconstructed 3d data to characterize the structural orientation and degree of alignment of the heart tissue by an algorithm based on the local structure tensor ST[185, 256]. In order to extract the sarcomeric periodicity from the high-resolution data, a local Fourier-analysis of the electron density was used[256].

We implement this approach by an illumination scheme based on three different configurations of the *Göttingen Instrument for Nano-Imaging with X-Rays* (GINIX). The different configurations allow to image field of views (FOVs) with a range from several mm to a few hundred micrometer and are characterized by the profile of their wave front. For overview scans of the heart with high photon flux, we introduce a configuration based on the illumination of a pair of Kirkpatrick-Baez mirrors (KB). This setup enables to capture a FOV of about $7{\times}7$ mm^2 with an effective pixel size of 3.25 µm. Higher resolution was achieved by illumination of the sample using the natural divergence θ of the undulator in a parallel beam (PB) geometry. With this configuration for ROIs with a size of about $1.6{\times}1.4$ mm^2 were probed with high photon flux and an effective pixel size of 650 nm. In order to resolve the sarcomeric structure of the heart tissue, the cone beam geometry of a waveguide (WG) illumination was used. This configuration, with a scalable geometric magnification M, enables high-resolution scans of a biopsy punch with an FOV of few hundred µm^2 and an effective pixel size of less than 200 nm.

3.2 Experimental approach

The goal of this work is to study the structure of murine heart tissue on multiple length scales from the level of the whole organ down to the (sub-cellular) sarcomeric level. This requires a very particular experimental approach involving different optical schemes for the illumination with synchrotron radiation, as detailed below. The corresponding sample preparation and the experimental setup are sketched in Fig. 3.1. While the whole heart scan with FOV $= 7 \times 7$ mm$^2/vx = 3.25$ µm as well as the ROI scan with FOV $= 1{\times} 1$ mm$^2/vx = 0.65$ µm were acquired on an entire unsliced paraffin-embedded mouse heart, the high-resolution data set with
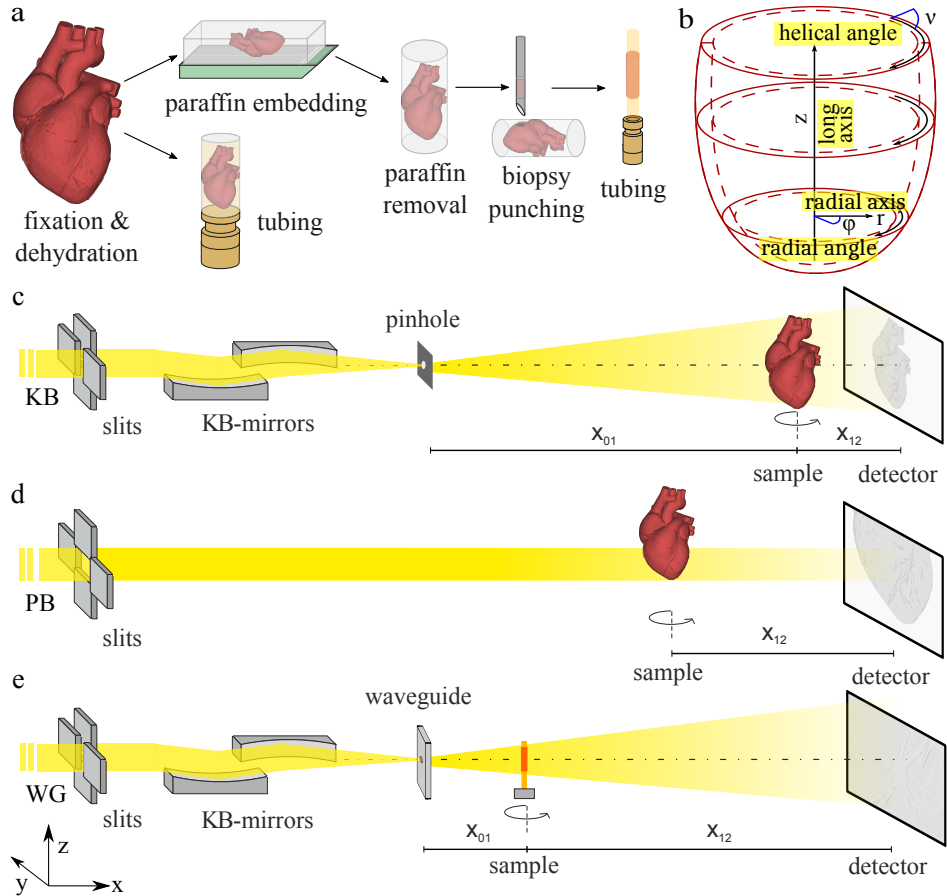
Fig. 3.1: (a) Schematic visualization of the sample preparation. Explanted hearts were fixed in 4% formaldehyde solution, and dehydrated in an increasing series of ethanol. One heart was stored in ethanol and the second organ was embedded in paraffin. Excess paraffin was removed with a scalpel. For high-resolution measurements, a biopsy was taken and placed in a polyimide tube. (b) Sketch of the coordinate cylindrical system for the description of the structural characterization. The long axis z is positioned in the center of the left ventricle and structural orientation can be parameterized by the radial plane defined by $\mathbf{r}$ and φ and the helical angle ν. (c) Experimental setup with KB illumination for overview scans with an FOV of several mm^2. The beam is focused by a pair of KB mirrors and cleaned by a pinhole with a diameter of 3 μm. The sample tower is placed at distance x_{01}. Projections are taken at distance x_{12} behind the sample. (d) Experimental setup with parallel beam illumination for ROI scan with an FOV of about 1 mm^2. Projections are taken with a microscope detection system at distance x_{12}. (e) Experimental setup with waveguide illumination for high resolution scans of tissue biopsies with an FOV of a few hundred μm. Due to the cone beam geometry, the magnification can be scaled by the source-sample distance x_{01}. Projections are taken at distance x_{12} behind the sample.

FOV $= 0.3 \times 0.3$ mm^2/$vx = 167.5$ nm was recorded from a 1 mm biopsy obtained from the paraffin block after the first two scans. For comparison, an ethanol-embedded heart was also scanned at large FOV and intermediate FOV.

Sample preparation: Freshly explanted hearts from two male 16 weeks old wildtype C57BL/6 mice were fixed in 4% formaldehyde solution for 24 hours. The fixed hearts were then dehydrated in an increasing series of ethanol. In order to determine structural differences depending on sample preparation, the first organ was stored in 100% ethanol solution and the second organ was washed in 100% xylene solution and embedded in paraffin. To decrease x-ray absorption, excess paraffin was removed with a scalpel. For high-resolution measurements, a biopsy with a diameter of 1 mm was taken and mounted in a polyimide tube. The structural orientation was analyzed and described in the coordinate system shown in Fig. 3.1b.

Synchrotron instrument: Data were acquired at the *Göttingen Instrument for Nano-Imaging with X-Rays* (GINIX) at the P10 beamline of the PETRA III storage ring at DESY (Hamburg, Germany). The endstation is dedicated to coherent nano-diffraction with focused undulator radiation, and in particular high-resolution holographic imaging using KB-waveguide compound optics [196, 258]. As a full-field technique it is ideally suited for tomography of extended samples such as biological tissue [164]. The 5 m long undulator (U29) creates an x-ray source of about 85 μm × 14 μm (FWHM, horizontal × vertical) with a divergence θ of 28 μrad ×3.7μrad (1σ, h × v). For the scans at large and intermediate FOV, a photon energy of $E = 13.8$ keV was chosen by a double crystal Si(111) monochromator. For the high-resolution scan on the heart biopsy, the energy was changed to $E = 8$ keV to increase interactions between wavefront and sample. The GINIX endstation is located about 87 m behind the source. For x-ray tomography this endstation can be operated in three different geometries which enable different resolutions and a multi-scale analysis, covering samples sizes with an FOV ranging from several mm^2 down to a few μm^2. The different configurations are characterized by their illumination optics and wavefront:

1. Kirkpatrick-Baez mirror (KB) illumination: Configuration for overview scans with high photon flux and an effective pixel size of 3.25 μm and FOV of about 8×7 mm^2.

2. Parallel beam (PB) illumination: Configuration for the region of interest (ROI) scans with high photon flux enabling an effective pixel size of 650 nm and an

FOV of about 1.6×1.4 mm^2.

3. Waveguide (WG) illumination: Setup with a scalable geometric magnification M for high-resolution scans with an FOV of a few hundred µm^2 and an effective pixel size of less than 200 nm.

A sketch of the different geometries is shown in Fig. 3.1b-d. The three experimental setups, the acquisition and the handling of the data is described in more detail below.

illumination	KB	PB	WG
photon energy (keV)	13.8	13.8	8
source-sample-dist. x_{01} (m)	5.06	88	0.12
sample-detector-dist. x_{12} (m)	0.34	0.22	4.98
effective pixel size (µm)	3.25	0.65	0.1675
field-of-view (mm^2)	8×7	1.6×1.4	0.42×0.36
acquisition time (s)	1	0.035	1
number of projections	2001	1500	1500
number of flats	200	150	50

Table 3.1: Data acquisition parameters for the three different geometries: (KB) broadened beam after focusing by KB-mirrors for whole organ, (PB) Parallel beam, (WG) waveguide setup for holo-tomography at high geometric magnification.

3.2.1 KB illumination

Since the natural divergence of the undulator beam is too small in order to reach a sufficiently large beam size to cover entire mouse heart even at 87 m, the beam is focused by a pair of KB mirrors. The KB focus then serves as a secondary source with a much higher divergence and hence a beam size which is easily adjusted by the defocus position. Since the KB reflectivity is about 95%, this scheme almost preserves the full flux impinging onto the mirrors with 400 µm active area (entrance pupil). In this work, the spot size in the KB focus was about $\omega \simeq 400$ nm $\times$ 440 nm (FWHM, h $\times$ v), as measured by waveguide scans through the focus. The size of the illumination area is then simply given by divergence θ of the KB beam, which is about 2.0 mrad $\times$ 1.3 mrad and the defocus distance $x_{01} = 5.1$ m yielding FOV $\simeq x_{01} \cdot \theta = 10.2$ mm $\times$ 6.6 mm ($h \times v$). The height deviation from the ideal elliptic profile and residual roughness of the KB mirror surface result in a pronounced pattern of vertical and horizontal stripes

in the illumination wavefront, which impedes the empty beam correction [146, 259–261]. In order to smoothen the wavefront and to remove these high-spatial frequency contributions, a pinhole with a diameter of 3 μm (tungsten, thickness 300 μm) was placed in the KB-focus. The pinhole acts as a spacial filter in reciprocal space and smooths the intensity variations in the detector plane.

The sample was mounted on a sample stage (SmarAct GmbH) at distance $x_{12} = 34$ cm upstream from the detector plane. For the alignment of the sample respective to the axis of rotation, two compact linear piezo positioners are used on top of the rotation stage. The rotation axis was aligned with respect to the illumination using an xyz-translation below the rotation. Furthermore, the whole stage was mounted on an aluminum plate which could be manually tilted by four adjustable screws to align the tomographic nick angle. Projections were recorded using an imaging system (Optique Peter) equipped with a 50 μm LuAG scintillator and an objective revolver (2x, 4x or 10x) coupled to a sCMOS camera (PCO edge 5.5, 2560 × 2160 pixels) with a physical pixel size $px = 6.5$ μm. The detector stage is also described in Fig. 3.2.

The geometry of the KB-illumination has a low geometric magnification $M = \frac{x_{02}}{x_{01}} \approx 1$ with $x_{02} = x_{01} + x_{12}$, but enables a relatively large FOV. Using the 2x objective resulting in an effective pixel size of 3.25 μm, projections of a whole mouse heart can be acquired in a single scan. For tomographic reconstruction, 2001 projections over 180 degrees with an acquisition time of 1 s were recorded. Additionally, 100 empty projections were acquired before and after each tomographic scan. All acquisition parameters are given in Tab. 3.1.

The spatial filtering of the illumination wavefront by the pinhole facilitates empty beam division without strong artifacts. Only some impurities of the scintillator occasionally led to overexposed and saturated pixels, which were removed by a median filter. However, small variations in the empty-beam divided near-field pattern remain since the illumination shifts slightly between the time of recording of the image and empty beam, respectively. To account for this, a suitable empty beam was generated for each projection by a linear combination of empty beam basis functions, generated by principal component analysis (PCA) from the pre- or post-recorded stream of empty beam patterns. The processing of the projections acquired at the KB configuration is also shown in Fig. 3.3
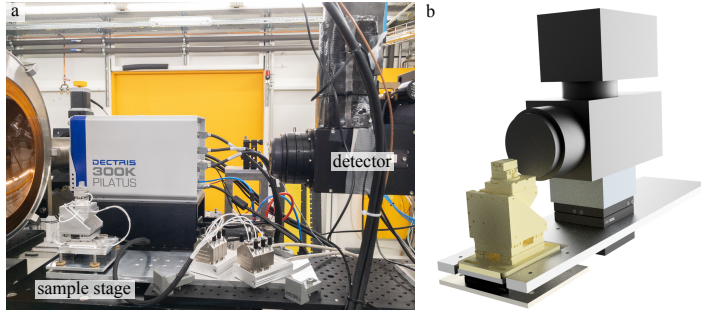
Fig. 3.2: (a) Image of the detector and sample stage positioned about 5 m behind the focus of the KB-mirrors. b) Technical drawing of the tomography stage used for KB-illumination. The sample stage (yellow) including two compact linear piezo positioners for alignment of the axis of rotation, one rotation and a linear triaxial translation system for sample positioning, is placed on a kinematic mount of an aluminum plate which can manually be tilted by four adjusting screws in order to align the nick angle. The imaging system (Optique Peter with a PCO edge camera, black) was placed at distance x_{12} behind the sample.
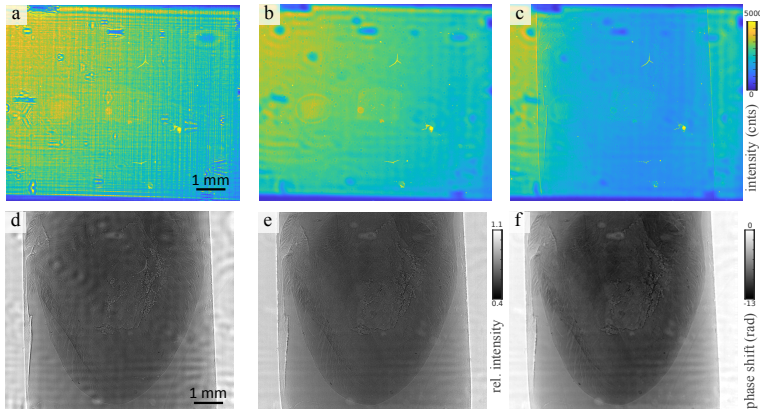
Fig. 3.3: Processing of the data acquired with KB illumination. (a) The plane KB illumination profile with yields frequency artifacts emerging from the nanostructures of the mirrors. (b) By positioning a pinhole with a diameter of 3 μm in the focus of the beam, the profile of the illumination is smoothed. (c) An exemplary projection of murine heart embedded in paraffin. (d) The conventional empty beam corrected projection yield artifacts from small variations in the illumination profile. (e) By creating an artificial flat field using a principal component analysis approach these variations can be reduced. (f) The phase reconstruction was performed by the nonlinear-Tikhonov CTF approach.

3.2.2 Parallel beam illumination

For ROI scans with higher resolution, the second configuration sketched in Fig. 3.1 was used. The sample tower is roughly in the same location as for the high resolution KB-waveguide configuration (configuration # 3, see below), but the KB is moved out by a few millimeters to use the primary beam without focusing. With slits fully opened, the beam size (FWHM) as defined by the divergence is about 5.8 mm × 0.77 mm (h × v) at the position of the endstation about 88 m behind the undulator source. In the vertical directions, all beamline slits are opened to exploit the natural beam size of the undulator beam at the position of the endstation; the horizontal slits were adjusted to fill the detector. The sample was placed on a completely motorized tomography stage with an air bearing rotation stage (UPR-160 Air, Micos, Germany). Due to the accuracy and reproducibility of the rotation, it is possible to acquire projections in a continuous scan, i.e. projections with a short acquisition time are taken while the sample is rotated continuously. For the data shown here, projections were recorded with the microscope camera system described above with a 10x objective at distance $x_{12} = 22$ cm behind the sample. In this work, we focused especially on the area near the apex of the heart. Over 180 degrees 1500 projections with an acquisition time of 0.035 s were acquired. In continuous scan mode, the acquisition time for one tomogram was 75 s. Before each tomography scan, empty projections were taken.

Due to the high stability of the illumination, it was not necessary to correct the flat field by a PCA approach. The flat field was computed by a median of all recorded empty projections. The processing of the projections acquired within parallel beam geometry is illustrated in the top row of Fig. 3.4.

3.2.3 Waveguide illumination

For imaging of the cardiac tissue with sub-cellular resolution, a biopsy of the heart tissue near the apex was taken from the previously scanned heart and investigated by holographic tomography using the cone beam geometry with WG illumination, i.e. configuration # 3 (see Fig. 3.1e). In this geometry, a waveguide is positioned in the focus of the KB mirrors. X-rays are coupled into the waveguide channel which acts as a spatial and coherence filter, similar to the pinhole of the KB setup but with a lateral confinement of ≤ 100 nm. Therefore, no artifacts from preceding optical components are visible and the empty beam intensity profile is smooth and Gaussian shaped. The small secondary source size at the exit of the waveguide and the high coherence of
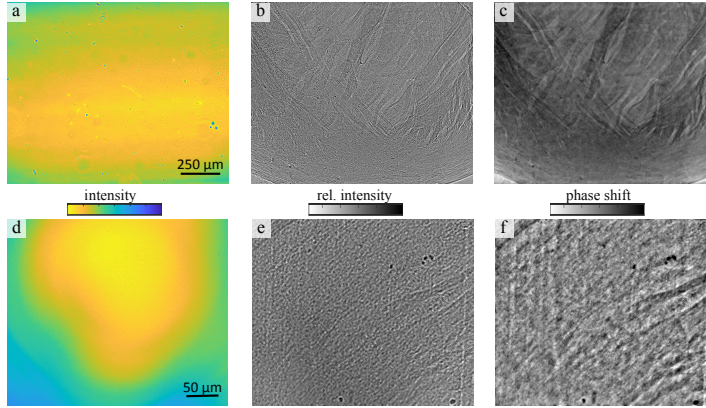
Fig. 3.4: (a) Illumination profile of the parallel beam. The colorbar of the intensity is scaled from 10 000 to 30 000 counts. (b) Exemplary flat field corrected projection of a ROI at the apex of the paraffin-embedded heart. Relative intensity: 0.4-0.75. (c) Phase reconstruction of the projection using the nonlinear-Tikhonov CTF. (d) Profile of the waveguide illumination. The colorbar of the intensity is given in logarithmic scale and set to 2 - 4.5. (e) Exemplary projection with a relative intensity of 0.2 - 0.9. (f) CTF reconstruction of the projection.

the WG illumination enables high geometric magnification $M = \frac{x_{02}}{x_{01}}$ which can be scaled by changing the source sample distance x_{01}. Projections were recorded with a sCMOS Camera (2560 × 2160 pixel) with 15 µm Gadox scintillator and a physical pixel size of 6.5 µm (Andor). The biopsy was scanned with an effective pixel size of 167.5 nm, 1500 projections over 180 degrees, and acquisition time of 1 s.

The flat field was created by the PCA analysis explained above. Additionally, the low frequency intensity variations of the background were corrected by Gaussian filtering. The processing of the projections acquired with in WG geometry is also illustrated in the lower part of Fig. 3.4.

3.2.4 Phase retrieval and tomographic reconstruction

For all projections, recorded at the three different configurations of the endstation, phase retrieval was performed after the empty beam correction. To this end, we first inspected data by linearized phase retrieval according to the contrast transfer function (CTF) algorithm. To this, the approximation of a homogeneous object was used,

illumination	KB	PB	WG
Fresnel number	0.3240	0.0216	0.0015
δ/β ratio	1/35	1/35	1/80
α_1	10^{-5}	10^{-5}	$3 \cdot 10^{-3}$
α_2	0.1	0.05	0.2
maximal phase shift	0	0	0
maximal number of iterations	100	100	100

Table 3.2: Parameters of the phase retrieval using the nonlinear-Tikhonov approach of the CTF.

specifying the phase distribution in the object plane $\phi(\mathbf{r}_\perp)$ by

$$\phi(\mathbf{r}_\perp) = \mathcal{F}^{-1}\left[\frac{(\sin(\chi) + \frac{\beta}{\delta}\cos(\chi)) \cdot \mathcal{F}\left[I^{(exp)}(\mathbf{r}_\perp) - 1\right]}{2(\sin(\chi) + \frac{\beta}{\delta}\cos(\chi))^2 + \alpha(\mathbf{k}_\perp)}\right],$$

with natural units $\chi = \frac{\lambda x k_x^2}{4\pi}$ for the (squared) spatial frequencies, measured intensities in the detector plane $I^{(exp)}(\mathbf{r}_\perp)$, $\frac{\beta}{\delta}$ ratio of imaginary and real part of the refractive index n, and a frequency-dependent regularization parameter $\alpha(\mathbf{k}_\perp)$. The results of the CTF then served as an initial guess for subsequent iterative phase retrieval based on a nonlinear Tikhonov approach, which does not require the assumption of a weakly varying phase. Further, additional object constraints such as range constraints for the phase shift can be included[149]. The method can be regarded as a nonlinear generalization of CTF phase retrieval, and for a weakly phase-shifting sample (linear approximation) without further constraints, both approaches yield exactly the same result. The minimization of the Tikhonov-functional is implemented by a gradient-descent method with adaptive step sizes[149].

The parameters of the phase retrieval were selected manually, optimizing contrast for tissue and paraffin. They are shown in Tab.3.2. If anomalous refraction effects can be neglected (far from absorption edges), the phase shift in the sample exit plane is directly proportional to the projected electron density $\int \rho_e(\mathbf{r})dx$. Hence, if the phase shift is with respect to the beam passing at the side of the object in air, the projected electron density can be obtained. For ROI tomography, the density values correspond to excess electron density with respect to the (average) medium defined by the object, i.e. it can be both positive and negative. Further complications arise from the fact that phase retrieval of inline holography is often hampered at small spatial frequen-

cies. The retrieved electron density must therefore be interpreted with caution and should in most cases be regarded as an effective excess density. Nevertheless, it is instructive to express the obtained values in terms of electrons per unit volume. After reconstruction by the inverse Randon transform, we therefore compute the local electron density from the phase shift induced by each voxel length vx as

$$\rho_e(\mathbf{r}) = \frac{\varphi_{vx}(\mathbf{r})}{vx\lambda \cdot r_0} \, ,$$

with wavelength λ and r_0 classical electron radius. For the tomographic reconstruction of the volumes the Astra toolbox with filtered back projection was used[248, 262]. Additionally, ring removal (wavelet and additive ring removal) was performed following [149, 249].

3.3 3d heart structure on different length scales

Figure 3.5 shows the tomographic reconstruction of the whole heart scans acquired with the KB illumination. In the top row, the reconstructed volume of the paraffin-embedded heart is depicted, and in the bottom row the reconstruction of the heart stored in ethanol. For both preparations, a transverse, a sagital slice and a rendering of the reconstructed volume are displayed. In terms of data quality (i.e. quality of phase retrieval and tomographic reconstruction), the paraffin-embedded sample exhibits less low frequency artifacts, which appear especially in the sagital slice Fig. 3.5e of the reconstruction of the heart in ethanol solution. This can be attributed to the better performance of the PCA analysis for the empty field correction. There were fewer variations in the illumination during the recording of the solid embedded heart, and also slight movements of the liquid embedded sample may have occurred. Note that motion artifacts are to be expected if the heart is not mounted tightly inside the tube, or if bubbles form due to the energy transfer from the radiation[263]. Furthermore, the fact that the x-ray absorption of the ethanol is higher and causes a higher difference between the empty illumination profile and the respective projection may have had an influence. However, whole heart phase contrast tomography in this configuration is possible for paraffin and liquid embedded hearts, showing a way to scan large tissues exceeding the natural beam width with brilliant undulator radiation and at small acquisition time.
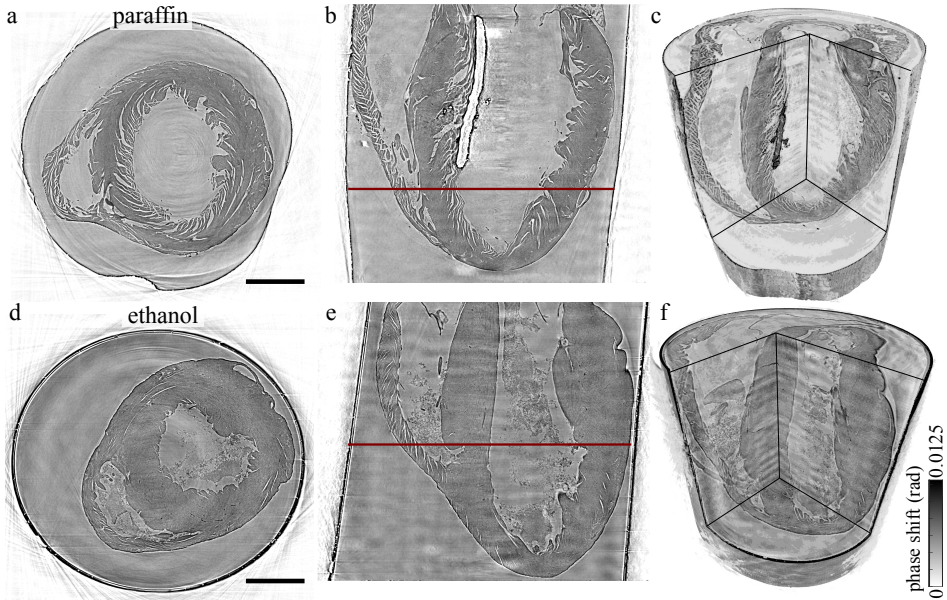
Fig. 3.5: Three-dimensional structure of the murine hearts acquired with the KB illumination. The top row: tomographic reconstruction of the paraffin-embedded heart, bottom row: tomographic reconstruction of the heart in 100% ethanol solution. From left to right a transverse and a sagital slice of the reconstructed volume and a volume rendering of the samples is shown for both sample preparations. The reconstruction of the paraffin-embedded sample yields fewer artifacts, due to a more stable flat field correction. However, the cardiac structure of the heart in 100% ethanol solution is better conserved. Scale bar: 1 mm.

With this configuration the influence of sample preparation on the integrity of the specimen was analyzed. The overall structure of the heart tissue can be well identified for both preparations, however, with differences characteristic for sample preparation. By comparing the tomographic results of both reconstructions shown in Fig. 3.5, there is no noteworthy difference in the size of the hearts. However, differences in data quality and in preservation of the cardiac structures were observed. The signal-to-noise (SNR) was determined for the given slices of both preparations by

$$\text{SNR} = \frac{\overline{A}_{\text{tissue}} - \overline{A}_{\text{medium}}}{\sigma_{\text{medium}}}$$

with $\overline{A}$ the difference of the mean intensities of tissue and surrounding medium in a ROI of 100×100 px and the standard derivation of the intensities in the medium

σ_{medium}. For paraffin embedding a SNR of 8.3 and for storage in 100% ethanol solution a SNR of 4.2 was determined. The tissue is significantly more homogeneous for the case of liquid embedding, while paraffin embedding results in pronounced fissures and ruptures between single muscle bundles. The fact that the integrity of the cardiac tissue is better preserved by the ethanol fixation could be explained based on changes associated with washing in xylene and subsequent exposure of the tissue to heat during the transfer to the liquid paraffin. This standard procedure can result in a removal of lipids and fatty acids which might contribute to increased spacing within the myofibrils. Furthermore, the small air bubbles in the ventricle, which can be identified as the dark region in the left ventricle (LV) in the volume rendering in Fig. 3.5c, cause scattering and lead to artifacts in the phase reconstruction near the bubble. At the same time, tissue in paraffin offers higher contrast for single muscle bundles and allow a better identification of the myocyte orientation. The ethanol-embedded heart with almost no visible ruptures in the myocardium and a larger amount of erythrocytes in the ventricles is more challenging in view of the CT measurement, but cardiac structures are still clearly revealed, in line with literature results at 20 keV [181]. Altogether, this geometry was well suited to acquire a fast overview scan of the whole heart with a resolution below 10 μm.

To resolve smaller tissue structures, the hearts were scanned with the configuration using PB illumination. For these measurements no further preparation of the sample was necessary. The ROIs were identified based on the overview scans. For the paraffin-embedded sample, a biopsy near the apex was taken and analyzed using the WG configuration with cone beam geometry.

Figure 3.6 shows the results of the tomographic reconstructions for the paraffin-embedded heart, based on the three different modalities of the beamline setup. In Fig. 3.6a, a slice near the apex of the heart from the overview scan is shown. Besides the myocardium and some ruptures along the bundles of myocytes, the single cell layers of endo- and epicardium as well as some blood residues and a tendon within the left ventricle were identified. The red box indicates the area in which a ROI scan was recorded with PB illumination. The corresponding slice is shown in Fig. 3.6b. In this scan, more details of the tissue structure were resolved. For instance, single vessels and also the single cell layer of endothelial cells in the endocardium are visible. Sub-cellular structures of the cardiomyocytes, such as the nuclei, starts to appear in the reconstruction. The typical elongated shape of the nuclei is also clearly visible as black dots within the myocardium. Moreover, the orientation of the cardiomyocyte chains becomes visible. Figure 3.6c shows high resolution data acquired with the WG configuration. This
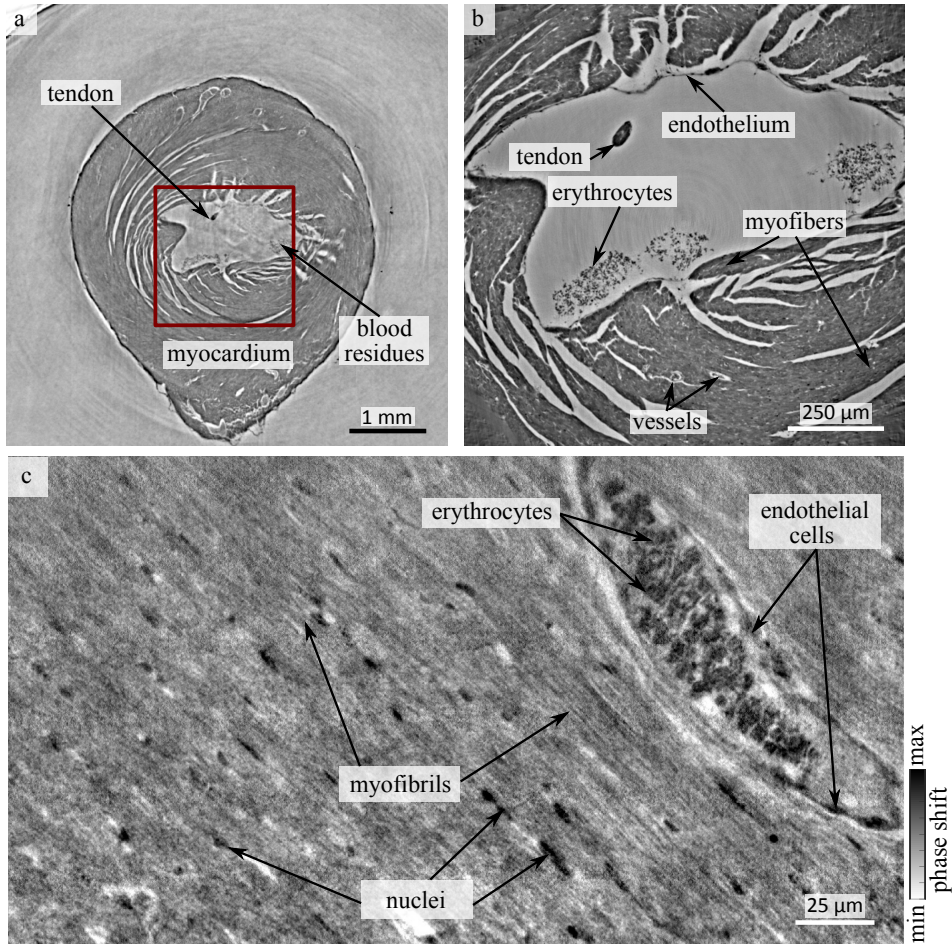
Fig. 3.6: Reconstruction of the cardiac structure of a paraffin embedded heart on multiple length scales. (a) Slice of the tomographic reconstruction acquired by KB-illumination with an effective pixelsize of 3.25 µm. The coarse interior structure can be identified, but smaller details such as capillaries and sub-cellular features are below the resolution of the setup. The red box marks a ROI of a scan with the PB illumination which is shown in (b). Erythrocytes and a layer of cells of the endothelium can be identified at this magnification. (c) In order to image sub-cellular features such as myofibrils, a biopsy of the heart was scanned at high resolution with the WG optic. In this geometry, details such as vessels filled with erythrocytes, endothelial cells surrounding the vessels, and nuclei in between myofibrils become visible.

geometry allows identification of sub-cellular structures such as nuclei, erythrocytes and myofibrils. In the given slice, also a blood vessel with a layer of endothelial cells is visible.

Based on the tomographic reconstructions, the orientation of the cardiomyocytes within the heart tissue was analyzed. The procedure and the results of the analysis of the structural organization will be described in the next section.

3.4 Orientation of the cardiac structures

The structural orientation of the cardiomyocytes can be extracted from the reconstructed volumes using an approach which is based on gradient-based structure tensor ST[2, 185, 194, 256]. A detailed description of the analysis is given in [2]. A small sub-volume with edge length l is chosen around the central pixel of the sub-volume. ST is defined by the first derivatives of the reconstructed (electron) density

$$ST = \begin{pmatrix} \sum g_{xx} & \sum g_{xy} & \sum g_{xz} \\ \sum g_{yx} & \sum g_{yy} & \sum g_{yz} \\ \sum g_{zx} & \sum g_{zy} & \sum g_{zz} \end{pmatrix},$$

with $\sum g_{ij}$ the sum of the products of the gradient along i and j. From the eigenvalue problem

$$ST \cdot \mathbf{b_i} = \lambda_i \cdot \mathbf{b_i}$$

three eigenvectors $\mathbf{b_i}$ and eigenvalues λ_i can be determined, representing the structural orientation within the chosen sub-volume, which is subsequently shifted throughout the entire volume. The direction is defined by the eigenvector with the smallest eigenvalue. The coordinate system used to describe the orientation of the entire structures is given in Fig. 3.1b.

In addition, the tissue anisotropy, i.e. local degree of orientation, is quantified in terms of an order parameter Ω defined as

$$\Omega = \sqrt{\frac{(\frac{1}{\lambda_1} - \frac{1}{\lambda_2})^2 + (\frac{1}{\lambda_2} - \frac{1}{\lambda_3})^2 + (\frac{1}{\lambda_3} - \frac{1}{\lambda_1})^2}{2(\frac{1}{\lambda_1}^2 + \frac{1}{\lambda_2}^2 + \frac{1}{\lambda_3}^2)}} = \sqrt{\frac{1}{2}\left(3 - \frac{1}{\text{trace}(R'^2)}\right)},$$

with $R' = \frac{D^{-1}}{\text{trace}(D^{-1})}$ and D the normalized diagonalized ST of the local sub-volume. Without preferable direction we get $\Omega = 0$, while $\Omega = 1$ is the limit of perfect struc-

tural alignment. Ω describes the degree of orientation and varies within the tissue. By sliding a sub-volume though the whole reconstructed volume, the local orientation and degree of alignment of the entire heart can be determined. In order to save computational power, the orientation parameters can be calculated for areas containing cardiac structures, while voxels containing air or paraffin are masked out, based on their gray value. Only areas containing tissue are shown.
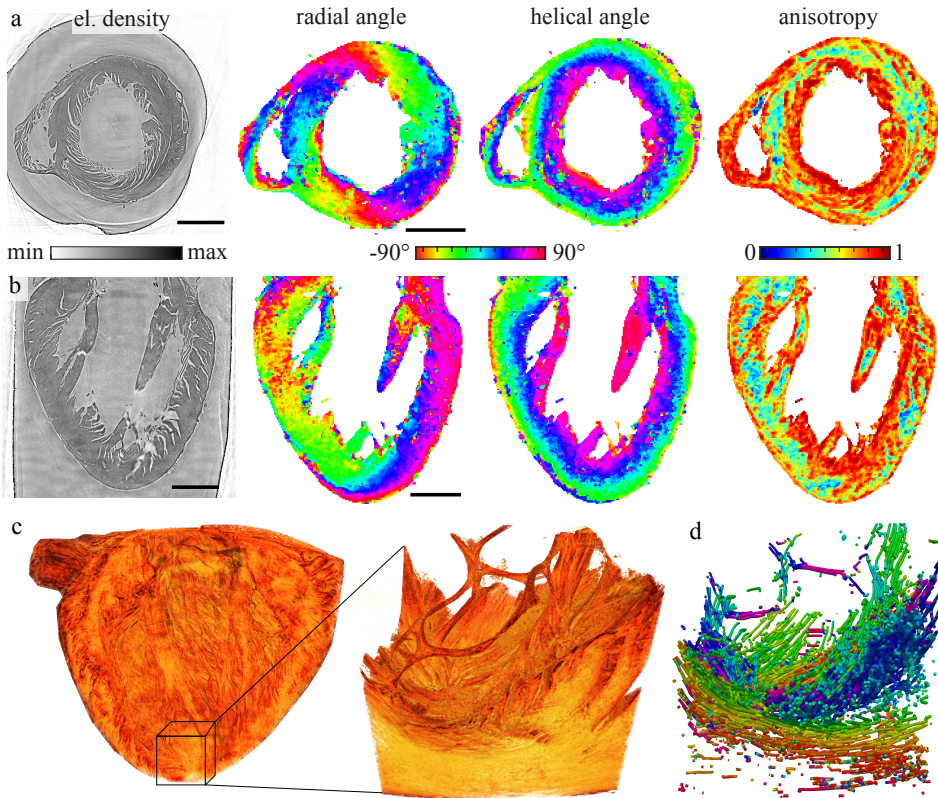
Fig. 3.7: Orientation of the cardiac tissue for the paraffin-embedded heart. (a) Transverse and (b) sagital slice through the reconstructed volume, showing (from left to right) reconstructed density (proportional to phase) in gray value, radial angle, helical angle, and anisotropy parameter Ω, as computed based on the local structure tensor. (c) Volume rendering of the whole heart (KB illumination) along with a ROI near the apex (PB illumination). The orientation was determined in the same way as for the overview scan. (d) A stream tracing algorithm [264] applied to the vector field to visualize the 3d alignment of the cardiomyocytes. The radial orientation color is coded as in the orthogonal slices shown above. Scale bars: 1 mm.

Figure 3.7 shows the reconstruction of the myocyte orientation of the paraffin-embedded heart. The top two rows show the reconstructed phase, the radial and helical angle and the anisotropy of two orthogonal slices. The circular alignment of the muscle bundles, which clearly appears in the phase reconstruction of the transverse plane, is corroborated and quantified by the radial angle φ obtained form the ST. The radial direction is oriented continuously around the left ventricle and is almost point symmetrical with respect to the center of the lumen. The helical angle, describing the elevation of the cardiac orientation from the radial plane, is directed along the long axis in the area around the left ventricle. Apart from the internal structure of the tissue, a significant contribution to the ST and resulting anisotropy must be attributed to interfaces created the detachment of the myocytes aggregates and by fissures associated with the standard procedure of paraffin embedding. However, the interfaces do not seem to form arbitrarily, but preferentially follow the muscle orientation. For this reason, we consider the ST results to still give a reasonable portrait of the cardiac structure. Note that the results of the ethanol-embedded heart are hardly affected by this complication, and can hence serve as benchmark for the ST results. Next, the (pseudo-)vector field describing the myocyte orientation was further analyzed by a stream tracing algorithm which treats the data effectively as a flow problem probed by tracer particles [264]. This can help to visualize the long range connectivity of muscle tissue. The analysis was performed on a ROI probed by the PB configuration, as shown in Fig. 3.7c, resulting in data visualized in Fig. 3.7d. Future extension of such work could be directed at establishing the relationship between the connectivity of cardiomyocytes and the signal propagation of excitation waves.

In a next step, the ethanol-embedded heart was analyzed at higher resolution, based on the PB configuration. To this end, a ROI near the apex was chosen. Compared to the paraffin embedding, the ethanol embedding enables better preservation of cardiac structure, see also Fig. 3.5.

Figure 3.8 shows the myocyte orientation of the ethanol-embedded heart as a result of the structural analysis, with Fig. 3.8a the volume rendering of the reconstructed density. Note, that the blood residues near the apex are masked out, based on a threshold in anisotropy, which excludes the connected area with values of $\Omega < 0.4$. In addition, small holes in the mask were closed. Four representative and equidistantly spaced slices, located just below the left ventricle blood pool are presented. Slice in Fig. 3.8b is shown at large to give an impression of the structural details visible in the data. Notably, the dense organization of cardiomyocytes, nuclei and small blood vessels can be recognized. Aside the density distribution, anisotropy as well as helical and radial an-
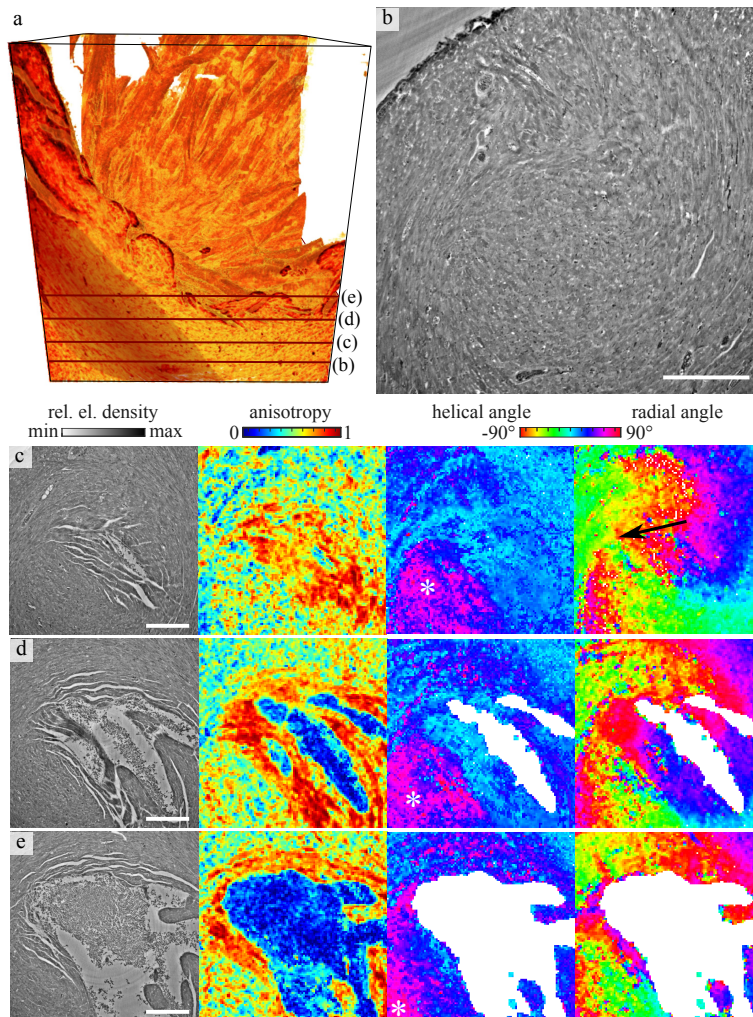
Fig. 3.8: Orientation of the cardiomyocytes near the tip of the left ventricle, shown for the ethanol-embedded heart. (a) Volume rendering of the heart tissue, with (b) a representative transverse slice through the reconstructed density. The location of the slice is marked as a red line in the volume rendering. Details as small capillaries and nuclei can be identified in the dense arrangement of cardiomyocytes. Further, on the left of the 3d volume one bundle of cardiomyocytes is highlighted. (c-e) Further slices through the reconstruction volume are located below the left ventricle and consecutively shown from apex upwards. For each slice, the density, anisotropy, modulus of the helical angle and radial angle are plotted. The locations of the slices are also marked as dark red line line in (a). The white asteroid in the display of the helical angle marks a muscle bundle which is oriented in the direction of the long axis. The black arrow in (c) indicates a vortex of the cardiomyocyte arrangement. Scale bar: 250 μm.

gle of the cardiac network were again analyzed, see the examples shown in Fig. 3.8c-e. The position of all slices in the volume is marked by dark red line in Fig. 3.8a. Note that the determination of the structural parameters is based on a sub-volume around each pixel of the phase reconstruction. Therefore, the structures in the anisotropy and angle maps may appear slightly larger than in the two dimensional slice.

The anisotropy indicates a clear alignment of the cardiomyocytes, especially for the regions around the ventricle, where some gaps between the cells can be identified. But also within the dense tissue some, areas of high anisotropy are encountered. For regions with no preferable directions as for the blood residues, the anisotropy is very low. As explained in the previous paragraph, areas of no significant alignment have been masked out for the display of the corresponding angles. Next to the anisotropy, the absolute value of the helical angle is shown. Blue areas indicate an in-plane orientation while purple indicates an alignment towards the long axis. On the right of each row in Fig. 3.8, the radial angle is shown. It indicates a vortex evolving below the left ventricle (see black arrow). From the combination of both angular representations, areas of different orientations can be identified. These correspond to chains of cardiomyocytes which are oriented in the same direction. For example, one muscle bundle which is oriented towards the long axis is located in the bottom left of the ROI (see asterisk). This bundle of cardiomyocytes is also highlighted in the 3d volume rendering. Another bundle in this region (directly next to the lumen) is oriented in the radial plane in the slice shown in Fig. 3.8d. However, inside these areas of structural alignment some irregularities appear. For example, in the representation of the helical angle in the slice shown in Fig. 3.8e a band of irregularities appears in the myocardium. This may indicate an entanglement of the cardiomyocytes similar to a mesh-like structure. These small details were not recognized at lower resolution, i.e. in the KB data.

Figure 3.9 shows that the sarcomeric periodicity can be extracted from the high resolution data (WG optic). To this end, a cubic sub-volume, containing mostly tissue and no blood vessels, with an edge length of 600 px was selected from the tomographic reconstitution and probed by a Fourier analysis. In Fig. 3.9a a maximum projection over 20 layers of the sub-volume is displayed. The corresponding (central) slice of the 3d Fourier space is shown in Fig. 3.9b. Orthogonal to the myofibrils, a pronounced streak is observed indicative for a broader distribution of inter-myofibril distances. The sarcomeric periodicity, oriented perpendicular to the myofibrils, is encoded in the two peaks visible in the Fourier space. The direction of the structural orientation was
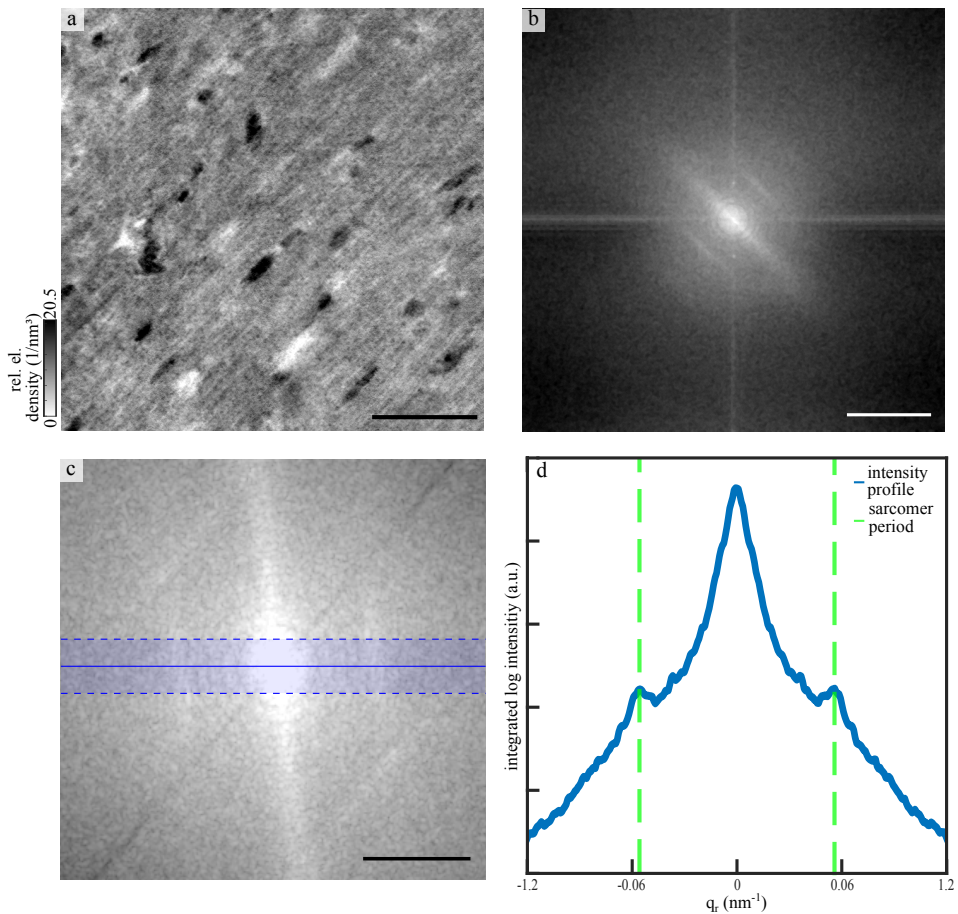
Fig. 3.9: Reconstruction of the sarcomeric periodicity. (a) Reconstructed electron density of the biopsy taken from the paraffin-embedded heart. A maximum projection over 20 layers around a slice of a small cubic sub-volume with an edge length of 600 px. Scale bar: 25 μm. (b) Central slice of the 3d Fourier transform in the same direction as the slice shown in (a). Logscale, scale bar: 1.2 nm^{-1}. (c) Zoom into the low spatial frequencies, after a rotation, which aligns the signal direction of the sarcomeric periodicity to the horizontal. Logscale, scale bar: 0.6 nm^{-1}. (d) Fourier intensity profile along the direction of the sarcomeric signal, showing the side peaks corresponding to the sarcomeric periodicity. To reduce noise, the signal was integrated in the orthogonal direction in a range of +-20 px, as indicated by the horizontal boundary lines in (c). The peaks appearing correspond to a real-space periodicity of 1.8 μm.

identified by a Fourier transform based algorithm[256]. To this end, the covariance matrix of the signal in Fourier space was calculated, and subjected to PCA analysis. For this purpose, a mask corresponding to the expected sarcomeric periodicity of 1.5-3.5 μm (windowing of the Fourier signal) was applied before PCA analysis was performed[265]. The volume was then rotated in such a way that the sarcomeric signal was aligned along a main axis.

Figure 3.9c shows the rotated Fourier space. To increase the signal of the sarcomeric periodicity, the intensities in a range of 20 px from the main axis were integrated. The corresponding intensity profile is shown in Fig. 3.9d. The two peaks correspond to an averaged sarcomeric periodicity of about 1.8 μm for the fixed tissue embedded in paraffin.

3.5 Outlook

In summary, we have demonstrated a multi-scale phase contrast tomography approach, which allows to image the structure of cardiac muscle starting from the scale of the the entire organ down to the sarcomere. To this end, we have implemented three levels of magnification and tomography configurations at the GINIX instrument of the PETRAIII storage ring, with correspondingly matched optics and detection. Importantly, phase retrieval by non-linear iterative reconstruction has allowed us to achieve high image quality for analysis of structural orientation in the whole heart as well as detailed views of the cyto-architecture down to sub-cellular features. As an outlook, we note that important improvements and extensions can be foreseen on various levels, including sample preparation, data analysis, instrumentation and optics.

Concerning sample preparation, further improvements could include fixation via perfusion to remove blood residuals. Air inclusions in the paraffin also often result in tomography artifacts and more efforts will be made to avoid formation of air bubbles or the removal thereof. Finally, better structure preservation of heart muscle can be expected without solvent exchange and paraffin embedding. We have already scanned hearts in PBS/Formalin. The challenge here is the much weaker contrast compared to dehydrated samples, see also [242], which requires higher propagation distance and careful optimization of photon energy.

Future extension of this work will be directed at bridging the gap between structure and function. Multi-scale phase contrast tomography of *post mortem* small animal hearts is already capable to provide 3d data, which can then be used as input for the

simulation of cardiovascular functions. Modeling of signal excitation and transduction as well as mechanical functions require a quantitative understanding not only of tissue macrostructure, but also of (sub-)cellular orientation, as provided by the present approach. In particular, even the local sarcomere periodicity as well as the relative strength of the signal could be mapped by stitching high resolution tomograms.

Further, full-field tomography with continuous rotation, as shown here for the PB setup with tissue volume rates of $\simeq 3 \cdot 10^7 \, \mu m^3/s$, enables high throughput of samples, as required for biomedical studies with statistically sufficient number of diseased and control specimens. Small animal models for fibrosis and hypertension are currently under investigation, and show a very distinct pathologies of the 3d heart structure, which can complement conventional histological analysis.

Finally, it is of interest to briefly address the prospects for dynamic (time-resolved) propagation phase contrast tomography of a beating heart. Impressive instrumentation for a tomography and beamline compatible Langendorff perfusion system has been recently demonstrated at the TOMCAT beamline of the Swiss Light Source (SLS) by A. Bonnin and coworkers. Tremendous challenges are associated with this goal, not only in sufficiently fast data acquisition, reconstruction with *a posteriori* gating of projections, but also with keeping the dose at tolerable levels. To this end, we believe that full-field illumination with highly coherent undulator beams in the range of 25 keV-40 keV as will be provided by the next generation of (diffraction-limited) storage rings could provide a significant advantage for balancing contrast and dose, in combination with dose efficient single-photon counting detectors. However, this advantage can only be fully exploited if (i) undulator beams can be broadened by divergence behind a secondary focus, and (ii) if the effective pixel size can be sufficiently reduced by geometric magnification. To this end, the current work already shows how the cone beam illumination optics can improved significantly by filtering the beam in the secondary focal plane, keeping wavefront distortions at a tolerable level.

Funding

Acknowledgments

Disclosures

The authors declare no conflicts of interest.

3D virtual histopathology of cardiac tissue from Covid-19 patients based on phase-contrast X-ray tomography

4

M. Reichardt, P. Møller Jensen, V. Andersen Dahl, A. Bjorholm Dahl, M. Ackermann, H. Shah, F. Länger, C. Werlein, M. Kühnel, D. Jonigk and T. Salditt

Abstract

We have used phase-contrast X-ray tomography to characterize the three-dimensional (3d) structure of cardiac tissue from patients who succumbed to Covid-19. By extending conventional histopathological examination by a third dimension, the delicate pathological changes of the vascular system of severe Covid-19 progressions can be analyzed, fully quantified and compared to other types of viral myocarditis and controls. To this end, cardiac samples with a cross section of 3.5 mm were scanned at a laboratory setup as well as at a parallel beam setup at a synchrotron radiation facility. The vascular network was segmented by a deep learning architecture suitable for 3d datasets (V-net), trained by sparse manual annotations. Pathological alterations of vessels, concerning the variation of diameters and the amount of small holes, were observed, indicative of elevated occurrence of intussusceptive angiogenesis, also confirmed by high resolution cone beam X-ray tomography and scanning electron microscopy. Furthermore, we implemented a fully automated analysis of the tissue structure in form of shape measures based on the structure tensor. The corresponding distributions show that the histopathology of Covid-19 differs from both influenza and typical coxsackie virus myocarditis.

4.1 Introduction

The coronavirus disease 2019 (Covid-19) is caused by the serve acute respiratory syndrome coronavirus (SARS-CoV-2), predominantly entering the body via the respiratory tract. SARS-CoV-2 infects cells by binding its spike protein to the surface protein angiotensin-converting enzyme 2 (ACE2) of the host cell [266]. Severe cases are most frequently affected by viral pneumonia and acute respiratory distress syndrome (ARDS), with a pathophysiology distinctly different from e.g. influenza infection [169]. Mediated by a distinct inflammatory microenvironment, an uncontrolled infection can develop and result in massive tissue damage, again primarily reported in the lung. Apart from diffuse alveolar damage, the main histological hallmark of ARDS, specific findings in the lung histopathology are high prevalence of micro-thrombi and high levels of intussusceptive angiogenesis (IA) [169, 170, 267]. The latter is a rapid process of intravascular septation that produces two lumens from a single vessel. It is distinct from sprouting angiogenesis because it has no necessary requirement for cell proliferation, can rapidly expand an existing capillary network, and can maintain organ function during replication [268]. The mechanistic link between branch angle remodeling and IA is the intussusceptive pillar. The pillar is a cylindrical 'column' or 'pillar' that is 1–3 µm in diameter [269]. In short, the capillary wall extends into the lumen and split a single vessel in two. Opposing capillary walls are first dilated, and intraluminal pillars form at vessel bifurcations by an intraluminal intussusception of myofibroblasts, creating a core between the two new vessels. These cells begin depositing collagen fibers into the core, providing an extracellular matrix (ECM) for the growth of the vessel lumen. The extension of the pillar along the axis of the vessel then results in vessel duplication. These structural changes of the vasculature have been reported in various non-neoplastic and neoplastic diseases [270–272]. These finding underline the notion that Covid-19 is a disease driven by, and centered around, the vasculature with direct endothelial infection, thus providing SARS-CoV-2 an easy entry route into other organs, subsequently resulting in multi-organ damage [273, 274].

Clinically, the heart appears to be a particular organ at risk in Covid-19. Acute cardiac involvement (e.g. lowered ejection fraction, arrhythmia, dyskinesia, elevated cardiac injury markers) is reported in a broad range of cases. In contrast to other respiratory viral diseases affecting the heart (e.g. coxsackie virus), in the few Covid-19 cases reported so far that included cardiac histopathology, no classic lymphocytic myocarditis –characterized by a T-lymphocyte predominant infiltrate with cardiomy-

ocyte necrosis– was observed [275–280]. Furthermore, the underlying pathomechanisms are still poorly understood with both direct virus induced (cellular) damage and indirect injury being discussed [275, 281–285]. Particularly, it is not known to which extent the vasculature of the heart, including the smallest capillaries, are affected and whether IA is also a dominant process in this organ. More generally, one would like to delineate the morphological changes of cytoarchitecture from other well described pathologies. Recently, we have used three-dimensional (3d) virtual histology based on phase-contrast X-ray tomography as a new tool for Covid-19 pathohistology and investigated these structural changes in *post mortem* tissue biopsies from Covid-19 diseased lung tissue [171, 172]. Exploiting phase contrast based on wave propagation, the 3d structure of formalin-fixed, paraffin–embedded (FFPE) tissue -the mainstay for histopathological samples worldwide- can be assessed at high resolution, i.e. with sub-micron voxel size and with sufficient contrast also for soft and unstained tissues [164]. By relaxing the resolution to voxel sizes in the range of 25 microns and stitching of different tomograms, the entire human organ can be covered and an entire FFPE tissue block 'unlocked' by destruction-free 3d analysis [172]

In this work, we now focus on the 3d architecture of cardiac tissue. We have scanned unstained, paraffin embedded tissue, prepared by a biopsy punch from paraffin embedded tissue blocks, collected from patients which have succumbed to Covid-19 (Cov). For comparison, we have scanned tissue from influenza (Inf) and myocarditis (Myo) patients as well as from a control group (Ctr). In total, we have scanned 26 samples, all which had undergone routine histopathological assessment beforehand. We used both a synchrotron holo-tomography setup and a laboratory μCT with custom designed instrumentation and reconstruction workflow, as described in [171]. Based on the reconstructed volume data, we then determined structural parameters, such as the orientation of the cardiomyocytes and the degree of anisotropy, as well as a set of shape measures defined from the structure tensor analysis. This procedure is already well established for Murine heart models [181]. Segmentation of the vascular network enabled by deep learning methods is used to quantify the architecture of the vasculature.

Following this introduction, we describe the methodology, which is already summarized in Fig.4.1. We then describe the reconstructed tissue data in terms of histopathological findings and compare the different groups. We then apply automated image processing for classification and quantification of tissue pathologies. Finally, we segment the vasculature using a deep-learning based approach based on sparse annotations and quantify the structure of the capillary network by graph representations of

the segmented vessels. From the generalized shape measures, as well as the inspection of particular vessel architectures exhibiting the IA phenomenon, distinct changes of Cov with respect to the other pathologies and to Ctr are observed. The paper closes with a short conclusions and outlook section.

4.1.1 Autopsy, clinical background and tissue preparation

In total, 26 *post mortem* heart tissue samples were investigated: 11 from Covid-19 patients (Cov), 4 from H1N1/A influenza patients (Inf), 5 from patients who died due to coxsackie virus myocarditis (Myo), as well as 6 control samples (Ctr). The age and sex of all patients are summarized in Tab. 4.1. Detailed information about age, sex, cause of death, hospitalization, clinical, radiological and histological characteristics of all patients is given in Appendix Tab. 4.5.

Figure 4.1 illustrates the sample preparation and the tomographic scan geometries

Table 4.1: Sample and medical information of patients.

sample group	N patients	sample quantity	age	sex
Control	2	6	31 ± 7	2 F
Covid-19	11	11	76 ± 13	10 M, 1 F
Myocarditis	5	5	43 ± 17	4 M, 1 F
Influenza	4	4	63 ± 9	3 M, 1 F

used to assess the 3d cytoarchitecture on different length scales. FFPE-tissue from autopsies was prepared by standard formalin fixation and paraffin embedding. From the paraffin-embedded tissue block, sections of $3\,\mu m$ thickness were prepared for histomorphological assessment using conventional haematoxylin and eosin (HE) staining. One representative microscopy image of a Covid-19 patient is shown in Fig. 4.1. An overview of HE stained sections from all samples is shown in Fig. 4.2. In previous studies, we could show the correlation of 3d X-ray phase contrast tomography data with conventional 2d histology [164, 171].

Biopsy punches with a diameter of $3.5\,mm$ were then taken and transferred onto a holder for the tomographic scans. All samples were first scanned at a laboratory μCT instrument using a liquid metal jet anode. Next, tomograms of Covid-19 and control samples were scanned at the GINIX endstation of the P10 beamline at the PETRAIII storage ring (DESY, Hamburg), using the parallel (unfocused) synchrotron beam. Finally, biopsy punches with a diameter of $1\,mm$ was taken from the $3.5\,mm$ biopsy of
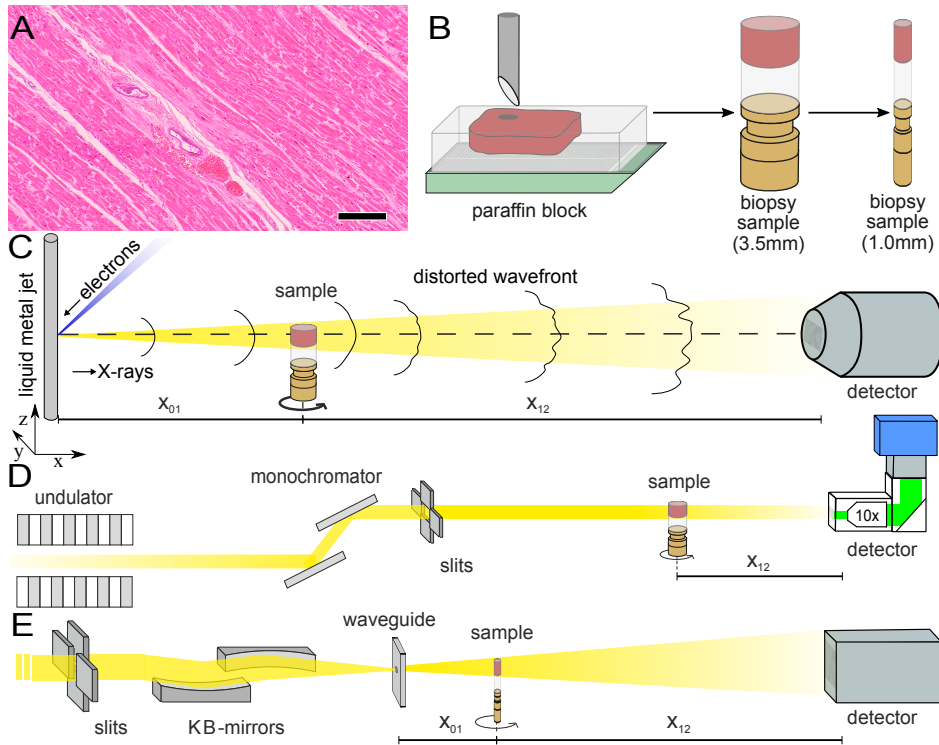
Fig. 4.1: Sample preparation and tomography setups. (A) HE stain of a $3\,\mu m$ thick paraffin section of one sample from a patient who died from Covid-19 (Cov-I, Scalebar: $100\,\mu m$). In total, 26 *post mortem* heart tissue samples were investigated: 11 from Covid-19 patients, 4 from influenza patients, 5 from patients who died with myocarditis and 6 control samples. (B) From each of the samples a biopsy punch with a diameter of $3.5\,mm$ was taken and transferred onto a holder for the tomography acquisition. After tomographic scans of all samples at the laboratory setup, Covid-19 and control specimens were investigated at at the synchrotron. Furthermore, one punch with a diameter of $1\,mm$ was taken from one of the control and Covid-19 samples for investigations at high resolution. (C) Sketch of the laboratory micro-CT setup. Tomographic scans of all samples were recorded in cone beam geometry with an effective pixel size of $px_{\text{eff}} = 2\,\mu m$ using a liquid metal jet source (EXCILLUM, Sweden). (D) Sketch of the parallel beam setup of the GINIX endstation (P10 beamline, DESY, Hamburg). In this geometry, datasets of Covid-19 and control samples were acquired at an effective voxel size of $650\,nm^3$. One plane of each sample was covered by 3×3 tomographic recordings. (E) Cone beam setup of the GINIX endstation. After the investigation in parallel geometry, the $1\,mm$ biopsy punches of one control and Covid-19 sample were probed in cone beam geometry. This configuration is based on a coherent illumination by a wave guide and allows for high geometric magnification and effective voxel sizes below $200\,nm$.

one control and one Covid-19 sample and scanned at high geometric magnification M using a cone beam illumination emanating from a X-ray waveguide (WG).

4.1.2 Tomographic recordings

Liquid metal jet (LJ) setup: All samples were scanned using a home-built laboratory phase-contrast μCT-setup, as sketched in Fig. 4.1C. X-rays emitted from a liquid metal jet anode (Excillum, Sweden) are used in cone beam geometry with a geometric magnification $M = \frac{x_{01}+x_{12}}{x_{01}}$ controlled by the source-sample x_{01} and sample-detector distance x_{12}. The spectrum of photon energy E is dominated by the characteristic K_α lines of galinstan (Ga, Zn, In alloy), in particular the Ga line $E_{Ga} = 9.25$ keV. Projections were acquired by a sCMOS detector with a pixel size of $px = 6.5\,\mu$m coupled by a fiber-optic to a $15\,\mu$m thick Gadox-scintillator (Photonic Science, UK) [2, 286]. In this work, data was acquired at an effective pixel size of $px_{\text{eff}} = \frac{px}{M} = 2\,\mu$m. For each of the 1501 angular positions 3 projections at 0.6 s acquisition time were averaged. Further, 50 flat field images before and after the tomographic acquisition, as well as 50 dark field images after the scan were recorded. The total scan time was approximately one hour per sample.

Parallel beam (PB) setup: All Cov and Ctr samples were also scanned with an unfocused, quasi-parallel synchrotron beam at the GINIX endstation, at a photon energy E_{ph} of 13.8 keV. Projections were recorded by a microscope detection system (Optique Peter, France) with a $50\,\mu$m thick LuAG:Ce scintillator and a $10\times$ magnifying microscope objective onto a sCMOS sensor (pco.edge 5.5, PCO, Germany) [165]. This configuration enables a field-of-view (FOV) of $1.6\,$mm$\times 1.4\,$mm, sampled at a pixel size of 650 nm. The continuous scan mode of the setup allows to acquire a tomographic recording with 3000 projections over $360°$ in less than 2 minutes. For each sample one plane of the 3.5 mm biopsy punch was covered by 3×3 tomographic acquisitions. Afterwards, dark field and flat field images were acquired. In total more than 150 tomographic scans (9 tomograms for each of the 17 samples) were recorded in this configuration.

Waveguide (WG) setup: As a proof-of-concept that sub-cellular resolution can also be obtained on cardiac tissue samples, a 1 mm-diameter biopsy punch was taken from both a Covid-19 and control sample, both of which were previously-scanned (PB geometry). The highly coherent cone beam geometry and clean wavefront of the
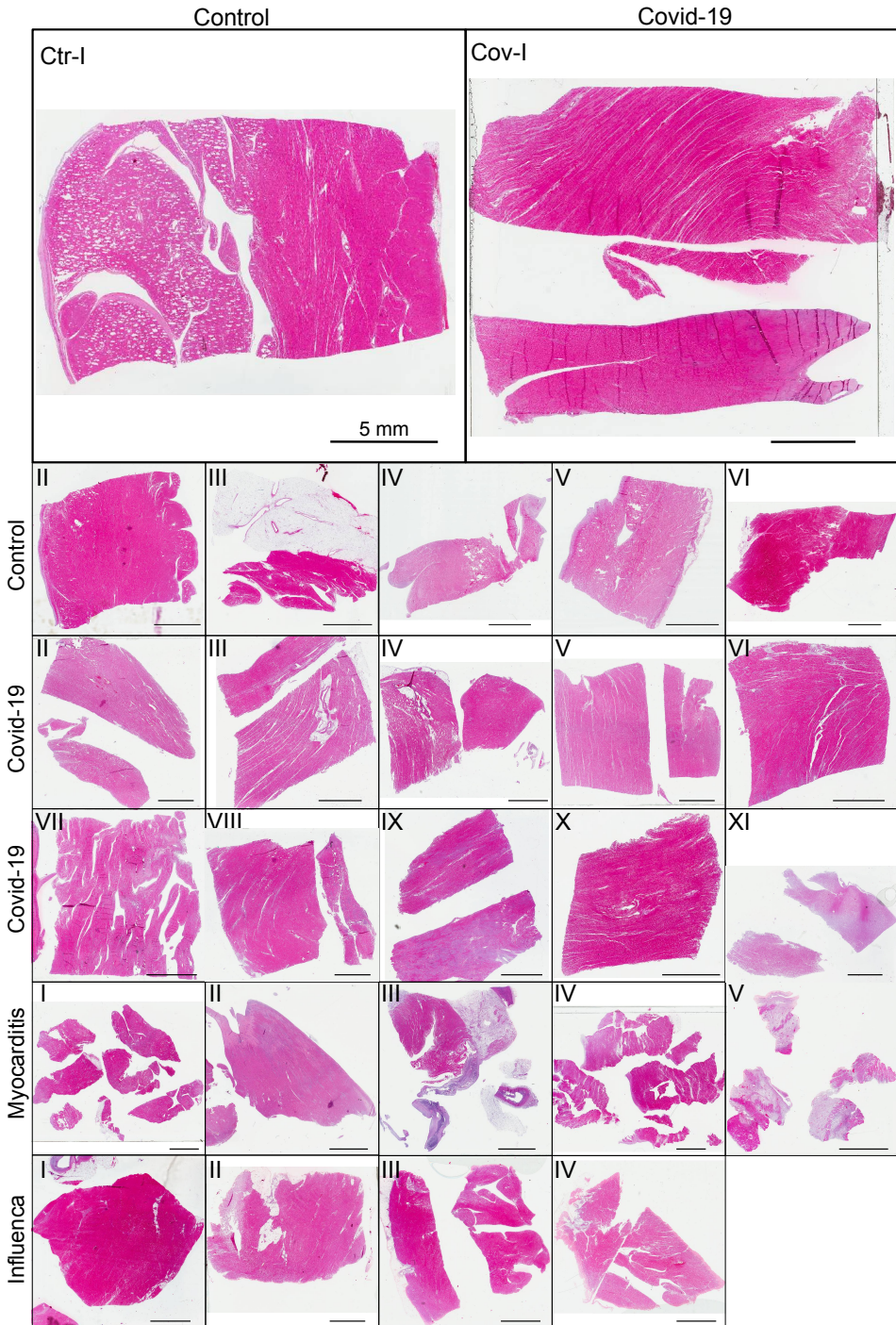
Fig. 4.2: HE stain of all cardiac samples. Scale bar: 5 mm.

WG illumination allows for samples to be probed at high magnification in the holographic regime. Here, the sample was aligned at $M \simeq 40$, resulting in an effective pixel size of 159 nm. Images of the Ctr were acquired by a sCMOS Camera (15 µm Gadox scintillator, 2560×2160 pixel) with a physical pixel size of 6.5 µm (Andor Technology Ltd, UK). Cov datasets were recorded by a 1:1 fiber-coupled scintillator-based sCMOS camera (2048 x 2048 pixels, Photonic Science, Sussex, UK) with a custom 15 µm thick Gadox scintillator with pixel size of 6.5 µm. For Ctr data the photon energy was $E =$ 10 keV and 1500 projections over 180 degrees were recorded with an acquisition time of 0.3 s, for the Cov sample 1500 projections were acquired for four slightly different propagation distances at $E =$ 10.8 keV. The difference in acquisition time of both scans (Ctr: $\simeq 10$ min, Cov $\simeq 3$ h) is given by different wavguide channel diameters and guiding layer materials (Ctr: Ge, Cov: Si). Before and after each tomographic scan 50 empty beam projections as well as 20 dark fields after the scan were recorded. The experimental and acquisition parameters for all imaging modalities are listed in Tab. 4.2.

Table 4.2: Data acquisition parameters of the laboratory and synchrotron scans.

parameter	LJ setup	PB setup	WG setup (Ctr/Cov)
photon energy (keV)	9.25	13.8	10/10.8
source-sample-dist. x_{01} (m)	0.092	$\simeq 90$	0.125/0.125 0.127 0.131 0.139
sample-detector-dist. x_{12} (m)	0.206	0.5	4.975
geometric magnification M	$\simeq 3$	$\simeq 1$	$\simeq 40$
pixel size (µm)	6.5	0.65	6.5
effective pixel size (µm)	2	0.65	0.159
field-of-view h×v (mm^2)	4.8×3.4	1.6×1.4	0.344×0.407/0.325 × 0.325
acquisition time (s)	3×0.6	0.035	0.3/2.5
number of projections	1501	3000	1500
number of flat field	50	1000	50
number of dark field	50	150	20

4.1.3 Phase retrieval and tomographic reconstruction

The 3d structure of the cardiac tissue was reconstructed from the raw detector images. To this end, we computed the phase information of each individual projection and performed tomographic reconstruction to access the 3d electron density distribution. For image processing and phase retrieval, we used the HOLOTOMOTOOLBOX developed by

our group, and made publicly available [149]. First, flat field and dark field corrections were performed for all raw projections. In addition, hot pixel and detector sensitivity variations were removed by local median filtering. Phase retrieval of LJ scans was carried out with the Bronnikov aided Correction (BAC) algorithm [142, 143]. For the PB scans, a local ring removal (width of $\pm$40 pixel) was applied around areas where wavefront distortions from upstream window materials did not perfectly cancel out after empty beam division. Phase retrieval of PB scans was performed using the linear CTF-approach [148, 287]. Phase retrieval of WG scans was performed using a nonlinear approach of the CTF. This advanced approach does not rely on the assumption of a weakly varying phase, and iteratively minimizes the Tikhonov-functional starting from the CTF result as an initial guess. For a weakly phase-shifting sample (linear approximation) without further constraints, both approaches yield exactly the same result [149]. Apart from phase retrieval, the HOLOTOMOTOOLBOX provides auxiliary functions, which help to refine the Fresnel number or to identify the tilt and shift of the axis of rotation [149]. Tomographic reconstruction of the datasets was performed by the ASTRA toolbox [262, 288]. For the LJ and WG scans recorded at large cone beam geometry, the FDK-function was used, while the PB was reconstructed by the iradon-function with a Ram-Lak filter.

To combine the 3×3 tomographic volumes, covering one plane of the 3.5 mm biopsy in PB geometry, a non-rigid stitching tool of was used [289]. Region-of-interest artefacts of the PB reconstructions, which led to circular low frequency artefacts at the borders of the biopsy reconstruction volume, were removed by radial fitting of cosine functions. In order to decrease the size of the stitched volume, and thus also computational power needed for further analysis, the datasets were binned by a factor of 2.

Table 4.3: Phase retrieval algorithms and parameters used for the different setups.

setup	LJ setup	PB setup	WG setup
Fresnel number	0.47125	0.0095	0.0017
phase retrieval	BAC	CTF	nonlinear CTF
δ/β-ratio	-	1/45	1/130
parameter	$\alpha = 8 \cdot 10^{-3}$	$\alpha_1 = 10^{-3}$	$\alpha_1 = 8 \cdot 10^{-4}$
	$\gamma = 1$	$\alpha_2 = 0.5$	$\alpha_2 = 0.2$
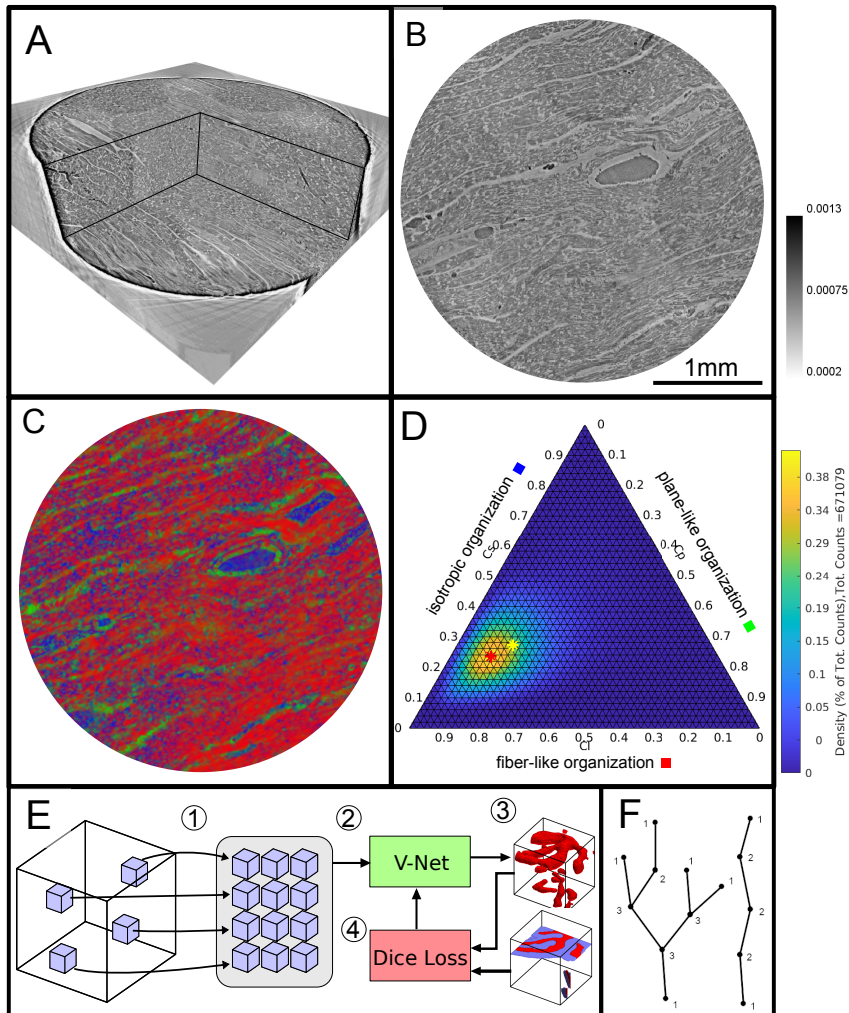
Fig. 4.3: Data analysis workflow of cardiac samples. (A) Volume rendering of a tomographic reconstruction from PB data. (B) Orthogonal slice of the masked tissue. Scale bar: 1 mm (C) Shape measure distribution (C_l red, C_p green and C_s blue) of the slice shown in B. (D) Ternary plot of shape measure distribution. The peak (red) and mean (yellow) values are marked with an asterisk. (E) Overview of the training process for the neural network. (1) Random subvolumes (containing labelled voxels) are sampled from the full volume and are collected in a batch. (2) The batch is fed through the neural network, resulting in (3) a segmentation (top) and labels for one subvolume (bottom). (4) The dice loss is computed from segmented subvolumes based on labelled voxels, and the parameters of the neural network are updated. (F) Scheme of branching and the relation to degree of the vessel nodes obtained by a graph representation of the segmented microvasculature.

4.1.4 Structure tensor analysis

The laboratory datasets and the stitched datasets reconstructed from the PB recordings were used for further analysis of the cardiac structure and the corresponding pathological changes, see the workflow sketched in Fig. 4.3. For each reconstruction of the 3d electron density map (Fig. 4.3A), the biopsy punches were first masked based on their higher electron density compared to the surrounding air. Missing areas in the PB acquisition (from corrupted datasets) were excluded. The intensities of the reconstructions were normalized. Figure 4.3B shows an exemplary masked 2D slice. For each sample, the local tissue orientation and the degree of alignment was then determined from structure tensor analysis [290]. Accordingly, the local structural orientation at point $\mathbf{r}$ can be described by a vector w

$$w(\mathbf{r}) = \text{argmin}_{v=1}(I(\mathbf{r} + v) - I(\mathbf{r}))^2$$

with $v \in \mathbb{R}^3$ and $|v| = 1$ in voxel units. Since the vector w or set of vectors is computed from partial derivatives, one has to first compensate for the ill-posedness of computing derivatives of noisy intensity values by convolving intensities $I_\sigma = \mathcal{K}_\sigma * I$ with a Gaussian kernel $\mathcal{K}_\sigma$. The structure tensor J_ρ then is defined as follows

$$J_\rho = \mathcal{K}_\rho * \begin{pmatrix} (\partial_x I_\sigma)^2 & (\partial_x I_\sigma)(\partial_y I_\sigma) & (\partial_x I_\sigma)(\partial_z I_\sigma) \\ (\partial_y I_\sigma)(\partial_x I_\sigma) & (\partial_y I_\sigma)^2 & (\partial_y I_\sigma)(\partial_z I_\sigma) \\ (\partial_z I_\sigma)(\partial_x I_\sigma) & (\partial_z I_\sigma)(\partial_y I_\sigma) & (\partial_z I_\sigma)^2 \end{pmatrix},$$

where a second convolution $\mathcal{K}_\rho$ is applied with length scale ρ, thus defining the structural scale on which the tissue structure is analyzed/reported. Since the reconstructed electron density $I(\mathbf{r})$ along a fiber is approximately constant along the fiber tangent, the vector describing the local structural orientation is given by the eigenvector with the smallest eigenvalue of the symmetric matrix J_ρ. The implementation of the structure tensor analysis is provided in https://lab.compute.dtu.dk/patmjen/structure-tensor. In this work, the size of ρ, determining the sub-volume on which the structural analysis is performed, was set to 32 pixels for PB datasets and 12 pixels for LJ acquisitions. This corresponds to $\approx 20.8\mu$m and 24μm, respectively, i.e. a value slightly smaller than the diameter of a cardiomyocyte ($\approx 25\mu$m). A smoothing parameter σ of 2 pixels was chosen to reduce noise. From the eigenvalues ($\lambda_1 \geq \lambda_2 \geq \lambda_3$) of J_ρ, quantitative shape measures (as first introduced for diffusion tensor MRI data) can be determined [291]. These parameters describe the degree of anisotropy of the local structure orien-

tation. Tissue structure with fiber-like symmetry are indicated by a high value of

$$C_l = \frac{\lambda_2 - \lambda_3}{\lambda_1} \; .$$

Plane-like (lamellar) symmetry is described by a high value of

$$C_p = \frac{\lambda_1 - \lambda_2}{\lambda_1} \; ,$$

and isotropic structures are described by a high value of the spherical shape measure

$$C_s = \frac{\lambda_3}{\lambda_1} \; .$$

The shape measure distribution of the exemplary slice is shown in Fig. 4.3C. Red areas indicate a high C_l value and correlate with the well aligned chains of cardiomyocytes. Planar structures as collagen sheets and separated muscle bundles show a high C_p value and are color-coded in green. Isotropic areas as blood filled vessels are represented by a high C_s value (blue). The values of the three measures range between zero and one, and sum up to one

$$C_l + C_p + C_s = 1 \; .$$

Thus, one of the three shape measures is redundant. The data can be plotted in a ternary diagram as used to represent phase diagrams of ternary mixtures (see Fig. 4.3D). To characterize the distribution of the shape measures for each sample, a principal component analysis (PCA) was performed. Note, that for the LJ datasets, the paraffin surrounding the cardiac tissue was removed by an intensity-based mask. Since one axis of the shape measure is redundant, the distribution of all data points can be described by two eigenvectors ($\mathbf{u_1}, \mathbf{u_2}$ with the largest eigenvalues (η_1, η_2)). The PCA analysis is equivalent to a two-dimensional Gaussian with standard deviation $\sqrt{\eta_1}, \sqrt{\eta_2}$. The two eigenvectors ($\mathbf{u_1}, \mathbf{u_2}$) can be represented by the major and minor axis of an ellipse centred around the mean (μ_l, μ_p, μ_s) (yellow asteroid) representing the 'point cloud' of all shape measures. The eccentricity of the ellipse is given by

$$e = \sqrt{1 - \frac{\sqrt{\eta_2}}{\sqrt{\eta_1}}}$$

and describes how much the ellipse deviates from being circular. The area of the ellipse is given by $A_\eta = \pi\sqrt{\eta_1\eta_2}$ and is a measure for the dispersion of the shape measure distribution. The eccentricity indicates whether the dispersion is isotropic in the plane of the shape parameters. Large values of e indicate a sharp elongated distribution along the major axis of the ellipse.

4.1.5 Segmentation by deep learning

A deep learning approach based on the V-Net architecture [292] was used to segment the vascular network in the PB datasets. The V-Net can be regarded as a 3D version of the popular U-Net architecture [293] often used for segmentation of medical images. Training was performed using the Dice loss [292] and the ADAM optimizer [294] with step size 0.001 and hyperparameters $\beta_1 = 0.9$ and $\beta_2 = 0.999$. To avoid the need of a fully labelled training dataset, a training strategy using sparsely annotated data sets was adopted, inspired by [295]. In each dataset, a small number of axis-aligned 2D slices was annotated manually, and the Dice loss was evaluated only for these annotated voxels. Prior to training, the annotated volumes were split into a training set and a smaller validation set. The network was trained on the training set, while the quality of the current model (network weights) was tested on the validation set, as sketched in Fig. 4.3E. Instead of segmenting the entire volume before computing the loss, batches of 12 random subvolumes of size $96 \times 96 \times 96$ voxels were selected, ensuring that each contained annotated voxels. These were then fed into the network, the loss was computed, and the parameters (network weights) were updated. After running on 256 subvolumes, the network was evaluated by running it on the validation set. Rotations by 90 degrees and mirror reflections (axis flips) were used both on the training and the validation subvolumes to augment the data. The neural network code of this implementation was uploaded to GitHub (`github.com/patmjen/blood-vessel-segmentation`).

A separate model was trained for a Covid-19 volume (Cov-IV) and a control volume (Ctr-III). The models were trained for 24 hours (~900 epochs) using an NVIDIA Tesla V100 32 GB GPU, and the model version which achieved the highest validation score during the training was kept. Finally, the training was performed over two rounds. First, an initial training and validation set was created to train the model. Then, the training set was improved by adding additional annotations to areas which were falsely segmented, and a new model was trained on the improved data.

As the segmentation masks produced by the neural networks typically contained a

number of errors, a post-processing pipeline was designed to reduce the errors' effect. The first step is to reduce the number of false positives. These typically materialize as small, roughly spherical regions of background which was erroneously detected as blood vessels. To remove them, the structure tensor shape measures C_l, C_p, and C_s are computed for the segmentation mask (treating background as 0 and foreground as 1) with σ and ρ set to 1 and 8 voxels, respectively. Then, all connected components with a volume less than 10^4 voxels or a mean value of C_s greater than 0.2 are removed. The thresholding on C_s ensures that isotropic components are removed regardless of their size while still preserving smaller sections of correctly segmented blood vessels. The last step is to reduce the number of false negatives by reconnecting segments of blood vessels which are disconnected due to small errors in the segmentation. Since endpoints of blood vessels will typically have a large value of C_s, small gaps in the vessels can be closed by performing a morphological closing of the isotropic regions of the segmentation mask. Specifically, the cleaned binary mask, $\hat{B}$, is given by

$$\hat{B} = \max(B, \text{close}(C_l \odot B, S_4) > 0.2) \,,$$

where B is the original binary mask (after the first post processing step), C_l is the line-like measure for all voxels in B, and $\text{close}(C_l \odot B, S_4)$ denotes a closing of the elementwise product between C_l and B with a ball of radius 4. For performance reasons the closing uses an approximated ball as described in [296].

4.1.6 Quantification of the vascular system

A quantitative description of the vascular system was achieved by modelling the segmented vessels as a mathematical graph. A graph consists of a set of vertices and a set of edges where each edge connects a pair of vertices. If vertices are connected via an edge they are said to be neighbors and the degree of a vertex (nodes) n is equal to its number of neighbors. In Fig. 4.3F a sketch of a vessel graph is shown for a straight vessel and for a vessel with multiple branching points. The degree of connectivity n is added to the sketch. This gives a natural correspondence to the complex vascular system by modelling bifurcation points as vertices and the blood vessels between pairs of bifurcation points as edges. Furthermore, structural phenomena such as excessive vessel bifurcation and intussusceptive angiogenesis can now be detected by, respectively, a large number of high degree vertices and loops in the graph. The graph corresponding to the vascular system is extracted from the segmentation created by the neu-

ral network. First, a skeletonization ([297]) is computed, which reduces all structures in the binary volume to 1-voxel wide centerlines without changing the connectivity. These centerlines are then converted to a graph as described in [298]. Once the graph is constructed the vertex degrees can readily be extracted by counting the number of edges connected to each vertex. Loops are detected using the algorithm from [299] which detects all atomic cycles in a given graph. A cycle is a path through the graph that begins and ends at the same vertex without reusing edges. An atomic cycle is a cycle which cannot be decomposed into shorter cycles. Only reporting atomic cycles is more robust, since small errors in the segmentation may cause the skeletonization to contain long cycles that do not correspond to anatomical structures. The 3d data sets (including tomographic reconstructions and segmentations) was visualized using the software Avizo (Thermo Fisher Scientific).

4.1.7 Vascular Corrosion Casting, Scanning Electron Microscopy, and Morphometry

The microvascular architecture of Covid-19 hearts was also examined using scanning electron microscopy (SEM) and microvascular corrosion casting [269]. So far, corrosion casting coupled with SEM represents the gold standard for assessing the subtypes of angiogenesis. The afferent vessels of heart specimens were cannulated with an olive-tipped cannula. The vasculature was flushed with saline (at body temperature) followed by glutaraldehyde fixation solution (2.5%, pH 7.4, Sigma Aldrich, Munich, Germany). Fixation was followed by injection of prepolymerized PU4ii resin (VasQtec, Zurich, Switzerland) mixed with a hardener (40% solvent) and blue dye as casting medium. After curing of the resin, the heart tissue was macerated in 10% KOH (Fluka, Neu-Ulm, Germany) at 40°C for 2 to 3 days. Specimens were then rinsed with water and frozen in distilled water. The casts were freeze-dried and sputtered with gold in an argon atmosphere and examined using a Philips ESEM XL-30 scanning electron microscope (Philips, Eindhoven, Netherlands). Vascular morphometry of variants of angiogenesis were then assessed: high power images of the capillary network were scanned and quantified.
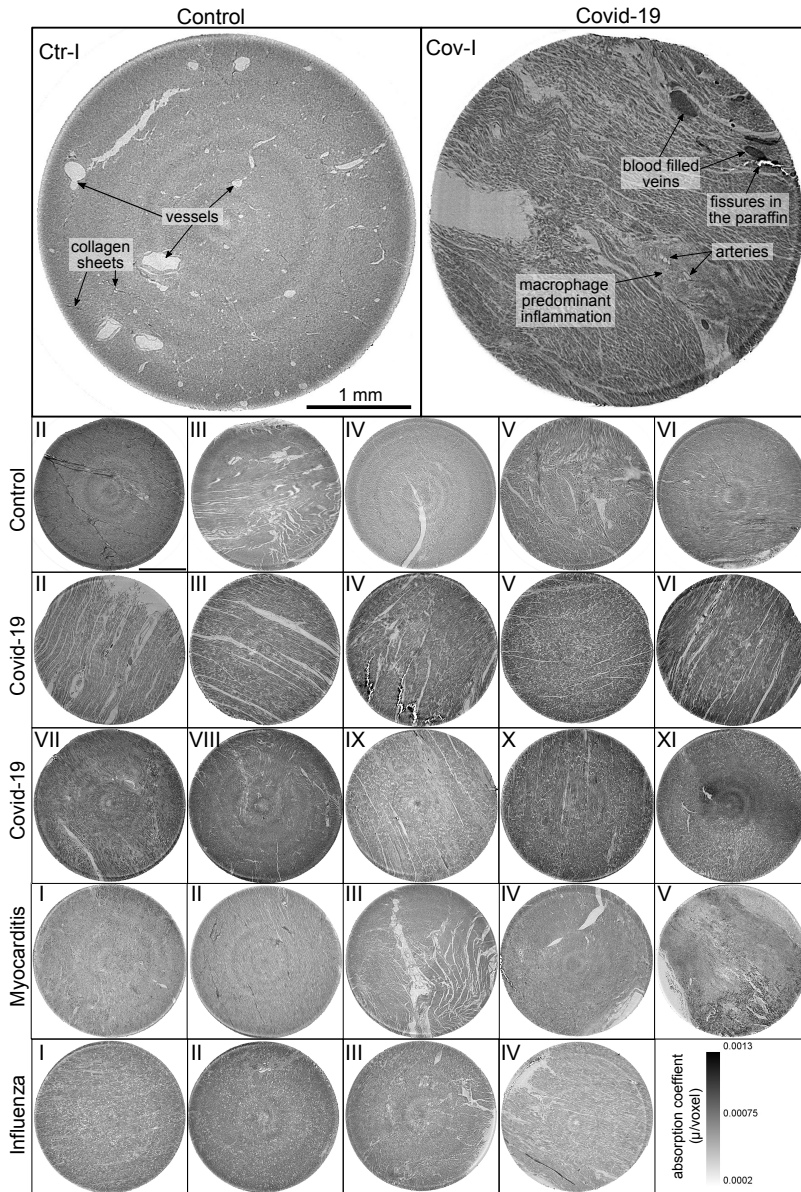
Fig. 4.4: Overview of reconstruction volumes: Laboratory setup. For each sample analyzed at the LJ μ-CT setup one slice of the reconstructed volume is shown. In the top row, a slice of a tomographic reconstruction of a control sample (Ctr-I) and of a sample from a patient who died from Covid-19 (Cov-I) are shown. Below, further slices from control (Ctr-II to Ctr-VI), Covid-19 (Cov-II to Cov-XI) as well as myocarditis (Myo-I to Myo-V) and influenza (Inf-I to Inf-IV) samples are shown. Scale bars: 1 mm.

4.2 Results

4.2.1 Reconstructed electron density: laboratory data

Figure 4.4 shows representative slices of the tomographic reconstruction for all samples scanned at the laboratory LJ setup. The image quality is sufficient to identify the cytoarchitecture and main structural features of interest, such as the general orientation of the cardiomyocytes, large arteries and veins, as well as smaller capillaries. Occasionally, artefacts from sample preparation, such as small air filled micro-fractures of the paraffin, also appear in the reconstructions. In the top row of Fig. 4.4, two annotated slices representative for the Covid-19 and control group are shown enlarged. In the following, the structural appearance of the different groups (Ctr, Cov, Inf and Myo) is briefly described.

Control (Ctr)   The reconstructions of the control hearts are shown in the top row (Fig.4.4 (Ctr-I to Ctr-VI)). Biopsies Ctr-I to Ctr-III and Ctr-IV to Ctr-VI were taken from different areas of the same heart, respectively. In general, the cardiac structure with interload cardiomyocytes and vasculature of the control group is well preserved. The cardiomyocytes are arranged in close proximity and form bundled elongated myocyte chains. Vessels appear as bright tubes within the dense, homogeneous muscle tissue and only a few blood residues can be found in the vessels. Ctr-III differs from the other control samples. The alignment of the cardiomyocytes is not directed along the same direction, and the amount of collagen sheets and paraffin inclusions is comparably high. Further, a high amount of adipose tissue can be identified, as accumulations of less electron-dense (i.e. brighter) spheroids, see for example the top of the slice. Ctr-III also shows a high amount of collagen sheets, which appear as dark stripes in the reconstructions. Ctr-V contains many electron-dense spheres.

Covid-19 (Cov)   The cardiac samples of the hearts from patients who died from Covid-19 are shown in the next two rows of Fig.4.4 (Cov-I to Cov-XI). Compared to Ctr, all Cov samples show a high amount of blood filled, ectatic vessels with abrupt changes in diameter, plausibly correlating to micro-thrombi. The cardiomyocytes are not densely packed with substantial interstitial edema, and correspondingly there is a high amount of paraffin inclusions between the cells. This may also explain a higher amount of micro-fractures (e.g. in Cov-I and IV) in the paraffin, which are filled with air. Furthermore, Cov-I also shows an inflammatory infiltrate, predominantly consist-

ing of macrophages, around the intramyocardial vessel, marked in the corresponding slice (top, right) of Fig.4.4.

Coxsackie virus myocarditis (Myo)   In Figure 4.4 representative slices from tomographic reconstructions of biopsies of patients who died from coxsackie myocarditis (Myo-I to Myo-V) are shown. The tissue of the Myo group is almost as densely packed as the Ctr group. Only in the biopsy of Myo-III, which was sampled near an artery, are some large paraffin inclusions between the cardiomyocytes visible. Characteristic for all myocardits samples is a high amount of lymphocytes, which appear as small electron-dense spheres in the reconstructions. They are primarily located close to vessels (as in Myo-II), but also appear inside the ECM between cardiomyocytes (Myo-I), or infiltrate extensive areas of tissue devoid of vital cardiomyocytes, corresponding to necrosis (Myo-V).

Influenza (Inf)   The biopsies taken from patients who succumbed to H1N1/A influenza (Inf-I to Inf-IV) are shown in the bottom row of Fig.4.4. The tissue structure in this group is also densely packed. Inf-IV shows a high amount of blood filled vessels with abrupt changes in caliber, plausibly correlating to micro-thrombi. Otherwise, changes include lymphocytic infiltration and regions devoid of vital cardiomyocytes indicating necrosis, similar to (Myo)

In summary, the quality of the reconstructions from laboratory data was already sufficiently high to identify the main anatomical features of the cardiac tissue, readily by eye in selected slices. The full reconstruction volumes were therefore targeted by automated geometric analysis based on a structure tensor approach, as described in the next section. However, smaller capillaries and sub-cellular features were not resolved at the laboratory LJ setup. Thus, imaging using high coherent synchrotron radiation was chosen to analyze vascular changes within the tissue.

4.2.2 Reconstructed electron density: synchrotron data

PB setup   The samples from Ctr and Cov patients were scanned at the PB setup of the GINIX endstation (Hamburg, DESY). Compared to the laboratory acquisitions, this allows for smaller effective voxel sizes and enables a higher contrast for smaller tissue structures as erythrocytes and capillaries (as shown in Fig. 4.5). Slices of the

tomographic reconstruction of the 3d electron density distribution are shown in the top row of Fig. 4.6. The data was used for the segmentation of the vascular system.
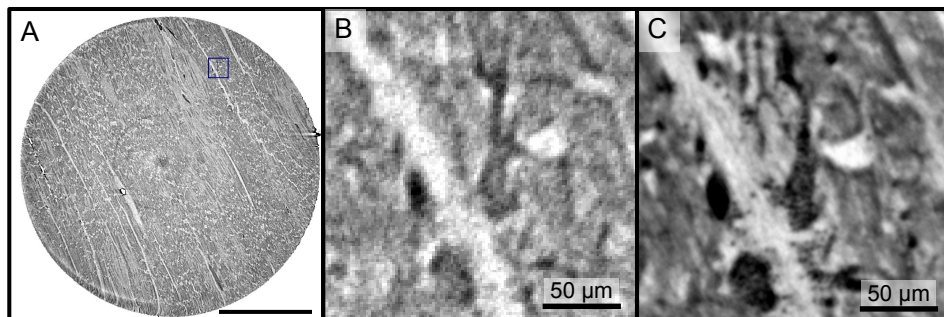
Fig. 4.5: Reconstructions of the LJ compared to the PB setup. Comparison of the data quality of laboratory and synchrotron measurements. (A) slice of a laboratory reconstruction at a voxelsize of 2 μm. A region of interest containing a branching vessel is marked by a blue box which is shown in (B). The same area cropped from a tomographic reconstruction at the PB setup at a voxelsize of 650 nm is shown in (C). The smaller voxelsize, higher contrast and SNR of the PB scans is necessary to segment the vascular system. Scale bars: (A) 1 mm, (B,C) 50 μm.

WG setup   In order to further explore high resolution imaging capabilities, tomograms of two selected biopsies (Ctr-VI and Cov-III) with a diameter of 1 mm were recorded at the WG setup of the GINIX endstation, exploiting cone beam magnification and high coherence filtering based on the waveguide modes. Figure 4.7 shows the corresponding results. A cut of the entire control volume with a size of about $340 \times 340 \times 400 \ \mu m^3$ is shown in Fig. 4.7A. Figure 4.7B shows a slice through the tomographic reconstruction perpendicular to the orientation of the cardiomyocytes. A closer inspection of a single cardiomyocyte marked with a red box is shown on the right. The nucleus of the cell with nucleoli can be clearly seen. Within the cytosol, the myofibrils appear as small discs in the slice. Figure 4.7C shows a second slice through the 3d volume which is oriented along the orientation of the cardiomyocytes. In this view, intercalated discs can be identified. They appear as dark lines connecting two cardiomyocytes. A magnification of the area is marked with a red box. In this view, the myofibrils can be identified as elongated lines within the cell. This region also contains a nucleus of one cardiomyocyte, but also an intercalated disc at the bottom of the image. The tomographic reconstruction of the Cov sample is shown in the lower part of Fig. 4.7 in the same manner as the Ctr. In this dataset capillaries, nuclei and
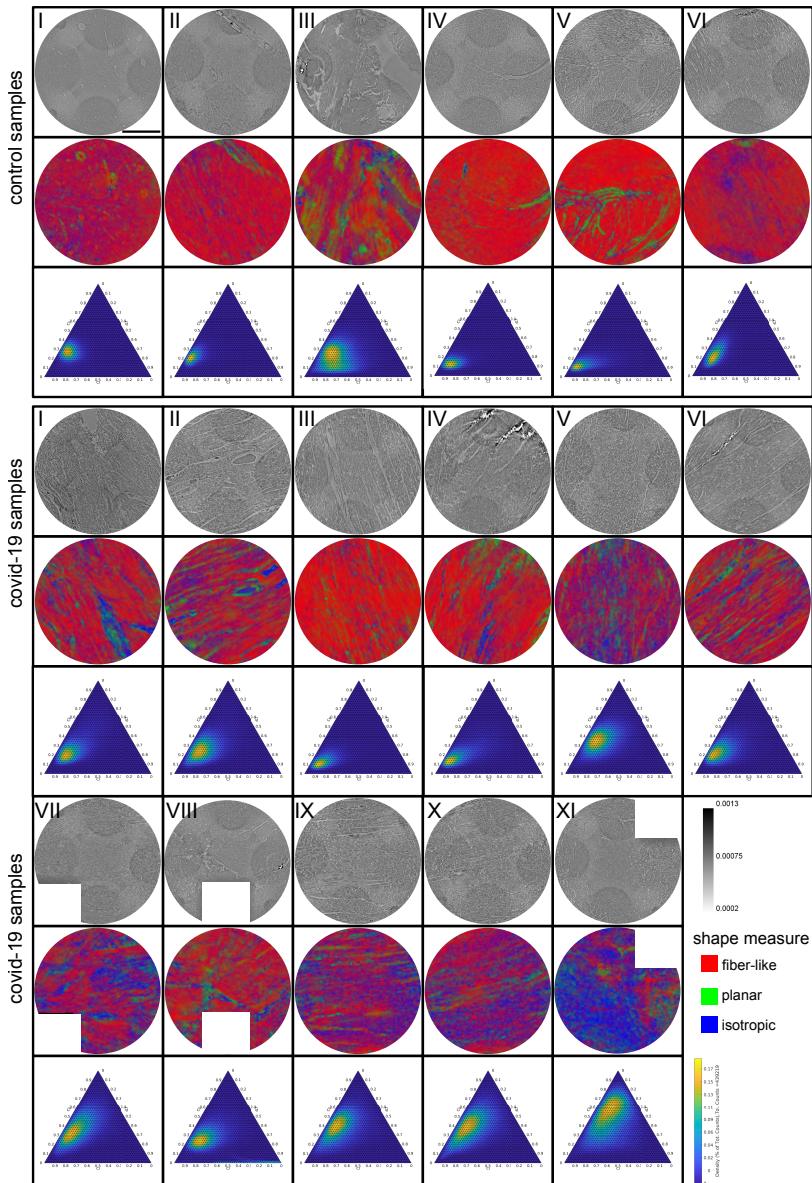
Fig. 4.6: Shape measure of all Covid-19 and control samples reconstructed from PB data. Slices of the reconstructed electron density (stitched volumes of 3 × 3 tomographic reconstructions), the corresponding slice of the shape measure and the ternary plot of the shape distribution in the entire volume are shown. Corrupted datasets were excluded from the analysis and masked in white. Scale bar: 1 mm.
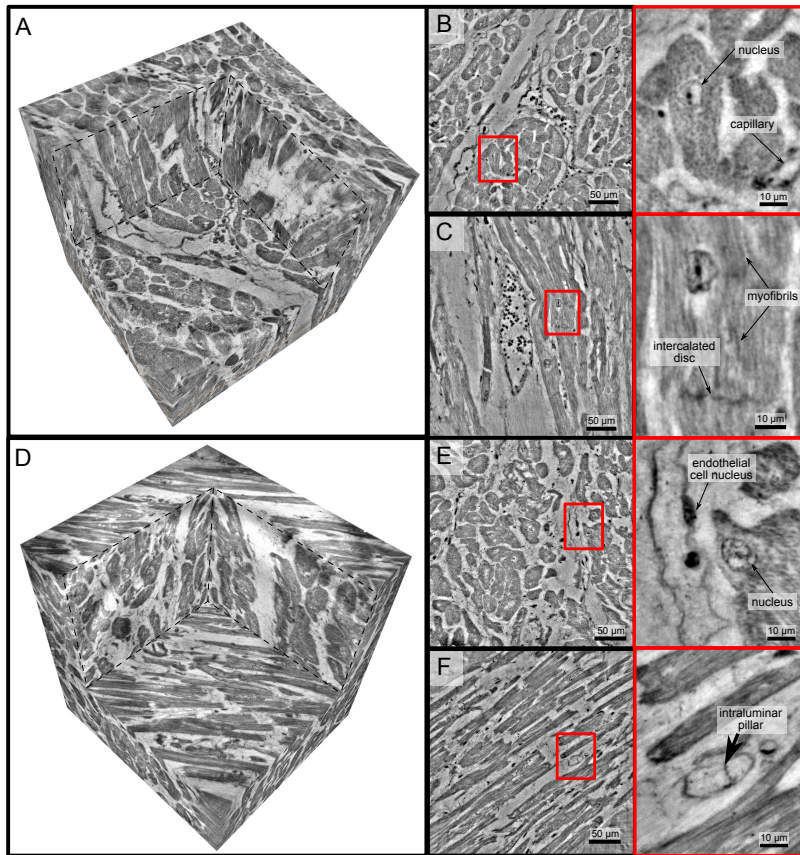
Fig. 4.7: High resolution tomogram of cardiac tissue recorded in cone beam geometry. (A) Volume rendering of a tomographic reconstruction from a control sample recorded in cone beam geometry based on a wave guide illumination. After the analysis in parallel beam geometry a biopsy with a diameter of 1 mm was taken from the 3.5 mm biopsy punch. This configuration reveals sub-cellular structures such as nuclei of one cardiomyocytes, myofibrils and intercalated discs. (B) Slice of the reconstructed volume perpendicular to the orientation of the cardiomyocytes. The red box marks an area which is magnified and shown on the right. One cardiomyocyte is located in the center of the magnified area. In this view, the nucleus can be identified. It contains two nucleoli, which can be identified as dark spots. The myofibrils appear as round discs. (C) Orthogonal slice which oriented along the orientation of the cardiomyocytes. A magnification of the area marked with a red box. In this view, a nucleus but also the myofibrils can be identified as dark, elongated structures in the cell. Further, an intercalated disc is located at the bottom of the area. (D) Volume rendering of a tomographic reconstruction from a Covid-19 sample. Slices orthogonal (E) and along (F) to the cardiomyocyte orientation are shown on the right. In the magnified areas, a nucleus of an endothelial cell and an intraluminar pillar -the morphological hallmark of intussusceptive angiogenesis- are visible. Scale bars: orthoslices 50 μm; magnified areas 10 μm.

myofibrils can also be identified. The volume contains smaller capillaries compared to the control, but this circumstance is probably due to a different location within the myocardium. The most important difference between the Ctr and Cov sample is the presence of small bars in the lumen of capillaries in the Cov sample. These intraluminal pillars are an indicator for IA.

Since the FOV in this configuration is limited, and stitching of larger volumes required more beamtime than available, quantitative and statistical analysis was performed only on the datasets acquired in the laboratory and in PB geometry. At the same time, this proof-of-concept shows that much more structural information could be exploited by stitching tomography and speeding-up the measurement sequence in the WG configuration.

The tomographic datasets recorded at the WG setup as well as the PB datasets used for the segmentation of the vascular system and the respective laboratory datasets were uploaded to `https://doi.org/10.5281/zenodo.5658380` [300].

4.2.3 Automated tissue analysis and classification of pathologies

Next, the reconstructed 3d tissue structure is analyzed by an automated workflow involving differential operators and subsequent statistical representations based on the structure tensor analysis. Instead of semantic analysis of specific structures (vessels, cardiomyocytes, ect), which is considered further below, we first target geometric properties encoded by grey value derivatives, possible prototypical distribution of these parameters in a sample, and the respective variations within and between groups. This can then later be interpreted also in view of semantic image information. A high local anisotropy and consistent orientation field, for example, can be indicative of an intact tissue with well-ordered cardiomyocyte chains. For all samples, eigenvectors and eigenvalues were computed for all sampling points in the reconstructed volume. This information then includes the orientation (quasi-)vector as defined by the smallest eigenvector, as well as the shape measures for all points. As a word of caution, however, one has to keep in mind that these properties also depend on tissue preservation and preparations, as well as on the measurement and reconstruction. For this reason, the latter has to be carried out using identical workflows and parameters for all samples.

Figure 4.8 shows the results of the structure tensor analysis for all samples reconstructed from LJ scans. In Fig. 4.8A the mean values of the shape measures (μ_l, μ_p, μ_s)
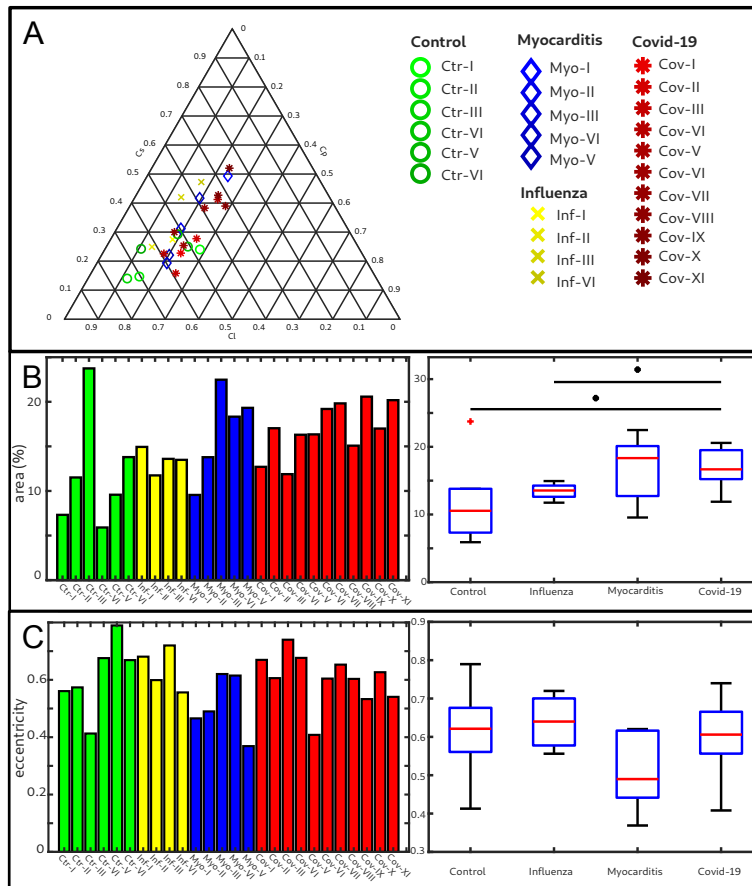
Fig. 4.8: Clustering of LJ data sets. (A) Ternary diagram of the mean value of the shape measures for all datasets. The control samples (green) show low C_s values, while samples from Covid-19 (red), influenza and myocarditis (blue) patients show a larger variance for C_s. (B) The fitted area of the elliptical fit from the PCA analysis of the shape measure distribution is an indicator for the variance in tissue structure. For Control and influenza sample this value differs significantly from the Covid-19 tissue. (C) The eccentricity of the fit is indicates if the structural distribution in shape measure space has a preferred direction along any axis. The value of the myocarditis samples is comparable low.

Table 4.4: Parameters of the cardiac tissue obtained from LJ reconstructions. For all sample groups the mean value and standard deviation of the mean shape measures $\overline{\mu_l}$, $\overline{\mu_p}$, $\overline{\mu_s}$ area of the elliptical fit $\overline{A_\eta}$ (%) and the eccentricity $\overline{e}$ is shown.

group	$\overline{\mu_l}$	$\overline{\mu_p}$	$\overline{\mu_s}$	$\overline{A_\eta}$ (%)	$\overline{e}$
Control	0.60 ± 0.11	0.18 ± 0.07	0.22 ± 0.06	11.98 ± 6.42	0.61 ± 0.13
Covid-19	0.44 ± 0.12	0.23 ± 0.03	0.32 ± 0.11	16.92 ± 2.91	0.61 ± 0.09
Myocarditis	0.47 ± 0.14	0.21 ± 0.02	0.33 ± 0.13	16.69 ± 5.06	0.51 ± 0.12
Influenza	0.49 ± 0.11	0.16 ± 0.02	0.35 ± 0.12	13.44 ± 1.31	0.63 ± 0.07

for all datasets are plotted in a shape-measure diagram, constructed as for ternary mixtures. Sample groups are indicated by color: control-green, Covid-19-red, myocarditis-blue and influenza-yellow. Already in this plot, differences between the groups can be identified. Compared to the Ctr, the pathological groups are shifted towards lower C_l, indicating a less-pronounced fiber-like structure, and to higher C_s, reflecting a larger amount of isotropic symmetry. The Cov, Inf and Myo groups differ mainly in the C_p coefficient. From Inf, to Myo and Cov, the point clouds of each group exhibit successive shifts towards increased C_p. However, these differences in μ are quite small, and it is not possible to classify samples only based on the average value of the shape measure. Instead, the distribution of real-space sampling points in each sample should be taken into account. Figure 4.8B and C show the area A_η and the eccentricity e, respectively, of the ellipse formed by the PCA eigenvectors $\mathbf{u_1}, \mathbf{u_2}$, for each sample, color-coded by groups. The corresponding box-whisker plots indicate a significant difference in A_η between Cov and Ctr (Welch t-test, $p = 0.0389$) as well as a Cov and Inf (Welch t-test, $p = 0.0403$). Concerning e, Cov tissues differs also from Myo (Welch t-test, $p = 0.0611$). Small values of A_η, as obtained for Ctr, indicate a homogeneous tissue structure, while large values are obtained for samples with a more heterogeneous tissue composition. The parameters for each sample group are tabulated in Tab.4.4. The large intra-group variance reflects the pronounced variability between individual subject, which is in line with experience of conventional histology. The complete summary of all samples individually is given in Appendix Tab.4.6. The results for the stitched tomographic datasets (PB setup) of Cov and Ctr are also shown in Fig. 4.5.
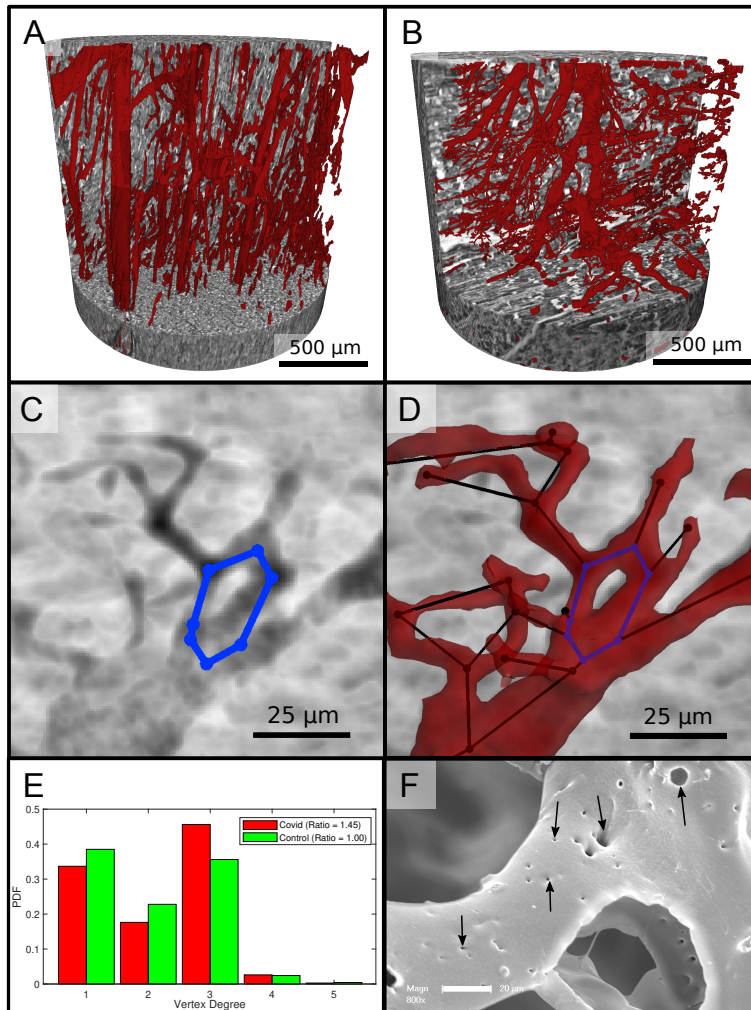
Fig. 4.9: Segmentation of the vascular system in cardiac samples. (A) Segmentation of the vessels of a Ctr sample. The vessels are well oriented and show a relatively constant diameter. (B) Segmentation of the vessels of a Covid-19 sample. The vessels show large deviations in diameter and the surface of the vessels is not as smooth as in the control sample. (C) Filtered minimum projection of an area of the reconstructed electron density of the Cov sample to highlight a vessel loop marked in blue. (D) Surface rendering of the segmented vessel and vessel graph of in an area of the Cov sample. Scale bars 25 μm. (E) Comparison of node degree n between control and Covid-19. Ratio refers to the number of graph branch points ($n > 2$) divided by the number of end points ($n = 1$). (F) Exemplary scanning electron microscopy image of a microvascular corrosion casting from a Covid-19 sample. The black arrows mark the occurrence of some tiny holes indicating intraluminar pillars with a diameter of 2–5 μm, indicating intussusceptive angiogenesis. Magnification 800x, scale bar 20 μm.

4.2.4 Characterization of the vascular system

Figure 4.9 reports on the segmentation and analysis of the vasculature. A surface rendering of the segmented vessels is shown in the top row, on the left for a Ctr sample (Ctr-III) and on the right for a Cov sample (Cov-IV). In Ctr, the vessels are well oriented and show a relatively constant diameter and a smooth surface. In Cov, the vessels show large deviations in diameter and the surface of the vessels is not as smooth as in Ctr. Furthermore, closed loops within the microvasculature can be identified. In Fig. 4.9C, one of these vessel loops (marked with a blue line) in the Cov dataset is highlighted by a minimum intensity projection over ± 30 slices around the centered slice. This pathological formation of a loop is indicative for an intermediate state in the process of IA. The corresponding vessel segmentation is depicted in Fig. 4.9D, with a simplified vessel graph superimposed as black lines. Based on the simplified vessel graph, the connectivity of the capillaries can further be quantified. In total 19893 nodes and for the Cov sample graph 8068 nodes in the segmentation of the Ctr were used. Figure 4.9E shows the probability density function (PDF) of the degree of connectivity n for control and Covid-19 samples. It indicates a higher amount of branching points in the Covid-19 sample. This is also confirmed by the ratio of endpoints of vessels ($n = 1$) to the branching points ($n \geq 3$). Note, that the amount of nodes with $n > 3$ is almost negligible. While the Ctr data shows approximately the same number of endpoints and branching points, the Cov segmentation show almost a ratio of 1:1.5, indicating a higher degree of cross-linking or loop formation of the capillary network.

An exemplary scanning electron micrograph of a Covid-19 sample is shown in Fig. 4.9F. IA was identified via the occurrence of tiny holes with a diameter of 2-5µm in SEM of microvascular corrosion casts. Capillaries display the presence of characteristic intussusceptive pillars (marked by black arrows).

4.3 Summary, conclusion and outlook

This is the first report of a comprehensive 3d analysis of cardiac involvement in tissue of Covid-19, influenza and coxsackie virus infections using X-ray phase-contrast tomography of human FFPE heart tissue. In summary, a high amount of distinct caliber changes of blood filled capillaries in samples of Covid-19 (Cov) patients was identified compared to the control group (Ctr) as well as to coxsackie virus myocarditis (Myo) and influenza (Inv). This can readily be explained by a much higher prevalence of

micro-thrombi in Cov compared to other viral pneumoniae (e.g. influenza), as has previously been reported in Covid-19 lungs. Most importantly, high resolution synchrotron data revealed distinct alterations of the vasculature, with larger variation in vessels diameters, intravascular pillars and amount of small holes, indicative for IA. Branching points of vessels were quantified based on graph representations, after segmentation of vessels based on deep learning. For this purpose, a network for 3d datasets (V-net) was trained with sparse annotations. In Cov, the vasculature also showed a higher degree of branching. Further, SEM data showed a high amount of holes in the capillaries, indicating the presence of multiple intussusceptive pillars as a first stage of IA. The presence of intraluminar pillars was also confirmed by the high resolution reconstruction obtained from WG acquisitions. Accordingly, we could -for the first time– visualize the presence of IA via X-ray phase-contrast tomography not only in the heart but also for the first time in FFPE-tissue. Thus, IA is also a hallmark of Covid-19 inflammation in the heart, analogous to pulmonary previously reported for lung [169]. This finding is in line with the concept of Covid-19 as a systemic and multi-organ angiocentric entity.

The reconstructed electron density of the Cov sample group also showed that concordant with the edema found in conventional histopathology assessment, the cardiomyocytes are not as densely packed as in the control (Ctr) group, leading to larger paraffin inclusions between the cells. Pathological alterations of the tissue architecture were further quantified in terms of non-semantic shape measures, derived from grey value differential operators, using the structure tensor approach. Since the shape measures not only depend on the tissue structure but also on the data acquisition and reconstruction parameters, the entire data acquisition and workflow was optimized and then kept constant for the entire sample series, covering the different pathologies (Cov, Inf, Myo) and control (Ctr) group samples. Importantly, this was already possible at a home-built compact laboratory μCT, based on a liquid metal jet source and optimized phase retrieval, which is important for future translation and dissemination of the methodology developed here. Fully automated PCA analysis then yielded the eigenvectors of the structure tensor at each sampling point of the reconstruction volume, and for each sample. The corresponding distributions showed significant difference in architecture between Cov from all other groups Inf, Myo or Ctr groups, and these differences could be interpreted again by inspection of the reconstruction volumes, i.e. reflecting for example tissue compactness, orientation of the cardiomyocytes and the degree of anisotropy.

Compared to related studies[172], which focused on the analysis of entire human or-

gans, we investigated the cardiac structure from the scale of 3.5 mm biopsy punches down to a resolution showing subcellular and supramolecular structures such as myofibrils and intussusceptive pillars.

Future improvements in segmentation and quantification will be required to fully exploit the structural data acquired here, or in similar studies. To this end, augmented image processing algorithms, deep learning, classification for example based on optimal transport, and the consolidation of the above in form of specialized software packages has to be considered. Technical improvements towards higher resolution and throughput can also be foreseen. Already at present, parallel beam synchrotron data acquisition (GINIX endstation, P10 beamline of PETRA III/DESY) completes a biopsy punch tomogram within 1.5 min, at a a pixel size of 650 nm, and a volume throughput of $10^7 \frac{\mu m^3}{s}$. Importantly, the image resolution and quality is sufficient to segment vasculature and cytoarchitectural features of interest, also and especially for standard unstained paraffin-embedded tissue used in routine diagnostics. The data acquisition rate and dwell time in the range of 10–20 ms (per projection) is dictated by detector readout, motor synchronisation, and data flow rather than by photon flux density for the PB setup. This is also underlined by the fact that (single-crystal) attenuators had to be used to prevent detector saturation. The situation is entirely different, however, for the waveguide cone beam setup, where the lower waveguide exit flux density, which comes with the significantly higher coherence and resolution, requires acquisition times of 200–2500 ms. Here, the projected source upgrade foreseen for PETRA IV will provide a significant gain in resolution and throughput. Robotic sample exchange will therefore be required, and a serious upscaling of the data management and online reconstruction pipeline. First reconstructions of heart biopsies exploiting the enhanced coherence and resolution of a waveguide holo-tomography setup already indicate that this is a very promising direction.

With our presented workflow, especially in view of the laboratory system, we have for the first time implemented destruction free analysis of the ubiquitous FFPE embedded tissue readily available in every pathology lab around the world, based on an automated structure tensor and shape measures. This represents a first and major step in unlocking the extensive international FFPE archives for sub-light-microscope resolution destruction-free 3d-tissue analysis, unfolding manifold future research possibilities in human diseases far beyond Covid-19. This approach has been successfully used to classify the distinct changes in the myocardial cytoarchitecture induced by Covid-19. More importantly still, we have provided first proof for the suspected presence of IA in cardiac Covid-19 involvement, putting forward morphological evidence

of a so far imprecisely defined clinical entirety of great importance.

Competing Interests

The authors declare no competing interests.

Acknowledgements

Funding

Ethics

Formalin-fixed paraffin-embedded tissue blocks of control hearts, influenza and cox-sackie virus myocarditis hearts were retrieved from archived material from the Institute of Pathology at Hannover Medical School in accordance with the local ethics committee (ethics vote number: 1741-2013 and 2893-2015). Formalin-fixed paraffin-embedded tissue blocks of Covid-19 autopsy cases were retrieved after written consent in accordance with the local ethics committee at Hannover medical school (ethics vote number: 9022 BO K 2020)

Supplementary Information: Medical Background & Datasets

Medical Information

sample no.	age, sex	hospitalization (days), clinical, radiological and histological characteristics
Cov-I	86,M	5d, RF, D, H, I
Cov-II	96,M	3d, RF, H
Cov-III	78,M	3d, CRF, V, D, S, H
Cov-IV	66,M	9d, RF, V, S, H
Cov-V	74,M	3d, RF, D, S, H
Cov-VI	81,F	4d, RF, S, H
Cov-VII	71,M	0d, V
Cov-VIII	88,M	2d, V, H, I
Cov-IX	85,M	5d, V, S, H
Cov-X	58,M	7d, V, H
Cov-XI	54,M	15d, V
Ctr-I to Ctr-III	26, F	-
Ctr-IV to Ctr-VI	36, F	-
Myo-I	57,M	V, H
Myo-II	23,M	
Myo-III	59,M	S, H, D
Myo-IV	50,M	V, S, D
Myo-V	25,F	
Inf-I	74,M	9d, CRF into MOF, V, S, H
Inf-II	66,F	17d, MOF, V, H
Inf-III	56,M	3d, CRF into MOF, V
Inf-IV	55,M	24d, RF into MOF, V, S

Table 4.5: Sample and medical information. Age and sex, clinical presentation with hospitalization and treatment. RF:respiratory failure, CRF: cardiorespiratory failure, MOF: multi-organ failure, V: ventilation, S: Smoker, D: Diabetes TypeII, H: Hypertension, I: imunsupression

Structural analysis

sample	mean (Cl,Cp, Cs)	fitted area	eccentricity
Ctr-I	(0.6508 , 0.1069 , 0.2423)	7.3194	0.5607
Ctr-II	(0.5167 , 0.1907 , 0.2926)	11.5130	0.5736
Ctr-III	(0.5074 , 0.2427 , 0.2499)	23.7443	0.4128
Ctr-IV	(0.7434 , 0.1166 , 0.1400)	5.9026	0.6757
Ctr-V	(0.7038 , 0.1495 , 0.1467)	9.5763	0.7896
Ctr-VI	(0.4765 , 0.2835 , 0.2400)	13.7973	0.6688
mean	$(0.60 \pm 0.11, 0.18 \pm 0.07, 0.22 \pm 0.06)$	11.98 ± 6.42	0.61 ± 0.13
Cov-I	(0.5398 , 0.2327 , 0.2275)	12.7052	0.6696
Cov-II	(0.4676 , 0.2550 , 0.2774)	17.0347	0.6059
Cov-III	(0.5896 , 0.2526 , 0.1578)	11.8845	0.7399
Cov-IV	(0.5911 , 0.1833 , 0.2255)	16.3040	0.6765
Cov-V	(0.3371 , 0.2505 , 0.4124)	16.3445	0.4081
Cov-VI	(0.5184 , 0.2279 , 0.2537)	19.1954	0.6044
Cov-VII	(0.3912 , 0.2262 , 0.3826)	19.8206	0.6530
Cov-VIII	(0.5227 , 0.1776 , 0.2997)	15.0791	0.6033
Cov-IV	(0.3253 , 0.2851 , 0.3897)	20.5768	0.5329
Cov-X	(0.3283 , 0.2446 , 0.4271)	16.9989	0.6266
Cov-XI	(0.2484 , 0.2314 , 0.5202)	20.1815	0.5407
mean	($0.44 \pm 0.12, 0.23 \pm 0.03, 0.32 \pm 0.11$)	16.92 ± 2.91	0.61 ± 0.09
Myo-I	(0.5777 , 0.2018 , 0.2206)	9.5528	0.4656
Myo-II	(0.3887 , 0.1943 , 0.4170)	13.7853	0.4899
Myo-III	(0.5984 , 0.2081 , 0.1935)	22.4768	0.6202
Myo-IV	(0.4974 , 0.1908 , 0.3117)	18.3306	0.6149
Myo-V	(0.2664 , 0.2402 , 0.4933)	19.3212	0.3689
mean	$(0.27 \pm 0.14, 0.24 \pm 0.02, 0.49 \pm 0.13)$	16.69 ± 5.06	0.51 ± 0.12
Inf-I	(0.3561 , 0.1714 , 0.4724)	14.9393	0.6808
Inf-II	(0.4423 , 0.1376 , 0.4201)	11.7445	0.5991
Inf-III	(0.6150 , 0.1361 , 0.2489)	13.5988	0.7198
Inf-IV	(0.5404 , 0.1849 , 0.2747)	13.4885	0.5561
mean	$(0.49 \pm 0.11, 0.16 \pm 0.02, 0.35 \pm 0.11)$	13.44 ± 1.31	0.63 ± 0.07

Table 4.6: Parameters of the cardiac tissue (laboratory data).

Datasets

The tomographic datasets recorded at the WG setup as well as the PB datasets used
for the segmentation of the vascular system were uploaded to
https://doi.org/10.5281/zenodo.5658380.

X-ray structural analysis of single adult cardiomyocytes: tomographic imaging and micro-diffraction

5

M. Reichardt, C. Neuhaus, J.-D. Nicolas, M. Bernhardt, K. Toischer and T. Salditt
Reproduced from Biophysical Journal (2020).

Abstract

We present a multi-scale imaging approach to characterize the structure of isolated adult murine cardiomyocytes based on a combination of full-field three-dimensional (3d) coherent x-ray imaging and scanning x-ray diffraction. Using these modalities, we probe the structure from the molecular to the cellular scale. Holographic projection images on freeze-dried cells have been recorded using highly coherent and divergent x-ray waveguide radiation. Phase retrieval and tomographic reconstruction then yield the 3d electron density distribution with a voxel size below 50 nm. In the reconstruction volume, myofibrils, sarcomeric organisation and mitochondria can be visualized and quantified within a single cell without sectioning. Next, we use micro-focusing optics by compound refractive lenses to probe the diffraction signal of the acto-myosin lattice. Comparison between recordings of chemically fixed and untreated, living cells indicate that the characteristic lattice distances shrink by approximately 10% upon fixation.

Significance

Diffraction with synchrotron radiation has played an important role to decipher the molecular structure underlying force generation in muscle. In this work, the diffraction signal of the actomyosin contractile unit has for the first time been recorded from

living cardiomyocytes, bringing muscle diffraction to the scale of single cells. In addition to scanning diffraction, we use coherent optics at the same synchrotron endstation to perform holographic imaging and tomography on a single cardiomyocyte. By this hard x-ray microscopy modality, we extend the length scales covered by scanning diffraction and reconstruct the electron density of an entire freeze-dried cardiomyocyte, visualizing the 3d architecture of myofibrils, sarcomers, and mitochondria with a voxel size below 50 nm.

5.1 Introduction

Force generation in heart muscle relies on a hierarchically ordered structural organization, reaching from the actomyosin assembly in the sarcomere to the entire structural organization of cardiomyocytes (CMs). The latter includes, for example, the dense packing of myofibrils, the high number of mitochondria, and the structural and dynamical properties underlying excitability. Classical x-ray diffraction studies of skeletal [301] and heart muscle [302] have helped to shape our understanding of the average structure of the sarcomere. In contrast to electron microscopy, muscle structure analysis by x-ray diffraction is compatible with *in situ* mechanical loading, physiological parameters, and simultaneous measurements of the contractile force. Many molecular details of the myosin head dynamics, binding, and stroke have been revealed by third generation synchrotron radiation [220, 303–305]. In these experiments, however, structural information is averaged over macroscopically large volumes of the muscle tissue, without sensitivity to the cellular organization, or cell-to-cell variations. Electron microscopy, on the other hand can unravel the molecular and sub-cellular organization of myocytes [306, 307], but requires invasive staining and sectioning, while confocal fluorescence microscopy is compatible with *in vivo* recordings of contracting cells [308], but lacks the resolution for the molecular scale and also contrast for unlabeled structure.

With recent progress in x-ray focusing optics, as reviewed in [223], it has become possible to perform diffraction experiments with spot sizes in the micron and nanometer range. This enables recordings of the small-angle x-ray scattering (SAXS) while scanning the sample in real space, as initially introduced for biomaterials [309, 310], more recently also for soft matter [311], as well as for 3d vector SAXS [312]. Scanning diffraction from biological cells with spot sizes smaller than a single organelle are still more challenging in terms of signal-to-noise [229–231, 236, 313, 314], as well as

radiation damage [315]. Recently, we have used this approach to study the cytoskeletal structure of single CMs in order to compare the signal level for different preparation states [226]. For freeze-dried heart muscle cells [233, 236], we have observed anisotropic diffraction patterns, and by correlating the x-ray signal to fluorescence data obtained by *in situ* stimulated emission depletion (STED) microscopy recordings, we have linked the signal to the actin portion of the cell [234]. A diffraction signature of a sarcomeric complex was observed for the first time for hydrated and chemically fixed cardiomyocytes [226]. Hence, by this technique, variations of structural parameters in single isolated cells or in muscle tissue have now become accessible, unaffected by macroscopic averaging. However, it cannot be expected that the signal level and amount of structural details can compete with macroscopic muscle diffraction.

Regarding sub-cellular and cellular organization, a second line of development, not in x-ray diffraction but in coherent imaging with hard x-rays has also matured [118, 148, 316, 317], providing 3d electron density maps for unstained cells, reconstructed either by coherent diffractive imaging [318], ptychography [314, 319, 320], or by x-ray holography [140, 147, 244, 258]. While the resolution is still lower than in x-ray microscopy with Fresnel zone plate lenses [321], the size of adult CMs is too large to be penetrated by soft x-rays in the water window.

In this work, we now combine full-field 3d imaging of the electron density by holographic x-ray tomography (holo-tomography) and scanning x-ray diffraction to study the structure of isolated murine adult CMs on the molecular and cellular scale. As illustrated in Fig. 5.1, this multi-modal x-ray approach has been implemented at the same synchrotron endstation, where both modalities can be realized by a simple rearrangement of its modular compound optics [196]. The purpose of the current work is threefold. First, this study is a benchmark of current x-ray method development geared towards cellular biophysics and cell biology. Second, it can contribute to computational modeling of the contractile functions of CMs. Third, it illustrates the capability and limitations how x-ray imaging methods can contribute to future multi-modal correlative imaging approaches. Such efforts will most certainly comprise visible light, electron microscopy and fluorescence microscopy, and hopefully also cover structural dynamics. To this end, the 'x-ray contrast' offering quantitative electron density as well as actomyosin lattice parameters without slicing or staining, will be complementary to the other more established microscopy methods. The following achievements highlight the progress that has been made with respect to prior work: (i) The first demonstration of diffraction analysis for (initially) living cells, which shows a proper exploitable acto-myosin signal. (ii) The demonstration how the actomyosin

lattice spacing changes when the CMs are chemically fixed. (iii) The first 3d electron density reconstruction by phase contrast x-ray tomography, albeit at this time only for a freeze-dried cell.

Beyond the technical focus, this work also reports structural insight regarding adult cardiomyocytes. Specifically, we can quantifying the distribution of the acto-myosin lattice spacing within a single adult cardiomyocyte. We also show that fixation which is ubiquitous in cellular biophysics and cellular biology, results in shrinkage of the acto-myosin lattice. Finally, regarding tomography, we provide data on the 3d distribution of mitochondria in the cell which is valuable information to model energy supply.

The manuscript is organized as follows. Following this introduction, we describe methods of sample preparation, instrumentation, optics, reconstruction, and analysis. We then present the holo-tomography results for single CMs, followed by the x-ray micro-diffraction results for living CMs, before closing with a brief summary and outlook.

5.2 Materials and methods

5.2.1 Preparation of CMs for x-ray analysis

The workflow of the sample preparation is sketched in Fig. 5.1a. After the dissociation of the hearts, single CMs were prepared for the x-ray analysis. The structure of CMs, as sketched in Fig. 5.1c, was analyzed using the two modalities of the beam line setup. For the investigation of sub-cellular structures such as the nucleus and mitochondria, full-field holographic x-ray tomography was used, while the molecular actomyosin structure (sketched in the magnification of Fig. 5.1c) was probed by scanning x-ray diffraction. For diffraction measurements, the CMs were mounted in liquid chambers, whereas for tomographic scans the cells were either freeze dried or embedded in agararose to increase stability. A detailed description of the preparation steps is given below.

Isolation of cardiomyocytes The isolation of adult CMs followed the procedure described in [322]. Before sacrifice, the wild type mice (C57BL/6) were anesthetized with isoflurane. The hearts were explanted and put in an ice-cold tyrode-solution to wash out remaining blood. After this, a canula was put in the aorta and the heart
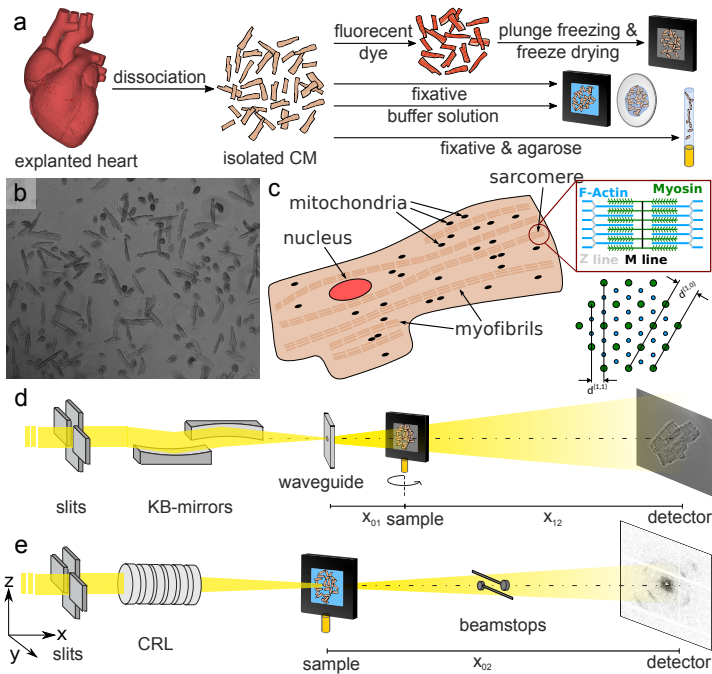
Fig. 5.1: (a) Sample preparation. CMs were isolated by dissociation of healthy mouse hearts. One part (top row) of the cells was chemically fixed, mounted on a silicon nitride window and actin was stained with a fluorescent dye (Atto633-Ph). Afterwards, the samples were plunge frozen and freeze dried. For experiments in hydrated conditions (middle rows), the cells were either analyzed in buffer solution or chemically fixed. They were placed in liquid chambers made of SiN (chemically fixed cells) or polypropylene windows (living cells). For tomography, fixed cells were mixed and embedded in agarose and mounted in a polyimide tube with a diameter of 1 mm (bottom row). (b) Microscopy image of freshly isolated CMs. Healthy, contracting cells and apoptotic cells can be identified. (c) Schematic overview of the cellular structures of a CM. The nucleus, mitochondria and myofibrils are sketched. The red circle marks a sarcomeric unit which is magnified in the scheme on the right. A cross section of the sarcomere and the definition of the sarcomeric lattice spacing is shown below. (d) Experimental setup for x-ray phase contrast tomography at the GINIX endstation of the P10 beamline at the PETRAIII storage ring (DESY, Hamburg, Germany). The x-ray beam is focused by a pair of Kirkpatrick-Baez (KB)-mirrors and coupled into a waveguide channel for further reduction of the beam size and for coherence filtering. The sample is placed on a fully motorized tomography stage at distance $x_{01} \approx 0.35$ m and the detector is placed at $x_{12} \approx 5$ m behind the sample. The resulting cone beam geometry of the highly coherent wavefront is used to acquire projections at high geometric magnification $M \gg 1$ and low Fresnel number $F \ll 1$. (e) The same endstation can also be used for scanning diffraction experiments. In this mode, the beam is focused by CRLs and the sample is moved into the focus. Diffraction patterns are acquired by an EIGER 4M detector at distance $x_{02} \approx 5$ m. The primary beam is blocked by beam stops to protect the detector.

was washed with the tyrode solution. The hearts with the canula was put into a Langendorff perfusion system containing a liberase solution which was pre-heated to $36.5°$ C. The hearts were perfused by this solution, starting the digestion of the heart tissue. After 5 minutes, the hearts were transferred to a Petri dish, also containing the enzyme-solution. The hearts were cut into smaller pieces and resuspended in the same medium using a 10 ml pipette with a cut off tip. The resuspended cells were mixed with a stop solution (containing bovine calf serum (BCS) and $CaCl_2$) in a Falcon tube. The remaining tissue sinks to the bottom, the supernatant is transferred to another falcon tube and the cells sediment and form pellets. Afterwards, the cells were washed twice with tyrode-solution. Directly after the isolation, the extracted cells were observed in the microscope. The success of the isolation was evaluated by the vitality of the cells. Figure 5.1b shows a microscopy image of freshly extracted CMs. The healthy, contracting cells can be distinguished from apoptotic cells. Only isolations with a vitality rate above 50% were used for further analysis.

Preparation of CMs for diffraction   For the diffraction experiments, the isolated CMs were transferred to liquid sample chambers, see middle row of Fig. 5.1a. Part of the cells were chemically fixed right after the extraction. Karlsson-Schultz (KS) fixation solution [323] containing 4% formaldehyde and 2.5% glutaraldehyde was used as a fixative. The cells were incubated in the solution for 15 minutes and stored in PBS at $4°$ C for 2 weeks before the experiment started. For the x-ray diffraction measurement a chamber from Silson Ltd. (Warwickshire, United Kingdom) was used. The chamber consists of two $1\,\mu$m thick silicon nitride membranes in silicon frames. One of the frame has a $70\,\mu$m polymer spacer, keeping the frames apart in order protect the CMs from squeezing. The cells, with a diameter of approximately 10-25 μm and a length of 50-100 μm, are carefully sandwiched between the two silicon nitride frames. To seal the chamber, the silicon nitride frames are placed in a metal frame, which is sealed with two gaskets and screwed together. The metal frame is then inserted into a sample holding pin. The investigation of living CMs required a higher effort in the planning of the experiments. Right after the extraction, the living CMs were transported from Göttingen to the beamline in a mobile incubator ($37°$C). The cells were stored in tyrode buffer during transport and measurement. At the beamline the living cells were sandwiched between two polypropylene membranes. To keep the membranes apart, a gasket of the silson chambers with a thickness of $300\,\mu$m were used. The polypropylene membranes were sealed tightly by applying nailpolish to the edges. The chamber was then inserted into a sample holding pin for the measure-

ment. Additionally, plunge frozen and freeze-dried CMs mounted on SiN windows were analyzed. Since this preparation was primarily used for holographic and tomographic imaging, the procedure is described in the next paragraph.

Preparation of CMs for x-ray holography and tomography For the tomographic scans, CMs were either coated to SiN windows, plunge frozen and freeze dried (top row of Fig. 5.1a) or embedded and hydrated in 1% agarose gel (bottom row of Fig. 5.1a) to increase stability. In order to reduce absorption for the agarose embedded cells and to allow for a rotation of the sample, the cells were transferred into a capillary using a 1 mm biopsy punch. The protocol of the preparation for freeze-dried samples closely followed [226, 233, 236]. CMs were pipetted onto SiN-windows coated with a 1% fibronectin coating and incubated for 15 min. Afterwards the cells were chemically fixed (15 min in 7% formaldehyde). Additionally, the actin skeleton of the CMs was stained with a fluorescent dye (Atto633-phalloidin, ATTO-TEC GmbH, Siegen, Germany). Plunge freezing of CMs was performed with a grid plunger (Leica EM GP). Afterwards, the cells were freeze dried. The stained samples were stored in a light-protected desiccator until the measurements were performed. As an alternative to freeze-dried preparations which compromise the structural preservation of the ultra-structure, we also used embedding in a gel to prevent dehydration, while at the same time increasing positional stability for the tomographic scan. Since the native electron density contrast in hydrated CMs was found insufficient, contrast enhancement by staining, namely by 1% OsO_4 and phosphotungstic acid (PTA) [241, 324] was used.

Inspection of CMs by STED Before x-ray holography and tomography experiments were performed, the freeze-dried CMs were imaged with a custom build STED microscope (Abberior Instruments, Göttingen, Germany)[234]. This setup is compatible with the GINIX endstation of the P10 beamline. For the beamtime block of the current work, however, the STED microscope was only available in 'offline mode' at the institute for x-ray physics in Göttingen. It allowed to pre-characterize the freeze-dried samples before the beamtime. In this way, cells which did not show any ruptures from the procedure of plunge freezing and freeze drying were selected for x-ray imaging. First, the cells were analyzed in confocal mode and raster scanned with a step size of 200 nm in lateral and 400 nm in axial direction. Additionally, one slice was acquired in STED mode and a step size of 50 nm.

5.2.2 Synchrotron beamline and instrumentation

The x-ray experiments were carried out at the undulator beamline P10 at Deutsches Elektronen-Synchrotron (DESY) in Hamburg, Germany, using the GINIX (*Göttingen instrument for nanoscale imaging with x-rays*) endstation [196]. The modular design of the GINIX endstation enables rapid switching between the two modalities used here: holo-tomography based on a Kirkpatrick-Baez (KB) and x-ray waveguide compound optics [164, 258, 325] and scanning diffraction based on micro-focusing by a Beryl-lium compound refractive lens (CRL) transfocator system. Both settings are sketched in Fig. 5.1d. Experimental parameters, concerning the instrumentation and optics, are tabulated in Tab. 5.1 and described in more detail below.

For x-ray diffraction, the undulator beam was monochromatized by a Si(111) channel-cut crystal to an energy of $E_{\text{ph}} = 8\,\text{keV}$. The beam was focused by a set of Beryllium CRLs to a size of $2 \times 3\,\mu\text{m}^2$. The total photon flux was $2.5 \cdot 10^{10}$ photons/s. The sample was placed in the focal plane and moved by a fully motorized sample stage using a piezo-motor. To protect the detector, the primary beam was blocked using two beam-stops. The diffraction signal was recorded by a single photon counting detector with a pixel size of $px = 75\,\mu\text{m}$ (Eiger 4M, Dectris, Switzerland) located approximately 5 m behind the sample.

For the holographic and tomographic scans, the photon energy was set to $E_{\text{ph.}} = 8\,\text{keV}$ and 7.5 keV in two subsequent beamtimes. The beam was focused by a set of Kirkpatrick-Baez (KB) mirrors to a focal spot size with a full width at half maximum of about $\text{FWHM}_{y,z} = 300 \times 300\,\text{nm}^2$ in horizontal (y) and vertical (z) direction. The photon flux was $I_0 \approx 1.1 \cdot 10^{11}$ photons/s. The KB-focused beam was then coupled into a lithographic x-ray waveguide channel [326, 327], which is placed in the focal plane. The waveguide serves the purposes of further beam confinement as well as spatial and coherence filtering, providing a clean wavefront for inline holography [258]. At the detector plane a photon flux of $I_0 \approx 1.1 \cdot 10^9$ photons/s was detected. The sample was moved by a fully-motorized sample stage to a defocus plane and probed by the highly coherent exit wave field emanating from the waveguide. Small phase shifts of the wavefront after interaction with the object transform into a measurable intensity pattern by free space propagation of the beam and self-interference of the divergent wave field. The geometrically magnified hologram was recorded by a detector placed approximately 5 m behind the sample. The hologram encodes the local phase shift, or equivalently the projected electron density distribution of the object. By choice of the focus-to-sample distance x_{01}, which is typically a few millimeters to centimeters, the

geometrical magnification $M = \frac{x_{01}+x_{12}}{x_{01}}$ with sample-detector distance x_{12} and the effective pixel size $px_{\text{eff}} = \frac{p}{M}$ are adjusted, as well as the field of view.

Table 5.1: Beamline specifications of the setups for scanning SAXS and tomography of the GINIX endstation.

	sSAXS	tomography
energy (keV)	8	7.5
monochromator	Si(111) channel-cut	Si(111) channel-cut
detector	Eiger 4M	sCMOS (15 μm Gadox scintillator)
source-to-detector distance x_{02} (cm)	507.5	501.14
pixel size px (μm)	75	6.5
focus (horz. $\times$ vert.)	2×3 μm^2	< 50 nm
I$_0$ (photons/s)	$2.5 \cdot 10^{10}$	$1.1 \cdot 10^9$

5.2.3 Data acquisition and image analysis

Scanning SAXS measurements

For the scanning SAXS experiments, the samples are continuously scanned by a piezo motor. Positioning of the sample in the focal spot is facilitated by an on-axis microscope. In view of radiation damage a 'diffract before damage' strategy is adopted [315]:

1. position a pristine cell or pristine cellular region in the focal spot,
2. record a diffraction pattern with an exposure time, for which the signal is unaffected by structural damage,
3. move to a new cell/spot.

Regarding (2), the critical dose for damage is estimated from a test involving a variation of accumulation time, or from fractionating the dose over several sub-frames. This strategy is based on the tested assumption that the signal is stable up to a critical time depending on dose, dose-rate and resolution. This is the case for a pristine spot. Since previous exposures of neighboring scan points can induce a 'bystander effect', the step size is a further important parameter and has to be chosen sufficiently large [315]. Therefore, this scheme results in rather coarse-grained real space maps of the cells. Tab. 5.2 presents the data acquisition parameters for the three different sample preparations. Data analysis was performed using the MATLAB nanodiffraction toolbox developed in our institute [227].

Table 5.2: Data acquisition parameters of the SAXS experiments.

	living	fixed	freeze-dried
fixative	-	KS	formaldehyde
step size (μm)	5	10	2
step size (μm^2)	200×200	180×180	200×200
stitching	1	5×5	1
acquisition time	0.1 s	0.1 s	0.05 s

X-ray holography

As a full field technique, x-ray holography does not require any lateral scanning of the sample, which makes it ideally suited for tomography. However, before any tomographic scan, the signal level, i.e. the contrast of the hologram has to be evaluated and the geometry and detector configuration has to be optimized. An overview of the different configurations of the beamline setup and the sample preparation tested in this work, is summarized in Tab. 5.3. Since contrast depends on the variations in electron density, freeze-dried cells result in much higher contrast than cells in solution. For CM recordings, we compared different detectors. We performed scans with a single-photon counting pixel detector (Eiger 4M, Dectris Ltd,Baden-Daettwil, Switzerland), offering highest dose efficiency due to photon counting. However, the large pixel size $px = 75$ μm requires the sample to be moved very close to waveguide to reach high magnification, impeding tomographic rotations at high magnification. We therefore then turned to indirect detection based scintillator-based fiber-coupled sCMOS detectors. To this end, we used a single crystal scintillator (LuAG, thickness 20 μm) with an sCMOS (Hamamatsu Photonics K.K., Hamamatsu, Japan) coupled by a 1:1 fiber optic plate, as well as another 1:1 fiber-coupled scintillator-based sCMOS camera (2048 x 2048 pixels, Photonic Science, Sussex, UK) with a custom 15 μm thick Gadox scintillator with pixel size of $px = 6.5$ μm. This configuration was favored, since the whole cardiomyocyte fitted into the FOV and at the same time the effective pixel size was sufficiently small, namely $px_{\text{eff}} = 45$ nm at $M = 143$. The sample preparation and environment was also tested in view of compatibility with holographic tomography (holo-tomography). As described above, we tested hydrated unstained CMs as well as CMs with 1% OsO_4 or PTA staining embedded in agarose. All cases resulted in a rather weak signal. For unstained cells embedded in agarose, almost no signal could be detected at the given photon energy. Sample mounting was another concern. As isolated

CMs are not attaching to a substrate, one easily encounters drift during scan. For these reasons, we decided in this work to perform tomography scans only on freeze-dried CMs mounted on thin foils made from silicon nitride (Silson Ltd.). It is to mention, that for these experiments the size and shape of the SiN-frames is a compromise between the caused missing wedge, the tolerable tilt angle and the window's stability: Thick and broad frameworks lead to a rather stable window at the cost of a large missing wedge. Windows with large edge lengths diminish the maximum tolerable tilt angle of the sample in horizontal and vertical direction due to the small x_{01} distance as required for high resolution cone beam recordings. Also the cell density must be chosen relatively low, otherwise neighboring cells will enter the field-of-view upon rotation and disturb the reconstruction of the target cell.

Table 5.3: Acquisition parameters of the x-ray holography experiments.

	I	II	III	IV
preparation	freeze-dried	freeze-dried	freeze-dried	hydrated, stained
detector	Eiger 4M	sCMOS (20μm LuAG)	sCMOS (15μm Gadox)	sCMOS (15μm Gadox)
px (μm)	75	6.5	6.5	6.5
$x_0 1$ (mm)	20.8	20.8	35	35
$x_0 2$ (mm)	5413	5413	5011	5011
px_{eff} (nm)	300	24	45	45
photon energy (keV)	8	8	7.5	7.5
acquisition time (s)	10×0.1	1	1	1

X-ray tomography

The configuration of the tomography setup as well as the sample preparation was chosen after the evaluation of the 2D holographic data sets. In order to avoid lack of contrast and motion artifacts, which would influence the quality of reconstructions, we focused on freeze-dried cells for tomographic recordings. At the same time, the size of single CMs (typically around 150 μm) prompted us to choose a moderate magnification resulting in a pixel size of $px_{\text{eff}} = 45$ nm. To perform a proper phase reconstruction, projections were taken for four slightly different propagation distances (see Tab. 5.4) for each angular position. For each distance, 720 equidistant angular

positions were recorded over 180°. At the beginning and the end of the tomographic recording, a set of 50 empty beam images were recorded in order to characterize the probing wave front. After the scan, 20 images of the camera dark current were acquired. The acquisition parameters of the experiment are summarized in Tab. 5.4.

Table 5.4: Acquisition parameters of the x-ray tomography experiments.

parameter	value
photon energy E (keV)	7.5
source-detector-distance x_{02} (mm)	5011.4
source-sample-distance x_{01} (mm)	{35, 36, 39, 45}
magnification M	{143, 139, 128, 111}
pixel size px (μm)	6.5
effective pixel size dx_{eff} (nm)	{45.40, 46.69, 50.58, 58.37}
number of projections over 180°	720
number of empty beam projections	50
number of darks	20
acquisition time (s)	1

Phase retrieval and tomographic reconstruction

The phase and amplitude of the exit wave is reconstructed from the recorded holograms by phase retrieval, either based on iterative projection algorithms or in some cases direct Fourier-filtering, which enables to obtain a phase or projected electron density map of the cell. Note, that for a biological cell at the given photon energy, absorption can be neglected, and the cell can essentially be regarded as a pure phase object. In this study a nonlinear approach of the contrast transfer function (CTF) was used for phase retrieval [149, 257]. The phase distribution in the object plane $\phi(\mathbf{r}_\perp)$ retrieved by the linear form of the CTF is given by

$$\phi(\mathbf{r}_\perp) = \mathcal{F}^{-1}\left[\frac{\sum_N (\sin(\chi) + \frac{\beta}{\delta}\cos(\chi)) \cdot \mathcal{F}\left[I^{(exp,N)}(\mathbf{r}_\perp) - 1\right]}{\sum_N 2(\sin(\chi) + \frac{\beta}{\delta}\cos(\chi))^2 + \alpha(\mathbf{k}_\perp)}\right] \, ,$$

with natural units $\chi = \frac{\lambda x k_x^2}{4\pi}$ for the (squared) spatial frequencies, measured intensities in the detector plane $I^{(exp)}(\mathbf{r}_\perp)$, $\frac{\beta}{\delta}$ ratio of imaginary and real part of the refractive index n, N indicated the index of the respective distance and a frequency-dependent regularization parameter $\alpha(\mathbf{k}_\perp)$ (lim$_1$ for high and lim$_2$ for low spatial frequencies). The nonlinear approach uses the solution of the CTF as input for an iterative phase

Table 5.5: Phase retrieval parameters for the nonlinear Tikhonov approach of the CTF for the x-ray tomography experiments.

parameter	value
maximum phase shift	0
β/δ-ratio	1/40
$\lim_1$	0.09
$\lim_2$	0

retrieval based on a minimization of the Tikhonov functional [149]. Thus, the accuracy of the reconstructed phase is not less than the results of the CTF. The parameters of the phase retrieval are given in Tab. 5.5.

Before tomographic reconstruction, an alignment of the single projections based on the linogram was performed to correct for a vertical movement of the sample. A ring removal was not necessary since artifacts from oversensitive pixels were reduced from the previous shifting based in the alignment of the linogram. For tomographic reconstruction the ASTRA toolbox was used [248, 262]. Projections in the range where the frame of the SiN window enters the FOV were excluded.

After tomographic reconstruction, the local electron density can be computed from the phase shift induced by each voxel length v as

$$\rho_e(\mathbf{r}) = \frac{\varphi_v(\mathbf{r})}{v\lambda \cdot r_0} \; ,$$

with wavelength λ and r_0 the classical electron radius.

Dose calculation

The dose was calculated using [328, 329]

$$D = \frac{I_0 \tau E_{ph}}{l\rho\Delta x\Delta y},$$

with the total photon flux I_0, the exposure time τ, the energy E_{ph} and the size of the illuminated area $\Delta x\Delta y$ as listed in Tab. 5.1. Cellular samples are commonly described by $H_{50}C_{30}N_9O_{10}S$. For the used experimental parameters this yields a mass density $\rho = 1.35\,\frac{g}{cm^3}$ and a mass attenuation length $l = 7.46\cdot10^{-4}\,m$ [328, 329]. The choice of image acquisition parameters for diffraction experiments was guided by our previous

investigation and simulation of radiation damage [315]. The average dose per shot in the diffraction experiments was $D = 5.3 \cdot 10^5$ Gy. For the holo-tomography, the total dose for a tomography scan with 720 projections an acquisition time of 1 second was estimated to $D = 1.1 \cdot 10^5$ Gy, where the illuminated area $\Delta x \Delta y$ is given by the effective area (FOV) covered by the detector. This shows that the dose of a complete tomographic scan is still lower than a single shot of the diffraction measurements.

5.3 Results and discussion

2D holography of isolated CMs

Figure 5.2 shows single projections for different sample preparations, detectors and magnifications, which were acquired to test contrast and stability imaging conditions. Table 5.3 summarizes the parameters tested for the different sample preparations and beamline configurations. Additionally, an intensity profile highlights the interference fringes originating from phase effects caused by the interface of the cell and the surrounding medium is marked by the red lines in the image. Noise was reduced by averaging the intensities from pixels perpendicular to the lines corresponding to a linewidth of 1 μm. The fringes originating from changes in electron density indicate the holographic nature of image formation, and contain structural information. In Fig. 5.2a a projection of a freeze-dried CM recorded with a single photon counting detector (Eiger 4M) at an effective pixel size of $px_{\text{eff}} = 300$ nm is shown. In this projection the interface between cell and surrounding air dominates the contrast. Besides that, the position of the nucleus can be determined and the signal of the sarcomeric structure starts to appear. For this configuration, the field of view (FOV) is not limited by the detector size (FOV $= px_{\text{eff}} \cdot N_{\text{pixel}}$) but by the illuminated area of the waveguide. Only 351×351 pixels of the detector are shown in the image. In order to go to higher magnifications, the sample-detector distance has to be increased. Since the detector distance cannot exceed the length of the experimental hutch, the sample has to be moved closer to the wave guide. This would be possible for 2d holographic measurements, but since it is the goal to image the 3d structure and therefore the sample has to be rotated, the minimal source-to-sample x_{01} distance is limited by the size of the SiN frame on which the CMs are mounted.

Figure 5.2b shows a projection of the same cell acquired with a fiber coupled sCMOS Camera (LuAG) at an effective pixel size of $px_{\text{eff}} = 24$ nm. In this case the entire
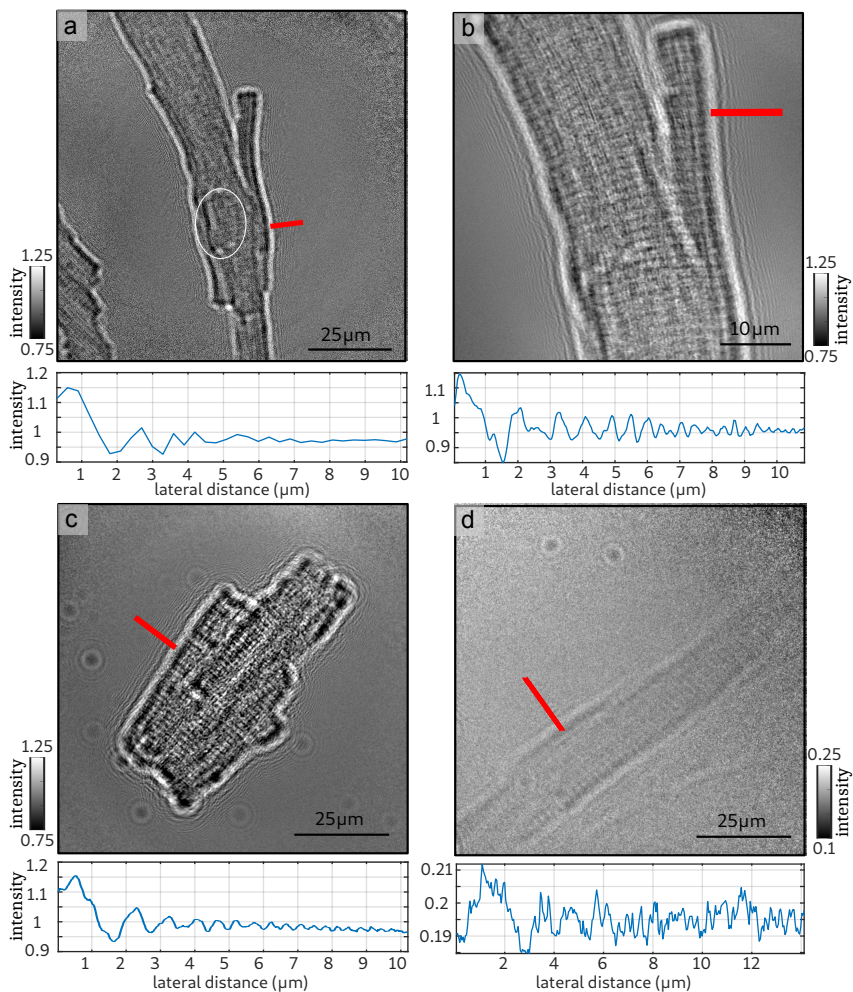
Fig. 5.2: Exemplary projections of the 2D holography measurements. To optimize the imaging conditions, different detectors, magnifications and sample preparations were tested. The red lines mark the area of the intensity profiles shown below each projection. (a) Projection of a freeze-dried CM using a single photon counting detector (Eiger 4M) resulting in an effective pixel size of $px_{\mathrm{eff}} = 300$ nm. (b) Projection of the same CM using a fiber coupled sCMOS Camera (20 μm LuAG) with $px_{\mathrm{eff}} = 24$ nm. (c) Projection of a freeze-dried CM at an effective pixel size of $px_{\mathrm{eff}} = 45$ nm (15 μm Gadox) (d) Projection of a CM stained with 1% OsO_4, embedded in agarose and mounted in a polyimide tube with a diameter of 1 mm.

detector is illuminated and smaller effective pixel sizes can be achieved. The signal from the cellular membrane and also sarcomeric structure is much stronger than in the projection at lower effective pixel size. The fringes around the CM are very clear as also indicated by the profile shown below the projection. At this high magnification only a part of the cell can be imaged due to the relatively small FOV. Further, thermal drift of the sample and vibrations of the setup in the range of a few manometers led to artifacts in the tomographic reconstruction. Fig. 5.2c shows a projection of a freeze-dried CM was acquired at moderate effective pixel size of 45 nm using the sCMOS camera with a 15 μm Gadox scintillator. In this case an entire CM could be imaged within a single projection and the signal emerging from the cell-air interface as well as from the sarcomeric structure can be identified. Since the goal is to image an entire CM we decided to use this beamline configuration for the x-ray tomography.

In a next step, the CM in hydrated condition were investigated. Figure 5.2d shows a projection of a CM stained with 1% OsO_4, embedded in agarose and mounted in a polyimide tube with a diameter of 1 mm. The image was acquired with the same beamline configuration as for the freeze-dried cell shown in Fig. 5.2c. In this case, the signal from the cell is very weak. Note that the quality of the signal is also diminished by the strong absorption from the agarose in the 1 mm tube. In view of the above, tomographic scans were recorded for the freeze-dried sample with the sCMOS (15 μm Gadox) camera at an effective pixel size of 45 nm.

5.3.1 3D structure of a single cardiomyocyte

The 3D structure of the cardiomyocyte was reconstructed by propagation-based phase-contrast tomography in the holographic regime. Figure 5.3 shows the results of the 3D cellular structure. For all projections phase retrieval was performed by the nonlinear Tikhonov approach of the CTF as explained above. An example for a projection and the corresponding reconstruction by phase retrieval is shown in Fig. 5.3a. The sarcomeric structure is clearly visible. The brighter stripes with a lower phase shift, perpendicular to the orientation of the cell correspond to cellular structures with a lower electron density and probably indicate the M-line of the sarcomere. Based on the phase retrieved projections, tomographic reconstruction was performed. Figure 5.3b shows a volume rendering of the entire CM. The total volume of the cell was determined to about 16200 μm^3. A slice of the reconstructed 3d electron density is shown in Fig. 5.3c. Sub-cellular structures of the CM are resolved. In the case of this cell, we have two nuclei instead of just one nucleus, see white arrows in Fig. 5.3c. Both
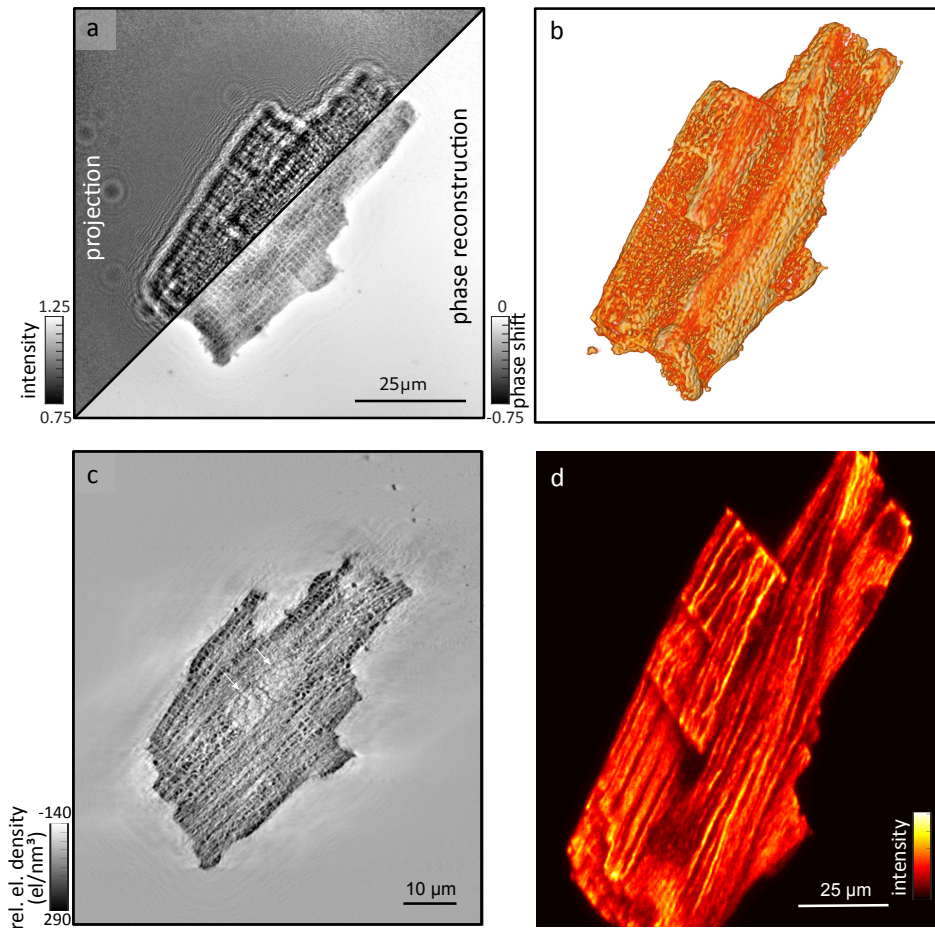
Fig. 5.3: Phase retrieval and reconstruction. For each of the 720 angular positions, phase retrieval was performed based on the projections acquired at different Fresnel numbers. An exemplary projection and the corresponding phase retrieval is shown in (a). The 3d structure was reconstructed by the inverse radon transform. A volume rendering of the CM is shown in (b). A 2d slice though the reconstructed volume is shown in (c). While arrows indicate nuclei. Sub-cellular structures such as the nuclei, mitochondria and myofibrils can be identified. Further, the fluorescently labeled actin skeleton of the same cell was imaged by a confocal scan. A maximum projection of the microscopy stack is shown in (d).

are located in the center of the cell. Further, the myofibrils and the sarcomeric struc-
ture can be identified. Between the elongated myofibrils small dense organelles with
a diameter of roughly 500 nm are visible. As justified further below, these structures
can be attributed to mitochondria, which are known to be abundant in CMs, provid-
ing the required energy for force generation/contraction. They are arranged in chains
next to the myofibrils. Within the range of one sarcomere the mitochondria frequently
appear in pairs of two elongated blobs. Figure 5.3d shows a maximum projection of
the 3d confocal microscopy stack. The actin skeleton was fluorescently labeled and
the orientation and position of the elongated actin structures indicate that fibers of 3d
electron density correspond to the actomyosin filaments (myofibrils) of the CM.

5.3.2 Segmentation of mitochondria

The dense structures observed in the electron density can be attributed to mitochon-
dria for several reasons. First, mitochondria exhibit a high electron density close to
that of a protein crystal [330] and therefore appear as dark structures compared to the
surrounding actomyosin in the reconstruction . Second, they are of elliptical shape
with a diameter in the range of 0.5-1 μm [331]. Third, they are located next to the
elongated myofibrils, as already known from histological observations and 2d elec-
tron microscopy images of healthy cardiomyocytes [332]. Most importantly, apart
from the actomyosin which appears in form of the expected sarcomeric and myofib-
rilar structure in the reconstruction, there is no equally abundant organelle in CMs
which could explain this additional structure.

The segmentation of the mitochondria was performed using a software designed for
the analysis of 3d (fluorescence) microscopy and tomography data sets (Vision 4D,
arivis AG, Munich, Germany). To this end, the 3d volume from the x-ray tomography
analysis was converted to a 8 bit .tif stack and loaded into the program. Using a
'blobfinder' tool, roundish structures can be identified. For the present data set a
characteristic size of 12 px $\hat{=}$ 520 nm was chosen, which fits well to the size of murine
mitochondria. After this step more than 45 000 blobs, which could be associated to mi-
tochondria, parts of the sarcomeres, membrane residues and other sub-cellular com-
partments, were tracked. Next, false positive blobs were removed by thresholding the
minimal volume to a minimal voxel count of 500 voxels per detected volume. This vol-
ume corresponds to a perfect sphere with a radius of 5 px (225 nm). Further selection
of the mitochondria was done by a threshold in density. Only blobs containing voxels
with at least 100 electrons/nm^3 were included. As a result of this analysis pipeline, 14
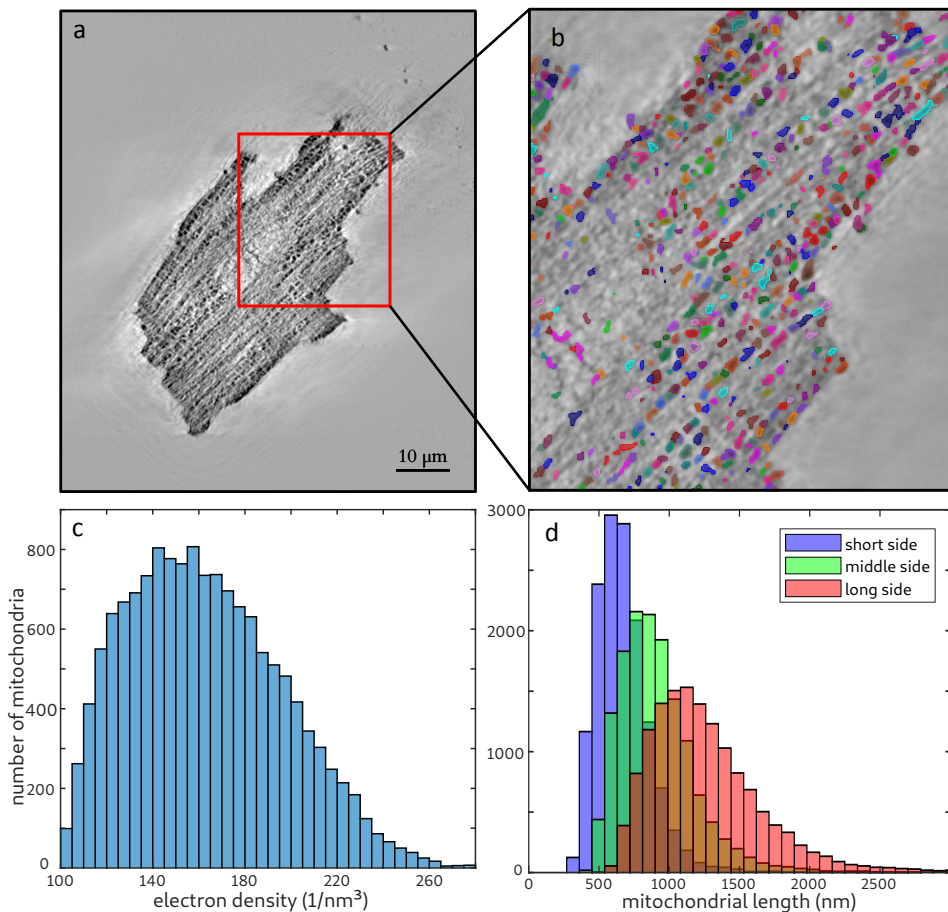
Fig. 5.4: Mitochondria were segmented based on the reconstructed 3d electron density of the CM. We used an image processing software (Vision 4D, arivis AG, Munich, Germany) developed for microscopy data. The dense roundish mitochondria were identified by a 'blob-finder' algorithm and a threshold in size and density. In (a) one slice from the tomographic reconstruction is shown. In order to visualize the quality of the data analysis a magnification of the area marked with a red box and the corresponding segmentation is shown in (b). The segmentation is colorized in a random color to distinguish neighboring mitochondria. Based on the segmented data from the entire volume further analysis can be performed. In (c) a histogram of the maximal electron density of the segmented mitochondria is shown. (d) Distribution of the short (blue), medium (green) and long (red) axis of the segmentation. From this information the diameter and length of an average mitochondrium can be calculated.

334 blobs matching the size and position of the mitochondria remained, which corresponds to an estimated average density of about 0.88 mitochondria per μm^3.

Figure 5.4 shows the results of the segmentation. The mitochondria appear as small dark spots in the slice of the reconstructed electron density shown in Fig. 5.4a. The red box marks an area for which the quality of the segmentation is shown in Fig. 5.4b. The segmented mitochondria of this slice are shown in random color, in order to facilitate to distinguish between neighbors. In the area at the bottom of the slice, two mitochondria can be assigned for each sarcomere (from M-line to M-line). Based on this segmentation of the entire 3d volume, the electron density of all mitochndria was analyzed. A histogram of the extracted electron density is shown in Fig. 5.4c. From this distribution a mean electron density of freeze-dried mitochondria was determined to 162 el/nm^3. Further, the size of the mitochondria can be quantified by the length of the segmented volumes along its main axis. The short, middle and long side of segmented blobs are shown in Fig. 5.4d. From this distribution, the diameter and length of the elipsoid-shaped mitochondria can be extracted. The peak in the histogram of the short axis (blue) corresponds to an diameter of 585 nm, while the long side (red) has a peak for a length of 1125 nm. For the short side a small increase can also be seen at about 1200 nm, and also for the medium and long axis an increase in the range of the double length of the peak can be identified. This increase can be explained by a pooling of neighboring mitochondria as one selection. Thus, we conclude that the total number of mitochondria is underrated. The mean volume of a mitochondrium was determined to 0.23 μm^3. The smaller size of the mitochondria may result from a volume change at the mitochondrial level during the sample preparation. The volume fraction was determined to about 20% by comparing the sum of mitochondria volume to the total cell volume. Considering the shrinking of the mitochondrial level by a factor of approximately 2, these results are consistent with a volume fraction between 29% and 36% in the literature. Besides analysis of density, size and shape of mitochondria, this analysis yields the location of the mitochondria in the cell.

5.3.3 Characterization of the actomyosin lattice

The molecular structure of heart tissue cells was analyzed by scanning x-ray diffraction. Figure 5.5 shows a typical result for scanning diffraction from freeze-dried CMs, using a microfocus beam. We include this example for comparison with the live recordings below. As becomes immediately evident, the x-ray darkfield signal is particularly strong in this case. Furthermore, freeze-dried CMs can be imaged with rel-

atively high sampling in real space, since less free radicals are produced in the absence of water/buffer. More importantly, free radicals do not spread by diffusion as in hydrated environments [315]. In Fig. 5.5a, an optical micrograph of (fluorescently labeled) freeze-dried CMs taken by the beamline on-axis video microscope (OAV) is shown. The cells are clearly visible in bright field contrast. Using the live images of the OAV, the samples were aligned for the x-ray diffraction measurements. An example for an x-ray darkfield image from the analysis of freeze-dried cells is shown in Fig. 5.5b. Pixels with an intensity below $1.5 \cdot 10^6$ counts were masked in white. The step size was $2\,\mu$m, the acquisition time 0.05 s. In Fig. 5.5c, an isolated diffraction
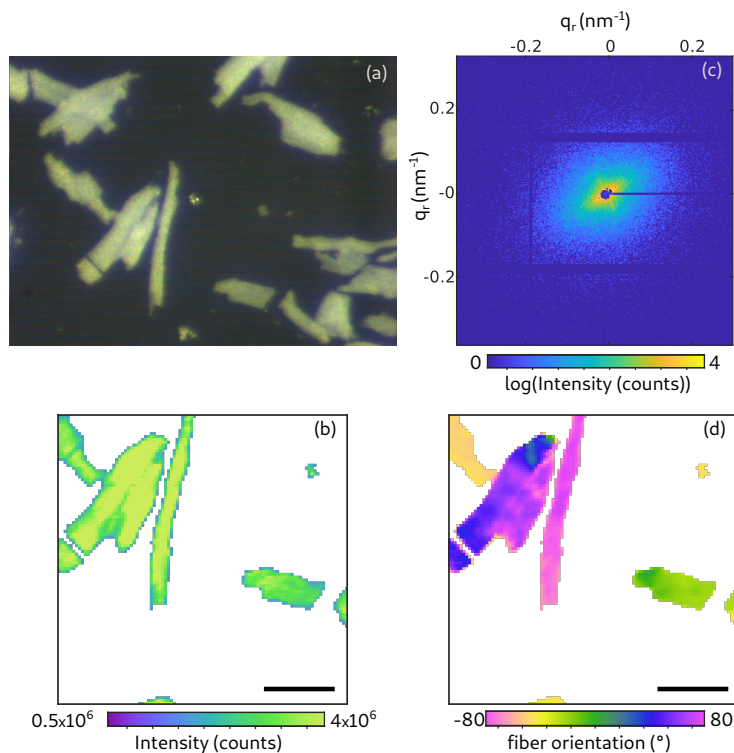
Fig. 5.5: Scanning diffraction from freeze-dried CMs. (a) Micrograph recorded with the beamline on-axis optical microscope (brightfield). (b) X-ray darkfield image. The image is formed by integration of all detector counts (outside the beamstop), i.e. the integrated scattering signal. Pixels with an intensity below $1.5 \cdot 10^6$ counts are masked in white. Scale bar: $50\,\mu$m. (c) Isolated diffraction pattern of a single shot on a freeze-dried cell (0.05 s accumulation time). (d) Orientation of the acto-myosin fibrils.

pattern is shown, representing a single shot from the freeze-dried cells. There are no actomyosin reflections visible in the diffraction pattern, indicating that the structure of the cells is damaged by freeze drying. The diffraction pattern shows an anisotropy which makes it nevertheless possible to determine the local actomyosin fibril orientation. The fiber orientation and anisotropy, shown in Fig. 5.5d, is obtained from an automatized principal component analysis (PCA) in the same way as in [227, 236]. In order to improve the quality of the diffraction data, we turn to recordings of hydrated and living cells using a polypropylene chamber. In view of radiation damage, a 'diffract before damage' strategy is adopted [315].
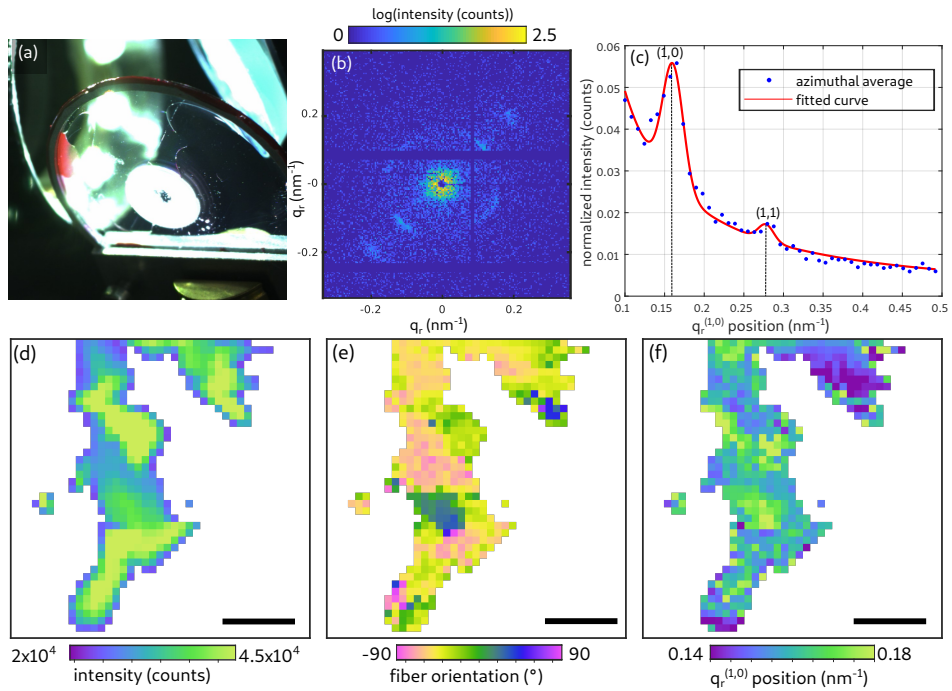
Fig. 5.6: Signal processing of scanning diffraction data: living CMs. (a) Photograph of the sample chamber used for measuring living CMs. (b) Diffraction pattern of a living muscle cell. The (1,0) and the (1,1) reflection is visible in the pattern. (c) 1d azimuthal average of the diffraction pattern on the left. The fitted curve was obtained using the fitting function introduced in Equation 5.3.3. (d) Darkfield map of a cluster of living cells. Scale bar: $50\,\mu$m. (e) Orientation of the myosin fibers obtained by performing a principal component analysis. (f) Position of the (1,0) reflection obtained from the fitted curves. In (c)-(e) all pixels, with a darkfield intensity below $2 \cdot 10^4$ counts were masked in white.

Figure 5.6 illustrates the data collection and processing, which closely followed [226], but now applied to living cells. We also took into account the constraints of sparse sampling and reduced dose to collect a signal which is not spoiled by radiation damage [315]. For data analysis, the nanodiffraction-toolbox [227] was used. In Fig. 5.6a the liquid chamber used for the measurement of living CMs is shown. Figure 5.6b shows the example of an isolated diffraction pattern recorded by a single shot. The acquisition time was 0.1 s. In contrast to the freeze-dried CMs, the signal of the living CM shows clearly both the (1,0) and the (1,1) reflection in the diffraction pattern. The cells were raster scanned with a step size of 5 μm, yielding a coarse darkfield map of the scanned CMs. An example for such a map can be seen in Fig. 5.6d. Note, that the background in the map is colored in white based on a threshold of minimum photon counts. Next, each diffraction pattern above this threshold was azimuthally averaged and a mean background was subtracted to obtain a local SAXS curve. The model function

$$I(q_r) = A q_r^{-B} + C \exp\left(\left(\frac{q_r - q^{(1,0)}}{\sigma}\right)^2\right) + D \exp\left(\left(\frac{q_r - \sqrt{3}q^{(1,0)}}{\sigma}\right)^2\right) + E$$

was fitted to this data, where $A - E$ and $q^{(1,0)}$ are fit parameters. While $A \cdot q_r^{-B}$ describes a monotonous SAXS contribution, the actomyosin reflections are modeled as Gaussians with amplitudes C and D and positions $q^{(1,0)}$ and $q^{(1,1)}$. Note that the relation $q_r^{(1,1)} = \sqrt{3}q_r^{(1,0)}$ was used to obtain the position of the (1,1) reflection. The reflection width was set to $\sigma = 0.0184$ nm^{-1}. An example of this fit for the isolated shot can be seen in Fig. 5.6c. This fit yields the position of the (1,0) position. In Fig. 5.6f the $q^{(1,0)}$ reflection positions of the sample are plotted. Using PCA, the fiber orientation was determined for the diffraction pattern for all scan points. An example for the fiber orientation is shown in Fig. 5.6e.

For comparison to the living CM, we also investigated chemically fixed, hydrated cardiac tissue cells. Figure 5.7a shows an example for a darkfield map of such a recording. Multiple scan areas covered by continuous piezo scanning, each with a size of $200 \times 200\,\mu$m^2 and an acquisition time of 0.05 s per scan point, were stitched using a stepper motor below the piezo. The entire composite with 5×5 piezo scans results in the darkfield map in Fig. 5.7a. The different scans areas are indicated by boxes. The acquisition time for each scan point was 0.05 s. In Fig. 5.7b, a zoom of the marked box in (a) is shown. In Fig. 5.7c the calculated fiber orientation of this region is plotted. The data shows, that the fiber orientation throughout a cell is roughly constant. An
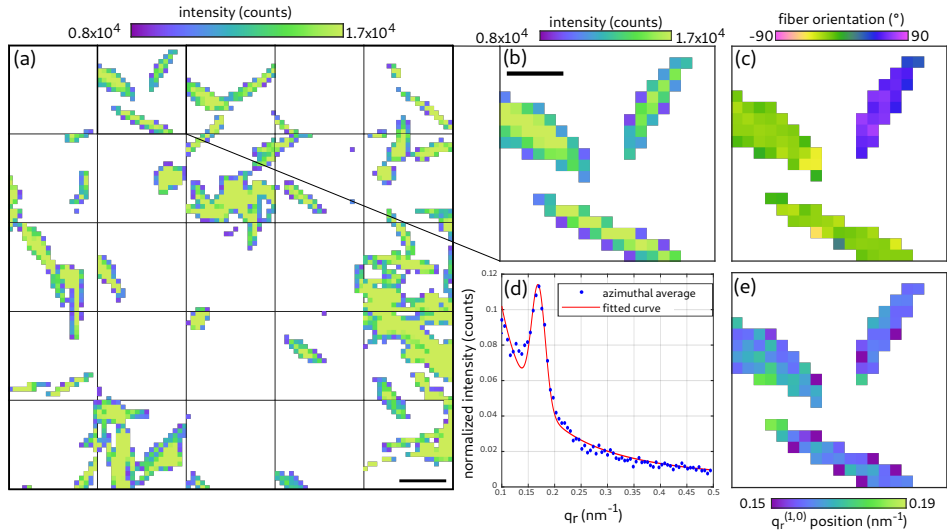
Fig. 5.7: Scanning diffraction: hydrated and chemically fixed CMs. (a,b) Darkfield maps of isolated, fixed cardiomyocytes. Scale bar: (a) $100\,\mu$m, (b) $50\,\mu$m. (c) Orientation map of the actomyosin fibrils. (d) 1d azimuthal average of a single shot from a fixed cardiomyocyte. In contrast to Fig. 5.6 (c) only the (1,0) reflection is visible. (e) Position of the (1,0) reflection. All pixels with a darkfield intensity below $0.8 \cdot 10^4$ counts were masked in white.

example for an azimuthal average of a single diffraction pattern of a chemically fixed cell is shown in Fig. 5.7d. Only the first peak representing the (1,0) reflection is visible. This was the case for all shots recorded from all chemically fixed cells. Therefore, the signal of the (1,1) reflection was excluded for the fit of the fixed cells. The results for the $q_r^{(1,0)}$ position for one region of the map shown in Fig. 5.7e.

Next, we turn to the recordings of living cells, which are displayed in Fig. 5.8. These cells were in an initially living state as one could derive from their contraction inside the sample chamber before the measurement. However, one has to keep in mind the challenging issue of radiation damage arising during data acquisition which will have a considerable effect on cellular structures. Thus, we can only claim that the cells are living initially at the beginning of the scan or when recording shots from a new cell. In Fig. 5.8a a darkfield map of a cluster of living CMs is depicted; the same which was already shown before when explaining the workflow. The boxes marked in in the map of the darkfield signal are represented in detailed view in Fig. 5.8b-d . For the three areas, the amplitude of the first peak representing the (1,0) reflection is shown in (1).
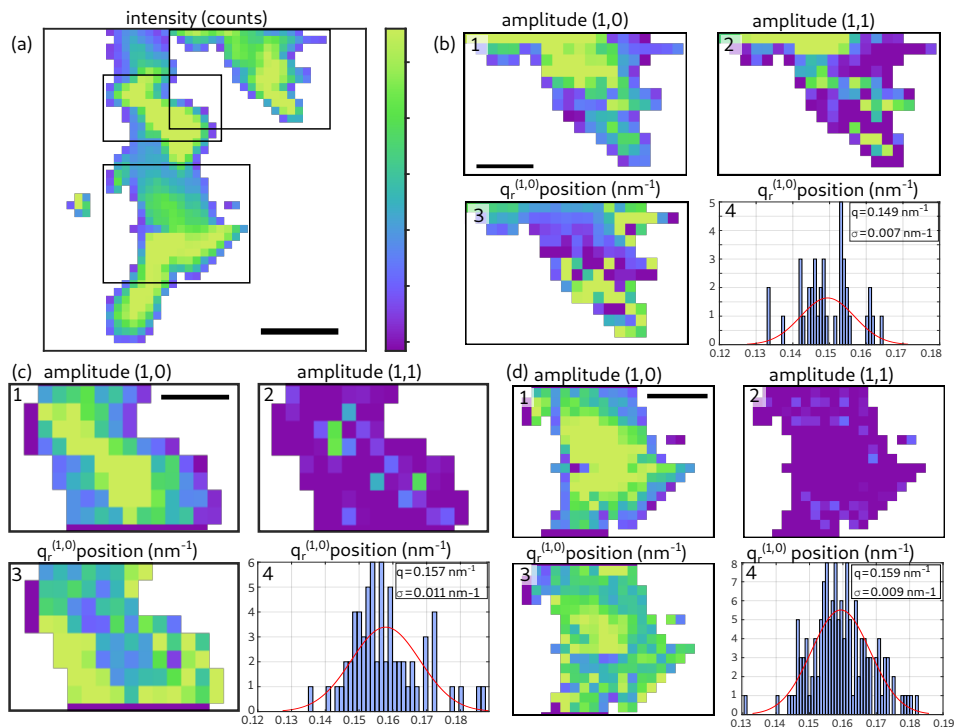
Fig. 5.8: Scanning diffraction: living CMs. (a) Darkfield image showing three CM clusters magnified in (b,d and d). Scale bar: $50\,\mu$m, colorbar: linear range $2 \cdot 10^4$- $4.5 \cdot 10^4$ counts. In all figures pixels with a darkfield intensity below $2 \cdot 10^4$ counts where masked in white. The structural parameters of the actomyosin lattice were calculated, namely 1. amplitude of the (1,0) reflection, 2. amplitude of the (1,1) reflection, 3. $q_r^{(1,0)}$-lattice spacing and 4. histogram of the $q_r^{(1,0)}$ position. (1) Scale bar: $25\,\mu$m, colorbar: linear range 0 - 0.1 counts/pixel. (2) Colorbar: linear range $0.5 \cdot 10^{-3}$- $4 \cdot 10^{-3}$ counts/pixel. (3) Colorbar: linear range 0.14 nm- 0.18 nm^{-1}. (4) In area (b) only shots where two peaks are visible, contributed to the histogram.

The first peak was visible in all observed boxes. On the contrary, this is not the case for the amplitude of the second peak representing the (1,1) reflection which is shown in (2). The harmful effect of radiation damage can be observed by the loss of (1,1) reflection signal which is visible in the first few lines of the first area (Fig. 5.8b.2). In this region, the signal of the (1,1) reflection is clearly visible in the first scan points, but then vanished. This observation is consistent with previous observations on muscle tissue, where the intensity of the second peak vanished when tissue was affected by radiation damage [315]. Here we also observe that the intensity of the second peak

decreases, indicating that living cells are strongly affected by radiation damage. This signal decrease is plausible, since the scan points were acquired row by row from top left to bottom right, and free radicals spread easily during the scan. Hence, for the first region, the concentration of free radicals was lower, and less time was available for their diffusion or for an apototic reaction of the cells. The map of the (1,1) peak amplitude also shows that the intensity decreases line-by-line.

The q-spacing of the the actomyosin lattice was evaluated for the entire dataset. The subfigures with index (3) show the map for the q-spacing of the different areas. Boxes with index (4) show the distribution of the q-spacing (histogram). In Fig. 5.8b.4 only shots with two visible peaks were selected for the histogram. In Fig. 5.8c.4, and Fig. 5.8d.4 only shots with one peak contributed to the histogram. A Gaussian was fitted to every histogram to obtain the mean and standard deviation. The analysis of the histograms shows that the q-spacing for the first box ($q = 0.149 \pm 0.007\,\mathrm{nm}^{-1}$) is smaller than the q-spacing in box (c) ($q = 0.157 \pm 0.011\,\mathrm{nm}^{-1}$) and box (d) ($q = 0.159 \pm 0.009\,\mathrm{nm}^{-1}$). This leads us to the conclude that the q-spacing increases when the cells are affected by radiation damage. Since the presented scans were also partly affected by damage as inferred from the decrease of the (1,1) peak, we adapted our measurement strategy, and in addition to the scans also took diffraction pattern from isolated points within the CMs, moving to new cells for each shot.

Finally, the violin plot in Fig. 5.9 compares the distribution of the q-spacing for (initially) living, hydrated CMs and CMs, which were chemically fixed. In fixed CMs, only the (1,0) reflection was visible in the diffraction pattern. For the characterization of living cells, the diffraction patterns from the data already seen in 5.8, as well as additional single shots from freshly prepared samples were used. Only patterns with two visible peaks were used for the calculation of the lattice spacing of living CMs. The q-spacing determined for fixed cells is larger than the one found for the living cells. To quantify the mean and standard deviation, Gaussians were fitted to the distributions. The horizontal lines in the violin plot indicate the mean value. For living CMs a q-spacing of $q = 0.148 \pm 0.006\,\mathrm{nm}^{-1}$ and for chemically fixed CMs $q = 0.167 \pm 0.006\,\mathrm{nm}^{-1}$ was obtained. The corresponding actomyosin lattice spacing $d^{(1,0)} = \frac{2\pi}{q^{(1,0)}}$ was $37.6\,\mathrm{nm}$ and $42.5\,\mathrm{nm}$, for the fixed and living cells, respectively.
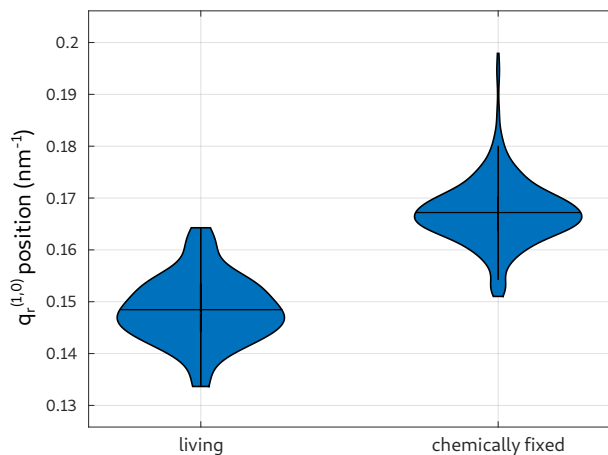
Fig. 5.9: Actomyosin lattice spacings. Distribution of the lattice spacing obtained by the position of the $q_r^{(1,0)}$ reflection for living and chemically fixed CMs. The horizontal lines in the violin plot indicate the mean value of the q-spacing. The corresponding actomyosin lattice spacing determined to $37.6\,\text{nm}$ for chemically fixed CMs and $42.5\,\text{nm}$ for living cells.

5.4 Summary and conclusion

In this work, we have combined full-field 3d coherent x-ray imaging and scanning x-ray diffraction to analyze the cellular and molecular structure of isolated adult CMs of wild type mice. The 3d electron density distribution of a single CM was reconstructed from propagation-based x-ray phase contrast tomography with a voxel size smaller than $50\,\text{nm}$. Single myofibrils, the sarcomeric organization and location of mitochondria were visualized within a single cell without sectioning. The molecular structure of the actomyosin lattice was probed by scanning x-ray diffraction, using CRLs for micro-focusing.

For the first time, the diffraction signal of the acto-myosing contractile unit could be observed for living cells. Importantly, while previous recordings of living cells only showed a monotonous decay of the SAXS signal [230], the diffraction signal of CMs shows characteristic peaks which can be fitted to determine the actomyosin lattice spacing. A comparison between living cell and chemically fixed cell recordings indicates that the characteristic lattice distances (d_{10}) shrink by approximately 10% upon fixation, namely from $42.5\,\text{nm}$ to $37.6\,\text{nm}$ in the $(1, 0)$ lattice planes. The values fall into the range reported in the literature for rodent cardiac muscle (rat trabecula), i.e.

$42.5\,\text{nm} - 44.5\,\text{nm}$ and $34\,\text{nm} - 36\,\text{nm}$ reported in [265] for relaxed (skinned) and intact (unskinned) trabecula, respectively, and $38\,\text{nm}$ reported in [304].

Despite its merit in extending diffraction analysis to living CMs, the present study also indicated limitations of this approach, imposed by radiation damage and low signal-to-noise. For future work, it would be desirable to probe different states of contraction, eventually in combination with well controlled forces acting on the cell. To this end, only isolated shots in fresh spots should be collected, guided by online light microscopy, and correlated with the contraction state. Continuous replenishment of samples and washing out of free radicals could be achieved by suitable microfluidic devices. Finally, high throughput lattice parameter determination at the single cell level, eventually in form of 'diffraction flow cytometry' could be used as a diagnostic tool for dissociated tissue. To this end, genes regulating actomyosin structure in patient-derived stem cells would be targets of particular interest [333]. Concerning the tomography, investigations of hydrated or even living cells seem very challenging based on our present results. Frozen hydrated (vitrified) cells after plunge freezing [231, 232, 318, 334, 335], however, could be a suitable approach to probe the native structure in 3d. In this study, we could for example determine an average density of about 0.88 mitochondria per μm^3 as well as the average size of a mitochondrium in such a CM. A number of technical improvements can also be foreseen: a small glass tube with thin walls and a hydrogel could provide stability for single cells and minimize absorption. The sample could be moved closer to source spot for higher magnification and single photon counting pixel detectors with higher quantum efficiency could be used. Concerning the sequence of correlative imaging of the same cell, it is important to first perform optical fluorescence microscopy, second holo-tomography, and finally diffraction, in view of mitigating the radiation damage. The final state could then be probed again by optical microscopy to evaluate damage.

Acknowledgments

Summary and outlook

<div style="text-align: right">6</div>

This thesis has investigated the structure of cardiac tissue on multiple length scales. We could show, that propagation-based X-ray phase-contrast tomography is a technique which enables the reconstruction of the 3d structure of the heart. For laboratory measurements, we have compared multiple sample preparation methods and were able to image the structure of entire murine hearts at a resolution of about 5 μm. In order to characterize the arrangement of the cardiac structure, we have developed a novel Fourier-analysis-based algorithm, which yields the local structural orientation as well as the degree of alignment and the distance between the main features within a small subvolume. Using highly coherent synchrotron radiation, we have investigated the cardiac structure in a multiscale approach. The experimental setups allow to record tomograms at different magnifications and enable to investigate the 3d cardiac structure from the scale of the organ down to sub-cellular features. We could show that this imaging approach also enables the characterization of pathological alterations caused by diseases such as Covid-19. Furthermore, we have investigated the structure of isolated cardiomyocytes using X-ray phase-contrast tomography and scanning X-ray diffraction. In the 3d reconstruction of the electron density subcellular features such as the nucleus, myofibrils and mitochondria were resolved for a freeze-dried cardiomyocyte at a voxelsize of less than 50 nm. The image quality enabled a segmentation of mitochondria within the cell. Additionally, the pristine structure of the actomyosin lattice of isolated cardiomyocytes was probed for the first time in an *ex vitro* scanning X-ray diffraction experiment.

In order to achieve these results, sample preparation protocols, experimental parameters and imaging setups were evaluated and optimized for both imaging modalities. In the following, the main findings of this work as well as preliminary results of followup experiments and future possibilities for structural investigations of cardiac tissue are briefly addressed.

6.1 Structural analysis of cardiac cells and tissue on the nanoscale

In proof-of-concept experiment, presented in chapter 5, we have investigated the structure of isolated cardiomyocytes using a multimodal X-ray imaging approach. We have combined scanning SAXS with confocal fluorescence imaging and high resolution X-ray tomography of freeze-dried cardiomyocytes. While the fluorescent dye could show the structure of the cytoskeleton, the entire 3d information of the electron density distribution within the cell was obtained by X-ray tomography. Based on the 3d reconstruction, the location of subcellular structures, such as mitochondria, was determined. Furthermore, we have investigated the actomyosin lattice spacing of cardiomyocytes in buffer solution using scanning X-ray diffraction. We were able to record X-ray diffraction patterns of living cardiomyocytes in buffer solution for the first time. Thus, the pristine structure of the actomyosin lattice was observed. In previous scanning SAXS experiments the strong influence of the choice of the chemical fixative on the molecular actomyosin arrangement was shown [226]. Now we could show that the lattice spacing of living cardiomyocytes is approximately 10% larger compared to chemically fixed cells.

The sample preparation and experimental setup presented in this work, pave the way for followup experiments. For instance, the work can be extended to *in vivo* investigations of contracting cardiomyocytes. Furthermore, the imaging schemes can be transferred to investigations of engineered muscle tissue. Scanning SAXS allows to probe the molecular actomyosin structure of engineered heart muscle (EHM) and to investigate structural changes due to drug treatment [336]. First scanning diffraction experiments of EHM were already performed. However, due to the immature state of the cells and the small X-ray spot size, the diffraction signal of the actomyosin lattice was quite low [226]. Nonetheless, progress in development of EHM patches of more mature cells gives hope for a detailed structural analysis [337, 338]. Furthermore, the structural changes of the sarcomeric structure caused by genetic diseases such as Duchenne Muscle dystrophy could be investigated in a follow up experiment. To this end, the impact of possible treatment involving genetic modifications using CRISPR(clustered regularly interspaced short palindromic repeats)/Cas9 could also be analyzed [339]. It is also conceivable to perform X-ray diffraction experiments on cardiac biopsies obtained during surgery in order to investigate the molecular structure and to introduce an additional readout to extend conventional clinical observa-

tions. Figure 6.1 shows preliminary results from a scanning SAXS experiments on human atrial appendage tissue slices conducted at the GINIX endstation of the P10 beamline (PETRAIII storage ring, DESY, Hambug) [340]. An averaged diffraction pattern as well as the integrated angular signal is shown in the top row Fig. 6.1. A strong signal of the oriented actomyosin reflex as well as a signal resulting from the collagen structure was observed. The lower part of the figure shows the local signal caused by the myofilaments (C) and the collagen fibers (E) as well as the corresponding orientations of the structures. It is possible to analyze actomyosin structure of human tissue and to calculate the local actomyosin-to-collagen ratio. Furthermore, the structural results can be correlated to cardiac functionality of the patients. In this way, pathologies of the sarcomeric structure can be characterized in higher detail.

However, before the procedure can be used for for diagnostic purposes, a database has to be created in order to categorize the results. Therefore, the entire 3d molecular structure of muscle tissue from healthy as well as pathological samples has to be understood.

The 3d vectorfield of structured biological samples can be investigated by scanning SAXS tomography. To this end, the sample is rotated and 2d scanning SAXS maps are acquired for multiple angular positions. Scanning SAXS tomography data was already recorded from wood, bone and tooth samples [341–344]. So far, the long acquisition time and the associated radiation-induced damage do not allow to investigate for soft biological tissue. One possibility to overcome this problem is to extend the beam size and thus relax spacial resolution [315]. In future experiments, scanning SAXS tomography analysis of soft tissue samples, such as cardiac biopsies, could be possible in combination with cryogenic sample preparation, as currently also developed for 3d electron microscopy [345–349].

In summary, X-ray diffraction is an excellent technique to analyze the periodic components of the muscle structure such as the actomyosin lattice. The diffraction patterns yield information on inter-molecular distances as well as structural orientation. However, it is not possible to investigate the 3d structural information directly. The arrangement of structures, such as mitochondria and nuclei which are not periodically arranged, cannot be reconstructed if the illuminated area extends the size of the cell. Therefore, X-ray diffraction is often combined with complementary techniques. In this work, we could show that it is possible to investigate the 3d structure of single cardiomyocytes using X-ray phase-contrast tomography. In the following, results of 3d histological investigations on the tissue and organ scale will be discussed.
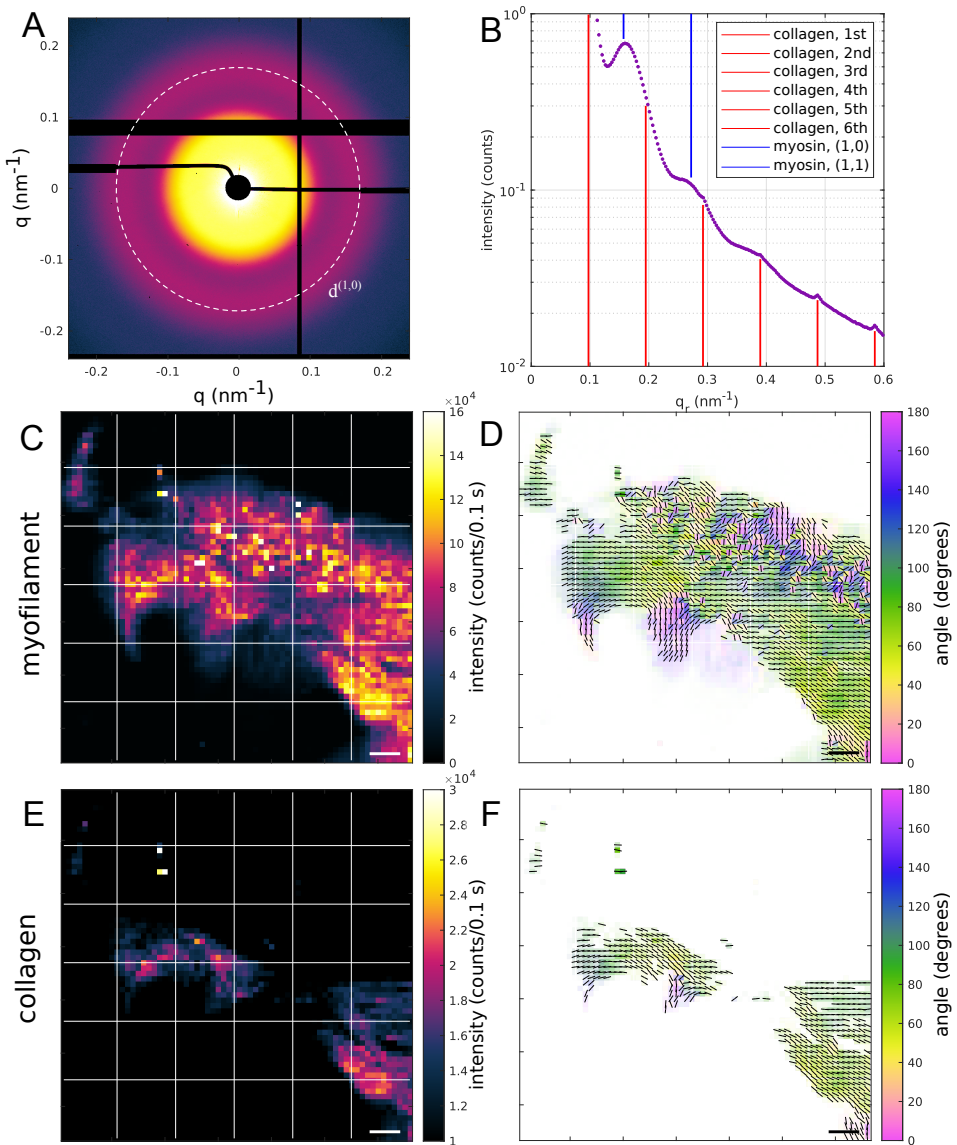
Fig. 6.1: Scanning small angle X-ray scattering on human tissue. (A) Averaged X-ray diffraction pattern of human atrial appendage tissue. (B) Angular average of the diffraction pattern. The myofibril signal as well as the reflexes of collagen can be identified. (C) Map of the integrated intensity of the muscle signal. (D) Corresponding orientation of the myofiber. (E) Map of the integrated intensity of the muscle signal. (F) Corresponding orientation of the collagen alignment. Scale bars: 100 μm [340].

6.2 Laboratory X-ray phase-contrast tomography of entire murine hearts

Using a laboratory X-ray phase-contrast tomography setup, presented in chapter 2, the 3d structure of entire murine heart tissue was investigated. We could show, that the image quality of tomographic reconstructions of samples embedded in paraffin or prepared by the evaporation of solvent (EOS) method is sufficient to identify the cardiac structures. The use of high-Z element stains is not necessary. On the contrary, diffusion related stainig artefacts might alter the tissue properties and lead to inconsistent results. Contrarily, a specific labeling or rather the development of X-ray immunostains would facilitate the identification of different cell types. Follow up experiments to this work, could include the investigation of the cardiac conduction system using heavy ion labeling, e.g provided by the India Ink stain for ungulate hearts [350].

Furthermore, in this work a novel approach to characterize the structural organization was presented. The Fourier-space-based analysis delivers the local structural orientation as well as the degree of alignment. The performance of this method was compared to a gradient-based algorithm, which was already established for the characterization of cardiac structure [185]. The Matlab implementation of both approaches is given in Appendix A.2. While the resulting orientations are practically the same for both approaches, our novel analysis additionally allows to identify characteristic distances, corresponding to the spacing between the tissue structures. The functionality of the algorithm was shown for a murine heart prepared by the EOS method. This method increases the contrast by dehydration and thus leads to organ shrinking and detachment of the cells. So far, it is not possible to investigate the native cardiac structure with high detail using laboratory X-ray sources. In order to analyze unstained, tissue in solution with subcellular resolution, the high coherent illumination provided by X-ray radiation facilities is needed.

6.3 X-ray phase-contrast tomography of cardiac tissue using synchrotron radiation

The publication presented in chapter 3 introduces a multiscale imaging approach to analyze the 3d structure of murine hearts using synchrotron radiation. Using a diffraction broadened X-ray beam behind a nanofocus, overview scans with a field of view

extending the primary beam emitted by the undulator can be acquired. In parallel
beam geometry, region of interest were probed with a voxelsize of 650 nm. The tomo-
graphic reconstructions allow to investigate the 3d cardiac structure on a subcellular
level. Furthermore, 3d molecular structures as myofibrils were resolved using a cone
beam waveguide illumination. Reconstructions of paraffin embedded samples as well
as tissue stored in ethanol were presented. The structural arrangement was probed by
the algorithm described above.

Using a multiscale X-ray imaging approach, 3d structural changes caused by cardio-
vascular diseases can be investigated. In a followup experiment, similar to a study
recently published by Planinc et. al.[197], we investigated structural changes caused
by cardiovascular and genetic pathologies in hydrated conditions. Datasets of entire
murine hearts were acquired at a voxelsize of 2.8 μm and regions of interest were
probed at 650 nm voxelsize. Preliminary results are shown in Fig. 6.2 [351, 352]. Based
on the overview scans, the myocyte orientation as well as the anisotropy were deter-
mined. Furthermore, structural changes of the 3d tissue, such as a thinning of the
left ventricle wall or changes in ventricular load, can be observed. The high resolu-
tion recording in combination with phase reconstruction shows a different contrast
for individual cells within the heart, as shown in Fig. 6.2. In contrast to the results
of Planinc et. al. the quality of the tomographic data allows to segment individual
cardiomyocytes automatically. Thus, structural properties of single cells, such as size,
orientation or mean electron density, can be characterized without manual segmen-
tation for the entire reconstruction.

The concept of 3d virtual histology can be transferred to different samples without
further restrictions. In chapter 4, the 3d structure of cardiac biopsies of patients who
succumbed to Covid-19, influenza or coxackie myocarditis was probed. Based on lab-
oratory recordings, the structural arrangement of the tissue was analyzed.

Furthermore, tomographic reconstructions of control and Covid-19 samples acquired
at the synchrotron allowed for a deep learning-based segmentation of the capillary net-
work. A further analysis of the vasculature using graph theory indicated the synthesis
of new vessels in cardiac tissue of Covid-19 patients. These results were confirmed us-
ing high resolution cone beam tomography. The presence of intraluminar pillars was
observed, indicating the process of intussusceptive angiogenesis, which is a hallmark
for Covid-19. These results were further supported by scanning electron microscopy
micrographs.

The destruction- and label-free concept of multiscale 3d virtual histology presented
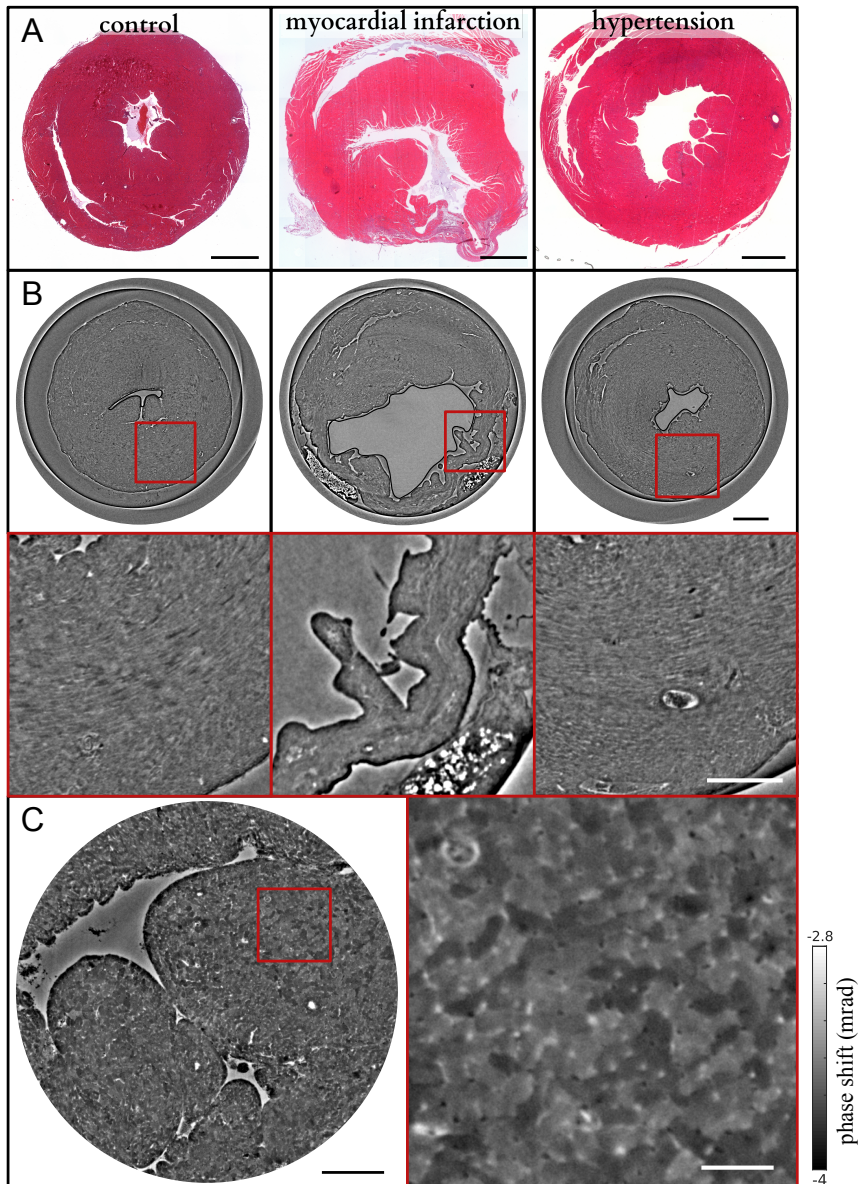
Fig. 6.2: X-ray Imaging of cardiac pathologies. (A) HE stain of wild type heart, a mouse model for myocardial infarction and hypertension (B) slices of the tomographic reconstructions acquired at a voxelsize of 2.8 μm. Magnification of the areas marked in red are shown below. (C) For each of the hearts investigated at low resolution, regions of interest were probed at a voxelsize of 650 nm. An exemplary slice of a volume located at the bottom of the left ventricle. In the magnification marked in red, individual cells can be differentiated based on their electron density. Scale bars: (A) 1 mm, (B) 1 mm, magnification 500 μm, (C) 250 μm, magnification 50 μm [351, 352].

in this work can be transferred to investigations of other types of tissue embedded in paraffin at sub-light-microscope resolution. In future, 3d virtual histology can be used to better understand the functions of the organs and the influence of diseases on the 3d tissue structure.

6.4 Future opportunities for phase-contrast tomography of cardiac tissue

In this work, we have demonstrated that propagation-based X-ray phase-contrast tomography enables a destruction-free multiscale imaging approach to analyze the structure of soft tissue such as the heart. It is possible to investigate the 3d structure of the cardiomyocyte arrangement in entire (murine) hearts at laboratory setups as well as the subcellular structure in regions-of-interest using synchrotron radiation.

Future experiments could include investigation of hearts extending the size of small animal models. Recently, we have investigated the structure of chemically fixed macaque hearts stored in buffer solution at a laboratory setup. While the gross anatomy of the organ can be identified in the reconstructions, the contrast is too low to resolve the myocyte arrangement. A solution to this problem can be provided by synchrotron radiation. One issue in large scale X-ray tomography analysis at synchrotron radiation facilities is the limited field of view. In order to image an entire organ a stack of multiple scans has to be acquired and the tomographic reconstructions stitched together [172, 181]. The concept of beam widening using X-ray focusing optics presented in chapter 3 can be used to record projections of larger organs at beamlines available. Currently, a new beamline providing the capability to image larger organs at cellular resolution (BM18) at the ESRF is under construction.

Furthermore, the results of the structural analysis can be used to support simulations of the heart. These computational models can help to understand the cardiac structure and functionality and may allow in future for individual treatment of patients suffering from CVDs. For instance they could help to calculate the optimal positions of future optogenetic pacemakers [44] or deliver important information about the local myofiber orientation, which is needed for the application of engineered heart patches [338, 353, 354]. The first clinical trial treating patients with severe heart failure using heart muscle tissue derived from stem cells started in the scope of the BioVAT-HF-DZHK20 study.

In summary, the multiscale *ex vivo* 3d cardiac imaging approach using X-ray phase-contrast tomography presented in this work allows to characterize the structure of cardiac tissue from the organ scale down to the molecular arrangement of myofibrils.

In future studies, the imaging concept can be extended from static structural analysis to time-resolved, dynamic studies of the heart. First attempts of 3d imaging of a beating (mouse) heart were already performed. Using a laboratory X-ray imaging setup and iodine-based contrast agents, the dynamics of murine hearts was investigated in time-gated 4d studies [355, 356]. However, they lack in resolution and the image quality is insufficient to characterize the structure of the myocardium.

In a future experiment the 3d structure of a beating heart could be analyzed using high flux synchrotron radiation with an extended beamsize in the range of an entire heart. By recording projections of entire, freshly sectioned hearts, connected to a Langendorff perfusion system, the dynamics of cardiac contraction could be studied.

In conclusion, the tools and workflows presented in this work, including image acquisition, phase retrieval and post-processing of the reconstructed volumes, allow for automated investigations of the cardiac structure. Thus, this work contributes to the question how the structural arrangement of individual cells within the heart enables the continuous contractile functionality that the natural sciences address since the era of the ancient Egyptians.

Appendix

<div style="text-align: right; font-size: 3em;">A</div>

The following Matlab codes were developed for the data analysis of this thesis and use functions from the *holotomotoolbox* which was developed in our group [149].

A.1 Matlab code: Phase retrieval using a heart phantom

```matlab
%% load toolbox
addpath(genpath('/home/holotomotoolbox/holotomotoolbox/functions/'));

%% read data
cd('/PathToData')
slices= readraw('EOSHeart_1500x1500x1536.raw','single', [1500 1500 1536]);

%% create 3d Phantom
tic
heart3dPhantom=squeeze(slices>=1e-4 & slices<=3e-4); %grayvalue threshold
heart3dPhantom = imopen(heart3dPhantom,strel('sphere',2));
heart3dPhantom = imdilate(heart3dPhantom,strel('sphere',2));
% find lagest connected component
CC = bwconncomp(heart3dPhantom);
numPixels = cellfun(@numel,CC.PixelIdxList);
biggest,idx] = max(numPixels);

heart3dPhantom=false(size(heart3dPhantom,[1 2 3]));
heart3dPhantom(CC.PixelIdxList{idx}) = 1;

%% create projection
heartPhantom= squeeze(sum(heart3dPhantom,1))';
heartPhantom=heartPhantom./max(heartPhantom(:));

%% set phase shift and absorption
maxPhaseShift=pi/2;
maxAbsorption = 0.1;

```

```matlab
29  deltaBeta=-2*maxPhaseShift/(log(1-maxAbsorption));
30  %% chosse line for improfile
31  xi =[55 155];
32  yi =[175  175];
33  showImage((-maxPhaseShift*heartPhantom(700:900,950:1150)))
34  caxis([-maxPhaseShift 0])
35  line(xi,yi,'Color','blue','LineWidth',3)
36  title(sprintf('phase shift zoom %i',maxPhaseShift))
37  %% calculate intensity distributions and phase retrieval for different
       fresnel numbers
38  arrayFresnel=[1 0.1 1*10^-2 10^-3 ];
39  for f=1:numel(arrayFresnel)
40      fresnelNumber=arrayFresnel(f);%5*10^-(f-1);
41      subplot(231)
42      imagesc((1-(maxAbsorption*heartPhantom)))
43      axis equal tight
44      title(sprintf('absorption %d',maxAbsorption))
45      subplot(232)
46      showImage((-maxPhaseShift*heartPhantom))
47      title(sprintf('phase shift %i',maxPhaseShift))
48      caxis([-maxPhaseShift 0])
49      subplot(233)
50      showImage((-maxPhaseShift*heartPhantom(700:900,950:1150)))
51      caxis([-maxPhaseShift 0])
52      line(xi,yi,'Color','blue','LineWidth',3)
53      title(sprintf('phase shift zoom %i',maxPhaseShift))
54      subplot(234)
55      proj =abs(fresnelPropagate(sqrt((1-maxAbsorption*heartPhantom)).*exp(-
       i*maxPhaseShift*heartPhantom),fresnelNumber)).^2;
56      minVal= (round(mean(proj(:))-3*std(proj(:)),2));
57      maxVal= (round(mean(proj(:))+3*std(proj(:)),2));
58      showImage(proj)
59      caxis([minVal maxVal])
60      title(sprintf('projection @ %i',fresnelNumber))
61      subplot(235)
62      showImage(proj(700:900,950:1150))
63      title(sprintf('zoom @ %i',fresnelNumber))
64      caxis([minVal maxVal])
65      colormap(gray)
66      subplot(236)
67      improfile(-maxPhaseShift*heartPhantom(700:900,950:1150),xi ,yi)
68      title(sprintf('proj improfile @ %i abs %d',fresnelNumber,
       maxAbsorption))
69      drawnow
```

```matlab
70      saveas(gcf, sprintf('projection_Abs=%d_Ph=%dF=%d.svg',maxAbsorption,
        maxPhaseShift,fresnelNumber))
71
72      %% PhaseReconstruction
73      % settings for CTF
74      settingsCTF=phaserec_ctf;
75      settingsCTF.lim1 = 10^(-12+f);
76      settingsCTF.lim2 = 5*10^(-10+2*f);
77      if maxAbsorption >= 0.4
78          settingsCTF.lim2 = 1e-1;
79      end
80      settingsCTF.padx = 100;
81      settingsCTF.pady = 100;
82      settingsCTF.maxPhase = inf;
83      settingsCTF.betaDeltaRatio = 1/deltaBeta;
84
85      % phase retrieval CTF
86      recoCTF = phaserec_ctf(proj, fresnelNumber , settingsCTF);
87      recoCTFNL = phaserec_nonlinTikhonov(proj, fresnelNumber, settingsCTF);
88      %%
89      clf
90      subplot(221)
91      showImage(recoCTF)
92      title(sprintf('Reco CTF @%i abs %d',fresnelNumber, maxAbsorption))
93      caxis([-maxPhaseShift 0])
94      subplot(222)
95      showImage(recoCTFNL)
96      title(sprintf('Reco nlCTF @%i abs %d',fresnelNumber, maxAbsorption))
97      caxis([-maxPhaseShift 0])
98      subplot(223)
99      showImage(recoCTF(700:900,950:1150))
100     line(xi,yi,'Color','blue','LineWidth',3)
101     title(sprintf('Reco Zoom CTF @%i abs %d',fresnelNumber,maxAbsorption))
102     caxis([-maxPhaseShift 0])
103     subplot(224)
104     improfile(recoCTF(700:900,950:1150),xi ,yi)
105     title(sprintf('CTF improfile @%i abs %d',fresnelNumber,maxAbsorption))
106
107     drawnow
108     saveas(gcf, sprintf('RecoCTF_Abs=%d_Ph=%dF=%d.svg',maxAbsorption,
        maxPhaseShift,fresnelNumber))
109
110     % phase retrieval BAC
111     settingsBAC = struct;
112     settingsBAC.padx = 00;
```

```matlab
113     settingsBAC.pady = 000;
114     settingsBAC.reg_alpha = 1/deltaBeta*(4*pi*fresnelNumber);
115
116     if maxAbsorption==0
117         settingsBAC.reg_alpha = 1e-6;
118     end
119     % Reconstruction with MBA-algorithm
120     projRecMBA = phaserec_mba(proj, fresnelNumber, settingsBAC);
121
122     % Reconstruction with BAC-algorithm
123     settingsBAC.reg_gamma = 1;
124     recoBAC = phaserec_bac(proj, settingsBAC);
125
126     clf
127     subplot(221)
128     showImage(projRecMBA)
129     title(sprintf('Reco MBA @ %i abs %d',fresnelNumber, maxAbsorption))
130     caxis([-maxPhaseShift 0])
131     subplot(222)
132     showImage(exp(-recoBAC))
133     title(sprintf('Reco BAC @ %i abs %d',fresnelNumber, maxAbsorption))
134     subplot(223)
135     showImage(exp(-recoBAC(700:900,950:1150)))
136     line(xi,yi,'Color','blue','LineWidth',3)
137     subplot(224)
138     improfile(exp(-recoBAC(700:900,950:1150)),xi ,yi)
139     title(sprintf('BAC improfile @%i abs %d',fresnelNumber,maxAbsorption))
140
141     title(sprintf('Reco BAC Zoom @%i abs %d',fresnelNumber,maxAbsorption))
142     drawnow
143     saveas(gcf, sprintf('RecoBAC_Abs=%d_Ph=%dF=%d.svg',maxAbsorption,
        maxPhaseShift,fresnelNumber))
144
145     % Reconstruction with SMO-algorithm
146     settingsSMO=phaserec_smo;
147     settingsSMO.betaDeltaRatio = 1/deltaBeta;
148     if settingsSMO.betaDeltaRatio==0
149         settingsSMO.betaDeltaRatio=1e-7;
150     end
151
152     recoSMO = phaserec_smo(proj,fresnelNumber, settingsSMO);
153     clf
154     subplot(221)
155     showImage(-maxPhaseShift*heartPhantom)
156     caxis([-maxPhaseShift 0])
```

```matlab
157     subplot(222)
158     showImage(recoSMO)
159     title(sprintf('Reco SMO @ %i abs %d',fresnelNumber, maxAbsorption))
160     caxis([-maxPhaseShift 0])
161     subplot(223)
162     showImage(recoSMO(700:900,950:1150))
163     line(xi,yi,'Color','blue','LineWidth',3)
164     title(sprintf('Reco SMO zoom @%i abs %d',fresnelNumber,maxAbsorption))
165     caxis([-maxPhaseShift 0])
166     subplot(224)
167     improfile(recoSMO(700:900,950:1150),xi ,yi)
168     title(sprintf('SMO improfile @%i abs %d',fresnelNumber,maxAbsorption))
169
170     drawnow
171     saveas(gcf, sprintf('RecoSMO_Abs=%d_Ph=%dF=%d.svg',maxAbsorption,
        maxPhaseShift,fresnelNumber))
172 end
```

A.2 Matlab code: Orientation analysis

Fourier-transform-based orientation

```matlab
1 %% Fibre tracking algorithm for small volumes
2 % INPUT:
3 % data: fft of a volume (multiplied with Kaiser Bessel function)
4 % q_x,q_y,q_z : coordinates in reciprocal space
5 % OUTPUT:
6 % eig_vec: matrix of eigenvectors
7 % eigval: corresponding eigenvalues
8 % I: integrated Intensity of the fourier pattern
9 % omega: anisotropy of the fft-pattern
10
11 function [eigvec, eigval, I, omega] = fiber_orientation(data,q_x,q_y,q_z)
12     I_tmp=abs(data.^2);
13     I=sum(I_tmp(:));
14     q=zeros(3);
15
16     q(1,1)= sum(sum(sum(I_tmp.*q_x.^2))); %q_xx
17     q(1,2)= sum(sum(sum(I_tmp.*q_x.*(q_y)))); % q_xy
18     q(1,3)= sum(sum(sum(I_tmp.*q_x.*q_z))); %q_xz
19
20     q(2,1)= q(1,2); % q_xy
21     q(2,2)= sum(sum(sum(I_tmp.*q_y.^2))); %q_yy
22     q(2,3)= sum(sum(sum(I_tmp.*q_y.*q_z))); %q_yz
```

```
23
24      q(3,1)= q(1,3) ;
25      q(3,2)= q(2,3);
26      q(3,3)= sum(sum(sum(I_tmp.*q_z.^2))); %q_zz
27      q=q/I;
28
29      [eigvec,D] = eig(q);
30      eigval=eig(D);
31
32      omega= abs(max(eigval)-min(eigval))/(max(eigval)+min(eigval));
33 end
```

Fourier-transform-based distance

```
1  %% Fiber distances from Fourier peaks
2  % Estimates the fiber thickness from most frequent Signal in Fourier space
3  % INPUT:
4  % data:  fft of a volume (multiplied with Kaiser Bessel function
5  % eig_vec_max: maximal Eigenvektoren von PCA
6  % eig_vec_min: minimal Eigenvektoren von PCA
7  % cone: Hoergass shaped mask
8  % angular_norm_mask: Normalization of Fourier Intensities [
       angular_norm_mask=angularAverage(cone);]
9  % OUTPUT:
10 % distance: Distance between two fibers
11 % peakheight: Ratio of signal from peak to backgrounf
12
13 function [distance, peakheight]=fiber_distance(data,eig_vec_max,
       eig_vec_min,cone)
14   % define mask for signal
15   [azimuth,eleva,r] = cart2sph(eig_vec_max(1),eig_vec_max(2),eig_vec_max
       (3));
16   azimuth=azimuth/pi*180;
17   eleva = 90-eleva/pi*180;
18   cone_mask=single(cone);
19   cone_mask=(imrotate3(cone_mask,eleva,[1 0 0],'crop','FillValues',0));
20   cone_mask=(imrotate3(cone_mask,azimuth,[0 0 1],'crop','FillValues',0));
21
22   %define mask for background
23   [azimuth,eleva,r] = cart2sph(eig_vec_min(1),eig_vec_min(2),eig_vec_min
       (3));
24   azimuth=azimuth/pi*180;
25   eleva = 90-eleva/pi*180;
26   cone_mask_background=single(cone);
27   cone_mask_background=(imrotate3(cone_mask_background,eleva,[1 0 0],'crop
```

```matlab
    ','FillValues',0));
28  cone_mask_background=(imrotate3(cone_mask_background,azimuth,[0 0 1],'
    crop','FillValues',0));
29
30  % calculate Inensity distribution
31  I_0=angularAverage(abs(((data).*cone_mask).^2))./(angularAverage(abs(((
    data).*cone_mask_background).^2)));
32  I_0(~isfinite(I_0))=0;
33  [peakheight, peakpos] = max(I_0);
34  distance = 1/((peakpos-1)./(length(I_0)-1)/2);
35 end
```

Gradient-based orientation

```matlab
1  %% Fibre tracking algorithm for small volumes
2  % INPUT:
3  % data: fft of a volume (multiplied with Kaiser Bessel function
4  % q_x,q_y,q_z : coordinates in reciprocal space
5  % OUTPUT:
6  % eig_vec: matrix of eigenvectors
7  % eigval: corresponding eigenvalues
8  % I: integrated Intensity of the fourier pattern
9  % omega: anisotropy of the fft-pattern
10
11 function [eigvec, eigval, Itot, omega] = fiber_orientation_grad(data)
12     [Gy,Gx,Gz] = imgradientxyz(data,'central');
13
14     Itot = sum(data(:));
15
16     % covariance matrix
17     cov = zeros(3);
18
19     % diagonal elements
20     cov(1,1)= sum(sum(sum(Gx.^2)));
21     cov(2,2)= sum(sum(sum(Gy.^2)));
22     cov(3,3)= sum(sum(sum(Gz.^2)));
23
24     % off-diagonal elements
25     cov(1,2)= sum(sum(sum(Gx.*Gy)));
26     cov(1,3)= sum(sum(sum(Gx.*Gz)));
27     cov(2,3)= sum(sum(sum(Gy.*Gz)));
28
29     cov(2,1)= cov(1,2);
30     cov(3,1)= cov(1,3) ;
31     cov(3,2)= cov(2,3);
```

```
32
33    % diagonalize matrix
34    [eigvec,D] = eig(cov);
35    eigval=eig(D);
36
37    % sort eigenvalues
38    [eigval, i_sort] = sort(eigval,'descend');
39    eigvec = eigvec(:,i_sort);
40
41    % anisotropy
42    omega = sqrt((((1/eigval(1)-1/eigval(2)).^2+(1/eigval(2)-1/eigval(3))
      .^2+(1/eigval(3)-1/eigval(1)).^2)/(2*((1/eigval(1)).^2+(1/eigval(2))
      .^2+(1/eigval(3)).^2)));
43 end
```

A.3 Matlab code: Ring removal

Alignment of projections

```
1  %% shift projections to mean position to correct for detector movement
2
3  refPosition= median(raws(dirtPositionX(1):dirtPositionX(2),dirtPositionY
      (1):dirtPositionY(2),:),3);
4  %%
5  iProj=1;
6  prjTmp = raws(dirtPositionX(1):dirtPositionX(2),dirtPositionY(1):
      dirtPositionY(2),iProj);
7  settingsAlign=alignImages;
8  settingsAlign.registrationMode = 'shift';  %'shiftRotation'
9  settingsAlign.registrationAccuracy = 100;
10 settingsAlign.sigmaHighpass = 1;
11 settingsAlign.sigmaLowpass = 1;
12 settingsAlign.medfilt = false;
13 [imAligned,shifts,rotAngleDegree,imToAlignFiltered] = alignImages(prjTmp,
      refPosition, settingsAlign);
14 %
15 showImage(refPosition-(shiftRotateImage(prjTmp,shifts, 0)))
16 %% correct movement of detector
17 raws_shifted=zeros(size(raws),'single');
18
19 for iProj=1:numAngles
20   prjTmp = raws(dirtPositionX(1):dirtPositionX(2),dirtPositionY(1):
      dirtPositionY(2),iProj);
21   [~,shifts] = alignImages(prjTmp,refPosition, settingsAlign);
```

```matlab
22    if sum(abs(shifts))<2
23        raws_shifted(:,:,iProj) = shiftRotateImage(raws(:,:,iProj),shifts,
      0);
24    end
25 end
26
27 %%
28 raws  = raws_shifted;
29 clear raws_shifted
30 %% also  align flats
31 flatsAll=cat(3,flats,flats_post);
32 flats_shifted= zeros(size(flatsAll),'single');
33 for iProj=1:size(flatsAll,3)
34   prjTmp = flatsAll(dirtPositionX(1):dirtPositionX(2),dirtPositionY(1):
      dirtPositionY(2),iProj);
35   [~,shifts] = alignImages(prjTmp,refPosition, settingsAlign);
36   if sum(abs(shifts))<2
37        flats_shifted(:,:,iProj) = shiftRotateImage(flatsAll(:,:,iProj),
      shifts, 0);
38   %                  shifts
39   end
40 end
41 %%
42 flats = flats_shifted;
43 flat = mean(flats_shifted(:,:,10:end),3);
```

Local ring removal

```matlab
1 %% local ring remove
2 % find bad areas by flat field to create a ring remove mask
3 showImage((flat))
4 %%
5 [gradX gradY gradZ]=imgradientxyz(single(cat(3,flats,flats_post)));
6 %%
7 stdFlats=mean(sqrt(gradX.^2+gradY.^2),3);
8
9 %% find dirt position by movement of detector via standard varriance
10 showImage(stdFlats>5*std(stdFlats,0,'all'))
11 %%
12 ringMask2D=stdFlats>5*std(stdFlats,0,'all');
13 ringMask2D= imerode(ringMask2D,strel('disk',1));
14 ringMask2D= imdilate(ringMask2D,strel('disk',10));
15
16 showImage(ringMask2D)
17 %%
```

```
18  clear gradX gradY gradZ
19  %% perform ring remove mor multiple distances
20  for iDist=1:numel(distToUse)
21        iSlice=1630; %test slice
22        sino = squeeze(projs(iSlice,:,:,iDist));
23        lowVal = -0.002;
24        highVal =  0.002;
25        sliceOriginal = astraFBP(sino,thetas);
26        if doPlot
27            figure(1); showImage(sliceOriginal); title('Original slice');
      colormap gray;
28            zoom(1)
29            caxis([lowVal, highVal])
30        end
31
32        %% additive approach for ring removal
33        settingsRingremove = ringremove;
34        settingsRingremove.method = 'additive';
35        settingsRingremove.additive_SmoothMethod = 'median';
36        settingsRingremove.additive_WindowSize = 50;
37        settingsRingremove.additive_GaussSigma = 5;
38        settingsRingremove.additive_Region=[];
39
40        sinoAdditive = ringremove(sino,settingsRingremove);
41        sliceAdditive = astraFBP(sinoAdditive,thetas);
42        if doPlot
43            figure(2); showImage(sliceAdditive) ;
44            title('Additive ring removal') ;
45            colormap gray;
46            zoom(1)
47            caxis([lowVal, highVal])
48        end
49        %% wavelet-based approach for ring removal
50        settingsRingremove.method = 'wavelet';
51        settingsRingremove.wavelet_DecNum = 7;
52        settingsRingremove.wavelet_Wname = 'sym8';
53        settingsRingremove.wavelet_Sigma = 4;
54
55        sinoWavelet = ringremove(sino,settingsRingremove);
56        sliceWavelet = astraFBP(sinoWavelet,thetas);
57        if doPlot
58            figure(3);
59            showImage(sliceWavelet);
60            title('Wavelet-based ring removal');
61            colormap gray;
```

```matlab
62                 zoom(1)
63                 caxis([lowVal, highVal])
64             end
65         %%
66
67         settingsRingremove2.method = 'wavelet';
68         settingsRingremove2.wavelet_DecNum = 7;
69         settingsRingremove2.wavelet_Wname = 'sym8';
70         settingsRingremove2.wavelet_Sigma = 5;
71 %          settingsRingremove2.method = 'additive';
72 %          settingsRingremove2.additive_SmoothMethod = 'median';
73 %          settingsRingremove2.additive_WindowSize = [];
74 %          settingsRingremove2.additive_GaussSigma = 5;
75 %          settingsRingremove2.additive_Region=[];
76
77         % new Ansatz "flat mask"
78         sinoCorr=sino;
79         ringMask=double(ringMask2D(iSlice,:));
80         sinoCorr = imgaussfilt(ringMask,2)'.*ringremove(sinoCorr,
    settingsRingremove2)+sinoCorr.*(1-imgaussfilt(ringMask,2))';
81         sliceCorr = astraFBP(sinoCorr,thetas);
82         if doPlot
83             figure(4); showImage(sliceCorr) ;
84             colormap gray;
85             zoom(1)
86             caxis([lowVal, highVal])
87         end
88         projs_corr= projs;
89         %%
90         fprintf('... perform ring removal... \n')
91         parfor sliceIdx = 1:size(projs,1)
92             sino=squeeze(projs_corr(sliceIdx,:,:,iDist));
93             ringMask=double(ringMask2D(sliceIdx,:));
94             %% local ring remove
95             if sum(ringMask)>0
96                 projs_corr(sliceIdx,:,:,iDist) = imgaussfilt(ringMask,2)
    '.*ringremove(sino,settingsRingremove2)+sino.*(1-imgaussfilt(ringMask
    ,2))';
97             end
98             %% standard ring remove
99             projs_corr(sliceIdx,:,:,iDist)= ringremove(squeeze(projs_corr(
    sliceIdx,:,:,iDist)),settingsRingremove);
100         end
101         fprintf('... ringremoval done ... \n')
102 end
```

Bibliography

[1] S. Standring. *Gray's Anatomy*. Elsevier LTD, Oxford, 2020. ISBN: 0702077054.

[2] M. Reichardt, M. Töpperwien, A. Khan, F. Alves, and T. Salditt. "Fiber orientation in a whole mouse heart reconstructed by laboratory phase-contrast micro-CT." In: *Journal of Medical Imaging* 7.02 (2020), p. 1. DOI: 10.1117/1.JMI.7.2.023501.

[3] M. Reichardt, J. Frohn, A. Khan, F. Alves, and T. Salditt. "Multi-scale x-ray phase-contrast tomography of murine heart tissue." In: *Biomed. Opt. Express* (2020).

[4] M. Reichardt, P. Jensen Møller, V. Andersen Dahl, A. Bjorholm Dahl, M. Ackermann, H. Shah, F. Länger, C. Werlein, M. Kühnel, D. Jonigk, and T. Salditt. "3D virtual histopathology of cardiac tissue from Covid-19 patients based on phase-contrast X-ray tomography." In: *eLife* (submitted).

[5] M. Reichardt, C. Neuhaus, J.-D. Nicolas, M. Bernhardt, K. Toischer, and T. Salditt. "X-Ray Structural Analysis of Single Adult Cardiomyocytes: Tomographic Imaging and Microdiffraction." In: *Biophysical Journal* 119.7 (2020), pp. 1309–1323. DOI: 10.1016/j.bpj.2020.08.019.

[6] F. P. S. H. Thomas Gaziano K. Srinath Reddy and V. Chaturvedi. "Disease Control Priorities in Developing Countries." In: WORLD BANK PUBN, 2006. Chap. Cardiovascular Disease, Chapter 33. ISBN: 0821361791.

[7] W. H. Organisation. *Cardiovascular diseases (CVDs)*. WHO. 2017. URL: https://www.who.int/news-room/fact-sheets/detail/cardiovascular-diseases-(cvds).

[8] A. Terzic and A. Behfar. "Stem cell therapy for heart failure: Ensuring regenerative proficiency." In: *Trends in Cardiovascular Medicine* 26.5 (2016), pp. 395–404. DOI: 10.1016/j.tcm.2016.01.003.

[9]   M. C. Mathers CD Lopez AD. "Disease Control Priorities in Developing Coun-
       tries." In: WORLD BANK PUBN, 2006. Chap. The Burden of Disease and Mor-
       tality by Condition: Data, Methods, and Results for 2001, Chapter 3. ISBN:
       0821361791.

[10]   Statistisches Bundesamt. "Gestorbene: Deutschland, Jahre, Todesursachen, Geschlecht."
       In: (2018). Ed. by Statistisches Bundesamt.

[11]   M. Litviňuková et al. "Cells of the adult human heart." In: *Nature* 588.7838
       (2020), pp. 466–472. DOI: 10.1038/s41586-020-2797-4.

[12]   D. Tirziu, F. J. Giordano, and M. Simons. "Cell Communications in the Heart."
       In: *Circulation* 122.9 (2010), pp. 928–937. DOI: 10.1161/circulationaha.
       108.847731.

[13]   R. H. Anderson, M. Smerup, D. Sanchez-Quintana, M. Loukas, and P. P. Lunken-
       heimer. "The three-dimensional arrangement of the myocytes in the ventric-
       ular walls." In: *Clinical Anatomy* 22.1 (2009), pp. 64–76. DOI: 10.1002/ca.
       20645.

[14]   W. Roberts, S. Salandy, G. Mandal, M. Holda, K. Tomaszewksi, J. Gielecki, R. S.
       Tubbs, and M. Loukas. "Across the centuries: Piecing together the anatomy of
       the heart." In: *Translational Research in Anatomy* 17 (2019), p. 100051. DOI:
       10.1016/j.tria.2019.100051.

[15]   M. Loukas, P. Youssef, J. Gielecki, J. Walocha, K. Natsis, and R. S. Tubbs. "His-
       tory of cardiac anatomy: A comprehensive review from the egyptians to today."
       In: *Clinical Anatomy* 29.3 (2016), pp. 270–284. DOI: 10.1002/ca.22705.

[16]   L. R. F. and. "Cardiovascular Research: Past, Present and Future." In: *Heart
       Research - Open Journal* 2.2 (2015), pp. 70–81. DOI: 10.17140/hroj-2-112.

[17]   J. T. Willerson and R. Teaff. "Egyptian contributions to cardiovascular medicine."
       In: *Texas Heart Institute journal* 23 (3 1996), pp. 191–200.

[18]   M. J. Kocica, A. F. Corno, V. Lackovic, and V. I. Kanjuh. "The Helical Ventric-
       ular Myocardial Band of Torrent-Guasp." In: *Seminars in Thoracic and Cardio-
       vascular Surgery: Pediatric Cardiac Surgery Annual* 10.1 (2007), pp. 52–60. DOI:
       10.1053/j.pcsu.2007.01.006.

[19]   J. M. Squire. "Muscle contraction: Sliding filament history, sarcomere dynam-
       ics and the two Huxleys." In: *Global Cardiology Science and Practice* 2016.2
       (2016). DOI: 10.21542/gcsp.2016.11.

[20] F. Torrent-Guasp, M. J. Kocica, A. F. Corno, M. Komeda, F. Carreras-Costa, A. Flotats, J. Cosin-Aguillar, and H. Wen. "Towards new understanding of the heart structure and function." In: *European Journal of Cardio-Thoracic Surgery* 27.2 (2005), pp. 191–201. DOI: 10.1016/j.ejcts.2004.11.026.

[21] P.-S. Jouk, Y. Usson, G. Michalowicz, and L. Grossi. "Three-dimensional cartography of the pattern of the myofibres in the second trimester fetal human heart." In: *Anatomy and Embryology* 202.2 (2000), pp. 103–118. DOI: 10.1007/s004290000103.

[22] R. H. Anderson, J. Yanni, M. R. Boyett, N. J. Chandler, and H. Dobrzynski. "The anatomy of the cardiac conduction system." In: *Clinical Anatomy* 22.1 (2009), pp. 99–113. DOI: 10.1002/ca.20700.

[23] F. Saremi, D. Sánchez-Quintana, S. Mori, H. Muresian, D. E. Spicer, C. Hassani, and R. H. Anderson. "Fibrous Skeleton of the Heart: Anatomic Overview and Evaluation of Pathologic Conditions with CT and MR Imaging." In: *Radio-Graphics* 37.5 (2017), pp. 1330–1351. DOI: 10.1148/rg.2017170004.

[24] J.-D. Nicolas. "Multiscale X-Ray Analysis of Biological Cells and Tissues by Scanning Diffraction and Coherent Imaging." PhD thesis. Georg-August-Universität Göttingen, 2018.

[25] D. Smith. "Understanding Muscle Contraction." In: *Sports-Specific Rehabilitation*. Elsevier, 2000, pp. 15–38. DOI: 10.1016/b978-044306642-9.50005-8.

[26] A. C. Hinken and R. J. Solaro. "A Dominant Role of Cardiac Molecular Motors in the Intrinsic Regulation of Ventricular Ejection and Relaxation." In: *Physiology* 22.2 (2007), pp. 73–80. DOI: 10.1152/physiol.00043.2006.

[27] S. M. Mijailovich, B. Stojanovic, D. Nedic, M. Svicevic, M. A. Geeves, T. C. Irving, and H. L. Granzier. "Nebulin and titin modulate cross-bridge cycling and length-dependent calcium sensitivity." In: *Journal of General Physiology* 151.5 (2019), pp. 680–704. DOI: 10.1085/jgp.201812165.

[28] P. Peterson, M. Kalda, and M. Vendelin. "Real-time determination of sarcomere length of a single cardiomyocyte during contraction." In: *American Journal of Physiology-Cell Physiology* 304.6 (2013), pp. C519–C531. DOI: 10.1152/ajpcell.00032.2012.

[29]   K. S. McDonald, L. M. Hanft, J. C. Robinett, M. Guglin, and K. S. Campbell. "Regulation of Myofilament Contractile Function in Human Donor and Failing Hearts." In: *Frontiers in Physiology* 11 (2020). DOI: 10.3389/fphys.2020.00468.

[30]   K. C. Holmes and G. Rosenbaum. "How X-ray Diffraction with Synchrotron Radiation Got Started." In: *Journal of Synchrotron Radiation* 5.3 (1998), pp. 147–153. DOI: 10.1107/s0909049597018578.

[31]   I. Morano. "Tuning the human heart molecular motors by myosin light chains." In: *Journal of Molecular Medicine* 77.7 (1999), pp. 544–555. DOI: 10.1007/s001099900031.

[32]   B. Mackenna and R. Callander. "Transport System The Heart, Blood Vessels And Body Fluids: Haemopoietic System." In: *Illustrated Physiology*. Elsevier, 1990, pp. 99–146. DOI: 10.1016/b978-0-443-05779-3.50011-2.

[33]   T. Hong and R. M. Shaw. "Cardiac T-Tubule Microanatomy and Function." In: *Physiological Reviews* 97.1 (2017), pp. 227–252. DOI: 10.1152/physrev.00037.2015.

[34]   G. L. J. Galli. "Design And Physiology Of The Heart | Cellular Ultrastructure Of Cardiac Cells In Fishes." In: *Encyclopedia of Fish Physiology*. Elsevier, 2011, pp. 1006–1014. DOI: 10.1016/b978-0-12-374553-8.00242-2.

[35]   openstax.org. *anatomy and physiology*. 2021. URL: https://openstax.org/books/anatomy-and-physiology/pages/19-1-heart-anatomy?query=heart.

[36]   S. Brandenburg, E. C. Arakel, B. Schwappach, and S. E. Lehnart. "The molecular and functional identities of atrial cardiomyocytes in health and disease." In: *Biochimica et Biophysica Acta (BBA) - Molecular Cell Research* 1863.7 (2016), pp. 1882–1893. DOI: 10.1016/j.bbamcr.2015.11.025.

[37]   S. Ourselin, D. Rueckert, and N. Smith, eds. *Functional Imaging and Modeling of the Heart*. Springer Berlin Heidelberg, 2013. DOI: 10.1007/978-3-642-38899-6.

[38]   R. S. Zimmermann and U. Parlitz. "Observing spatio-temporal dynamics of excitable media using reservoir computing." In: *Chaos: An Interdisciplinary Journal of Nonlinear Science* 28.4 (2018), p. 043118. DOI: 10.1063/1.5022276.

[39]   T. Lilienkamp and U. Parlitz. "Scaling behavior of the terminal transient phase." In: *Physical Review E* 98.2 (2018). DOI: 10.1103/physreve.98.022215.

[40] G. A. Holzapfel and R. W. Ogden. "Constitutive modelling of passive myocardium: a structurally based framework for material characterization." In: *Philosophical Transactions of the Royal Society A: Mathematical, Physical and Engineering Sciences* 367.1902 (2009), pp. 3445–3475. DOI: 10.1098/rsta.2009.0091.

[41] O. Gültekin, G. Sommer, and G. A. Holzapfel. "An orthotropic viscoelastic model for the passive myocardium: continuum basis and numerical treatment." In: *Computer Methods in Biomechanics and Biomedical Engineering* 19.15 (2016), pp. 1647–1664. DOI: 10.1080/10255842.2016.1176155.

[42] P. Lamata, A. Cookson, and N. Smith. "Clinical Diagnostic Biomarkers from the Personalization of Computational Models of Cardiac Physiology." In: *Annals of Biomedical Engineering* 44.1 (2015), pp. 46–57. DOI: 10.1007/s10439-015-1439-8.

[43] S. Mahida, F. Sacher, R. Dubois, M. Sermesant, F. Bogun, M. Haïssaguerre, P. Jaïs, and H. Cochet. "Cardiac Imaging in Patients With Ventricular Tachycardia." In: *Circulation* 136.25 (2017), pp. 2491–2507. DOI: 10.1161/circulationaha.117.029349.

[44] S. Luther, F. H. Fenton, B. G. Kornreich, A. Squires, P. Bittihn, D. Hornung, M. Zabel, J. Flanders, A. Gladuli, L. Campoy, E. M. Cherry, G. Luther, G. Hasenfuss, V. I. Krinsky, A. Pumir, R. F. Gilmour, and E. Bodenschatz. "Low-energy control of electrical turbulence in the heart." In: *Nature* 475.7355 (2011), pp. 235–239. DOI: 10.1038/nature10216.

[45] J. Christoph, M. Chebbok, C. Richter, J. Schröder-Schetelig, P. Bittihn, S. Stein, I. Uzelac, F. H. Fenton, G. Hasenfuß, R. F. Gilmour, and S. Luther. "Electromechanical vortex filaments during cardiac fibrillation." In: *Nature* 555.7698 (2018), pp. 667–672. DOI: 10.1038/nature26001.

[46] H. Gao, W. G. Li, L. Cai, C. Berry, and X. Y. Luo. "Parameter estimation in a Holzapfel–Ogden law for healthy myocardium." In: *Journal of Engineering Mathematics* 95.1 (2015), pp. 231–248. DOI: 10.1007/s10665-014-9740-3.

[47] L. Azzolin, L. Dedè, A. Gerbi, and A. Quarteroni. "Effect of fibre orientation and bulk modulus on the electromechanical modelling of human ventricles." In: *Mathematics in Engineering* 2.4 (2020), pp. 614–638. DOI: 10.3934/mine.2020028.

[48]   W. Lauterborn, T. Kurz, and M. Wiesenfeldt. "Die Entwicklung der Optik." In: *Kohärente Optik*. Springer Berlin Heidelberg, 1993, pp. 1–8. DOI: 10.1007/978-3-642-78264-0_1.

[49]   I. H. Hussein and M. Raad. "Once Upon a Microscopic Slide: The Story of Histology." In: *Journal of Cytology & Histology* 06.06 (2015). DOI: 10.4172/2157-7099.1000377.

[50]   S. K. Suvarna, C. Layton, and J. D. Bancroft. *Bancroft's Theory and Practice of Histological Techniques*. Elsevier, 2019. DOI: 10.1016/c2015-0-00143-5.

[51]   G. Rolls. *An Introduction to Specimen Preparation*. Leica Mikrosysteme Vertrieb GmbH. URL: https://www.leicabiosystems.com/knowledge-pathway/an-introduction-to-specimen-preparation.

[52]   H. A. Alturkistani, F. M. Tashkandi, and Z. M. Mohammedsaleh. "Histological Stains: A Literature Review and Case Study." In: *Global Journal of Health Science* 8.3 (2015), p. 72. DOI: 10.5539/gjhs.v8n3p72.

[53]   A. L. Mescher. *Junqueira's Basic Histology: Text and Atlas, Sixteenth Edition*. McGraw-Hill Education, 2021. 576 pp. ISBN: 1260462986.

[54]   K. Amunts, C. Lepage, L. Borgeat, H. Mohlberg, T. Dickscheid, M.-E. Rousseau, S. Bludau, P.-L. Bazin, L. B. Lewis, A.-M. Oros-Peusquens, N. J. Shah, T. Lippert, K. Zilles, and A. C. Evans. "BigBrain: An Ultrahigh-Resolution 3D Human Brain Model." In: *Science* 340.6139 (2013), pp. 1472–1475. DOI: 10.1126/science.1235381.

[55]   S.-L. Ding, J. J. Royall, et al. "Comprehensive cellular-resolution atlas of the adult human brain." In: *Journal of Comparative Neurology* 524.16 (2016), pp. 3127–3481. DOI: 10.1002/cne.24080.

[56]   M. Mancini, A. Casamitjana, L. Peter, E. Robinson, S. Crampsie, D. L. Thomas, J. L. Holton, Z. Jaunmuktane, and J. E. Iglesias. "A multimodal computational pipeline for 3D histology of the human brain." In: *Scientific Reports* 10.1 (2020). DOI: 10.1038/s41598-020-69163-z.

[57]   M. Gibb, R. A. B. Burton, C. Bollensdorff, C. Afonso, T. Mansoori, U. Schotten, D. J. Gavaghan, B. Rodriguez, J. E. Schneider, P. Kohl, and V. Grau. "Resolving the Three-Dimensional Histology of the Heart." In: *Computational Methods in Systems Biology*. Springer Berlin Heidelberg, 2012, pp. 2–16. DOI: 10.1007/978-3-642-33636-2_2.

[58]   R. A. Burton, G. Plank, J. E. Schneider, V. Grau, H. Ahammer, S. L. Keel-
       ing, J. Lee, N. P. Smith, D. Gavaghan, N. Trayanova, and P. Kohl. "Three-
       Dimensional Models of Individual Cardiac Histoanatomy: Tools and Challenges."
       In: *Annals of the New York Academy of Sciences* 1080.1 (2006), pp. 301–319. DOI:
       `10.1196/annals.1380.023`.

[59]   C. A. Glashan, A. F. A. Androulakis, Q. Tao, R. N. Glashan, L. J. Wisse, M.
       Ebert, M. C. de Ruiter, B. J. van Meer, C. Brouwer, O. M. Dekkers, D. A. Pijnap-
       pels, J. M. T. de Bakker, M. de Riva, S. R. D. Piers, and K. Zeppenfeld. "Whole
       human heart histology to validate electroanatomical voltage mapping in pa-
       tients with non-ischaemic cardiomyopathy and ventricular tachycardia." In:
       European Heart Journal 39.31 (2018), pp. 2867–2875. DOI: `10.1093/eurheartj/`
       `ehy168`.

[60]   D. D. Streeter and D. L. Bassett. "An engineering analysis of myocardial fiber
       orientation in pig's left ventricle in systole." In: *The Anatomical Record* 155.4
       (1966), pp. 503–511. DOI: `10.1002/ar.1091550403`.

[61]   A. J. Atkinson, S. R. Kharche, M. G. Bateman, P. A. Iaizzo, and H. Dobrzyn-
       ski. "3D anatomical reconstruction of human cardiac conduction system and
       simulation of bundle branch block after TAVI procedure." In: *2016 38th An-
       nual International Conference of the IEEE Engineering in Medicine and Biology
       Society (EMBC)*. IEEE, 2016. DOI: `10.1109/embc.2016.7591992`.

[62]   E. Abbe. "Beiträge zur Theorie des Mikroskops und der mikroskopischen Wahr-
       nehmung." In: *Archiv für Mikroskopische Anatomie* 9.1 (1873), pp. 413–468.
       DOI: `10.1007/bf02956173`.

[63]   H. Dejea, A. Bonnin, A. C. Cook, and P. Garcia-Canadilla. "Cardiac multi-scale
       investigation of the right and left ventricle ex vivo: a review." In: *Cardiovascu-
       lar Diagnosis and Therapy* 10.5 (2020), pp. 1701–1717. DOI: `10.21037/cdt-`
       `20-269`.

[64]   T. J. Mohun and W. J. Weninger. "Imaging heart development using high-
       resolution episcopic microscopy." In: *Current Opinion in Genetics & Develop-
       ment* 21.5 (2011), pp. 573–578. DOI: `10.1016/j.gde.2011.07.004`.

[65]   W. J. Weninger, S. H. Geyer, T. J. Mohun, D. Rasskin-Gutman, T. Matsui, I.
       Ribeiro, L. da F. Costa, J. C. Izpisúa-Belmonte, and G. B. Müller. "High-resolution
       episcopic microscopy: a rapid technique for high detailed 3D analysis of gene
       activity in the context of tissue architecture and morphology." In: *Anatomy*

and Embryology 211.3 (2006), pp. 213–221. DOI: 10.1007/s00429-005-0073-x.

[66] P.-S. Jouk, A. Mourad, V. Milisic, G. Michalowicz, A. Raoult, D. Caillerie, and Y. Usson. "Analysis of the fiber architecture of the heart by quantitative polarized light microscopy. Accuracy, limitations and contribution to the study of the fiber architecture of the ventricles during fetal and neonatal life." In: *European Journal of Cardio-Thoracic Surgery* 31.5 (2007), pp. 915–921. DOI: 10.1016/j.ejcts.2006.12.040.

[67] J. R. Sommer and R. A. Waugh. "Ultrastructure of heart muscle." In: *Environmental Health Perspectives* 26 (1978), pp. 159–167. DOI: 10.1289/ehp.7826159.

[68] V. Nikolova, C. Leimena, A. C. McMahon, J. C. Tan, S. Chandar, D. Jogia, S. H. Kesteven, J. Michalicek, R. Otway, F. Verheyen, S. Rainer, C. L. Stewart, D. Martin, M. P. Feneley, and D. Fatkin. "Defects in nuclear structure and function promote dilated cardiomyopathy in lamin A/C–deficient mice." In: *Journal of Clinical Investigation* 113.3 (2004), pp. 357–369. DOI: 10.1172/jci200419448.

[69] E. A. Rog-Zielinska, C. M. Johnston, E. T. O'Toole, M. Morphew, A. Hoenger, and P. Kohl. "Electron tomography of rabbit cardiomyocyte three-dimensional ultrastructure." In: *Progress in Biophysics and Molecular Biology* 121.2 (2016), pp. 77–84. DOI: 10.1016/j.pbiomolbio.2016.05.005.

[70] H. M. Daghistani, B. S. Rajab, and A. Kitmitto. "Three-dimensional electron microscopy techniques for unravelling mitochondrial dysfunction in heart failure and identification of new pharmacological targets." In: *British Journal of Pharmacology* 176.22 (2018), pp. 4340–4359. DOI: 10.1111/bph.14499.

[71] A. Hussain, S. Ghosh, S. B. Kalkhoran, D. J. Hausenloy, E. Hanssen, and V. Rajagopal. "An automated workflow for segmenting single adult cardiac cells from large-volume serial block-face scanning electron microscopy data." In: *Journal of Structural Biology* 202.3 (2018), pp. 275–285. DOI: 10.1016/j.jsb.2018.02.005.

[72] D. C. Jans, C. A. Wurm, D. Riedel, D. Wenzel, F. Stagge, M. Deckers, P. Rehling, and S. Jakobs. "STED super-resolution microscopy reveals an array of MINOS clusters along human mitochondria." In: *Proceedings of the National Academy of Sciences* 110.22 (2013), pp. 8936–8941. DOI: 10.1073/pnas.1301820110.

[73] G. Morton, A. Chiribiri, M. Ishida, S. T. Hussain, A. Schuster, A. Indermuehle, D. Perera, J. Knuuti, S. Baker, E. Hedström, P. Schleyer, M. O'Doherty, S. Barrington, and E. Nagel. "Quantification of Absolute Myocardial Perfusion in Patients With Coronary Artery Disease." In: *Journal of the American College of Cardiology* 60.16 (2012), pp. 1546–1555. DOI: 10.1016/j.jacc.2012.05.052.

[74] M. Dewey et al. "Clinical quantitative cardiac imaging for the assessment of myocardial ischaemia." In: *Nature Reviews Cardiology* 17.7 (2020), pp. 427–450. DOI: 10.1038/s41569-020-0341-8.

[75] S. W. Hell and J. Wichmann. "Breaking the diffraction resolution limit by stimulated emission: stimulated-emission-depletion fluorescence microscopy." In: *Optics Letters* 19.11 (1994), p. 780. DOI: 10.1364/ol.19.000780.

[76] Y. Eilers, H. Ta, K. C. Gwosch, F. Balzarotti, and S. W. Hell. "MINFLUX monitors rapid molecular jumps with superior spatiotemporal resolution." In: *Proceedings of the National Academy of Sciences* 115.24 (2018), pp. 6117–6122. DOI: 10.1073/pnas.1801672115.

[77] K. C. Gwosch, J. K. Pape, F. Balzarotti, P. Hoess, J. Ellenberg, J. Ries, and S. W. Hell. "MINFLUX nanoscopy delivers 3D multicolor nanometer resolution in cells." In: *Nature Methods* 17.2 (2020), pp. 217–224. DOI: 10.1038/s41592-019-0688-0.

[78] E. Wagner, M. A. Lauterbach, T. Kohl, V. Westphal, G. S. Williams, J. H. Steinbrecher, J.-H. Streich, B. Korff, H.-T. M. Tuan, B. Hagen, S. Luther, G. Hasenfuss, U. Parlitz, M. S. Jafri, S. W. Hell, W. J. Lederer, and S. E. Lehnart. "Stimulated Emission Depletion Live-Cell Super-Resolution Imaging Shows Proliferative Remodeling of T-Tubule Membrane Structures After Myocardial Infarction." In: *Circulation Research* 111.4 (2012), pp. 402–414. DOI: 10.1161/circresaha.112.274530.

[79] J. K. Pape, T. Stephan, F. Balzarotti, R. Büchner, F. Lange, D. Riedel, S. Jakobs, and S. W. Hell. "Multicolor 3D MINFLUX nanoscopy of mitochondrial MICOS proteins." In: *Proceedings of the National Academy of Sciences* 117.34 (2020), pp. 20607–20614. DOI: 10.1073/pnas.2009364117.

[80] J. R. Epp, Y. Niibori, H.-L. (Hsiang, V. Mercaldo, K. Deisseroth, S. A. Josselyn, and P. W. Frankland. "Optimization of CLARITY for Clearing Whole-Brain and Other Intact Organs." In: *eneuro* 2.3 (2015), ENEURO.0022–15.2015. DOI: 10.1523/eneuro.0022-15.2015.

[81] D. Jing, S. Zhang, W. Luo, X. Gao, Y. Men, C. Ma, X. Liu, Y. Yi, A. Bugde, B. O. Zhou, Z. Zhao, Q. Yuan, J. Q. Feng, L. Gao, W.-P. Ge, and H. Zhao. "Tissue clearing of both hard and soft tissue organs with the PEGASOS method." In: *Cell Research* 28.8 (2018), pp. 803–818. DOI: 10.1038/s41422-018-0049-z.

[82] C. Olianti, F. Giardini, E. Lazzeri, I. Costantini, L. Silvestri, R. Coppini, E. Cerbai, F. S. Pavone, and L. Sacconi. "Optical clearing in cardiac imaging: A comparative study." In: *Progress in Biophysics and Molecular Biology* (2021). DOI: 10.1016/j.pbiomolbio.2021.07.012.

[83] H. R. Ueda, H.-U. Dodt, P. Osten, M. N. Economo, J. Chandrashekar, and P. J. Keller. "Whole-Brain Profiling of Cells and Circuits in Mammals by Tissue Clearing and Light-Sheet Microscopy." In: *Neuron* 106.3 (2020), pp. 369–387. DOI: 10.1016/j.neuron.2020.03.004.

[84] M. D. Rocha, D. N. Düring, P. Bethge, F. F. Voigt, S. Hildebrand, F. Helmchen, A. Pfeifer, R. H. R. Hahnloser, and M. Gahr. "Tissue Clearing and Light Sheet Microscopy: Imaging the Unsectioned Adult Zebra Finch Brain at Cellular Resolution." In: *Frontiers in Neuroanatomy* 13 (2019). DOI: 10.3389/fnana.2019.00013.

[85] Y. Ding, Z. Bailey, V. Messerschmidt, J. Nie, R. Bryant, S. Rugonyi, P. Fei, J. Lee, and T. K. Hsiai. "Light-sheet Fluorescence Microscopy for the Study of the Murine Heart." In: *Journal of Visualized Experiments* 139 (2018). DOI: 10.3791/57769.

[86] P. Fei, J. Lee, R. R. S. Packard, K.-I. Sereti, H. Xu, J. Ma, Y. Ding, H. Kang, H. Chen, K. Sung, R. Kulkarni, R. Ardehali, C.-C. J. Kuo, X. Xu, C.-M. Ho, and T. K. Hsiai. "Cardiac Light-Sheet Fluorescent Microscopy for Multi-Scale and Rapid Imaging of Architecture and Function." In: *Scientific Reports* 6.1 (2016). DOI: 10.1038/srep22489.

[87] H. W. Goo, S. J. Park, and S.-J. Yoo. "Advanced Medical Use of Three-Dimensional Imaging in Congenital Heart Disease: Augmented Reality, Mixed Reality, Virtual Reality, and Three-Dimensional Printing." In: *Korean Journal of Radiology* 21.2 (2020), p. 133. DOI: 10.3348/kjr.2019.0625.

[88] D. Rohmer, A. Sitek, and G. T. Gullberg. "Reconstruction and Visualization of Fiber and Laminar Structure in the Normal Human Heart from Ex Vivo Diffusion Tensor Magnetic Resonance Imaging (DTMRI) Data." In: *Investigative Radiology* 42.11 (2007), pp. 777–789. DOI: 10.1097/rli.0b013e3181238330.

[89] Y. Amano, F. Yanagisawa, M. Tachi, K. Asai, Y. Suzuki, H. Hashimoto, K. Ishi-
      hara, and S. Kumita. "Three-dimensional Cardiac MR Imaging: Related Tech-
      niques and Clinical Applications." In: *Magnetic Resonance in Medical Sciences*
      16.3 (2017), pp. 183–189. DOI: 10.2463/mrms.rev.2016-0116.

[90] P. F. Ferreira, P. J. Kilner, L.-A. McGill, S. Nielles-Vallespin, A. D. Scott, S. Y.
      Ho, K. P. McCarthy, M. M. Haba, T. F. Ismail, P. D. Gatehouse, R. de Silva,
      A. R. Lyon, S. K. Prasad, D. N. Firmin, and D. J. Pennell. "In vivo cardiovas-
      cular magnetic resonance diffusion tensor imaging shows evidence of abnor-
      mal myocardial laminar orientations and mobility in hypertrophic cardiomy-
      opathy." In: *Journal of Cardiovascular Magnetic Resonance* 16.1 (2014). DOI:
      10.1186/s12968-014-0087-8.

[91] C. Mekkaoui, P. Porayette, M. P. Jackowski, W. J. Kostis, G. Dai, S. Sanders, and
      D. E. Sosnovik. "Diffusion MRI Tractography of the Developing Human Fetal
      Heart." In: *PLoS ONE* 8.8 (2013). Ed. by W. R. Bauer, e72795. DOI: 10.1371/
      journal.pone.0072795.

[92] T. Pawade et al. "Computed Tomography Aortic Valve Calcium Scoring in
      Patients With Aortic Stenosis." In: *Circulation: Cardiovascular Imaging* 11.3
      (2018). DOI: 10.1161/circimaging.117.007146.

[93] H. Machida, I. Tanaka, R. Fukui, Y. Shen, T. Ishikawa, E. Tate, and E. Ueno.
      "Current and Novel Imaging Techniques in Coronary CT." In: *RadioGraphics*
      35.4 (2015), pp. 991–1010. DOI: 10.1148/rg.2015140181.

[94] T. Salditt, A. Egner, and D. R. Luke, eds. *Nanoscale Photonic Imaging*. Springer
      International Publishing, 2020. DOI: 10.1007/978-3-030-34413-9.

[95] O. Ghekiere, R. Salgado, N. Buls, T. Leiner, I. Mancini, P. Vanhoenacker, P.
      Dendale, and A. Nchimi. "Image quality in coronary CT angiography: chal-
      lenges and technical solutions." In: *The British Journal of Radiology* 90.1072
      (2017), p. 20160567. DOI: 10.1259/bjr.20160567.

[96] F. A. Mettler, M. Mahesh, M. Bhargavan-Chatfield, C. E. Chambers, J. G. Elee,
      D. P. Frush, D. L. Miller, H. D. Royal, M. T. Milano, D. C. Spelic, A. J. Ansari,
      W. E. Bolch, G. M. Guebert, R. H. Sherrier, J. M. Smith, and R. J. Vetter. "Patient
      Exposure from Radiologic and Nuclear Medicine Procedures in the United
      States: Procedure Volume and Effective Dose for the Period 2006–2016." In:
      Radiology 295.2 (2020), pp. 418–427. DOI: 10.1148/radiol.2020192256.

[97] *Gesetz zum Schutz vor der schädlichen Wirkung ionisierender Strahlung (Strahlenschutzgesetz - StrlSchG)*. 2017.

[98] W. C. Röntgen. "Ueber eine neue Art von Strahlen." In: *Annalen der Physik* 300.1 (1898), pp. 1–11. DOI: 10.1002/andp.18983000102.

[99] M. M. Lell, J. E. Wildberger, H. Alkadhi, J. Damilakis, and M. Kachelriess. "Evolution in Computed Tomography." In: *Investigative Radiology* 50.9 (2015), pp. 629–644. DOI: 10.1097/rli.0000000000000172.

[100] M. M. Lell and M. Kachelrieß. "Recent and Upcoming Technological Developments in Computed Tomography." In: *Investigative Radiology* 55.1 (2020), pp. 8–19. DOI: 10.1097/rli.0000000000000601.

[101] W. K. Röntgen. *Hand mit Ringen*. 1895. URL: https://wellcomecollection.org/works/wjc8ejn2.

[102] R. Behling. *Modern Diagnostic X-Ray Sources*. CRC Press, 2015. DOI: 10.1201/b18655.

[103] P. Schardt, J. Deuringer, J. Freudenberger, E. Hell, W. Knüpfer, D. Mattern, and M. Schild. "New x-ray tube performance in computed tomography by introducing the rotating envelope tube technology." In: *Medical Physics* 31.9 (2004), pp. 2699–2706. DOI: 10.1118/1.1783552.

[104] T. Gureyev. "Composite techniques for phase retrieval in the Fresnel region." In: *Optics Communications* 220.1-3 (2003), pp. 49–58. DOI: 10.1016/s0030-4018(03)01353-1.

[105] F. Nachtrab, T. Ebensperger, B. Schummer, F. Sukowski, and R. Hanke. "Laboratory X-ray microscopy with a nano-focus X-ray source." In: *Journal of Instrumentation* 6.11 (2011), pp. C11017–C11017. DOI: 10.1088/1748-0221/6/11/c11017.

[106] D. E. Grider, A. Wright, and P. K. Ausburn. "Electron beam melting in microfocus X-ray tubes." In: *Journal of Physics D: Applied Physics* 19.12 (1986), pp. 2281–2292. DOI: 10.1088/0022-3727/19/12/008.

[107] F. Nachtrab, T. Hofmann, C. Speier, J. Lučić, M. Firsching, N. Uhlmann, P. Takman, C. Heinzl, A. Holmberg, M. Krumm, and C. Sauerwein. "Development of a Timepix based detector for the NanoXCT project." In: *Journal of Instrumentation* 10.11 (2015), pp. C11009–C11009. DOI: 10.1088/1748-0221/10/11/c11009.

[108]   M. Otendal, T. Tuohimaa, U. Vogt, and H. M. Hertz. "A 9keV electron-impact liquid-gallium-jet x-ray source." In: *Review of Scientific Instruments* 79.1 (2008), p. 016102. DOI: 10.1063/1.2833838.

[109]   J. G. Rocha and S. Lanceros-Mendez. "Review on X-ray Detectors Based on Scintillators and CMOS Technology." In: *Recent Patents on Electrical Engineeringe* 4.1 (2011), pp. 16–41. DOI: 10.2174/1874476111104010016.

[110]   A. Datta, Z. Zhong, and S. Motakef. "A new generation of direct X-ray detectors for medical and synchrotron imaging applications." In: *Scientific Reports* 10.1 (2020). DOI: 10.1038/s41598-020-76647-5.

[111]   E. R. Fossum and D. B. Hondongwa. "A Review of the Pinned Photodiode for CCD and CMOS Image Sensors." In: *IEEE Journal of the Electron Devices Society* 2.3 (2014), pp. 33–43. DOI: 10.1109/jeds.2014.2306412.

[112]   W. S. Boyle and G. E. Smith. "Charge Coupled Semiconductor Devices." In: *Bell System Technical Journal* 49.4 (1970), pp. 587–593. DOI: 10.1002/j.1538-7305.1970.tb01790.x.

[113]   L. M. Lohse, M. Vassholz, M. Töpperwien, T. Jentschke, A. Bergamaschi, S. Chiriotti, and T. Salditt. "Spectral μCT with an energy resolving and interpolating pixel detector." In: *Optics Express* 28.7 (2020), p. 9842. DOI: 10.1364/oe.385389.

[114]   E. S. Dreier, A. Bergamaschi, G. K. Kallon, R. Brönnimann, U. L. Olsen, A. Olivo, and M. Endrizzi. "Tracking based, high-resolution single-shot multimodal x-ray imaging in the laboratory enabled by the sub-pixel resolution capabilities of the MÖNCH detector." In: *Applied Physics Letters* 117.26 (2020), p. 264101. DOI: 10.1063/5.0027763.

[115]   M. Ramilli, A. Bergamaschi, M. Andrae, M. Brückner, S. Cartier, R. Dinapoli, E. Fröjdh, D. Greiffenberg, T. Hutwelker, C. Lopez-Cuenca, D. Mezza, A. Mozzanica, M. Ruat, S. Redford, B. Schmitt, X. Shi, G. Tinti, and J. Zhang. "Measurements with MÖNCH, a 25 µm pixel pitch hybrid pixel detector." In: *Journal of Instrumentation* 12.01 (2017), pp. C01071–C01071. DOI: 10.1088/1748-0221/12/01/c01071.

[116]   T. Shintake. "Review of the worldwide SASE FEL development." In: *2007 IEEE Particle Accelerator Conference (PAC)*. IEEE, 2007. DOI: 10.1109/pac.2007.4440331.

[117] R. Abela et al. "XFEL: The European X-Ray Free-Electron Laser - Technical Design Report." In: (2006). DOI: 10.3204/DESY_06-097.

[118] D. Paganin. *Coherent X-Ray Optics*. OXFORD UNIV PR, 2013. 424 pp. ISBN: 0199673861.

[119] M. Friebel and M. Meinke. "Determination of the complex refractive index of highly concentrated hemoglobin solutions using transmittance and reflectance measurements." In: *Journal of Biomedical Optics* 10.6 (2005), p. 064019. DOI: 10.1117/1.2138027.

[120] R. Fitzgerald. "Phase-Sensitive X-Ray Imaging." In: *Physics Today* 53.7 (2000), pp. 23–26. DOI: 10.1063/1.1292471.

[121] F. Zernike. "Phase contrast, a new method for the microscopic observation of transparent objects." In: *Physica* 9.7 (1942), pp. 686–698. DOI: 10.1016/s0031-8914(42)80035-x.

[122] F. Zernike. "How I Discovered Phase Contrast." In: *Science* 121.3141 (1955), pp. 345–349. DOI: 10.1126/science.121.3141.345.

[123] U. Bonse and M. Hart. "An X-ray Interferometer." In: *Applied Physics Letters* 6.8 (1965), pp. 155–156. DOI: 10.1063/1.1754212.

[124] D. Chapman, W. Thomlinson, R. E. Johnston, D. Washburn, E. Pisano, N. Gmür, Z. Zhong, R. Menk, F. Arfelli, and D. Sayers. "Diffraction enhanced x-ray imaging." In: *Physics in Medicine and Biology* 42.11 (1997), pp. 2015–2025. DOI: 10.1088/0031-9155/42/11/001.

[125] T. J. Davis, D. Gao, T. E. Gureyev, A. W. Stevenson, and S. W. Wilkins. "Phase-contrast imaging of weakly absorbing materials using hard X-rays." In: *Nature* 373.6515 (1995), pp. 595–598. DOI: 10.1038/373595a0.

[126] C. David, B. Nöhammer, H. H. Solak, and E. Ziegler. "Differential x-ray phase contrast imaging using a shearing interferometer." In: *Applied Physics Letters* 81.17 (2002), pp. 3287–3289. DOI: 10.1063/1.1516611.

[127] A. Momose, S. Kawamoto, I. Koyama, Y. Hamaishi, K. Takai, and Y. Suzuki. "Demonstration of X-Ray Talbot Interferometry." In: *Japanese Journal of Applied Physics* 42.Part 2, No. 7B (2003), pp. L866–L868. DOI: 10.1143/jjap.42.1866.

[128] F. Pfeiffer, T. Weitkamp, O. Bunk, and C. David. "Phase retrieval and differential phase-contrast imaging with low-brilliance X-ray sources." In: *Nature Physics* 2.4 (2006), pp. 258–261. DOI: 10.1038/nphys265.

[129] A. Olivo, F. Arfelli, G. Cantatore, R. Longo, R. H. Menk, S. Pani, M. Prest, P. Poropat, L. Rigon, G. Tromba, E. Vallazza, and E. Castelli. "An innovative digital imaging set-up allowing a low-dose approach to phase contrast applications in the medical field." In: *Medical Physics* 28.8 (2001), pp. 1610–1619. DOI: `10.1118/1.1388219`.

[130] P. C. Diemoz, M. Endrizzi, C. K. Hagen, C. Rau, A. Bravin, R. D. Speller, I. K. Robinson, and A. Olivo. "Edge illumination X-ray phase-contrast imaging: nanoradian sensitivity at synchrotrons and translation to conventional sources." In: *Journal of Physics: Conference Series* 499 (2014), p. 012006. DOI: `10.1088/1742-6596/499/1/012006`.

[131] T. Thuering and M. Stampanoni. "Performance and optimization of X-ray grating interferometry." In: *Philosophical Transactions of the Royal Society A: Mathematical, Physical and Engineering Sciences* 372.2010 (2014), p. 20130027. DOI: `10.1098/rsta.2013.0027`.

[132] F. Horn, M. Leghissa, S. Kaeppler, G. Pelzer, J. Rieger, M. Seifert, J. Wandner, T. Weber, T. Michel, C. Riess, and G. Anton. "Implementation of a Talbot-Lau interferometer in a clinical-like c-arm setup: A feasibility study." In: *Scientific Reports* 8.1 (2018). DOI: `10.1038/s41598-018-19482-z`.

[133] G. S. Zimmermann, K. Willer, W. Noichl, T. Urban, M. Frank, F. D. Marco, R. Schick, B. Renger, A. Fingerle, H. Hautmann, B. Haller, P. Meyer, T. Koehler, R. Proksa, H.-I. Maack, A. Yaroshenko, J. V. Berg, K. Rindt, D. Pfeiffer, E. Rummeny, J. Herzen, and F. Pfeiffer. "Performance of the First Dark-Field Chest X-ray System on Patients." In: *Imaging*. European Respiratory Society, 2020. DOI: `10.1183/13993003.congress-2020.850`.

[134] A. Olivo. "Edge-illumination x-ray phase-contrast imaging." In: *Journal of Physics: Condensed Matter* 33.36 (2021), p. 363002. DOI: `10.1088/1361-648x/ac0e6e`.

[135] A. Zamir, C. Hagen, P. C. Diemoz, M. Endrizzi, F. Vittoria, Y. Chen, M. A. Anastasio, and A. Olivo. "Recent advances in edge illumination x-ray phase-contrast tomography." In: *Journal of Medical Imaging* 4.04 (2017), p. 1. DOI: `10.1117/1.jmi.4.4.040901`.

[136] D. Gabor. "Microscopy by reconstructed wave-fronts." In: *Proceedings of the Royal Society of London. Series A. Mathematical and Physical Sciences* 197.1051 (1949), pp. 454–487. DOI: `10.1098/rspa.1949.0075`.

[137] A. Snigirev, I. Snigireva, V. Kohn, S. Kuznetsov, and I. Schelokov. "On the possibilities of x-ray phase contrast microimaging by coherent high-energy synchrotron radiation." In: *Review of Scientific Instruments* 66.12 (1995), pp. 5486–5492. DOI: 10.1063/1.1146073.

[138] P. Cloetens, R. Barrett, J. Baruchel, J.-P. Guigay, and M. Schlenker. "Phase objects in synchrotron radiation hard x-ray imaging." In: *Journal of Physics D: Applied Physics* 29.1 (1996), pp. 133–146. DOI: 10.1088/0022-3727/29/1/023.

[139] S. W. Wilkins, T. E. Gureyev, D. Gao, A. Pogany, and A. W. Stevenson. "Phase-contrast imaging using polychromatic hard X-rays." In: *Nature* 384.6607 (1996), pp. 335–338. DOI: 10.1038/384335a0.

[140] M. Krenkel, A. Markus, M. Bartels, C. Dullin, F. Alves, and T. Salditt. "Phase-contrast zoom tomography reveals precise locations of macrophages in mouse lungs." In: *Sci. Rep.* 5 (2015), p. 09973. DOI: 10.1038/srep09973.

[141] D. Paganin, S. C. Mayo, T. E. Gureyev, P. R. Miller, and S. W. Wilkins. "Simultaneous phase and amplitude extraction from a single defocused image of a homogeneous object." In: *J. Microsc.* 206.Pt 1 (2002), pp. 33–40.

[142] Y. D. Witte, M. Boone, J. Vlassenbroeck, M. Dierick, and L. V. Hoorebeke. "Bronnikov-aided correction for x-ray computed tomography." In: *J. Opt. Soc. Am. A* 26.4 (2009), pp. 890–894. DOI: 10.1364/JOSAA.26.000890.

[143] M. Töpperwien, M. Krenkel, F. Quade, and T. Salditt. "Laboratory-based x-ray phase-contrast tomography enables 3D virtual histology." In: *Proc. SPIE* 9964 (2016), p. 99640I. DOI: 10.1117/12.2246460.

[144] D. Gabor. "A New Microscopic Principle." In: *Nature* 161 (1948), pp. 777–778. DOI: 10.1038/161777a0.

[145] J. Hagemann, M. Töpperwien, and T. Salditt. "Phase retrieval for near-field X-ray imaging beyond linearisation or compact support." In: *Appl. Phys. Lett.* 113.4 (2018). DOI: doi.org/10.1063/1.5029927.

[146] J. Hagemann, A.-L. Robisch, D. R. Luke, C. Homann, T. Hohage, P. Cloetens, H. Suhonen, and T. Salditt. "Reconstruction of wave front and object for inline holography from a set of detection planes." In: *Opt. Express* 22.10 (2014), pp. 11552–11569. DOI: 10.1364/OE.22.011552.

[147] M. Krenkel, M. Toepperwien, F. Alves, and T. Salditt. "Three-dimensional single-cell imaging with x-ray waveguides in the holographic regime." In: *Acta Crystallographica Section A: Foundations and Advances* 73.4 (2017), pp. 282–292.

[148] P. Cloetens, W. Ludwig, J. Baruchel, D. Van Dyck, J. Van Landuyt, J. Guigay, and M. Schlenker. "Holotomography: Quantitative phase tomography with micrometer resolution using hard synchrotron radiation x rays." In: *Applied physics letters* 75.19 (1999), pp. 2912–2914.

[149] L. M. Lohse, A.-L. Robisch, M. Töpperwien, S. Maretzke, M. Krenkel, J. Hagemann, and T. Salditt. "A phase-retrieval toolbox for X-ray holography and tomography." In: *Journal of Synchrotron Radiation* 27.3 (2020), pp. 852–859. DOI: 10.1107/S1600577520002398.

[150] B. Sixou. "Regularization Methods for Phase Retrieval and Phase Contrast Tomography." In: *Abstract and Applied Analysis* 2015 (2015), pp. 1–11. DOI: 10.1155/2015/943501.

[151] J. Radon. "Über die Bestimmung von Funktionen durch ihre Integralwerte längs gewisser Mannigfaltigkeiten." In: *Akad. Wiss.* 69 (1917), pp. 262–277.

[152] T. Buzug. *Einführung in die Computertomographie: Mathematisch-physikalische Grundlagen*. Springer, 2005. ISBN: 9783540208082.

[153] S. J. LaRoque, E. Y. Sidky, and X. Pan. "Accurate image reconstruction from few-view and limited-angle data in diffraction tomography." In: *Journal of the Optical Society of America A* 25.7 (2008), p. 1772. DOI: 10.1364/josaa.25.001772.

[154] B. P. Fahimian, Y. Mao, P. Cloetens, and J. Miao. "Low-dose x-ray phase-contrast and absorption CT using equally sloped tomography." In: *Physics in Medicine and Biology* 55.18 (2010), pp. 5383–5400. DOI: 10.1088/0031-9155/55/18/008.

[155] Y. Chen, D. Gao, C. Nie, L. Luo, W. Chen, X. Yin, and Y. Lin. "Bayesian statistical reconstruction for low-dose X-ray computed tomography using an adaptive-weighting nonlocal prior." In: *Computerized Medical Imaging and Graphics* 33.7 (2009), pp. 495–500. DOI: 10.1016/j.compmedimag.2008.12.007.

[156] H. Zhang, L. Li, K. Qiao, L. Wang, B. Yan, L. Li, and G. Hu. "Image Prediction for Limited-angle Tomography via Deep Learning with Convolutional Neural Network." In: (2016).

[157] X. Yang, V. D. Andrade, W. Scullin, E. L. Dyer, N. Kasthuri, F. D. Carlo, and D. Gürsoy. "Low-dose x-ray tomography through a deep convolutional neural network." In: *Scientific Reports* 8.1 (2018). DOI: 10.1038/s41598-018-19426-7.

[158] J. Dong, J. Fu, and Z. He. "A deep learning reconstruction framework for X-ray computed tomography with incomplete data." In: *PLOS ONE* 14.11 (2019). Ed. by H. Liu, e0224426. DOI: 10.1371/journal.pone.0224426.

[159] A. Khimchenko, H. Deyhle, G. Schulz, G. Schweighauser, J. Hench, N. Chicherova, C. Bikis, S. E. Hieber, and B. Müller. "Extending two-dimensional histology into the third dimension through conventional micro computed tomography." In: *NeuroImage* 139 (2016), pp. 26–36.

[160] M. Saccomano, J. Albers, G. Tromba, M. Dobrivojević Radmilović, S. Gajović, F. Alves, and C. Dullin. "Synchrotron inline phase contrast μCT enables detailed virtual histology of embedded soft-tissue samples with and without staining." In: *Journal of synchrotron radiation* 25.4 (2018), pp. 1153–1161.

[161] I. Zanette, T. Weitkamp, G. L. Duc, and F. Pfeiffer. "X-ray grating-based phase tomography for 3D histology." In: *RSC Advances* 3.43 (2013), p. 19816. DOI: 10.1039/c3ra41372a.

[162] V. Cnudde, B. Masschaele, H. D. Cock, K. Olstad, L. Vlaminck, J. Vlassenbroeck, M. Dierick, Y. Witte, L. V. Hoorebeke, and P. Jacobs. "Virtual histology by means of high-resolution X-ray CT." In: *Journal of Microscopy* 232.3 (2008), pp. 476–485. DOI: 10.1111/j.1365-2818.2008.02142.x.

[163] J. Albers, M. A. Markus, F. Alves, and C. Dullin. "X-ray based virtual histology allows guided sectioning of heavy ion stained murine lungs for histological analysis." In: *Scientific reports* 8.1 (2018), pp. 1–10.

[164] M. Töpperwien, F. Van der Meer, C. Stadelmann, and T. Salditt. "Three-dimensional virtual histology of human cerebellum by X-ray phase-contrast tomography." In: *PNAS* 115.27 (2018), pp. 6940–6945. DOI: doi.org/10.1073/pnas.1801678115.

[165] J. Frohn, D. Pinkert-Leetsch, J. Missbach-Güntner, M. Reichardt, M. Osterhoff, F. Alves, and T. Salditt. "3D virtual histology of human pancreatic tissue by multiscale phase-contrast X-ray tomography." In: *Journal of Synchrotron Radiation* 27.6 (2020), pp. 1707–1719. DOI: 10.1107/s1600577520011327.

[166]   J. Missbach-Guentner, D. Pinkert-Leetsch, C. Dullin, R. Ufartes, D. Hornung, B. Tampe, M. Zeisberg, and F. Alves. "3D virtual histology of murine kidneys –high resolution visualization of pathological alterations by micro computed tomography." In: *Scientific Reports* 8.1 (2018). DOI: 10.1038/s41598-018-19773-5.

[167]   L. A. Walton, R. S. Bradley, P. J. Withers, V. L. Newton, R. E. B. Watson, C. Austin, and M. J. Sherratt. "Morphological Characterisation of Unstained and Intact Tissue Micro-architecture by X-ray Computed Micro- and Nano-Tomography." In: *Scientific Reports* 5.1 (2015). DOI: 10.1038/srep10074.

[168]   M. Eckermann, N. Peruzzi, J. Frohn, M. Bech, E. Englund, B. Veress, T. Salditt, L. B. Dahlin, and B. Ohlsson. "3d phase-contrast nanotomography of unstained human skin biopsies may identify morphological differences in the dermis and epidermis between subjects." In: *Skin Research and Technology* 27.3 (2020), pp. 316–323. DOI: 10.1111/srt.12974.

[169]   M. Ackermann, S. E. Verleden, M. Kuehnel, A. Haverich, T. Welte, F. Laenger, A. Vanstapel, C. Werlein, H. Stark, A. Tzankov, W. W. Li, V. W. Li, S. J. Mentzer, and D. Jonigk. "Pulmonary Vascular Endothelialitis, Thrombosis, and Angiogenesis in Covid-19." In: *New England Journal of Medicine* 383.2 (2020), pp. 120–128. DOI: 10.1056/nejmoa2015432.

[170]   M. Ackermann, S. J. Mentzer, M. Kolb, and D. Jonigk. "Inflammation and intussusceptive angiogenesis in COVID-19: everything in and out of flow." In: *European Respiratory Journal* 56.5 (2020), p. 2003147. DOI: 10.1183/13993003.03147-2020.

[171]   M. Eckermann, J. Frohn, M. Reichardt, M. Osterhoff, M. Sprung, F. Westermeier, A. Tzankov, C. Werlein, M. Kühnel, D. Jonigk, and T. Salditt. "3D virtual pathohistology of lung tissue from Covid-19 patients based on phase contrast X-ray tomography." In: *eLife* 9 (2020). DOI: 10.7554/elife.60408.

[172]   C. Walsh, P. Tafforeau, W. L. Wagner, D. J. Jafree, A. Bellier, C. Werlein, M. P. Kühnel, E. Boller, S. Walker-Samuel, J. L. Robertus, D. A. Long, J. Jacob, S. Marussi, E. Brown, N. Holroyd, D. D. Jonigk, M. Ackermann, and P. D. Lee. "Multiscale three-dimensional imaging of intact human organs down to the cellular scale using hierarchical phase-contrast tomography." In: *biorxiv* (2021). DOI: 10.1101/2021.02.03.429481.

[173]   M. Töpperwien, M. Krenkel, D. Vincenz, F. Stöber, A. M. Oelschlegel, J. Gold-
        schmidt, and T. Salditt. "Three-dimensional mouse brain cytoarchitecture re-
        vealed by laboratory-based x-ray phase-contrast tomography." In: *Sci. Rep.* 7
        (2017), p. 42847.

[174]   M. Eckermann, M. Töpperwien, A.-L. Robisch, F. van der Meer, C. Stadel-
        mann, and T. Salditt. "Phase-contrast x-ray tomography of neuronal tissue at
        laboratory sources with submicron resolution." In: *Journal of Medical Imaging*
        7.01 (2020), p. 1. DOI: 10.1117/1.jmi.7.1.013502.

[175]   B. D. Metscher. "MicroCT for developmental biology: A versatile tool for high-
        contrast 3D imaging at histological resolutions." In: *Developmental Dynamics*
        238.3 (2009), pp. 632–640. DOI: 10.1002/dvdy.21857.

[176]   M. Busse, J. P. Marciniszyn, S. Ferstl, M. A. Kimm, F. Pfeiffer, and T. Gul-
        der. "3D-Non-destructive Imaging through Heavy-Metal Eosin Salt Contrast
        Agents." In: *Chemistry – A European Journal* 27.14 (2021), pp. 4561–4566. DOI:
        10.1002/chem.202005203.

[177]   M. Busse, M. Müller, M. A. Kimm, S. Ferstl, S. Allner, K. Achterhold, J. Herzen,
        and F. Pfeiffer. "Three-dimensional virtual histology enabled through cytoplasm-
        specific X-ray stain for microscopic and nanoscopic computed tomography."
        In: *Proceedings of the National Academy of Sciences* 115.10 (2018), pp. 2293–
        2298. DOI: 10.1073/pnas.1720862115.

[178]   M. Müller, M. A. Kimm, S. Ferstl, S. Allner, K. Achterhold, J. Herzen, F. Pfeif-
        fer, and M. Busse. "Nucleus-specific X-ray stain for 3D virtual histology." In:
        Scientific Reports 8.1 (2018). DOI: 10.1038/s41598-018-36067-y.

[179]   R. S. Stephenson, M. R. Boyett, G. Hart, T. Nikolaidou, X. Cai, A. F. Corno, N.
        Alphonso, N. Jeffery, and J. C. Jarvis. "Contrast Enhanced Micro-Computed
        Tomography Resolves the 3-Dimensional Morphology of the Cardiac Conduc-
        tion System in Mammalian Hearts." In: *PLoS ONE* 7.4 (2012). Ed. by R. K.
        Roeder. DOI: 10.1371/annotation/1baecd19-92b6-4683-b7d7-39c13a3f2e15.

[180]   C. Dullin, R. Ufartes, E. Larsson, S. Martin, M. Lazzarini, G. Tromba, J. Missbach-
        Guentner, D. Pinkert-Leetsch, D. M. Katschinski, and F. Alves. "μCT of ex-
        vivo stained mouse hearts and embryos enables a precise match between 3D
        virtual histology, classical histology and immunochemistry." In: *PLOS ONE*
        12.2 (2017). Ed. by R. K. Roeder, e0170597. DOI: 10.1371/journal.pone.
        0170597.

[181] H. Dejea, P. Garcia-Canadilla, A. C. Cook, E. Guasch, M. Zamora, F. Crispi, M. Stampanoni, B. Bijnens, and A. Bonnin. "Comprehensive Analysis of Animal Models of Cardiovascular Disease using Multiscale X-Ray Phase Contrast Tomography." In: *Scientific Reports* 9.1 (2019). DOI: 10.1038/s41598-019-43407-z.

[182] R. S. Stephenson, P. Agger, P. P. Lunkenheimer, J. Zhao, M. Smerup, P. Niederer, R. H. Anderson, and J. C. Jarvis. "The functional architecture of skeletal compared to cardiac musculature: Myocyte orientation, lamellar unit morphology, and the helical ventricular myocardial band." In: *Clinical Anatomy* 29.3 (2015), pp. 316–332. DOI: 10.1002/ca.22661.

[183] R. S. Stephenson, A. Atkinson, P. Kottas, F. Perde, F. Jafarzadeh, M. Bateman, P. A. Iaizzo, J. Zhao, H. Zhang, R. H. Anderson, J. C. Jarvis, and H. Dobrzynski. "High resolution 3-Dimensional imaging of the human cardiac conduction system from microanatomy to mathematical modeling." In: *Scientific Reports* 7.1 (2017). DOI: 10.1038/s41598-017-07694-8.

[184] R. S. Stephenson, C. B. Jones, R. Guerrero, J. Zhao, R. H. Anderson, and J. C. Jarvis. "High-Resolution Contrast-Enhanced Micro-Computed Tomography to Identify the Cardiac Conduction System in Congenitally Malformed Hearts." In: *JACC: Cardiovascular Imaging* 11.11 (2018), pp. 1706–1712. DOI: 10.1016/j.jcmg.2018.05.016.

[185] V. Baličević, S. Lončarić, R. Cárdenes, A. Gonzalez-Tendero, B. Paun, F. Crispi, C. Butakoff, and B. Bijnens. "Assessment of Myofiber Orientation in High Resolution Phase-Contrast CT Images." In: *Functional Imaging and Modeling of the Heart*. Springer International Publishing, 2015, pp. 111–119. DOI: 10.1007/978-3-319-20309-6_13.

[186] T. Tsukube, N. Yagi, M. Hoshino, Y. Nakashima, K. Nakagawa, and Y. Okita. "Impact of synchrotron radiation-based X-ray phase-contrast tomography on understanding various cardiovascular surgical pathologies." In: *General Thoracic and Cardiovascular Surgery* 63.10 (2015), pp. 590–592. DOI: 10.1007/s11748-015-0565-4.

[187] Y. Kaneko, G. Shinohara, M. Hoshino, H. Morishita, K. Morita, Y. Oshima, M. Takahashi, N. Yagi, Y. Okita, and T. Tsukube. "Intact Imaging of Human Heart Structure Using X-ray Phase-Contrast Tomography." In: *Pediatric Cardiology* 38.2 (2016), pp. 390–393. DOI: 10.1007/s00246-016-1527-z.

[188] G. Shinohara, K. Morita, M. Hoshino, Y. Ko, T. Tsukube, Y. Kaneko, H. Morishita, Y. Oshima, H. Matsuhisa, R. Iwaki, M. Takahashi, T. Matsuyama, K. Hashimoto, and N. Yagi. "Three Dimensional Visualization of Human Cardiac Conduction Tissue in Whole Heart Specimens by High-Resolution Phase-Contrast CT Imaging Using Synchrotron Radiation." In: *World Journal for Pediatric and Congenital Heart Surgery* 7.6 (2016), pp. 700–705. DOI: 10.1177/2150135116675844.

[189] A. Zamir, M. Endrizzi, C. K. Hagen, F. A. Vittoria, L. Urbani, P. D. Coppi, and A. Olivo. "Robust phase retrieval for high resolution edge illumination x-ray phase-contrast computed tomography in non-ideal environments." In: *Scientific Reports* 6.1 (2016). DOI: 10.1038/srep31197.

[190] I. Mirea, F. Varray, Y. M. Zhu, L. Fanton, M. Langer, P. S. Jouk, G. Michalowicz, Y. Usson, and I. E. Magnin. "Very High-Resolution Imaging of Post-Mortem Human Cardiac Tissue Using X-Ray Phase Contrast Tomography." In: *Functional Imaging and Modeling of the Heart*. Springer International Publishing, 2015, pp. 172–179. DOI: 10.1007/978-3-319-20309-6_20.

[191] F. Varray, I. Mirea, M. Langer, F. Peyrin, L. Fanton, and I. E. Magnin. "Extraction of the 3D local orientation of myocytes in human cardiac tissue using X-ray phase-contrast micro-tomography and multi-scale analysis." In: *Medical Image Analysis* 38 (2017), pp. 117–132. DOI: 10.1016/j.media.2017.02.006.

[192] S. Wang, I. Mirea, F. Varray, W.-Y. Liu, and I. E. Magnin. "Investigating the 3D Local Myocytes Arrangement in the Human LV Mid-Wall with the Transverse Angle." In: *Functional Imaging and Modeling of the Heart*. Springer International Publishing, 2019, pp. 208–216. DOI: 10.1007/978-3-030-21949-9_23.

[193] P. Garcia-Canadilla, H. Dejea, A. Bonnin, V. Balicevic, S. Loncaric, C. Zhang, C. Butakoff, J. Aguado-Sierra, M. Vázquez, L. H. Jackson, D. J. Stuckey, C. Rau, M. Stampanoni, B. Bijnens, and A. C. Cook. "Complex Congenital Heart Disease Associated With Disordered Myocardial Architecture in a Midtrimester Human Fetus." In: *Circulation: Cardiovascular Imaging* 11.10 (2018). DOI: 10.1161/circimaging.118.007753.

[194] A. Gonzalez-Tendero, C. Zhang, V. Balicevic, R. Cárdenes, S. Loncaric, C. Butakoff, B. Paun, A. Bonnin, P. Garcia-Cañadilla, E. Muñoz-Moreno, E. Gratacós, F. Crispi, and B. Bijnens. "Whole heart detailed and quantitative anatomy,

myofibre structure and vasculature from X-ray phase-contrast synchrotron radiation-based micro computed tomography." In: *Eur Heart J Cardiovasc Imaging* 18.7 (2017), pp. 732–741. DOI: 10.1093/ehjci/jew314.

[195]   M. Reichardt, J. Frohn, M. Toepperwien, J.-D. Nicolas, A. Markus, F. Alves, and T. Salditt. "Nanoscale holographic tomography of heart tissue with x-ray waveguide optics." In: *Proc. SPIE 10391* (2017). Ed. by B. Müller and G. Wang. DOI: 10.1117/12.2276648.

[196]   T. Salditt, M. Osterhoff, M. Krenkel, R. N. Wilke, M. Priebe, M. Bartels, S. Kalbfleisch, and M. Sprung. "Compound focusing mirror and X-ray waveguide optics for coherent imaging and nano-diffraction." In: *Journal of synchrotron radiation* 22.4 (2015), pp. 867–878. DOI: 10.1107/S1600577515007742.

[197]   I. Planinc, P. Garcia-Canadilla, H. Dejea, I. Ilic, E. Guasch, M. Zamora, F. Crispi, M. Stampanoni, D. Milicic, B. Bijnens, A. Bonnin, and M. Cikes. "Comprehensive assessment of myocardial remodeling in ischemic heart disease by synchrotron propagation based X-ray phase contrast imaging." In: *Scientific Reports* 11.1 (2021). DOI: 10.1038/s41598-021-93054-6.

[198]   W. H. Bragg and W. L. Bragg. "The reflection of X-rays by crystals." In: *Proceedings of the Royal Society of London. Series A, Containing Papers of a Mathematical and Physical Character* 88.605 (1913), pp. 428–438. DOI: 10.1098/rspa.1913.0040.

[199]   S. Günther et al. "X-ray screening identifies active site and allosteric inhibitors of SARS-CoV-2 main protease." In: *Science* 372.6542 (2021), pp. 642–646. DOI: 10.1126/science.abf7945.

[200]   A. McPherson and J. A. Gavira. "Introduction to protein crystallization." In: *Acta Crystallographica Section F Structural Biology Communications* 70.1 (2013), pp. 2–20. DOI: 10.1107/s2053230x13033141.

[201]   J. Holcomb, N. Spellmon, Y. Zhang, M. Doughan, C. Li, and Z. Yang. "Protein crystallization: Eluding the bottleneck of X-ray crystallography." In: *AIMS Biophysics* 4.4 (2017), pp. 557–575. DOI: 10.3934/biophy.2017.4.557.

[202]   R. O. Herzog and W. Jancke. "Verwendung von Röntgenstrahlen zur Untersuchung metamikroskopischer biologischer Strukturen." In: *Festschrift der Kaiser Wilhelm Gesellschaft ⸗ur Förderung der Wissenschaften ⸗u ihrem Zehnjährigen Jubiläum Dargebracht von ihren Instituten*. Springer Berlin Heidelberg, 1921, pp. 118–120. DOI: 10.1007/978-3-662-30319-1_17.

[203] W. T. Astbury. "Some problems in the X-ray analysis of the structure of animal hairs and other protein fibres." In: *Transactions of the Faraday Society* 29.140 (1933), p. 193. DOI: 10.1039/tf9332900193.

[204] J. D. Watson and F. H. C. Crick. "Molecular Structure of Nucleic Acids: A Structure for Deoxyribose Nucleic Acid." In: *Nature* 171.4356 (1953), pp. 737–738. DOI: 10.1038/171737a0.

[205] R. S. Bear. "Small-angle X-ray Diffraction Studies On Muscle." In: *Journal of the American Chemical Society* 67.9 (1945), pp. 1625–1626. DOI: 10.1021/ja01225a516.

[206] H. E. Huxley. "X-ray analysis and the problem of muscle." In: *Proceedings of the Royal Society of London. Series B - Biological Sciences* 141.902 (1953), pp. 59–62. DOI: 10.1098/rspb.1953.0017.

[207] W. Kühne. *Untersuchungen über das Protoplasma und die Contractilität*. Leipzig: Wilhelm Engelmann, 1864.

[208] W. Krause. *Die motorischen Endplatten der quergestreiften Muskelfasern*. Hahn 'sche Hofbuchhandlung, 1869.

[209] H. Huxley and J. Hanson. "Changes in the Cross-Striations of Muscle during Contraction and Stretch and their Structural Interpretation." In: *Nature* 173.4412 (1954), pp. 973–976. DOI: 10.1038/173973a0.

[210] A. F. Huxley and R. Niedergerke. "Structural changes in muscle during contraction: interference microscopy of living muscle fibres." In: *Nature* 173.4412 (1954), p. 971.

[211] M. K. Reedy, K. C. Holmes, and R. T. Tregear. "Induced Changes in Orientation of the Cross-Bridges of Glycerinated Insect Flight Muscle." In: *Nature* 207.5003 (1965), pp. 1276–1280. DOI: 10.1038/2071276a0.

[212] S. Lowey, H. S. Slayter, A. G. Weeds, and H. Baker. "Substructure of the myosin molecule." In: *Journal of Molecular Biology* 42.1 (1969), pp. 1–29. DOI: 10.1016/0022-2836(69)90483-5.

[213] G. Elliott, J. Lowy, and C. Worthington. "An X-ray and light-diffraction study of the filament lattice of striated muscle in the living state and in rigor." In: *Journal of Molecular Biology* 6.4 (1963), 295–IN9. DOI: 10.1016/s0022-2836(63)80090-x.

[214]   H. Huxley and W. Brown. "The low-angle X-ray diagram of vertebrate striated muscle and its behaviour during contraction and rigor." In: *Journal of Molecular Biology* 30.2 (1967), 383–IN16. DOI: 10.1016/s0022-2836(67)80046-9.

[215]   J. B. Leigh and G. Rosenbaum. "Synchrotron X-Ray Sources: A New Tool in Biological Structural and Kinetic Analysis." In: *Annual Review of Biophysics and Bioengineering* 5.1 (1976), pp. 239–270. DOI: 10.1146/annurev.bb.05.060176.001323.

[216]   B. Kiss, E.-J. Lee, W. Ma, F. W. Li, P. Tonino, S. M. Mijailovich, T. C. Irving, and H. L. Granzier. "Nebulin stiffens the thin filament and augments cross-bridge interaction in skeletal muscle." In: *Proceedings of the National Academy of Sciences* 115.41 (2018), pp. 10369–10374. DOI: 10.1073/pnas.1804726115.

[217]   G. ROSENBAUM, K. C. HOLMES, and J. WITZ. "Synchrotron Radiation as a Source for X-ray Diffraction." In: *Nature* 230.5294 (1971), pp. 434–437. DOI: 10.1038/230434a0.

[218]   H. E. Huxley, R. M. Simmons, A. R. Faruqi, M. Kress, J. Bordas, and M. H. Koch. "Millisecond time-resolved changes in x-ray reflections from contracting muscle during rapid mechanical transients, recorded using synchrotron radiation." In: *Proceedings of the National Academy of Sciences* 78.4 (1981), pp. 2297–2301. DOI: 10.1073/pnas.78.4.2297.

[219]   M. Reconditi, M. Linari, L. Lucii, A. Stewart, Y.-B. Sun, P. Boesecke, T. Narayanan, R. F. Fischetti, T. Irving, G. Piazzesi, M. Irving, and V. Lombardi. "The myosin motor in muscle generates a smaller and slower working stroke at higher load." In: *Nature* 428.6982 (2004), pp. 578–581. DOI: 10.1038/nature02380.

[220]   M. Linari, E. Brunello, M. Reconditi, L. Fusi, M. Caremani, T. Narayanan, G. Piazzesi, V. Lombardi, and M. Irving. "Force generation by skeletal muscle is controlled by mechanosensing in myosin filaments." In: *Nature* 528.7581 (2015), pp. 276–279.

[221]   K. Wakabayashi, Y. Sugimoto, H. Tanaka, Y. Ueno, Y. Takezawa, and Y. Amemiya. "X-ray diffraction evidence for the extensibility of actin and myosin filaments during muscle contraction." In: *Biophysical Journal* 67.6 (1994), pp. 2422–2435. DOI: 10.1016/s0006-3495(94)80729-5.

[222]   H. Huxley, A. Stewart, H. Sosa, and T. Irving. "X-ray diffraction measurements of the extensibility of actin and myosin filaments in contracting muscle." In:

Biophysical Journal 67.6 (1994), pp. 2411–2421. DOI: 10.1016/s0006-3495(94) 80728-3.

[223] A. Sakdinawat and D. Attwood. "Nanoscale X-ray imaging." In: *Nature Photonics* 4.12 (2010), pp. 840–848.

[224] A. Snigirev and I. Snigireva. "High energy X-ray micro-optics." In: *Comptes Rendus Physique* 9.5-6 (2008), pp. 507–516. DOI: 10.1016/j.crhy.2008.02. 003.

[225] C. Riekel. "New avenues in x-ray microbeam experiments." In: *Reports on Progress in Physics* 63.3 (2000), pp. 233–262. DOI: 10.1088/0034-4885/63/3/201.

[226] J.-D. Nicolas, M. Bernhardt, S. F. Schlick, M. Tiburcy, W.-H. Zimmermann, A. Khan, A. Markus, F. Alves, K. Toischer, and T. Salditt. "X-ray diffraction imaging of cardiac cells and tissue." In: *Progress in biophysics and molecular biology* (2018). DOI: 10.1016/j.pbiomolbio.2018.05.012.

[227] J.-D. Nicolas, M. Bernhardt, A. Markus, F. Alves, M. Burghammer, and T. Salditt. "Scanning X-ray diffraction on cardiac tissue: automatized data analysis and processing." In: *J. Synchrotron Rad.* 24.6 (2017), pp. 1163–1172. DOI: 10.1107/ s1600577517011936.

[228] J.-D. Nicolas, A. Khan, A. Markus, B. A. Mohamed, K. Toischer, F. Alves, and T. Salditt. "X-ray diffraction and second harmonic imaging reveal new insights into structural alterations caused by pressure-overload in murine hearts." In: *Scientific Reports* 10.1 (2020). DOI: 10.1038/s41598-020-76163-6.

[229] B. Weinhausen, J.-F. Nolting, C. Olendrowitz, J. Langfahl-Klabes, M. Reynolds, T. Salditt, and S. Köster. "x-ray nano-diffraction on cytoskeletal networks." In: *New J. Phys.* 14.8 (2012), p. 085013.

[230] B. Weinhausen, O. Saldanha, R. N. Wilke, C. Dammann, M. Priebe, M. Burghammer, M. Sprung, and S. Köster. "Scanning X-Ray Nanodiffraction on Living Eukaryotic Cells in Microfluidic Environments." In: *Physical Review Letters* 112 (8 2014), p. 088102.

[231] M. Priebe, M. Bernhardt, C. Blum, M. Tarantola, E. Bodenschatz, and T. Salditt. "Scanning X-Ray Nanodiffraction on Dictyostelium discoideum." In: *Biophys. J.* 107.11 (2014), pp. 2662–2673. DOI: 10.1016/j.bpj.2014.10.027.

[232] M. Bernhardt, M. Priebe, M. Osterhoff, C. Wollnik, A. Diaz, T. Salditt, and F. Rehfeldt. "X-Ray Micro- and Nanodiffraction Imaging on Human Mesenchymal Stem Cells and Differentiated Cells." In: *Biophys. J.* 110.3 (2016), pp. 680–690. DOI: 10.1016/j.bpj.2015.12.017.

[233] J.-D. Nicolas, M. Bernhardt, M. Krenkel, C. Richter, S. Luther, and T. Salditt. "Combined scanning X-ray diffraction and holographic imaging of cardiomyocytes." In: *Journal of Applied Crystallography* 50.2 (2017), pp. 612–620. DOI: 10.1107/S1600576717003351.

[234] M. Bernhardt, J.-D. Nicolas, M. Osterhoff, H. Mittelstädt, M. Reuss, B. Harke, A. Wittmeier, M. Sprung, S. Köster, and T. Salditt. "Correlative microscopy approach for biology using x-ray holography, x-ray scanning diffraction, and STED microscopy." In: *Nature Communications* 9.3641 (2018). DOI: 10.1038/s41467-018-05885-z.

[235] M. Bernhardt, J.-D. Nicolas, M. Osterhoff, H. Mittelstädt, M. Reuss, B. Harke, A. Wittmeier, M. Sprung, S. Köster, and T. Salditt. "A beamline-compatible STED microscope for combined visible-light and X-ray studies of biological matter." In: *Journal of Synchrotron Radiation* 26.4 (2019), pp. 1144–1151. DOI: 10.1107/s1600577519004089.

[236] M. Bernhardt, J.-D. Nicolas, M. Eckermann, B. Eltzner, F. Rehfeldt, and T. Salditt. "Anisotropic x-ray scattering and orientation fields in cardiac tissue cells." In: *New Journal of Physics* 19.1 (2017), p. 013012.

[237] H. Scheffel, H. Alkadhi, A. Plass, R. Vachenauer, L. Desbiolles, O. Gaemperli, T. Schepis, T. Frauenfelder, T. Schertler, L. Husmann, J. Grunenfelder, M. Genoni, P. A. Kaufmann, B. Marincek, and S. Leschka. "Accuracy of dual-source CT coronary angiography: first experience in a high pre-test probability population without heart rate control." In: *European Radiology* 16.12 (2006), pp. 2739–2747. DOI: 10.1007/s00330-006-0474-0.

[238] K. Degenhardt, A. C. Wright, D. Horng, A. Padmanabhan, and J. A. Epstein. "Rapid 3D Phenotyping of Cardiovascular Development in Mouse Embryos by Micro-CT With Iodine Staining." In: *Circulation: Cardiovascular Imaging* 3.3 (2010), pp. 314–322. DOI: 10.1161/circimaging.109.918482.

[239] H. Dejea, P. Garcia-Canadilla, M. Stampanoni, M. Zamora, F. Crispi, B. Bijnens, and A. Bonnin. "Microstructural Analysis of Cardiac Endomyocardial Biopsies with Synchrotron Radiation-Based X-Ray Phase Contrast Imaging."

In: *Functional Imaging and Modelling of the Heart*. Springer International Publishing, 2017, pp. 23–31. DOI: `10.1007/978-3-319-59448-4_3`.

[240]   F. Varray, L. Wang, L. Fanton, Y.-M. Zhu, and I. E. Magnin. "High Resolution Extraction of Local Human Cardiac Fibre Orientations." In: *Functional Imaging and Modeling of the Heart*. Springer Berlin Heidelberg, 2013, pp. 150–157. DOI: `10.1007/978-3-642-38899-6_18`.

[241]   L. Silverman. "The Reactivity And Staining Of Tissue Proteins With Phosphotungstic Acid." In: *The Journal of Cell Biology* 40.3 (1969), pp. 761–767. DOI: `10.1083/jcb.40.3.761`.

[242]   M. Patzelt, J. Mrzilkova, J. Dudak, F. Krejci, J. Zemlicka, J. Karch, V. Musil, J. Rosina, V. Sykora, B. Horehledova, and P. Zach. "Ethanol fixation method for heart and lung imaging in micro-CT." In: *Japanese Journal of Radiology* 37.6 (2019), pp. 500–510. DOI: `10.1007/s11604-019-00830-6`.

[243]   O. Hemberg, M. Otendal, and H. Hertz. "Liquid-metal-jet anode electron-impact x-ray source." In: *Appl. Phys. Lett.* 83.7 (2003), pp. 1483–1485.

[244]   M. Krenkel, M. Töpperwien, C. Dullin, F. Alves, and T. Salditt. "Propagation-based phase-contrast tomography for high-resolution lung imaging with laboratory sources." In: *AIP Advances* 6.3, 035007 (2016), p. 035007. DOI: `10.1063/1.4943898`.

[245]   M. Töpperwien, R. Gradl, D. Keppeler, M. Vassholz, A. Meyer, R. Hessler, K. Achterhold, B. Gleich, M. Dierolf, F. Pfeiffer, T. Moser, and T. Salditt. "Propagation-based phase-contrast x-ray tomography of cochlea using a compact synchrotron source." In: *Sci. Rep.* 8 (2018), p. 4922.

[246]   D. Paganin and K. A. Nugent. "Noninterferometric phase imaging with partially coherent light." In: *Physical Review letters* 80.12 (1998), p. 2586.

[247]   A. Groso, R. Abela, and M. Stampanoni. "Implementation of a fast method for high resolution phase contrast tomography." In: *Opt. Express* 14.18 (2006), pp. 8103–8110.

[248]   W. J. Palenstijn, K. J. Batenburg, and J. Sijbers. "The ASTRA tomography toolbox." In: *13th International Conference on Computational and Mathematical Methods in Science and Engineering. CMMSE*. 2013.

[249]   R. A. Ketcham. "New algorithms for ring artifact removal." In: *Proc. SPIE* 6318 (2006), 63180O. DOI: `10.1117/12.680939`.

[250] M. van Heel and M. Schatz. "Fourier shell correlation threshold criteria." In: *J. Struct. Biol.* 151.3 (2005), pp. 250–262. DOI: 10.1016/j.jsb.2005.05.009.

[251] S. Faulwetter, T. Dailianis, A. Vasileiadou, and C. Arvanitidis. "Contrast enhancing techniques for the application of micro-CT in marine biodiversity studies." In: *Microsc. Anal.* 27 (2013), pp. 4–7.

[252] P. J. Basser and C. Pierpaoli. "Microstructural and Physiological Features of Tissues Elucidated by Quantitative-Diffusion-Tensor MRI." In: *Journal of Magnetic Resonance, Series B* 111.3 (1996), pp. 209–219. DOI: 10.1006/jmrb.1996.0086.

[253] R. H. Anderson, S. Y. Ho, D. Sanchez-Quintana, K. Redmann, and P. P. Lunkenheimer. "Heuristic problems in defining the three-dimensional arrangement of the ventricular myocytes." In: *The Anatomical Record Part A: Discoveries in Molecular, Cellular, and Evolutionary Biology* 288A.6 (2006), pp. 579–586. DOI: 10.1002/ar.a.20330.

[254] L. I. Krehl. *Beiträge zur kenntnis der füllung und entleerung des herzens*. Hirzel, 1891.

[255] B. Bijnens, M. Cikes, C. Butakoff, M. Sitges, and F. Crispi. "Myocardial Motion and Deformation: What Does It Tell Us and How Does It Relate to Function?" In: *Fetal Diagnosis and Therapy* 32.1-2 (2012), pp. 5–16. DOI: 10.1159/000335649.

[256] M. Reichardt, M. Töpperwien, A. Khan, F. Alves, and T. Salditt. "Fiber orientation in a whole mouse heart reconstructed by laboratory phase-contrast micro-CT." In: *Proc. SPIE 11113 Developments in X-Ray Tomography XII, 111130S* (2019). Ed. by B. Müller and G. Wang. DOI: 10.1117/12.2527744.

[257] S. Maretzke. "A uniqueness result for propagation-based phase contrast imaging from a single measurement." In: *Inverse Problems* 31.6 (2015), p. 065003.

[258] M. Bartels, M. Krenkel, P. Cloetens, W. Möbius, and T. Salditt. "Myelinated mouse nerves studied by x-ray phase contrast zoom tomography." In: *Journal of structural biology* 192.3 (2015), pp. 561–568.

[259] C. Homann, T. Hohage, J. Hagemann, A.-L. Robisch, and T. Salditt. "Validity of the empty-beam correction in near-field imaging." In: *Phys. Rev. A* 91 (1 2015), p. 013821. DOI: 10.1103/PhysRevA.91.013821.

[260]   A.-L. Robisch, J. Wallentin, A. Pacureanu, P. Cloetens, and T. Saldiu. "Holographic imaging with a hard x-ray nanoprobe: ptychographic versus conventional phase retrieval." In: *Opt. Lett.* 41.23 (2016), pp. 5519–5522. DOI: 10.1364/OL.41.005519.

[261]   P. Villanueva-Perez, F. Arcadu, P. Cloetens, and M. Stampanoni. "Contrast-transfer-function phase retrieval based on compressed sensing." In: *Opt. Lett.* 42.6 (2017), pp. 1133–1136. DOI: 10.1364/OL.42.001133.

[262]   W. Van Aarle, W. J. Palenstijn, J. Cant, E. Janssens, F. Bleichrodt, A. Dabravolski, J. De Beenhouwer, K. J. Batenburg, and J. Sijbers. "Fast and flexible X-ray tomography using the ASTRA toolbox." In: *Optics express* 24.22 (2016), pp. 25129–25147.

[263]   M. Töpperwien, A. Markus, F. Alves, and T. Saldiu. "Contrast enhancement for visualizing neuronal cytoarchitecture by propagation-based x-ray phase-contrast tomography." In: *NeuroImage* 199 (2019), pp. 70–80. DOI: 10.1016/j.neuroimage.2019.05.043.

[264]   U. Ayachit. *The ParaView Guide: A Parallel Visualization Application*. Kitware Inc. 2015. ISBN: 978-1930934306.

[265]   T. C. Irving, J. Konhilas, D. Perry, R. Fischetti, and P. P. de Tombe. "Myofilament lattice spacing as a function of sarcomere length in isolated rat myocardium." In: *American Journal of Physiology-Heart and Circulatory Physiology* 279.5 (2000), pp. 2568–2573.

[266]   M. Hoffmann, H. Kleine-Weber, S. Schroeder, N. Krüger, T. Herrler, S. Erichsen, T. S. Schiergens, G. Herrler, N.-H. Wu, A. Nitsche, M. A. Müller, C. Drosten, and S. Pöhlmann. "SARS-CoV-2 Cell Entry Depends on ACE2 and TMPRSS2 and Is Blocked by a Clinically Proven Protease Inhibitor." In: *Cell* 181.2 (2020), 271–280.e8. DOI: 10.1016/j.cell.2020.02.052.

[267]   M. C. Bois, N. A. Boire, A. J. Layman, M.-C. Aubry, M. P. Alexander, A. C. Roden, C. E. Hagen, R. A. Quinton, C. Larsen, Y. Erben, R. Majumdar, S. M. Jenkins, B. R. Kipp, P. T. Lin, and J. J. Maleszewski. "COVID-19–Associated Nonocclusive Fibrin Microthrombi in the Heart." In: *Circulation* 143.3 (2021), pp. 230–243. DOI: 10.1161/circulationaha.120.050754.

[268]   S. J. Mentzer and M. A. Konerding. "Intussusceptive angiogenesis: expansion and remodeling of microvascular networks." In: *Angiogenesis* 17 (3 2014), pp. 499–509. DOI: 10.1007/s10456-014-9428-3.

[269] M. Ackermann and M. A. Konerding. "Vascular Casting for the Study of Vascular Morphogenesis." In: *Vascular Morphogenesis: Methods and Protocols.* Ed. by D. Ribatti. Vol. 1214. New York, NY: Springer New York, 2015, pp. 49–66. ISBN: 978-1-4939-1462-3. DOI: 10.1007/978-1-4939-1462-3_5.

[270] P. Erba, R. Ogawa, M. Ackermann, A. Adini, L. F. Miele, P. Dastouri, D. Helm, S. J. Mentzer, R. J. D'Amato, G. F. Murphy, M. A. Konerding, and D. P. Orgill. "Angiogenesis in wounds treated by microdeformational wound therapy." In: *Annals of surgery* 253 (2 2011), pp. 402–409. DOI: 10.1097/SLA.0b013e31820563a8.

[271] M. Ackermann, W. L. Wagner, P. Rellecke, P. Akhyari, U. Boeken, and P. Reinecke. "Parvovirus B19-induced angiogenesis in fulminant myocarditis." In: *European heart journal* 41 (12 2020), p. 1309. DOI: 10.1093/eurheartj/ehaa092.

[272] M. Ackermann, B. A. Morse, V. Delventhal, I. M. Carvajal, and M. A. Konerding. "Anti-VEGFR2 and anti-IGF-1R-Adnectins inhibit Ewing's sarcoma A673-xenograft growth and normalize tumor vascular architecture." In: *Angiogenesis* 15 (4 2012), pp. 685–695. DOI: 10.1007/s10456-012-9294-9.

[273] M. Nishiga, D. W. Wang, Y. Han, D. B. Lewis, and J. C. Wu. "COVID-19 and cardiovascular disease: from basic mechanisms to clinical perspectives." In: *Nature Reviews Cardiology* 17.9 (2020), pp. 543–558. DOI: 10.1038/s41569-020-0413-9.

[274] T. Menter, J. Haslbauer, R. Nienhold, S. Savic, H. Hopfer, N. Deigendesch, S. Frank, D. Turek, W. N. and. Pargger H, S. Bassetti, J. Leuppi, G. Cathomas, M. Tolnay, K. Mertz, and A. Tzankov. "Post-mortem examination of COVID19 patients diffuse alveolar damage with massive capillary congestion and variegated findings of lungs and other organs suggesting vascular dysfunction." In: *Histopathology* (2020).

[275] G. Gauchotte, V. Venard, M. Segondy, C. Cadoz, A. Esposito-Fava, D. Barraud, and G. Louis. "SARS-Cov-2 fulminant myocarditis: an autopsy and histopathological case study." In: *International Journal of Legal Medicine* 135.2 (2021), pp. 577–581. DOI: 10.1007/s00414-020-02500-z.

[276] R. Kawakami, A. Sakamoto, K. Kawai, A. Gianatti, D. Pellegrini, A. Nasr, B. Kutys, L. Guo, A. Cornelissen, M. Mori, Y. Sato, I. Pescetelli, M. Brivio, M. Romero, G. Guagliumi, R. Virmani, and A. V. Finn. "Pathological Evidence for

SARS-CoV-2 as a Cause of Myocarditis." In: *Journal of the American College of Cardiology* 77.3 (2021), pp. 314–325. DOI: 10.1016/j.jacc.2020.11.031.

[277] G. Tavazzi, C. Pellegrini, M. Maurelli, M. Belliato, F. Sciutti, A. Bottazzi, P. A. Sepe, T. Resasco, R. Camporotondo, R. Bruno, F. Baldanti, S. Paolucci, S. Pelenghi, G. A. Iotti, F. Mojoli, and E. Arbustini. "Myocardial localization of coronavirus in COVID-19 cardiogenic shock." In: *European Journal of Heart Failure* 22.5 (2020), pp. 911–915. DOI: 10.1002/ejhf.1828.

[278] C. L. Albert, A. E. Carmona-Rubio, A. J. Weiss, G. G. Procop, R. C. Starling, and E. R. Rodriguez. "The Enemy Within." In: *Circulation* 142.19 (2020), pp. 1865–1870. DOI: 10.1161/circulationaha.120.050097.

[279] P. Wenzel, S. Kopp, S. Göbel, T. Jansen, M. Geyer, F. Hahn, K.-F. Kreitner, F. Escher, H.-P. Schultheiss, and T. Münzel. "Evidence of SARS-CoV-2 mRNA in endomyocardial biopsies of patients with clinically suspected myocarditis tested negative for COVID-19 in nasopharyngeal swab." In: *Cardiovascular Research* 116.10 (2020), pp. 1661–1663. DOI: 10.1093/cvr/cvaa160.

[280] M. K. Halushka and R. S. V. Heide. "Myocarditis is rare in COVID-19 autopsies: cardiovascular findings across 277 postmortem examinations." In: *Cardiovascular Pathology* 50 (2021), p. 107300. DOI: 10.1016/j.carpath.2020.107300.

[281] Y.-Y. Zheng, Y.-T. Ma, J.-Y. Zhang, and X. Xie. "COVID-19 and the cardiovascular system." In: *Nature Reviews Cardiology* 17.5 (2020), pp. 259–260. DOI: 10.1038/s41569-020-0360-5.

[282] D. Wichmann et al. "Autopsy Findings and Venous Thromboembolism in Patients With COVID-19." In: *Annals of Internal Medicine* 173.4 (2020), pp. 268–277. DOI: 10.7326/m20-2003.

[283] C. Chen, Y. Zhou, and D. W. Wang. "SARS-CoV-2: a potential novel etiology of fulminant myocarditis." In: *Herz* 45.3 (2020), pp. 230–232. DOI: 10.1007/s00059-020-04909-z.

[284] Q. Deng, B. Hu, Y. Zhang, H. Wang, X. Zhou, W. Hu, Y. Cheng, J. Yan, H. Ping, and Q. Zhou. "Suspected myocardial injury in patients with COVID-19: Evidence from front-line clinical observation in Wuhan, China." In: *International Journal of Cardiology* 311 (2020), pp. 116–121. DOI: 10.1016/j.ijcard.2020.03.087.

[285]   J.-H. Zeng, Y.-X. Liu, J. Yuan, F.-X. Wang, W.-B. Wu, J.-X. Li, L.-F. Wang, H. Gao, Y. Wang, C.-F. Dong, Y.-J. Li, X.-J. Xie, C. Feng, and L. Liu. "First case of COVID-19 complicated with fulminant myocarditis: a case report and insights." In: *Infection* 48.5 (2020), pp. 773–777. DOI: 10.1007/s15010-020-01424-5.

[286]   M. Bartels, V. H. Hernandez, M. Krenkel, T. Moser, and T. Salditt. "Phase contrast tomography of the mouse cochlea at microfocus x-ray sources." In: *Applied Physics Letters* 103.8 (2013), p. 083703.

[287]   L. D. Turner, B. Dhal, J. Hayes, A. Mancuso, K. A. Nugent, D. Paterson, R. E. Scholten, C. Tran, and A. G. Peele. "X-ray phase imaging: Demonstration of extended conditions with homogeneous objects." In: *Optics express* 12.13 (2004), pp. 2960–2965.

[288]   W. Van Aarle, W. J. Palenstijn, J. De Beenhouwer, T. Altantzis, S. Bals, K. J. Batenburg, and J. Sijbers. "The ASTRA Toolbox: A platform for advanced algorithm development in electron tomography." In: *Ultramicroscopy* 157 (2015), pp. 35–47.

[289]   A. Miettinen, I. V. Oikonomidis, A. Bonnin, and M. Stampanoni. "NRStitcher: non-rigid stitching of terapixel-scale volumetric images." In: *Bioinformatics* 35.24 (2019), pp. 5290–5297.

[290]   M. Krause, J.-M. Hausherr, B. Burgeth, C. Herrmann, and W. Krenkel. "Determination of the fibre orientation in composites using the structure tensor and local X-ray transform." In: *Journal of Materials Science* 45.4 (2010), pp. 888–896.

[291]   C.-F. Westin, S. E. Maier, H. Mamata, A. Nabavi, F. A. Jolesz, and R. Kikinis. "Processing and visualization for diffusion tensor MRI." In: *Medical image analysis* 6.2 (2002), pp. 93–108.

[292]   F. Milletari, N. Navab, and S.-A. Ahmadi. "V-net: Fully convolutional neural networks for volumetric medical image segmentation." In: *2016 fourth international conference on 3D vision (3DV)*. IEEE. 2016, pp. 565–571.

[293]   O. Ronneberger, P. Fischer, and T. Brox. "U-net: Convolutional networks for biomedical image segmentation." In: *International Conference on Medical image computing and computer-assisted intervention*. Springer. 2015, pp. 234–241.

[294]   D. P. Kingma and J. Ba. "Adam: A Method for Stochastic Optimization." In: *International Conference on Learning Representations, ICLR*. 2015, pp. 1–15.

[295]   Ö. Çiçek, A. Abdulkadir, S. S. Lienkamp, T. Brox, and O. Ronneberger. "3D U-Net: learning dense volumetric segmentation from sparse annotation." In: *International conference on medical image computing and computer-assisted intervention*. Springer. 2016, pp. 424–432.

[296]   P. M. Jensen, C. H. Trinderup, A. B. Dahl, and V. A. Dahl. "Zonohedral Approximation of Spherical Structuring Element for Volumetric Morphology." In: *Scandinavian Conference on Image Analysis*. Springer. 2019, pp. 128–139. DOI: 10.1007/978-3-030-20205-7_11.

[297]   T.-C. Lee, R. L. Kashyap, and C.-N. Chu. "Building skeleton models via 3-D medial surface axis thinning algorithms." In: *CVGIP: Graphical Models and Image Processing* 56.6 (1994), pp. 462–478. DOI: 10.1006/cgip.1994.1042.

[298]   P. Kollmannsberger, M. Kerschnitzki, F. Repp, W. Wagermaier, R. Weinkamer, and P. Fratzl. "The small world of osteocytes: connectomics of the lacuno-canalicular network in bone." In: *New Journal of Physics* 19.7 (2017), p. 073019. DOI: 10.1088/1367-2630/aa764b.

[299]   M. Gashler and T. Martinez. "Robust manifold learning with cyclecut." In: *Connection Science* 24.1 (2012), pp. 57–69. DOI: 10.1080/09540091.2012.664122.

[300]   M. Reichardt, P. Møller Jensen, V. Andersen Dahl, A. Bjorholm Dahl, M. Ackermann, H. Shah, F. Länger, C. Werlein, M. Kühnel, D. Jonigk, and T. Salditt. *3D virtual Histopathology of Cardiac Tissue from Covid-19 Patients based on Phase-Contrast X-ray Tomography*. Version 1. Zenodo, 2021. DOI: 110.5281/zenodo.4905971.

[301]   H. E. Huxley. "A Personal View of Muscle and Motility Mechanisms." In: *Annual Review of Physiology* 58 (1996), pp. 1–19.

[302]   I. Matsubara. "X-Ray Diffraction Studies of the Heart." In: *Annual Review of Biophysics and Bioengineering* 9.1 (1980), pp. 81–105.

[303]   V. Lombardi, G. Piazzesi, M. Reconditi, M. Linari, L. Lucii, A. Stewart, Y.-B. Sun, P. Boesecke, T. Narayanan, T. Irving, and M. Irving. "X-ray Diffraction Studies of the Contractile Mechanism in Single Muscle Fibres." In: *Philosophical Transactions: Biological Sciences* 359.1452 (2004), pp. 1883–1893.

[304] Y. Ait-Mou, K. Hsu, G. P. Farman, M. Kumar, M. L. Greaser, T. C. Irving, and P. P. de Tombe. "Titin strain contributes to the Frank-Starling law of the heart by structural rearrangements of both thin- and thick-filament proteins." In: *Proceedings of the National Academy of Sciences* 113.8 (2016), pp. 2306–2311.

[305] M. Reconditi, M. Caremani, F. Pinzauti, J. D. Powers, T. Narayanan, G. J. M. Stienen, M. Linari, V. Lombardi, and G. Piazzesi. "Myosin filament activation in the heart is tuned to the mechanical task." In: *Proceedings of the National Academy of Sciences* 114.12 (2017), pp. 3240–3245.

[306] M. Okabe, Y. Kanzaki, H. Shimomura, F. Terasaki, T. Hayashi, K. Kawamura, and Y. Kitaura. "Backscattered Electron Imaging." In: *Cardiovascular Pathology* 9.2 (2000), pp. 103–109. DOI: 10.1016/S1054-8807(00)00028-4.

[307] Y. Kanzaki, F. Terasaki, M. Okabe, S. Fujita, T. Katashima, K. Otsuka, and N. Ishizaka. "Three-Dimensional Architecture of Cardiomyocytes and Connective Tissue in Human Heart Revealed by Scanning Electron Microscopy." In: *Circulation* 122.19 (2010), pp. 1973–1974. DOI: 10.1161/circulationaha.110.979815.

[308] J. S. Jones, D. M. Small, and N. Nishimura. "In Vivo Calcium Imaging of Cardiomyocytes in the Beating Mouse Heart With Multiphoton Microscopy." In: *Frontiers in Physiology* 9 (2018). DOI: 10.3389/fphys.2018.00969.

[309] H. Lichtenegger, M. Müller, O. Paris, C. Riekel, and P. Fratzl. "Imaging of the helical arrangement of cellulose fibrils in wood by synchrotron x-ray microdiffraction." In: *Journal of applied crystallography* 32.6 (1999), pp. 1127–1133.

[310] P. Fratzl and R. Weinkamer. "Nature's hierarchical materials." In: *Progress in Materials Science* 52.8 (2007), pp. 1263–1334.

[311] V. Lutz-Bueno, J. Zhao, R. Mezzenga, T. Pfohl, P. Fischer, and M. Liebi. "Scanning-SAXS of microfluidic flows: nanostructural mapping of soft matter." In: *Lab on a Chip* 16 (20 2016), pp. 4028–4035.

[312] M. Liebi, M. Georgiadis, A. Menzel, P. Schneider, J. Kohlbrecher, O. Bunk, and M. Guizar-Sicairos. "Nanostructure surveys of macroscopic specimens by small-angle scattering tensor tomography." In: *Nature* 527.7578 (2015), p. 349.

[313] C. Y. J. Hémonnot and S. Köster. "Imaging of Biological Materials and Cells by X-ray Scattering and Diffraction." In: *ACS Nano* 11.9 (2017), pp. 8542–8559.

[314] R. N. Wilke, M. Priebe, M. Bartels, K. Giewekemeyer, A. Diaz, P. Karvinen, and T. Salditt. "Hard x-ray imaging of bacterial cells: nano-diffraction and ptychographic reconstruction." In: *Opt. Express* 20.17 (2012), pp. 19232–19254. DOI: 10.1364/OE.20.019232.

[315] J.-D. Nicolas, S. Aeffner, and T. Salditt. "Radiation damage studies in cardiac muscle cells and tissue using microfocused X-ray beams: experiment and simulation." In: *Journal of Synchrotron Radiation* 26.4 (2019), pp. 980–990. DOI: 10.1107/S1600577519006817.

[316] J. Miao, P. Charalambous, J. Kirz, and D. Sayre. "Extending the methodology of x-ray crystallography to allow imaging of micrometre-sized non-crystalline specimens." In: *Nature* 400.6742 (1999), p. 342.

[317] K. A. Nugent. "Coherent methods in the X-ray sciences." In: *Advances in Physics* 59.1 (2010), pp. 1–99.

[318] J. A. Rodriguez, R. Xu, C.-C. Chen, Z. Huang, H. Jiang, A. L. Chen, K. S. Raines, A. P. Jr, D. Nam, L. Wiegart, C. Song, A. Madsen, Y. Chushkin, F. Zontone, P. J. Bradley, and J. Miao. "Three-dimensional coherent X-ray diffractive imaging of whole frozen-hydrated cells." In: *IUCrJ* 2.5 (2015), pp. 575–583. DOI: 10.1107/s205225251501235x.

[319] K. Giewekemeyer, P. Thibault, S. Kalbfleisch, A. Beerlink, C. M. Kewish, M. Dierolf, F. Pfeiffer, and T. Salditt. "Quantitative biological imaging by ptychographic x-ray diffraction microscopy." In: *Proceedings of the National Academy of Sciences* 107.2 (2010), pp. 529–534.

[320] A. Diaz, B. Malkova, M. Holler, M. Guizar-Sicairos, E. Lima, V. Panneels, G. Pigino, A. G. Bittermann, L. Wettstein, T. Tomizaki, et al. "Three-dimensional mass density mapping of cellular ultrastructure by ptychographic x-ray nanotomography." In: *Journal of structural biology* 192.3 (2015), pp. 461–469.

[321] C. A. Larabell and K. A. Nugent. "Imaging cellular architecture with x-rays." In: *Current opinion in structural biology* 20.5 (2010), pp. 623–631.

[322] K. Toischer et al. "Differential Cardiac Remodeling in Preload Versus Afterload." In: *Circulation* 122.10 (2010), pp. 993–1003. DOI: 10.1161/CIRCULATIONAHA.110.943431.

[323] U. Karlsson and R. L. Schultz. "Fixation of the central nervous system for electron microscopy by aldehyde perfusion." In: *Journal of Ultrastructure Research* 12.1-2 (1965), pp. 160–186. DOI: 10.1016/S0022-5320(65)80014-4.

[324]   B. D. Metscher. "MicroCT for comparative morphology: simple staining meth-
        ods allow high-contrast 3D imaging of diverse non-mineralized animal tis-
        sues." In: *BMC Physiol.* 9.1 (2009), p. 11.

[325]   M. Bartels, M. Krenkel, J. Haber, R. N. Wilke, and T. Salditt. "X-ray holographic
        imaging of hydrated biological cells in solution." In: *Physical review letters* 114.4
        (2015), p. 048103.

[326]   H.-Y. Chen, S. Hoffmann, and T. Salditt. "X-ray beam compression by tapered
        waveguides." In: *Applied Physics Letters* 106.19 (2015), p. 194105.

[327]   S. Hoffmann-Urlaub, P. Höhne, M. Kanbach, and T. Salditt. "Advances in
        fabrication of x-ray waveguides." In: *Microelectronic Engineering* 164 (2016),
        pp. 135–138.

[328]   M. Howells, T. Beetz, H. Chapman, C. Cui, J. Holton, C. Jacobsen, J. Kirz, E.
        Lima, S. Marchesini, H. Miao, D. Sayre, D. Shapiro, J. Spence, and D. Staro-
        dub. "An assessment of the resolution limitation due to radiation-damage in
        X-ray diffraction microscopy." In: *Journal of Electron Spectroscopy and Related
        Phenomena* 170.1-3 (2009), pp. 4–12.

[329]   B. L. Henke, E. M. Gullikson, and J. C. Davis. "X-Ray Interactions: Photoab-
        sorption, Scattering, Transmission, and Reflection at E = 50-30,000 eV, Z =
        1-92." In: *At. Data Nucl. Data Tables* 54.2 (1993), pp. 181–342.

[330]   W. Kühlbrandt. "Structure and function of mitochondrial membrane protein
        complexes." In: *BMC Biology* 13.1 (2015). DOI: 10.1186/s12915-015-0201-
        x.

[331]   N. Chaffey. "Alberts, B., Johnson, A., Lewis, J., Raff, M., Roberts, K. and Walter,
        P. Molecular biology of the cell. 4th edn." In: *Annals of Botany* 91.3 (2003),
        pp. 401–401. DOI: 10.1093/aob/mcg023.

[332]   A. V. Stepanov, E. V. Baidyuk, and G. A. Sakuta. "The features of mitochondria
        of cardiomyocytes from rats with chronic heart failure." In: *Cell and Tissue
        Biology* 11.6 (2017), pp. 458–465. DOI: 10.1134/s1990519x17060086.

[333]   N. Sun, M. Yazawa, J. Liu, L. Han, V. Sanchez-Freire, O. J. Abilez, E. G. Navar-
        rete, S. Hu, L. Wang, A. Lee, A. Pavlovic, S. Lin, R. Chen, R. J. Hajjar, M. P. Sny-
        der, R. E. Dolmetsch, M. J. Butte, E. A. Ashley, M. T. Longaker, R. C. Robbins,
        and J. C. Wu. "Patient-Specific Induced Pluripotent Stem Cells as a Model for
        Familial Dilated Cardiomyopathy." In: *Science Translational Medicine* 4.130
        (2012), 130ra47–130ra47. DOI: 10.1126/scitranslmed.3003552.

[334]   E. Lima, A. Diaz, M. Guizar-Sicairos, S. Gorelick, P. Pernot, T. Schleier, and
A. Menzel. "Cryo-scanning x-ray diffraction microscopy of frozen-hydrated
yeast." In: *Journal of Microscopy* 249.1 (2013), pp. 1–7. DOI: 10.1111/j.1365-
2818.2012.03682.x.

[335]   M. Beckers, T. Senkbeil, T. Gorniak, M. Reese, K. Giewekemeyer, S.-C. Gleber,
T. Salditt, and A. Rosenhahn. "Chemical Contrast in Soft X-Ray Ptychogra-
phy." In: *Phys. Rev. Lett.* 107.20 (2011), p. 208101. DOI: 10.1103/PhysRevLett.
107.208101.

[336]   M. Tiburcy et al. "Defined Engineered Human Myocardium With Advanced
Maturation for Applications in Heart Failure Modeling and RepairClinical Per-
spective." In: *Circulation* 135.19 (2017), pp. 1832–1847.

[337]   M. Shahriyari, M. R. Islam, M. S. Sakib, A. Rika, D. Krüger, L. Kaurani, H.
Anandakumar, O. Shomroni, M. Schmidt, G. Salinas, A. Unger, W. A. Linke,
J. Zschüntzsch, J. Schmidt, A. Fischer, W.-H. Zimmermann, and M. Tiburcy.
"Human engineered skeletal muscle of hypaxial origin from pluripotent stem
cells with advanced function and regenerative capacity." In: (2021). DOI: 10.
1101/2021.07.12.452030.

[338]   W.-H. Zimmermann. "Tissue engineered heart repair from preclinical models
to first-in-patient studies." In: *Current Opinion in Physiology* 14 (2020), pp. 70–
77. DOI: 10.1016/j.cophys.2020.02.001.

[339]   U. Hanses, M. Kleinsorge, L. Roos, G. Yigit, Y. Li, B. Barbarics, I. El-Battrawy,
H. Lan, M. Tiburcy, R. Hindmarsh, C. Lenz, G. Salinas, S. Diecke, C. Müller, I.
Adham, J. Altmüller, P. Nürnberg, T. Paul, W.-H. Zimmermann, G. Hasenfuss,
B. Wollnik, and L. Cyganek. "Intronic CRISPR Repair in a Preclinical Model of
Noonan Syndrome–Associated Cardiomyopathy." In: *Circulation* 142.11 (2020),
pp. 1059–1076. DOI: 10.1161/circulationaha.119.044794.

[340]   M. Reichardt, J.-D. Nicolas, and T. Salditt. "Scanning X-ray diffraction data of
human atrial appendage tissue recorded at the GINIX endstation of the P10
beamline, PETRAIII storage ring, DESY, Hambug."

[341]   A. Reiterer, H. F. Jakob, S. E. Stanzl-Tschegg, and P. Fratzl. "Spiral angle of
elementary cellulose fibrils in cell walls ofPicea abies determined by small-
angle x-ray scattering." In: *Wood Science and Technology* 32.5 (1998), pp. 335–
345. DOI: 10.1007/bf00702790.

[342] R. Seidel, A. Gourrier, M. Kerschnitzki, M. Burghammer, P. Fratzl, H. S. Gupta, and W. Wagermaier. "Synchrotron 3D SAXS analysis of bone nanostructure." In: *Bioinspired, Biomimetic and Nanobiomaterials* 1.2 (2012), pp. 123–131. DOI: `10.1680/bbn.11.00014`.

[343] M. Georgiadis, M. Guizar-Sicairos, A. Zwahlen, A. J. Trüssel, O. Bunk, R. Müller, and P. Schneider. "3D scanning SAXS: A novel method for the assessment of bone ultrastructure orientation." In: *Bone* 71 (2015), pp. 42–52. DOI: `10.1016/j.bone.2014.10.002`.

[344] F. Schaff, M. Bech, P. Zaslansky, C. Jud, M. Liebi, M. Guizar-Sicairos, and F. Pfeiffer. "Six-dimensional real and reciprocal space small-angle X-ray scattering tomography." In: *Nature* 527.7578 (2015), pp. 353–356. DOI: `10.1038/nature16060`.

[345] R. F. Thompson, M. Walker, C. A. Siebert, S. P. Muench, and N. A. Ranson. "An introduction to sample preparation and imaging by cryo-electron microscopy for structural biology." In: *Methods* 100 (2016), pp. 3–15. DOI: `10.1016/j.ymeth.2016.02.017`.

[346] R. Danev, H. Yanagisawa, and M. Kikkawa. "Cryo-Electron Microscopy Methodology: Current Aspects and Future Directions." In: *Trends in Biochemical Sciences* 44.10 (2019), pp. 837–848. DOI: `10.1016/j.tibs.2019.04.008`.

[347] K. Giewekemeyer, C. Hackenberg, A. Aquila, R. Wilke, M. Groves, R. Jordanova, V. Lamzin, G. Borchers, K. Saksl, A. Zozulya, M. Sprung, and A. Mancuso. "Tomography of a Cryo-immobilized Yeast Cell Using Ptychographic Coherent X-Ray Diffractive Imaging." In: *Biophysical Journal* 109.9 (2015), pp. 1986–1995. DOI: `10.1016/j.bpj.2015.08.047`.

[348] T. Beetz, M. Howells, C. Jacobsen, C.-C. Kao, J. Kirz, E. Lima, T. Mentes, H. Miao, C. Sanchez-Hanke, D. Sayre, and D. Shapiro. "Apparatus for X-ray diffraction microscopy and tomography of cryo specimens." In: *Nuclear Instruments and Methods in Physics Research Section A: Accelerators, Spectrometers, Detectors and Associated Equipment* 545.1-2 (2005), pp. 459–468.

[349] G. Schneider, P. Guttmann, S. Rehbein, S. Werner, and R. Follath. "Cryo X-ray microscope with flat sample geometry for correlative fluorescence and nanoscale tomographic imaging." In: *J. Struct. Biol.* 177.2 (2012), pp. 212–223.

[350]   M. C. D. Almeida, F. Lopes, P. Fontes, F. Barra, R. Guimaraes, and V. Vil-
        hena. "Ungulates heart model: a study of the Purkinje network using India
        ink injection, transparent specimens and computer tomography." In: *Anatom-
        ical Science International* 90.4 (2014), pp. 240–250. DOI: 10.1007/s12565-
        014-0255-9.

[351]   M. Reichardt, J. Frohn, and T. Salditt. "Phase-contrast tomography data of
        murine hearts recorded at the TOMCAT beamline (Swiss Light Source, Paul
        Scherrer Institute, Villigen, Switzerland)."

[352]   M. Reichardt, J. Frohn, and T. Salditt. "Phase-contrast tomography data of
        murine hearts recorded at the ID17 beamline (ESRF, Grenoble, France)."

[353]   A.-F. Jebran, I. Kutschka, and W.-H. Zimmermann. "Tissue engineered heart
        repair." In: *Emerging Technologies for Heart Diseases*. Elsevier, 2020, pp. 285–
        290. DOI: 10.1016/b978-0-12-813706-2.00014-2.

[354]   W.-H. Zimmermann. "Remuscularization of the failing heart." In: *The Journal
        of Physiology* 595.12 (2017), pp. 3685–3690. DOI: 10.1113/jp273098.

[355]   C. T. Badea, E. Schreibmann, and T. Fox. "A registration based approach for
        4D cardiac micro-CT using combined prospective and retrospective gating."
        In: *Medical Physics* 35.4 (2008), pp. 1170–1179. DOI: 10.1118/1.2868778.

[356]   C. Badea, L. W. Hedlund, and G. A. Johnson. "Micro-CT with respiratory and
        cardiac gating." In: *Medical Physics* 31.12 (2004), pp. 3324–3329. DOI: 10.1118/
        1.1812604.

Authors contribution

Four peer-reviewed articles are considered for this cumulative thesis to fulfill the rules and regulations of the PhD program *GGNB* that is part of the Georg-August University School of Science (GAUSS):

(1) <u>M. Reichardt</u>, M. Töpperwien, A. Khan, F. Alves, and T. Salditt, "Fiber orientation in a whole mouse heart reconstructed by laboratory phase-contrast micro-CT", Journal of Medical Imaging, **7**(2),023501 (2020).

(2) <u>M. Reichardt</u>, J. Frohn, A. Khan, F. Alves, and T. Salditt, "Multi-scale X-ray phase-contrast tomography of murine heart tissue", Biomedical Optics Express, **11**(5),2633-2651 (2020).

(3) <u>M. Reichardt</u>, P. Møller Jensen, V. Andersen Dahl, A. Bjorholm Dahl, M. Ackermann, H. Shah, F. Länger, C. Werlein, M. Kühnel and D. Jonigk, T. Salditt, "3D virtual Histopathology of Cardiac Tissue from Covid-19 Patients based on Phase-Contrast X-ray Tomography", eLife 10:e71359 (2021)

(4) <u>M. Reichardt</u>, C. Neuhaus, J.-D. Nicolas, M. Bernhardt, K. Toischer and T. Salditt, "X-ray structural analysis of single adult cardiomyocytes: tomographic imaging and micro-diffraction", Biophysical Journal,**119**(7),1309-1323 (2020).

Article (1) introduces the Fourier-Transform-based analysis of the structural arrangement of cardiac tissue developed by MR and TS. The analysis routines have been written by MR. The cardiac samples were provided and prepared by AM and FA. Data acquisition, phase retrieval and tomographic reconstruction was performed by MR with assistance by MT. The results were discussed by all authors. MR and TS wrote the manuscript.

Article (2) describes an experimental multi-scale tomography setup at the GINIX endstation (P10 bamline, PETRAIII storage ring, DESY Hamburg), which allows to investigate biological samples at effective voxel sizes from 6μm down to less than 200 nm in three different configurations. The experimental setups were designed, further developed and expanded by MR, JF and TS. The cardiac samples were provided

and prepared by AM and FA. MR analyzed the data in terms of phase retrieval, tomographic reconstruction and analysis of the arrangements of the cardiac structures. MR and TS wrote the manuscript. All authors read and discussed the final results.

Article (3) presents a 3d virtual histology approach of human cardiac samples succumbed to Covid-19, coxachie myocarditis and influenza. The heart tissue samples were provided by DJ and MK. Tomographic data acquisition was carried out by MR and TS. MR conducted the phase retrieval, tomographic reconstruction. The structural tensor analysis was performed by MR and PMJ using a MATLAB implementation by PMJ. Statistical analysis was performed by MR and TS. PMJ implemented the deep learning network for the segmentation of the vascular system under the supervision of VAD and ABD. MR and PMJ performed the training of the network. MA performed the SEM image acquisition. CW, HS and FL performed the histological investigations. MR and TS wrote the manuscript. All authors read the manuscript and approved the final version of the results.

Article (4) shows in a proof of concept experiment, how to image isolated cadiomyocytes on the sub-cellular level using tomographic imaging and micro-diffraction. TS and MR designed research. KT developed adult cardiomyocyte protocols and contributed expertise. MR and TS carried out the x-ray holography experiments. MR, CN, TS, JDN, carried out the diffraction experiments. JDN wrote analysis software. MR carried out the phase retrieval and tomographic reconstruction, CN, JDN carried out the SAXS analysis, supervised by TS. MB and MR prepared the freeze-dried cells and recorded the florescent microscopy data. MR, TS, and CN wrote the article; all authors read the final version.

List of publications

(1) <u>M. Reichardt</u>, P. Møller Jensen, V. Andersen Dahl, A. Bjorholm Dahl, M. Ackermann, H. Shah, F. Länger, C. Werlein, M. Kühnel and D. Jonigk, T. Salditt, "3D virtual Histopathology of Cardiac Tissue from Covid-19 Patients based on Phase-Contrast X-ray Tomography", eLife 10:e71359 (2021).

(2) J. Frohn, D. Pinkert-Leetsch, J. Missbach-Güntner, <u>M. Reichardt</u>, M. Osterhoff, F. Alves, T. Salditt, "3D virtual histology of human pancreatic tissue by multiscale phase-contrast X-ray tomography", Journal of Synchrotron Radiation, **27**, 1707–1719 (2020).

(3) <u>M. Reichardt</u>, M. Töpperwien, A. Khan, F. Alves, and T. Salditt, "Fiber orientation in a whole mouse heart reconstructed by laboratory phase-contrast micro-CT", Journal of Medical Imaging, **7**(2),023501 (2020).

<u>M. Reichardt</u>, M. Töpperwien, A. Khan, F. Alves, and T. Salditt, "Fiber orientation in a whole mouse heart reconstructed by laboratory phase-contrast micro-CT", Proceedings SPIE Volume 11113, Developments in X-Ray Tomography XII, 111130S (2019).

(4) <u>M. Reichardt</u>, J. Frohn, A. Khan, F. Alves, and T. Salditt, "Multi-scale X-ray phase-contrast tomography of murine heart tissue", Biomedical Optics Express, **11**(5),2633-2651 (2020).

(5) M. Eckermann*, J. Frohn*, <u>M. Reichardt</u>*, M. Osterhoff, M. Sprung, F. Westermeier, A. Tzankov, C. Werlein, M. Kühnel and D. Jonigk, T. Salditt, "3d Virtual Patho-Histology of Lung Tissue from Covid-19 Patients based on Phase Contrast X-ray Tomography", eLife, **9**:e60408 (2020).

(6) <u>M. Reichardt</u>, C. Neuhaus, J.-D. Nicolas, M. Bernhardt, K. Toischer and T. Salditt, "X-ray structutral analysis of single adult cardiomyocytes: tomographic imaging and micro-diffraction", Biophysical Journal, **119**(7),1309-1323 (2020).

(7) <u>M. Reichardt</u>*, J. Frohn*, M. Töpperwien, J.-D. Nicolas, A. Markus, F. Alves, T. Salditt, "Nanoscale holographic tomography of heart tissue with x-ray waveguide optics", Proceedings SPIE 10391, Developments in X-Ray Tomography XI,

1039105 (2017).

(8) M. A. Markus, S. Borowik, M. Reichardt, G. Tromba, F. Alves, C. Dullin, "X-ray-based lung function measurement reveals persistent loss of lung tissue elasticity in mice recovered from allergic airway inflammation", American Journal of Physiology-Lung Cellular and Molecular Physiology, **313**(5), L763-L771 (2017).

* shared first authorship

Danksagung

An dieser Stelle möchte ich mich bei allen bedanken, die mich während der Zeit meiner Doktorarbeit unterstützt haben.

Zuächst gilt mein außerordentlicher Dank Prof. Tim Salditt für die erstklassige Betreuung meiner Arbeit. Die vielen fruchtbaren, fachlichen Diskussionen, in denen eine unglaubliche Begeisterung und Faszination vermittelt wurde, haben meine Motivation stets gefördert und zu dem Gelingen dieser Arbeit beigetragen. Vor allem möchte ich mich für das fortwährende Vertrauen seit Beginn meiner Masterarbeit und die Möglichkeit der Gestaltung von Projekten im Institut für Röntgenphysik bedanken.

Ein besonderer Dank gilt auch Prof. Dr. Stephan Luther und Prof. Dr. Wolfram-Hubertus Zimmermann für die Betreuung meiner Arbeit im Rahmen meines Prüfungskommitees. Des Weiteren danke ich Prof. Dr. Dr. hc. Eberhard Bodenschatz, Prof. Dr. Timo Betz sowie Prof. Dr. Frauke Alves für die Teilnahme an meiner Prüfungskommission. In diesem Zuge möchte ich mich noch einmal ganz herzlich bei der gesamten AG Alves für die schöne Zusammenarbeit sowie die Einladungen zu Institutsveranstaltungen bedanken. Ausdrücklich möchte ich mich Andrea Markus, Amara Khan und Bärbel Heidrich für die Unterstützung bei Probenpräparation der Herzproben bedanken. Ein weiterer Dank gilt der Arbeitsgruppe von Prof. Dr. Karl Toischer und insbesondere Alessia Kretschmar für die Bereitstellung der isolierten Kardiomyozyten.

Ich möchte allen Mitgliedern des Instituts für Röntgenphysik, aktiv und ehemalig, für die gemeinsame Zeit und das tolle Arbeitsklima sowie für die vielen gemeinsamen Veranstaltungen, die über den Arbeitsalltag hinaus gingen, herzlich danken. Insbesondere danke ich meinen langjährigen Bürokolleginnen Marina Eckermann und Dr. Mareike Töpperwien und dem weiteren Tomo-Team bestehend aus Jasper Frohn, Jannis Schäper, Jakob Reichmann, Paul Meyer und Anne Schnurpfeil, sowie Dr. Malte Vassholz und Leon Lohse für die interessanten Diskussionen. Dr. Marten Bernhardt, Dr. Jan-David Nicolas und Charlotte Neuhaus möchte ich für die Unterstützung bei der Probenpräparation sowie bei der Datenauswertung der Diffraktionsexperimente

Curriculum Vitae

Personal Information

Name:	Marius Christoph Gerald Reichardt
Born:	July 15, 1991 in Buxtehude
Nationality:	German

Studies

since 04/2018	Doctoral student in physics, Institut für Röntgenphysik, Group of Prof. Tim Salditt Georg-August-Universität Göttingen, Germany
03/2018	Master's thesis: *Multi-modal x-ray analysis of cardiac tissue*
10/2015 – 03/2018	Master of science in physics with major in biophysics and complex systems Georg-August-Universität Göttingen, Germany
09/2015	Bachelor's thesis: *Analysis of fluiddynamics in the narsal cavity of todpoles of the African clawed frog (larval Xenopus laevis) using line illumination microscopy*
10/2012 – 09/2015	Bachelor of science in physics Georg-August-Universität Göttingen, Germany
06/2011	Abitur (*general qualification for university entrance*) Gymnasium Buxtehude Süd, Germany

Göttingen, 30.08.2021

The cardiac function relies on an intricate molecular and cellular three-dimensional (3d) architecture of a complex, dense and co-dependent cellular network. Structural alterations of the cardiac structure can affect its essential function and lead to severe dysfunction of the organ. Cardiovascular diseases are the main cause of death worldwide with a rising incidence.

However, it is not possible to give a generalized answer how the heart is formed. Up to now, cardiac structure as well as physiologic and disease-related tissue alterations of the tissue are mainly investigated by established 2d imaging methods such as optical microscopy or electron microscopy.

This work presents a multiscale and multimodal X-ray imaging approach, which allows to probe the heart structure from the scale of entire intact murine hearts to the molecular organisation of the sarcomer structure.

While the molecular structure of the actomyosin complex is probed by scanning X-ray diffraction, the 3d arrangement of the cellular network is investigated by propagation-based X-ray phase-contrast tomography. In this context, the concept of 3d virtual histology of cardiac tissue by X-ray phase-contrast tomography using laboratory sources as well as highly coherent synchrotron radiation is being further developed.

GEORG-AUGUST-UNIVERSITÄT
GÖTTINGEN

Universitätsverlag Göttingen